The LHC Transverse Coupled-Bunch Instability

THÈSE N^{O} 5305 (2012)

PRÉSENTÉE LE 16 MARS 2012

À LA FACULTÉ DES SCIENCES DE BASE
LABORATOIRE DE PHYSIQUE DES ACCÉLÉRATEURS DE PARTICULES
PROGRAMME DOCTORAL EN PHYSIQUE

ÉCOLE POLYTECHNIQUE FÉDÉRALE DE LAUSANNE

POUR L'OBTENTION DU GRADE DE DOCTEUR ÈS SCIENCES

PAR

Nicolas MOUNET

acceptée sur proposition du jury:

Prof. O. Schneider, président du jury
Prof. L. Rivkin, Dr E. Métral, directeurs de thèse
Dr A. Burov, rapporteur
Prof. M. Q. Tran, rapporteur
Prof. V. Vaccaro, rapporteur

ÉCOLE POLYTECHNIQUE
FÉDÉRALE DE LAUSANNE

Suisse
2012

To Iriska, Alice and Sophie

Acknowledgements

Three years ago, engaging in this PhD,
Was still at the stage of an interesting dream
I knew not what was a collider nor a beam
Yet several people took the risk of helping me.
Among them, for sure, Elias Métral
Holds a place that is most special
To express how wonderful his supervision
Was to me, lies beyond my imagination.

Jean-Louis Basdevant, Francesco Mauri and Nicola Marzari
Devoted their time to give me a chance
To work at CERN, this temple of science.
My supervisor Leonid Rivkin
Gave great support and tutoring
With him was simply amazing.
Most grateful am I also to Gianluigi Arduini
For such a warm welcome within his section
So rarely have I felt so pleasant an integration.

At CERN I felt quite at ease with no delay
Thanks to an exceptional team, who accepted me right away
Benoît Salvant, Rama Calaga, Giulia Bellodi
Simon White, Rogelio Tomas, Tatiana Pieloni
Giovanni Rumolo, are to me a second family,
Later extended with Carlo Zannini, Nicolo Biancacci
Xavier Buffat and Kevin Li, all in the same wonderful spirit.
I also thank the good fortune that leads my path meet
The one of Alexey Burov, Vittorio Vaccaro and Bruno Zotter.
Now philosophy, history and physics together
Blend in my mind affording perfect protection
Against a fit of indigestion of Bessel functions.

Acknowledgements

Many people's contributions were needed to obtain
Experimental results, specially those of Verena Kain
And Daniel Valuch. Oliver Aberle, Ralph Assmann,
Alessandro Bertarelli, Roderik Bruce, Adriana Rossi, Daniel Wollmann
Were precious sources of data
As were also Riccardo De Maria,
Stéphane Fartoukh, Alexej Grudiev,
Wolfgang Höfle, Emanuele Laface
and Stefano Redaelli. I reserve a special place
To our main source of wisdom and good proverbs
The living memory of CERN, Fritz Caspers.

Je voudrais maintenant remercier
Ceux qui m'ont toujours accompagné
Mes amis, mes frères et mes parents
Et tous leurs encouragements.

Quant à l'immense dévouement d'Irina
Rien ne l'égale en élégance
Si ce n'est peut-être la patience
d'Alice et Sophie, si grandes déjà.

N. M., Lausanne, February 2012

Résumé

Ce travail de thèse traite du problème des instabilités transverses de paquets couplés dues à l'impédance du Grand Collisionneur de Hadrons (LHC), qui sont susceptibles de limiter l'opération de la machine. Ce type d'instabilités est traité ici à l'aide de nouvelles théories et de nouveaux outils algorithmiques. Une approche relativement complète est proposée ici, depuis le calcul des impédances et fonctions de sillage de certains éléments de la machine, jusqu'à l'étude de la dynamique du faisceau. En premier lieu, de nouveaux résultats théoriques sont obtenus concernant l'impédance de couplage au faisceau des structures axisymmétriques de dimension deux, généralisant les théories de Zotter, ainsi qu'une nouvelle théorie pour les structures plates de dimension deux. En outre, une nouvelle approche est trouvée pour calculer les fonctions de sillage à partir des expressions analytiques des impédances ainsi obtenues, surmontant de fait les limites rencontrées lorsqu'une transformée de Fourier discrète standard est utilisée. Ces résultats sont ensuite utilisés pour obtenir le modèle d'impédance et de fonction de sillage du LHC, basé sur l'impédance résistive de différents éléments (collimateurs, écrans de faisceau et tube à vide) ainsi que sur l'estimation de certaines contributions additionnelles de type géométrique. Finalement, un programme de simulation de la dynamique de macroparticules sous l'effet de champs de sillage, dénommé HEADTAIL et préexistant à cette étude, est amélioré afin de rendre possible la simulation de trains multipaquets, et une technique d'analyse spectrale est trouvée afin de faciliter l'analyse des données de sorties du programme, permettant ainsi l'obtention des décalages complexes du nombre d'onde des modes instables présents dans la simulation. Ces théories et outils sont utilisées pour obtenir de nouveaux résultats concernant les instabilités transverses de paquets couplés du LHC, permettant de démontrer l'impact relativement faible sur ce type d'instabilités, du nombre de paquets dans un train lorsque l'espace entre les paquets est fixé, ainsi que l'existence de telles instabilités exhibant également un mouvement à l'intérieur des paquets, ces instabilités étant plus critiques que leur équivalent à paquet unique. Une vérification complète de la procédure dans sa totalité (en particulier les théories des impédances, le modèle d'impédance du LHC et le code de simulation) est aussi conduite en comparant les résultats de simulations avec des mesures dans le LHC, donnant un très bon accord à l'énergie d'injection et un ordre de magnitude correct à 3.5 TeV/c. Pour finir, plusieurs prédictions sont obtenues concernant la stabilité à une énergie de 7 TeV/c qui sera atteinte lors de l'opération future de la machine, dans le cas d'un faisceau contenant 1404 paquets espacés de 50 ns, révélant que le seuil d'instabilité couplée transverse de paquets couplés est bien au-dessus de l'intensité ultime prévue, mais environ 20% plus petite que son équivalent en paquet unique. Les études de stabilité avec les octupoles Landau à leur courant maximum montrent que le faisceau reste stable à intensité nominale lorsque $Q' = 2$ dans les deux plans, à condition que les distributions transverses soient Gaussiennes. En revanche, pour une intensité ultime, le faisceau est instable aussi bien pour $Q' = 0$ que pour $Q' = 2$, ainsi qu'à

intensité nominale pour $Q' = 0$, même lorsque les octupoles sont à leur courant maximum.

Mots-clés : Accélérateur, faisceaux à haute intensité, effets collectifs, impédance, champ de sillage, collimateur, dynamique du faisceau, instabilités de paquets couplés, modes intrapaquets, instabilité couplée transverse de paquets couplés.

Abstract

In this thesis, the problem of the transverse coupled-bunch instabilities created by the Large Hadron Collider (LHC) beam-coupling impedance, that can possibly limit the machine operation, is addressed thanks to several new theories and tools. A rather complete vision of the problem is proposed here, going from the calculation of the impedances and wake functions of individual machine elements, to the beam dynamics study. Firstly, new results are obtained in the theory of the beam-coupling impedance for an axisymmetric two-dimensional structure, generalizing Zotter's theories, and a new general theory is derived for the impedance of an infinite flat two-dimensional structure. Then, a new approach has been found to compute the wake functions from such analytically obtained beam-coupling impedances, overcoming limitations that could be met with standard discrete Fourier transform procedures. Those results are then used to obtain an impedance and wake function model of the LHC, based on the (resistive-) wall impedances of various contributors (collimators, beam screens and vacuum pipe) and additional estimations of the geometrical impedance contributions. Finally, the existing code HEADTAIL, which is a macroparticle simulation code for beam dynamics studies with wake fields, is improved to make possible the simulation of multibunch trains, and a spectral analysis technique is found to facilitate the analysis of the output given by this code, giving the complex tune shifts of the unstable modes present in a simulation. All those theories and tools are used to obtain new results concerning the LHC transverse coupled-bunch instabilities, demonstrating the rather small impact on coupled-bunch instabilities of the number of bunches in a train when the bunch spacing is fixed, and the existence of coupled-bunch modes with intrabunch motion which are more critical than their single-bunch counterparts. A full verification of the complete procedure (impedance theories, impedance model and simulation code) is also performed by comparing the simulation results with actual measurements in the LHC, giving a very good agreement at injection energy and a correct order of magnitude at 3.5 TeV/c. In the end, several predictions concerning the beam stability at the future 7 TeV/c operation of the machine are performed in the case of 50 ns spacing (1404 bunches), revealing that the coupled-bunch transverse mode coupling instability threshold is far above the ultimate bunch intensity but about 20% smaller than its single-bunch counterpart. Stability studies with Landau octupoles at their maximum currents reveal that the beam remains stable at nominal intensity with $Q' = 2$ in both planes, provided the particle transverse distributions are Gaussian. At ultimate intensity with either $Q' = 0$ or $Q' = 2$, or at nominal intensity when the chromaticity is zero, the beam happens to be unstable, even with the octupoles at their maximum currents.

Keywords: Accelerator, high-intensity beam, collective effects, impedance, wake fields, collimator, beam dynamics, coupled-bunch instabilities, headtail modes, coupled-bunch transverse mode coupling.

Contents

List of Figures

List of Tables

List of notations

$(\vec{e}_r, \vec{e}_\theta, \vec{e}_s)$	Basis vectors in the cylindrical system of coordinates 7
$(\vec{e}_x, \vec{e}_y, \vec{e}_s)$	Basis vectors in the cartesian system of coordinates 7
(p)	Superscript added to all the quantities related to the layer p 9
(r, θ, s)	Cylindrical coordinates 6
(x, y, s)	Cartesian coordinates 5
(x', y', s)	Cartesian coordinates associated to jaws oriented with a certain skew angle α 56
$*$	Complex conjugate 8
a_1	Offset of the source macroparticle from the center of the structure 6
a_2	Offset of the test particle from the center of the structure 22
b	Inner radius of the beam pipe, or half gap of the flat chamber 9
$b^{(p)}$	Outer radius, or vertical coordinate at the outer boundary, of the layer p 9
$\vec{B}$	$\mu\vec{H}$ i.e. magnetic induction (components: B_x, B_y, B_s or B_r, B_θ, B_s) 7
c	Speed of light in vacuum (299792458 m/s) 4
$\mathscr{C}$	$\frac{jQ\omega\mu_0}{2\pi\beta^2\gamma^2}$ 15
$C_{e+}^{(p)}$	Constant in front of the exponential having a plus sign in its argument, in $E_s^{c(p)}$ 30
$C_{e-}^{(p)}$	Constant in front of the exponential having a minus sign in its argument, in $E_s^{c(p)}$ 30
$C_{g+}^{(p)}$	Constant in front of the exponential having a plus sign in its argument, in $G_s^{s(p)}$ 32
$C_{g-}^{(p)}$	Constant in front of the exponential having a minus sign in its argument, in $G_s^{s(p)}$ 32
$C_{h+}^{(p)}$	Constant in front of the exponential having a plus sign in its argument, in $H_s^{s(p)}$ 30
$C_{h-}^{(p)}$	Constant in front of the exponential having a minus sign in its argument, in $H_s^{s(p)}$ 30
$C_{Ie}^{m(p)}$	Constant in front of the modified Bessel function of the first kind, in $E_s^{m,c(p)}$ 14
$C_{Ke}^{m\ (p)}$	Constant in front of the modified Bessel function of the second kind, in $E_s^{m,c(p)}$ 14
$C_{Ig}^{m(p)}$	Constant in front of the modified Bessel function of the first kind, in $G_s^{m,s(p)}$ 16
$C_{Kg}^{m\ (p)}$	Constant in front of the modified Bessel function of the second kind, in $G_s^{m,s(p)}$ 16
$C_{Ih}^{m(p)}$	Constant in front of the modified Bessel function of the first kind, in $H_s^{m,s(p)}$ 14
$C_{Kh}^{m\ (p)}$	Constant in front of the modified Bessel function of the second kind, in $H_s^{m,s(p)}$ 14
d	Depth (or thickness) of a collimator jaw 55
$\vec{D}$	Electric displacement (components: D_x, D_y, D_s or D_r, D_θ, D_s) 7
e	Elementary charge ($1.60218 \cdot 10^{-19}$ C) 84
$\vec{E}$	Electric field (components: E_x, E_y, E_s or E_r, E_θ, E_s) 7
$\vec{E}^c$	Cosine Fourier transform along x of $\vec{E}$ (components: E_x^c, E_y^c, E_s^c) 27
$\vec{E}^{m,c}$	m^{th} cosine coef. of the Fourier series expansion of $\vec{E}$ (components: $E_r^{m,c}$, $E_\theta^{m,c}$, $E_s^{m,c}$) ... 10
$\vec{E}^{m,s}$	m^{th} sine coef. of the Fourier series expansion of $\vec{E}$ (components: $E_r^{m,s}$, $E_\theta^{m,s}$, $E_s^{m,s}$) 10
$\vec{E}^s$	Sine Fourier transform along x of $\vec{E}$ (components: E_x^s, E_y^s, E_s^s) 27

$\hat{\vec{E}}$	Fourier transform along s of $\vec{E}$ 9
$\hat{\vec{E}}^{m,c}$	m^{th} cosine coef. of the Fourier series expansion of $\hat{\vec{E}}$ (components: $\hat{E}_r^{m,c}$, $\hat{E}_\theta^{m,c}$, $\hat{E}_s^{m,c}$) 9
$\hat{\vec{E}}^{m,s}$	m^{th} sine coef. of the Fourier series expansion of $\hat{\vec{E}}$ (components: $\hat{E}_r^{m,s}$, $\hat{E}_\theta^{m,s}$, $\hat{E}_s^{m,s}$) 9
$\tilde{\vec{E}}^c$	Cosine Fourier transform along x of $\tilde{\vec{E}}$ (components: $\tilde{E}_x^c$, $\tilde{E}_y^c$, $\tilde{E}_s^c$) 26
$\tilde{\vec{E}}^s$	Sine Fourier transform along x of $\tilde{\vec{E}}$ (components: $\tilde{E}_x^s$, $\tilde{E}_y^s$, $\tilde{E}_s^s$) 26
$E_s^{vac,SC}$	Direct space charge part of E_s in the vacuum region 21
$E_s^{vac,W}$	Wall part of E_s in the vacuum region 22
f_r	Cut-off frequency of the LHC vacuum chamber. 71
$\vec{F}$	Electromagnetic (or Lorentz) force (components: F_x, F_y, F_s or F_r, F_θ, F_s)) 19
$\vec{G}$	$Z_0\vec{H}$ (components: G_x, G_y, G_s or G_r, G_θ, G_s) 15
h	Harmonic number (number of RF buckets in the total circumference) 92
$\vec{H}$	Magnetic field (components: H_x, H_y, H_s or H_r, H_θ, H_s) 7
$\vec{H}^c$	Cosine Fourier transform along x of $\vec{H}$ (components: H_x^c, H_y^c, H_s^c) 27
$\vec{H}^{m,c}$	m^{th} cosine coef. of the Fourier series expansion of $\vec{H}$ (components: $H_r^{m,c}$, $H_\theta^{m,c}$, $H_s^{m,c}$) . 10
$\vec{H}^{m,s}$	m^{th} sine coef. of the Fourier series expansion of $\vec{H}$ (components: $H_r^{m,s}$, $H_\theta^{m,s}$, $H_s^{m,s}$) 10
$\vec{H}^s$	Sine Fourier transform along x of $\vec{H}$ (components: H_x^s, H_y^s, H_s^s) 27
$\hat{\vec{H}}$	Fourier transform along s of $\vec{H}$ 9
$\hat{\vec{H}}^{m,c}$	m^{th} cosine coef. of the Fourier series expansion of $\hat{\vec{H}}$ (components: $\hat{H}_r^{m,c}$, $\hat{H}_\theta^{m,c}$, $\hat{H}_s^{m,c}$) .. 9
$\hat{\vec{H}}^{m,s}$	m^{th} sine coef. of the Fourier series expansion of $\hat{\vec{H}}$ (components: $\hat{H}_r^{m,s}$, $\hat{H}_\theta^{m,s}$, $\hat{H}_s^{m,s}$) 9
$\tilde{\vec{H}}^c$	Cosine Fourier transform along x of $\tilde{\vec{H}}$ (components: $\tilde{H}_x^c$, $\tilde{H}_y^c$, $\tilde{H}_s^c$) 26
$\tilde{\vec{H}}^s$	Sine Fourier transform along x of $\tilde{\vec{H}}$ (components: $\tilde{H}_x^s$, $\tilde{H}_y^s$, $\tilde{H}_s^s$) 26
IP	Interaction point, in the LHC (IP1, IP2, IP5 and IP8) 179
IR	Insertion region, in the LHC (IR1, IR2, IR3, IR4, IR5, IR6, IR7 and IR8) 70
I_ν	Modified Bessel function of the first kind of order ν 12
$\Im$	Imaginary part of a complex number 8
j	Imaginary constant ($\sqrt{-1}$) 6
J	Current density of the source macroparticle (along the s axis) 7
k	Longitudinal wave number 6
k_x	Horizontal wave number 26
k_y	Vertical wave number 29
K_ν	Modified Bessel function of the second kind of order ν 12
L	Length of the flat or cylindrical chamber (along the s axis) 22
m	Azimuthal mode number of the source 9
m_e	Electron mass ($9.10938 \cdot 10^{-31}$ kg) 180
M	Number of layers under $y = y_1$ (flat chamber) 25
n_{MP}	Number of macroparticles per bunch in HEADTAIL 92
n_{sl}	Number of slices per bunch in HEADTAIL 84
n_{wake}	Number of preceding turns used to compute the wake field kicks, in HEADTAIL 84
N	Number of layers above $y = y_1$ (flat chamber) or outside $r = a_1$ (axisymmetric chamber) . 9
N_b	Number of elementary particles per bunch (also called intensity) 91
p_0	Design momentum ($m\gamma v$) 75
q	Test particle charge 19
Q	Source macroparticle charge 5

$Z_y^{Wall,0}$	Constant term in the vertical wall impedance 41
$Z_y^{Wall,dip}$	Vertical dipolar wall impedance 25
$Z_y^{Wall,quad}$	Vertical quadrupolar wall impedance 25
α	Skew angle of a collimator 55
α_{mn}	Coef. of the decomposition of $E_s^{vac,W}$ into azimuthal modes for a flat chamber 38
α_p	Momentum compaction factor 91
α_{TE}^m	${C_{Ig}^{(1)}}^m / {C_{Ke}^{(1)}}^m$ (axisymmetric chamber) 19
α_{TM}^m	$-{C_{Ie}^{(1)}}^m / {C_{Ke}^{(1)}}^m$ (axisymmetric chamber) 19
β	Relativistic velocity factor of the beam 12
β_x	Horizontal beta function 75
β_y	Vertical beta function 75
β^*	Beta functions at the CMS and ATLAS interaction points. 56
γ	Relativistic mass factor of the beam 14
δ	Dirac distribution (or delta function) 6
δ_{m0}	1 if $m = 0$, 0 otherwise 9
δ_s	Skin depth 53
ε_0	Permittivity of vacuum ($8.85419 \cdot 10^{-12}$ F/m) 7
ε_1	Relative complex permittivity of the medium (including conductivity) 7
ε_b	Dielectric constant of the medium (real) 7
ε_c	Complex permittivity of the medium (including conductivity) 7
ε_x	Single particle horizontal emittance 75
ε_y	Single particle vertical emittance 75
ε_x^n	Normalized RMS horizontal beam emittance 92
ε_y^n	Normalized RMS vertical beam emittance 92
η_1	Coefficient relating $-C_{e+}^{(1)} \frac{k_y^{(1)}}{\mathscr{C}}$ to $e^{-k_y^{(1)} y_1}$ 36
η_2	Coefficient relating $-C_{e-}^{(-1)} \frac{k_y^{(1)}}{\mathscr{C}}$ to $e^{-k_y^{(1)} y_1}$ 36
θ_1	Azimuthal coordinate of the source macroparticle 6
θ_2	Azimuthal coordinate of the test particle 22
$\tan\vartheta_E$	Dielectric loss tangent of the medium 7
$\tan\vartheta_M$	Magnetic loss tangent of the medium 7
μ	Complex permeability of the medium 7
μ_0	Permeability of vacuum ($4\pi 10^{-7}$ H/m) 7
μ_1	Relative complex permeability of the medium 7
μ_r	Real part of the relative complex permeability of the medium 7
ν	Propagation constant in the medium 12
ρ	Charge density of the source macroparticle 5
ρ_{DC}	DC (i.e. at zero frequency) resistivity (real) 53
σ_{DC}	DC (i.e. at zero frequency) conductivity (real) 7
σ_z	Bunch length (RMS value, one fourth of the total bunch length for Gaussian bunches) .. 84
σ_δ	Longitudinal momentum spread (RMS value) 92
τ	Time between the source and test particles (positive if the test is behind the source) 44
τ_{AC}	Relaxation time of the complex AC conductivity 7
τ_b	Total bunch length in seconds (4 times the standard deviation for Gaussian bunches) ... 90
$v = \beta c$	Speed of the source and test particles 5
ϕ	$\theta - \frac{\pi}{2}$ 165

χ_1	Coefficient relating $-C_{e+}^{(1)} \frac{k_y^{(1)}}{\mathscr{C}}$ to $e^{k_y^{(1)} y_1}$	36
χ_2	Coefficient relating $-C_{e-}^{(-1)} \frac{k_y^{(1)}}{\mathscr{C}}$ to $e^{k_y^{(1)} y_1}$	36
$\omega = 2\pi f$	Angular frequency	4
ω_{rev}	Angular revolution frequency in the LHC	68

Introduction

Particle accelerators, together with storage rings and colliders, are nowadays a widely used class of tools in various research fields, for instance in high-energy physics, materials characterization or molecular biology. They are also present in our everyday life, the most obvious example being the cathode ray tube in televisions, but also in medicine for cancer therapy, or in industry for ion implantation and welding. While most everyday accelerators are of quite low intensity in terms of number of particles accelerated, some have very intense beams, in particular in high-energy physics experiments where one usually wants to produce collisions with the largest possible amount of particles involved in order to discover and/or investigate very rare events.

For such high intensity or high density accelerators (or storage rings), one of the main limitations arise from collective effects, that is, the class of phenomena in which the evolution of the particle beam cannot be studied as if the beam was a collection of single particles behaving independently, but rather as an ensemble of interacting particles. In these collective (or multi-particle) effects, one can identify several subjects of study, among which we can mention collisions between beam particles, interactions with trapped ions or electron cloud, interactions with particles of another counter-rotating beam in a circular collider, and the effect of the beam's own self-generated electromagnetic fields. All these phenomena usually increase in magnitude with higher beam intensity, and are in general responsible for a degradation of the beam quality or even particle losses, both of which one wants to avoid.

The Large Hadron Collider (LHC) at CERN is to date the largest and most powerful accelerator in the world, with very high intensity beam (at the time of writing, up to $2 \cdot 10^{14}$ protons per beam were accelerated and brought into collision) circulating in a ring of around 27 km circumference. For such high intenstity beams, studying collective effects is of primary importance. Among those, self-generated fields, and more specifically wake fields created by the interaction of the beam with its surroundings (vacuum pipe, collimators, kicker magnets, and many others), could lead to severe beam instabilities. In the case of the LHC the beams are actually made of many well separated bunches of particles constituting a "bunch train"; coupled-bunch instabilities can then in principle arise when self-generated instability modes grow along the bunch train during subsequent revolutions. In the LHC this type of instability is a crucial topic of study due to the almost complete filling scheme around the ring in nominal conditions (2808 bunches out of the 3564 possible locations in total). This kind of instability can be cured in several ways, typically transverse feedback and Landau damping, which both have their limitations. A good knowledge of such instabilities is therefore especially important, both to optimize the performance of the LHC in its current configuration, and for the design of the forthcoming upgrade of this collider into a version with higher collision rate, which will probably require even higher intensity.

In this thesis we study the LHC coupled-bunch transverse instabilities in details, from the theoretical computation of the self-generated fields responsible for them, until the simulations of their effect for various configurations of the machine, comparing the final results to beam-based measurements in the

LHC.
The first ingredient to any instability model are the wake fields (i.e. the self-generated electromagnetic fields created by the beam along the ring) or their frequency domain counterpart, namely the beam-coupling impedances. It turns out that in the LHC, the so-called collimators contribute significantly to the machine impedance. Those are devices made of two parallel and flat collimator jaws, intented to take out the beam halo to prevent it from damaging sensitive parts of the machine. The collimators jaws are often very close to the beam which make them be one of the main impedance contributors, and many jaws are in graphite with a poor conductivity, which, combined to the low revolution frequency of the LHC (giving in particular a very low frequency for the most unstable coupled-bunch mode – around 8 kHz [1, 2]), entails that the classic thick wall theory used usually for the impedance computation, breaks down. A more general theory was therefore reinvestigated and improved for infinitely long axisymmetric chambers, and a new one derived for infinitely long flat chambers. This first step is done in Chapter 1, along with the presentation of a new algorithm enabling fast and accurate computation of the Fourier transforms of the impedances, called the wake functions.
Then, using these theories and algorithm the transverse impedance and wake function model of the entire machine is computed in Chapter 2, taking into account only the elements that are thought to be the main contributors.
Investigation of coupled-bunch instabilities require to study beam dynamics, which is done thanks to a new multibunch code to simulate the effect of wake fields on a beam made of macroparticles, based on a previously existing single-bunch code "HEADTAIL" [3, 4]. This code has been parallelized to make it possible to simulate cases with a high number of bunches, as it is customary done in real LHC runs. The algorithm, as well as postprocessing tools and benchmarks with respect to theories in simplified cases, are presented in Chapter 3.
Results of the whole process (theory and simulations) in the case of the LHC are shown in Chapter 4, including some predictions at the yet unreached momentum of 7 TeV/c. Comparisons with experimental results from beam-based measurements are there also made, in order to validate the full process.
Finally, our concluding remarks are presented in Chapter 5.
Note that the whole thesis is expressed in SI (or MKSA) units.

1 Beam-coupling impedances and wake functions

Each charged particle in a beam creates in its surroundings an electromagnetic field that will affect other particles. When the beam evolves in a given structure or machine element (vacuum pipe, collimator, magnet, RF cavity, etc.), those self-generated fields couple with the structure and give rise to the so-called beam-coupling impedances, which can be seen as the response function, in frequency domain, of the machine element to a travelling point-like particle. Beam-coupling impedances are used in several synchrotron instability theories [5, 6]. In time domain one rather speaks about wake functions (or wake potentials [7, p. 57] when considering a full distribution of particles instead of a point-like particle); the term "wake" is related to the fact that in the particular case of ultrarelativistic beams those electromagnetic fields stay behind the travelling particle, since any location ahead of a particle travelling at the speed of light cannot receive any field from this particle.

Beam-coupling impedances and wake fields are a subject of interest for synchrotrons since many years [8]. Ideally the best approach to compute the impedance in a given synchrotron is to solve the tridimensional electromagnetic problem for all the elements around the beam. This task would require the extensive and time-consuming use of electromagnetic codes. Fortunately, in certain cases one can avoid such a huge work and still get a reliable impedance model.

A first simplification comes from the fact that one can usually distinguish two parts in the beam-coupling impedances, that can be computed independently most of the time. One part is due to the geometric features around the beam, such as edges, tapering, or cavities, and can be at least approximately computed assuming a perfect conductivity of the walls. They create a contribution of two different kinds depending on the type of geometric feature: smooth geometric features (such as taperings) typically create a broad-band impedance, i.e. inductive and constant up to the beam pipe cutoff (the frequency above which electromagnetic waves can propagate down the vacuum pipe) so short-ranged in time domain; on the contrary cavity-like geometries can create some resonant peaks due to "trapped modes" which are typically waves reflected back and forth, giving rise to long-ranged wake fields in time domain. Both contributions can be cured or at least attenuated (small angle tapering in the first case, lossy materials adequately placed in a cavity for the second case).

The second part of the beam-coupling impedances is due to the resistivity (or more generally the complex permitivity and permeability) of the materials surrounding the beam. This part, when omitting its perfectly conducting part, is usually called resistive-wall impedance; we will call it here simply wall impedance, following Ref. [9], because we do not take away the part of the impedance that would be there if the surroundings were perfectly conducting (see Section 1.4.6). Since the wall impedance is mostly dependent on the materials properties, a very common approximation to compute it for a given

element is to assume a two-dimensional geometry, i.e. with an infinite length along the beam pipe axis, and to compute the fields created by a beam near the center of the element. This contribution to the total beam-coupling impedance is more difficult to reduce than the geometric contribution: the only possibility is to increase the aperture (therefore increasing the costs) or to choose materials that give rise to the smallest possible impedance. Also, the wall impedance turns to long-ranged wake fields in time domain, typically decaying as the square root of the distance behind the particle creating the fields [10, p. 59].

Since we want to evaluate multibunch effects, we are more interested in long-ranged wake fields. Assuming we can neglect trapped modes (the validity of this assumption will be checked against beam-based measurement in Chapter 4), an efficient approach to evaluate the impedance of the LHC is to identify the main impedance contributors (basically, those contributors that are the nearest to the beam) and to calculate their wall impedance and associated wake fields assuming two dimensional (infinitely long) geometries. This is possible because one can actually analytically compute beam-coupling impedances for simple geometries, which has the asset to be much quicker than the use of a tridimensional code, and can also have less limitations, for instance with respect to the frequency range, the beam velocity or the material properties. Such two-dimensional analytical computations of the beam-coupling impedances have been developped for more than forty years [8]. Simple formulae exist and can be applied in many cases; one can mention for instance the widely used classic thick wall formula [10, p. 71]. In the LHC, the beam-coupling impedance coming from graphite collimators deviates significantly [9] from the classic thick wall formula at low frequency, due to the large skin depth [11, p. 220] in graphite that becomes comparable or even much larger than the half gap. Besides, other machine elements (among which certain collimators) have a thin coating and/or have a certain thickness that cannot be assumed to be infinite in particular when considering very long-ranged wake fields. For these reasons a general multilayer theory has to be considered. For an axisymmetric two dimensional geometry, analytical calculations have been existing since a long time: one can mention the general formalism of B. Zotter [1, 12–16], the one of A. Burov and V. Lebedev [17] which is simpler but slightly less general, and more recently some matrix formalisms using potentials [18–21].

For other simple but non-axisymmetric two-dimensional geometries (elliptic, rectangular, or flat and infinitely large), the usual approach is to deduce the impedance from the axisymmetric case multiplied by some constant form factors [22] depending on the geometry, often called Yokoya [23] or Laslett [24] factors. However, recently it has been shown that this approach to compute the beam coupling impedances of a flat chamber fails in the case of non metallic materials such as ferrite [25]. Indeed, the hypotheses on which the form factors theories rely break down for general non conductive materials and/or over certain frequency range: in Ref. [24] one is concerned only about perfectly conductive materials in the static case, whereas in Refs. [22, 23] one assumes that the beam is ultrarelativistic and that the chamber material is conductive with a skin depth much smaller than both the chamber thickness and its half gap. Since the skin depth is a monotically decreasing function of frequency, the latter assumption implies a lower bound in frequency. This approximation is known to break down in the case of the graphite collimators [9], in particular around 8 kHz which is the frequency of the first unstable betatron line in the LHC [1, 2]. While other more general aproaches exist, in single-layer [26–29], two-layer [30] or even multilayer [31] cases, none is completely general and valid from low to high frequencies and for any linear materials.

We note in passing that the assumption made in Refs. [17, 31], namely that in the frequency domain of interest the wave number $\frac{\omega}{c}$ (with ω the angular frequency and c the speed of light in vacuum) is much less than the inverse of the minimum transverse dimension of the pipe or flat chamber surrounding the beam, is most probably valid in the case of the LHC. There are nevertheless at least two reasons to

develop a more general formalism than Burov-Lebedev's one [17, 31]. The first one is that not only the beam-coupling impedances but also the electromagnetic fields components are of interest, including the longitudinal magnetic field which is assumed to be zero in Refs. [17, 31]. Knowledge of the electromagnetic fields is particularly useful when one wants to check the validity of some approximation made during measurement where the electric field is neglected with respect to the magnetic field [9]. The other reason to develop a more general theory is that in future linear colliders one might well need to go beyond this low frequency approximation since the bunches will be very short [32, 33], while the knowledge of the low frequency behaviour will also be needed, in particular if several bunches are circulating in a damping ring.
In order to provide tools to compute the LHC impedance and wake fields model, we present here complete general multilayer formalisms in frequency domain, in longitudinal and transverse, in both the axisymmetric and flat two-dimensional infinitely long cases. Both theories presented are valid with any number of layers, any beam velocity and any frequency, and give all nonlinear terms. Each layer can be made of any resistive, dielectric or magnetic materials, assuming only their linearity, isotropy, homogeneity and the validity of Ohm's law when they are conductive (thus neglecting the magnetoresistance and the anomalous skin effect).
We will begin by introducing in Section 1.1 the source of the electromagnetic fields, before writing Maxwell equations in Section 1.2 and the wave equations in Section 1.3. For the axisymmetric case, we will revisit and fully detail in Section 1.4 the analytical computation of B. Zotter [14], with improvements for better accuracy and computational time performance, and extension to any azimuthal mode instead of only $m = 0$ and $m = 1$. In the flat case, i.e. a chamber infinitely large horizontally, we provide in Section 1.5 a new analytical and general theory on the impedance of a multilayer chamber. Then in Section 1.6 we present a way to obtain the wake functions in time domain from these theories thanks to a Fourier transform technique involving an uneven sampling, to be able to deal with a large number of decades in the frequency domain.

1.1 Source charges and currents

We consider as the source of the electromagnetic fields a point-like particle of charge Q travelling at a speed v along the synchrotron beam line (Os), using the cartesian coordinates (O, x, y, s). Note that s is also assumed to be the azimuthal coordinate along the beam reference orbit in the accelerator, thus neglecting all curvature effects, which is a good approximation for accelerators of long radius of curvature like the LHC (we refer the reader to Refs. [34–39] for details about such effects). The origin O of the coordinates (and reference orbit) is supposed to be at the center of symmetry of the infinitely long structure (flat or axisymmetric) surrounding the beam line, except in the case of an asymmetric structure (see later in Section 1.5).
In time domain, the source particle is supposed to be slightly offset from the origin by x_1 in the horizontal direction and y_1 in the vertical one, so that its transverse coordinates are $x = x_1$ and $y = y_1$. Along the beam line, since the particle is travelling at the velocity v, and assuming that at $t = 0$ it is at $s = 0$, its coordinate is $s = vt$. In time domain, the corresponding charge density is then[1]

$$\rho(x, y, s; t) = Q\delta(x - x_1)\delta(y - y_1)\delta(s - vt). \tag{1.1}$$

[1] This charge density (and the corresponding current density) is valid for a single passage through the flat chamber. To take into account multiturn effects in circular rings, we have to replace $\delta(s - vt)$ by $\sum_{l=-\infty}^{\infty} \delta(s - v(t - lT_{rev}))$, or, since Maxwell equations are linear, we can perform such a multiturn sum later on, on the resulting fields we compute in this chapter. We choose the latter way in this work.

Here δ is the Dirac distribution, i.e. such that for any function f, $\int_{-\infty}^{\infty} f(x)\delta(x)\mathrm{d}x = f(0)$. As expected we get $\iiint_\Omega \rho(x,y,s;t)\mathrm{d}x\mathrm{d}y\mathrm{d}s = Q$ for any volume Ω around $x = x_1$, $y = y_1$ and $s = vt$.
It is convenient to solve Maxwell equations in frequency domain. We can do this without loss of generality except that any transient effect is then neglected[2]. To do so we write the factor $\delta(s-vt)$ in terms of its Fourier spectrum [41, 42]

$$\begin{aligned}\delta(s-vt) &= \frac{1}{2\pi}\int_{-\infty}^{\infty} e^{-jk(s-vt)}\mathrm{d}k \\ &= \frac{1}{2\pi v}\int_{-\infty}^{\infty} e^{j\omega\left(t-\frac{s}{v}\right)}\mathrm{d}\omega \\ &= \frac{1}{2\pi}\int_{-\infty}^{\infty} \mathrm{d}\omega e^{j\omega t}\frac{e^{-jks}}{v},\end{aligned} \tag{1.2}$$

where j is the imaginary constant, and

$$k \equiv \frac{\omega}{v}, \tag{1.3}$$

is the wave number. We drop the factor $\frac{1}{2\pi}\int_{-\infty}^{\infty}\mathrm{d}\omega e^{j\omega t}$ to proceed to the frequency domain, obtaining

$$\rho(x,y,s;\omega) = \frac{Q}{v}\delta(x-x_1)\delta(y-y_1)e^{-jks}. \tag{1.4}$$

To get back to the time domain we will have to put back the $\frac{1}{2\pi}\int_{-\infty}^{\infty}\mathrm{d}\omega e^{j\omega t}$ factor and integrate our frequency domain solutions (see Section 1.6).
In cylindrical coordinates (r,θ,s), defining a_1 and θ_1 such that $x_1 = a_1\cos\theta_1$ and $y_1 = a_1\sin\theta_1$, it is clear that the product $\delta(x-x_1)\delta(y-y_1)$ is non zero if and only if $r = a_1$ and $\theta = \theta_1 + 2p\pi$ for any p integer, such that it must be proportional to $\delta(r-a_1)\delta_p(\theta-\theta_1)$ with δ_p the $2\pi-$periodic Dirac distribution, i.e. $\delta_p(\theta) = \sum_{l=-\infty}^{\infty}\delta(\theta-2l\pi)$. Now since $\int_{r=0}^{\infty}\int_{\theta=0}^{2\pi}\delta(r-a_1)\delta_p(\theta-\theta_1)r\mathrm{d}r\mathrm{d}\theta = a_1 = a_1\iint\delta(x-x_1)\delta(y-y_1)\mathrm{d}x\mathrm{d}y$, the proportionality constant must be $\frac{1}{a_1}$, such that

$$\delta(x-x_1)\delta(y-y_1) = \frac{1}{a_1}\delta(r-a_1)\delta_p(\theta-\theta_1).$$

Therefore the charge density in time domain can be written in cylindrical coordinates as

$$\rho(r,\theta,s;t) = \frac{Q}{a_1}\delta(r-a_1)\delta_p(\theta-\theta_1)\delta(s-vt), \tag{1.5}$$

[2]Actually, at least two kinds of transients could appear. The first one concerns dielectric media, in which the time to reach a polarization parallel to an applied $\vec{E}$ field is in principle not instantaneous, being related to the binding energy of electrons in atoms, which is around visible light energies, so a time constant in the order of 10^{-14} - 10^{-15} s [11, p. 163]. The second one concerns conductive media: a transient occurs due to the migration of charge carriers toward the surface of the layer considered, with a time constant of the order of $\frac{\varepsilon_0}{\sigma}$ where ε_0 is the permittivity of vacuum and σ the conductivity (this can be obtained by injecting Ohm's law and Gauss' law into the continuity equation of the charge carriers density). Even for poor conductors, this time constant remains negligible, while for highly resistive materials the contribution from conductivity will be negligible with respect to that of the dielectric constant (see Eq. (1.14)). Problematic cases arise when the material is somewhat resistive, such that at certain frequencies, a transition between a resistive behaviour and a dielectric one appears. At such frequencies the transient time due to the migration of conduction electrons cannot be neglected anymore [40].

and in frequency domain as

$$\rho(r,\theta,s;\omega) = \frac{Q}{a_1}\delta(r-a_1)\delta_p(\theta-\theta_1)e^{-jks}. \tag{1.6}$$

Finally, since the particle is supposed to travel at the velocity v along the s axis, the current density is obtained in general by [43]

$$\vec{J} = \rho v \vec{e}_s, \tag{1.7}$$

$\vec{e}_s$ being the unit vector along the s axis.

1.2 Maxwell equations

The macroscopic Maxwell equations in frequency domain for the electric and magnetic fields $\vec{E}$ and $\vec{H}$ in a general linear, homogeneous and isotropic medium are [14]

$$\begin{aligned}
\mathrm{div}\vec{D} &= \rho, && (1.8)\\
\vec{\mathrm{curl}}\vec{H} - j\omega\vec{D} &= \vec{J}, && (1.9)\\
\vec{\mathrm{curl}}\vec{E} + j\omega\vec{B} &= 0, && (1.10)\\
\mathrm{div}\vec{B} &= 0, && (1.11)
\end{aligned}$$

where ρ and $\vec{J} = J\vec{e}_s$ are given in the whole space by Eqs. (1.4) and (1.7). The electric displacement $\vec{D}$ and the magnetic induction $\vec{B}$ are defined using complex permittivities and permeabilities ε_c and μ

$$\begin{aligned}
\vec{D} &= \varepsilon_c(\omega)\vec{E} = \varepsilon_0\varepsilon_1(\omega)\vec{E}, && (1.12)\\
\vec{B} &= \mu(\omega)\vec{H} = \mu_0\mu_1(\omega)\vec{H}, && (1.13)
\end{aligned}$$

where ε_c and μ are general frequency dependent complex permittivity and permeability. We will also often use the quantities ε_1 and μ_1 which are the relative complex permittivity and permeability of the medium. ε_0 and μ_0 are the permittivity and permeability of vacuum. We do not have to assume any particular frequency dependence of these properties, but the following expressions [9] can be considered as a relevant example, since they have a fairly general range of validity:

$$\begin{aligned}
\varepsilon_c(\omega) &= \varepsilon_0\varepsilon_1(\omega) = \varepsilon_0\varepsilon_b\left[1 - j\,\mathrm{sign}(\omega)\tan\vartheta_E\right] + \frac{\sigma_{DC}}{j\omega\left(1+j\omega\tau_{AC}\right)}, && (1.14)\\
\mu(\omega) &= \mu_0\mu_1(\omega) = \mu_0\mu_r\left[1 - j\,\mathrm{sign}(\omega)\tan\vartheta_M\right]. && (1.15)
\end{aligned}$$

In these expressions, μ_r is the real part of the relative complex permeability, $\tan\vartheta_M$ is the magnetic loss tangent, ε_b is the dielectric constant and $\tan\vartheta_E$ is the dielectric loss tangent. We also consider in this model a simple AC conductivity following the Drude model (see Refs. [11, p. 312] and [44, p. 16], with an opposite sign convention for ω in both references) where σ_{DC} is the DC conductivity of the material and τ_{AC} its relaxation time. It is here important to note that we assume that Ohm's law (in its local sense,

i.e. the proportionality between the induced conductive current density and the electric field, at any point) holds for the media involved. Doing so we neglect magnetoresistance effects (see Refs. [44, pp. 11-15 and 234-239] and [45]) and the so-called "anomalous skin effect" [45–52]. Both might appear at low temperature, and very high magnetic fields for the former (several Teslas), or very high frequencies for the latter (see Ref. [53] for some examples of relevant limits).
Note that Eqs. (1.12) and (1.13) can be derived from the general microsopic Maxwell equations, as shown in Appendix A. Sometimes in the literature the conductivity part of the complex permittivity is not included into the expression of $\vec{D}$, which was found to lead to an inconsistency when writing the boundary conditions for the electric displacement component perpendicular to a surface between different media, unless some surface charges are taken into account (see Appendix E.1.2 and footnote 1). Therefore here we prefer to include the conductivity part in the complex permittivity to avoid this problem.
Note that the signs in front of $\tan\vartheta_E$ and $\tan\vartheta_M$ are a convention (see e.g. Ref. [54]) to ensure that the energy dissipation is positive in the medium if $\varepsilon_b \tan(\vartheta_E) \geq 0$ and $\mu_r \tan(\vartheta_M) \geq 0$. This is shown in Ref. [55, p. 274] (where actually the opposite convention holds since the inverse Fourier transform is in $e^{-j\omega t}$ instead of $e^{j\omega t}$ here).
Finally, when needed we will assume a positive angular frequency ω. The fields in frequency domain for $\omega < 0$ can be obtained by noticing that all the time domain field components should be real, which means that for any field component φ and any t we have (with $\Im$ the imaginary part of a complex number):

$$0 = \Im\left[\int_{-\infty}^{\infty} \mathrm{d}\omega e^{j\omega t}\varphi(\omega)\right] = \int_{-\infty}^{\infty} \mathrm{d}\omega \Im\left[e^{j\omega t}\varphi(\omega)\right] = \frac{1}{2}\int_{-\infty}^{\infty} \mathrm{d}\omega\left[e^{j\omega t}\varphi(\omega) - e^{-j\omega t}\varphi(\omega)^*\right]$$
$$= \frac{1}{2}\int_{-\infty}^{\infty} \mathrm{d}\omega e^{j\omega t}\left[\varphi(\omega) - \varphi(-\omega)^*\right], \quad (1.16)$$

where * denotes the complex conjugate. This is true for any t if and only if

$$\varphi(-\omega) = \varphi(\omega)^*. \quad (1.17)$$

We can use Eq. (1.17) to compute the field components for negative frequencies.

1.3 Wave equations

Applying the $\vec{\mathrm{curl}}$ operator to Maxwell equation (1.10) in a homogeneous and isotropic medium, and using Eq. (1.13), we obtain

$$\vec{\mathrm{curl}}\left(\vec{\mathrm{curl}}\vec{E}\right) + j\omega\mu\vec{\mathrm{curl}}\vec{H} = 0.$$

Using the "$\vec{\mathrm{curl}}\,\vec{\mathrm{curl}}$" relation (Eq. (B.11) of Appendix B.3), injecting Maxwell equations (1.8) and (1.9) together with Eqs. (1.7) and (1.12), we then get

$$\nabla^2\vec{E} + \omega^2\varepsilon_c\mu\vec{E} = \frac{1}{\varepsilon_c}\vec{\mathrm{grad}}\rho + j\omega\mu\rho v\vec{e}_s. \quad (1.18)$$

Similarly, we can apply the $\vec{\text{curl}}$ operator to Maxwell equation (1.9) knowing Eqs. (1.7) and (1.12),to obtain

$$\vec{\text{curl}}\left(\vec{\text{curl}}\vec{H}\right) - j\omega\varepsilon_c\vec{\text{curl}}\vec{E} = \vec{\text{curl}}\left(\rho v\vec{e}_s\right),$$

which gives, with Eqs. (1.10) and (1.11), using also the expression of the $\vec{\text{curl}}$ operator in cartesian coordinates from Eq. (B.8) for the right-hand side

$$\nabla^2\vec{H} + \omega^2\varepsilon_c\mu\vec{H} = v\frac{\partial\rho}{\partial x}\vec{e}_y - v\frac{\partial\rho}{\partial y}\vec{e}_x. \tag{1.19}$$

Equations (1.18) and (1.19) are the so-called wave equations, derived in a homogeneous medium. Up to now no assumptions have been made on the particular boundary conditions and geometric structure the beam is evolving in.

1.4 Case of an axisymmetric multilayer chamber

We study now the particular case of a cylindrical multilayer tube (typically a vacuum pipe) of interior radius b, as shown in Fig. 1.1. The wall of the tube is made of $N-1$ (with $N \geq 2$) cylindrical layers of outer radii $b^{(p)}$, and in each of them properties such as ε_c and μ take uniform values. The superscript (p) is now added to all the quantities (material properties, electromagnetic fields, etc.) related to a certain layer (as in e.g. $\varepsilon_c^{(p)}$ and $\mu^{(p)}$), unless it is perfectly clear from the context which layer is being studied. To simplify the problem we can set the particle postion to $r = a_1$ and $\theta = \theta_1 = 0$ without loss of generality since the geometry is axisymmetric.
The approach followed here is equivalent but slightly different from that of Ref. [16]. To solve Maxwell equations we will decompose the electromagnetic fields in the following way (omitting for now the superscript (p)):

$$\begin{aligned}\vec{E}(r,\theta,s;\omega) &= \int_{-\infty}^{\infty} \mathrm{d}k' e^{-jk's}\vec{\hat{E}}\left(r,\theta;k',\omega\right) \\ &= \int_{-\infty}^{\infty} \mathrm{d}k' e^{-jk's}\left(\sum_{m=0}^{\infty}\frac{\vec{\hat{E}}^{m,c}\left(r;k',\omega\right)}{1+\delta_{m0}}\cos m\theta + \sum_{m=1}^{\infty}\vec{\hat{E}}^{m,s}\left(r;k',\omega\right)\sin m\theta\right),\end{aligned} \tag{1.20}$$

where $\vec{\hat{E}}$ is the Fourier transform along the s axis of $\vec{E}$, $\vec{\hat{E}}^{m,c}$ and $\vec{\hat{E}}^{m,s}$ the coefficients of the Fourier series decomposition on azimuthal modes of $\vec{\hat{E}}$, and $\delta_{m0} = 1$ if $m = 0$, 0 otherwise. We can decompose in the same way $\vec{H}$, introducing the quantities $\vec{\hat{H}}$, $\vec{\hat{H}}^{m,c}$ and $\vec{\hat{H}}^{m,s}$:

$$\begin{aligned}\vec{H}(r,\theta,s;\omega) &= \int_{-\infty}^{\infty} \mathrm{d}k' e^{-jk's}\vec{\hat{H}}\left(r,\theta;k',\omega\right) \\ &= \int_{-\infty}^{\infty} \mathrm{d}k' e^{-jk's}\left(\sum_{m=0}^{\infty}\frac{\vec{\hat{H}}^{m,c}\left(r;k',\omega\right)}{1+\delta_{m0}}\cos m\theta + \sum_{m=1}^{\infty}\vec{\hat{H}}^{m,s}\left(r;k',\omega\right)\sin m\theta\right).\end{aligned} \tag{1.21}$$

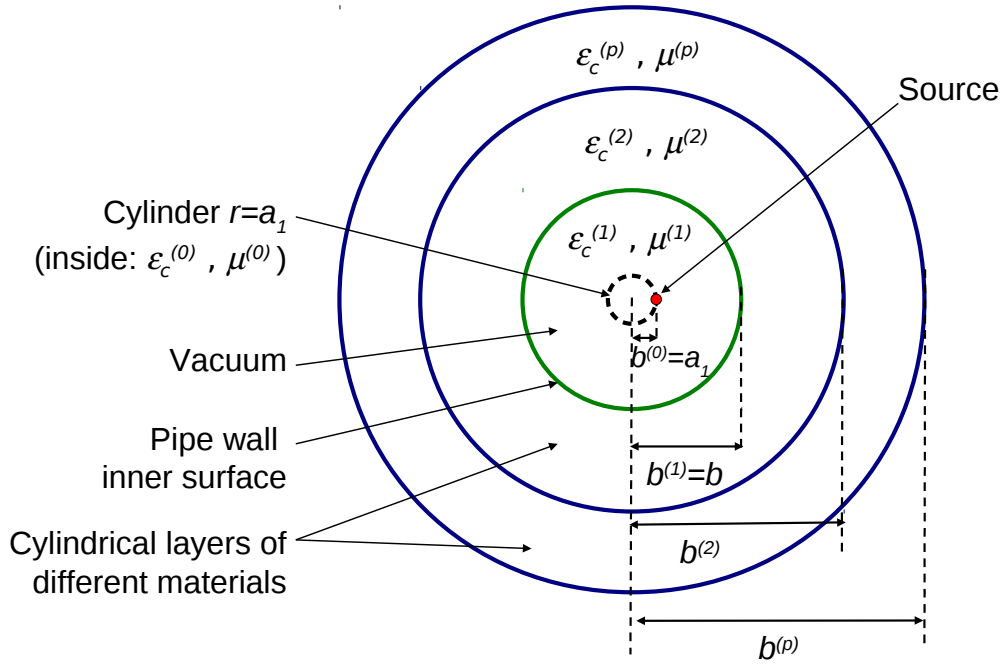

Figure 1.1: Cross section of the axisymmetric chamber. The region denoted by the superscript (0) is the vacuum inside a fictitious cylinder of radius a_1, and the region denoted by the superscript (1) is the vacuum between $r = a_1$ and the pipe wall at $r = b$. Subsequent layers can be made of any linear medium. The last layer (denoted by the superscript (N)) has an infinite radius $b^{(N)} = \infty$. In red is sketched the source particle at $r = a_1$ and $\theta = 0$.

We also define as $\vec{E}^{m,c}$, $\vec{E}^{m,s}$, $\vec{H}^{m,c}$ and $\vec{H}^{m,s}$ the Fourier series coefficients of $\vec{E}$ and $\vec{H}$, i.e.

$$\vec{E}(r,\theta,s;\omega) = \sum_{m=0}^{\infty} \frac{\vec{E}^{m,c}(r,s;\omega)}{1+\delta_{m0}} \cos m\theta + \sum_{m=1}^{\infty} \vec{E}^{m,s}(r,s;\omega) \sin m\theta, \tag{1.22}$$

$$\vec{H}(r,\theta,s;\omega) = \sum_{m=0}^{\infty} \frac{\vec{H}^{m,c}(r,s;\omega)}{1+\delta_{m0}} \cos m\theta + \sum_{m=1}^{\infty} \vec{H}^{m,s}(r,s;\omega) \sin m\theta, \tag{1.23}$$

such that

$$\vec{E}^{m,c}(r,s;\omega) = \int_{-\infty}^{\infty} \mathrm{d}k' e^{-jk's} \tilde{\vec{E}}^{m,c}(r;k',\omega), \qquad \vec{E}^{m,s}(r,s;\omega) = \int_{-\infty}^{\infty} \mathrm{d}k' e^{-jk's} \tilde{\vec{E}}^{m,s}(r;k',\omega), \tag{1.24}$$

$$\vec{H}^{m,c}(r,s;\omega) = \int_{-\infty}^{\infty} \mathrm{d}k' e^{-jk's} \tilde{\vec{H}}^{m,c}(r;k',\omega), \qquad \vec{H}^{m,s}(r,s;\omega) = \int_{-\infty}^{\infty} \mathrm{d}k' e^{-jk's} \tilde{\vec{H}}^{m,s}(r;k',\omega). \tag{1.25}$$

Finally we can rewrite the charge density from Eq. (1.6) by using the Fourier series expansion on azimuthal modes of the periodic Dirac distribution $\delta_p(\theta)$ [41, 43]

$$\delta_p(\theta) = \frac{1}{2\pi} + \sum_{m=1}^{\infty} \frac{\cos(m\theta)}{\pi}. \tag{1.26}$$

We then obtain for the charge density in frequency domain, recalling that here $\theta_1 = 0$:

$$\rho(r,\theta,s;\omega) = \sum_{m=0}^{\infty} \frac{Q\cos(m\theta)}{\pi v a_1(1+\delta_{m0})}\delta(r-a_1)e^{-jks} \tag{1.27}$$

$$= \int_{-\infty}^{\infty} \mathrm{d}k' e^{-jk's}\delta(k'-k) \sum_{m=0}^{\infty} \frac{Q\cos(m\theta)}{\pi v a_1(1+\delta_{m0})}\delta(r-a_1). \tag{1.28}$$

1.4.1 Longitudinal components of the electromagnetic fields

In a given layer, the wave equations (1.18) and (1.19) turn out to be relatively simple for the longitudinal field components. Using the expressions of the gradient and the laplacian in cylindrical coordinates (see Eqs. (B.1), (B.4) and (B.5) of Appendix B.1), we get the following scalar Helmholtz equations (still omitting the superscript (p)):

$$\left[\frac{1}{r}\frac{\partial}{\partial r}\left(r\frac{\partial}{\partial r}\right) + \frac{1}{r^2}\frac{\partial^2}{\partial\theta^2} + \frac{\partial^2}{\partial s^2} + \omega^2\varepsilon_c\mu\right] E_s = \frac{1}{\varepsilon_c}\frac{\partial\rho}{\partial s} + j\omega\mu\rho v, \tag{1.29}$$

$$\left[\frac{1}{r}\frac{\partial}{\partial r}\left(r\frac{\partial}{\partial r}\right) + \frac{1}{r^2}\frac{\partial^2}{\partial\theta^2} + \frac{\partial^2}{\partial s^2} + \omega^2\varepsilon_c\mu\right] H_s = 0. \tag{1.30}$$

Now we can rewrite those equations by introducing the decompositions from Eqs. (1.20), (1.21) and (1.28) of respectively $\vec{E}$, $\vec{H}$ and ρ. After identification of each term we get for the azimuthal coefficients of the fields longitudinal components:

$$\frac{d^2\hat{E}_s^{m,c}}{dr^2} + \frac{1}{r}\frac{d\hat{E}_s^{m,c}}{dr} - \left(\frac{m^2}{r^2} + k'^2 - \omega^2\varepsilon_c\mu\right)\hat{E}_s^{m,c} = \frac{jQ\delta(r-a_1)\delta(k'-k)}{\pi a_1(1+\delta_{m0})}\left(\frac{-k'}{\varepsilon_c v} + \omega\mu\right), \tag{1.31}$$

$$\frac{d^2\hat{E}_s^{m,s}}{dr^2} + \frac{1}{r}\frac{d\hat{E}_s^{m,s}}{dr} - \left(\frac{m^2}{r^2} + k'^2 - \omega^2\varepsilon_c\mu\right)\hat{E}_s^{m,s} = 0, \tag{1.32}$$

$$\frac{d^2\hat{H}_s^{m,c}}{dr^2} + \frac{1}{r}\frac{d\hat{H}_s^{m,c}}{dr} - \left(\frac{m^2}{r^2} + k'^2 - \omega^2\varepsilon_c\mu\right)\hat{H}_s^{m,c} = 0, \tag{1.33}$$

$$\frac{d^2\hat{H}_s^{m,s}}{dr^2} + \frac{1}{r}\frac{d\hat{H}_s^{m,s}}{dr} - \left(\frac{m^2}{r^2} + k'^2 - \omega^2\varepsilon_c\mu\right)\hat{H}_s^{m,s} = 0, \tag{1.34}$$

which is valid for any m, ω and k'. From the above system and the fact that the geometry studied does not allow any coupling between different wave numbers k' (from its translational invariance along the s axis), we can deduce that when $k' \neq k$, all the functions $\vec{\hat{E}}^{m,c}$, $\vec{\hat{E}}^{m,s}$, $\vec{\hat{H}}^{m,c}$ and $\vec{\hat{H}}^{m,s}$ are identically zero: they are solution of a system of differential equations with no right hand side, or, put in other words, without excitation of any external charge or current density. The only possibility for them not be zero is if some electromagnetic waves are present in the structure independently of the travelling beam, but this kind of solutions is not related to the beam-coupling impedance, therefore we will not consider them here. This means in particular that those functions have to be proportional to the only non zero right

hand side term in the above system, so to $\delta(k'-k)$. We get then, from Eqs. (1.24) and (1.25):

$$
\begin{aligned}
E_s^{m,c}(r,s;\omega) &= e^{-jks} R_E^{m,c}(r;\omega),\\
E_s^{m,s}(r,s;\omega) &= e^{-jks} R_E^{m,s}(r;\omega),\\
H_s^{m,c}(r,s;\omega) &= e^{-jks} R_H^{m,c}(r;\omega),\\
H_s^{m,s}(r,s;\omega) &= e^{-jks} R_H^{m,s}(r;\omega),
\end{aligned}
$$

where $R_E^{m,c}$, $R_E^{m,s}$,$R_H^{m,c}$ and $R_H^{m,s}$ are independent of k'. After multiplication by $e^{-jk's}$ and integration over k', we get from Eqs. (1.31) to (1.34) the following differential equations for those functions of r:

$$r^2\frac{d^2R_E^{m,c}}{dr^2}+r\frac{dR_E^{m,c}}{dr}-\left[m^2+r^2\left(k^2-\omega^2\varepsilon_c\mu\right)\right]R_E^{m,c}=\frac{jQr^2\delta(r-a_1)}{\pi a_1(1+\delta_{m0})}\left(\frac{-k}{\varepsilon_c v}+\omega\mu\right), \tag{1.35}$$

$$r^2\frac{d^2R_E^{m,s}}{dr^2}+r\frac{dR_E^{m,s}}{dr}-\left[m^2+r^2\left(k^2-\omega^2\varepsilon_c\mu\right)\right]R_E^{m,s}=0, \tag{1.36}$$

$$r^2\frac{d^2R_H^{m,c}}{dr^2}+r\frac{dR_H^{m,c}}{dr}-\left[m^2+r^2\left(k^2-\omega^2\varepsilon_c\mu\right)\right]R_H^{m,c}=0, \tag{1.37}$$

$$r^2\frac{d^2R_H^{m,s}}{dr^2}+r\frac{dR_H^{m,s}}{dr}-\left[m^2+r^2\left(k^2-\omega^2\varepsilon_c\mu\right)\right]R_H^{m,s}=0, \tag{1.38}$$

Now we define the radial propagation constant as in Ref. [1] (using the definitions of Eqs. (1.12) and (1.13), and the identity $\varepsilon_0\mu_0=\frac{1}{c^2}$ where c is the speed of light in vacuum)

$$\nu^2=k^2-\omega^2\varepsilon_c\mu=k^2\left(1-\beta^2\varepsilon_1\mu_1\right), \tag{1.39}$$

so that

$$\nu=|k|\sqrt{1-\beta^2\varepsilon_1\mu_1}, \tag{1.40}$$

where $\beta\equiv\frac{v}{c}$ is the relativistic velocity factor of the particle, and the square root of a complex number is defined by

$$\sqrt{\alpha e^{j\varphi}}=\sqrt{\alpha}e^{j\frac{\varphi}{2}}\ \text{with}\ -\pi<\varphi\leq\pi. \tag{1.41}$$

With the change of variable $z=\nu r$ and assuming from now on $\nu\neq 0$[3] we get for $r\neq a_1$ the differential equation (C.1), whose solutions are the modified Bessel functions $I_m(\nu r)$ and $K_m(\nu r)$[4]. Putting the integration constants into $R_E^{m,c}$, $R_E^{m,s}$, $R_H^{m,c}$ and $R_H^{m,s}$, the Fourier coefficients of the longitudinal components

[3] $\nu\neq 0$ requires $\omega\neq 0$ – the zero frequency can be recovered as the limiting case of this study. Even for $\omega\neq 0$, $\nu=0$ is still possible at the onset of Cherenkov radiation in the layer considered (see e.g. Refs. [11, p. 637] or [55, p. 406]), under very particular conditions: for instance, when Eqs. (1.14) and (1.15) apply, to get $\nu=0$ there must be no losses in the layer, zero conductivity and $\beta=\frac{1}{\sqrt{\varepsilon_b\mu_r}}$.

[4] $I_m(-\nu r)$ and $K_m(-\nu r)$ are also solutions of Eqs. (1.35) to (1.38), which depend on ν through its square, but these solutions are linearly bound to $I_m(\nu r)$ and $K_m(\nu r)$ from Eqs. 9.6.30 and 9.6.31 of Ref. [56], which give in our case

$$
\begin{aligned}
I_m(-\nu r) &= (-1)^m I_m(\nu r),\\
K_m(-\nu r) &= (-1)^m K_m(\nu r)-j\pi I_m(\nu r).
\end{aligned}
$$

of the electromagnetic fields in frequency domain can be written

$$E_s^{m,c}(r,s;\omega) = e^{-jks}\left[C_{Ie}^{m,c} I_m(\nu r) + C_{Ke}^{m,c} K_m(\nu r)\right], \tag{1.42}$$
$$E_s^{m,s}(r,s;\omega) = e^{-jks}\left[C_{Ie}^{m,s} I_m(\nu r) + C_{Ke}^{m,s} K_m(\nu r)\right], \tag{1.43}$$
$$H_s^{m,c}(r,s;\omega) = e^{-jks}\left[C_{Ih}^{m,c} I_m(\nu r) + C_{Kh}^{m,c} K_m(\nu r)\right], \tag{1.44}$$
$$H_s^{m,s}(r,s;\omega) = e^{-jks}\left[C_{Ih}^{m,s} I_m(\nu r) + C_{Kh}^{m,s} K_m(\nu r)\right], \tag{1.45}$$

where the subscripts (Ie, Ke, Ih and Kh) of the integration constants are self-explanatory.

1.4.2 Transverse components of the electromagnetic fields

When applying Maxwell equations in a region where ε_c and μ are constant, we can obtain relations for the electromagnetic fields transverse components in each region (p). These relations, derived in Appendix E.1.1, couple together $\hat{E}_s^{m,c}$ and $\hat{H}_s^{m,s}$, as well as $\hat{E}_s^{m,s}$ and $\hat{H}_s^{m,c}$, through the field matching between adjacent layers that will relate together only the same component of the fields $\vec{E}$ and $\vec{H}$ (i.e. it will relate radial components between them, azimuthal ones between them and longitudinal ones between them). It appears then that $\hat{E}_s^{m,c}$ is never coupled to $\hat{E}_s^{m,s}$ or $\hat{H}_s^{m,c}$, and since no external excitation appears in Eqs. (1.32) and (1.33) we can use the same argument as in Section 1.4.1 to get

$$\hat{E}_s^{m,s} = \hat{H}_s^{m,c} = 0, \tag{1.46}$$

meaning obviously that $E_s^{m,s}$ and $H_s^{m,c}$ are zero as well. Finally, from the calculations done in Appendix E.1.1 we obtain for the transverse components

$$E_r^{m,s} = E_\theta^{m,c} = H_r^{m,c} = H_\theta^{m,s} = 0, \tag{1.47}$$
$$E_r^{m,c} = \frac{jk}{\nu^2}\left(\frac{dE_s^{m,c}}{dr} + \frac{m\upsilon\mu}{r} H_s^{m,s}\right), \tag{1.48}$$
$$E_\theta^{m,s} = \frac{jk}{\nu^2}\left(-\frac{m}{r} E_s^{m,c} - \upsilon\mu\frac{dH_s^{m,s}}{dr}\right), \tag{1.49}$$
$$H_r^{m,s} = \frac{jk}{\nu^2}\left(\frac{m\upsilon\varepsilon_c}{r} E_s^{m,c} + \frac{dH_s^{m,s}}{dr}\right), \tag{1.50}$$
$$H_\theta^{m,c} = \frac{jk}{\nu^2}\left(\upsilon\varepsilon_c\frac{dE_s^{m,c}}{dr} + \frac{m}{r} H_s^{m,s}\right). \tag{1.51}$$

Those formulae were also obtained in Refs. [1, 14]. We can then sum all the azimuthal modes thanks to Eqs. (1.22) and (1.23), obtaining (reintroducing the superscript (p) for more generality):

$$E_r^{(p)} = \frac{jk}{\left(\nu^{(p)}\right)^2}\left(\frac{\partial E_s^{(p)}}{\partial r} + \frac{\upsilon\mu^{(p)}}{r}\frac{\partial H_s^{(p)}}{\partial\theta}\right), \tag{1.52}$$
$$E_\theta^{(p)} = \frac{jk}{\left(\nu^{(p)}\right)^2}\left(\frac{1}{r}\frac{\partial E_s^{(p)}}{\partial\theta} - \upsilon\mu^{(p)}\frac{\partial H_s^{(p)}}{\partial r}\right), \tag{1.53}$$

$$H_r^{(p)} = \frac{jk}{\left(\nu^{(p)}\right)^2}\left(-\frac{v\varepsilon_c^{(p)}}{r}\frac{\partial E_s^{(p)}}{\partial\theta} + \frac{\partial H_s^{(p)}}{\partial r}\right), \tag{1.54}$$

$$H_\theta^{(p)} = \frac{jk}{\left(\nu^{(p)}\right)^2}\left(v\varepsilon_c^{(p)}\frac{\partial E_s^{(p)}}{\partial r} + \frac{1}{r}\frac{\partial H_s^{(p)}}{\partial\theta}\right). \tag{1.55}$$

1.4.3 Field matching

To specify the field components we need to express the boundary conditions between all the cylindrical layers. For simplicity, we will assume from this section onward that the angular frequency ω is positive[5]. Since for E_s only the cosine Fourier coefficients are non zero while for H_s only the sine ones are non zero, we can avoid using the superscript c or s in the integration constants $C_{Ie}^{m,c}$, $C_{Ke}^{m,c}$, $C_{Ih}^{m,s}$ and $C_{Kh}^{m,s}$. Reintroducing then the superscript (p) for the quantites related to a certain layer p, we can rewrite Eqs. (1.42) and (1.45) in the following way:

$$E_s^{m,c(p)}(r,s;\omega) = e^{-jks}\left[C_{Ie}^{m(p)} I_m\left(\nu^{(p)}r\right) + C_{Ke}^{m\ (p)} K_m\left(\nu^{(p)}r\right)\right], \tag{1.56}$$

$$H_s^{m,s(p)}(r,s;\omega) = e^{-jks}\left[C_{Ih}^{m(p)} I_m\left(\nu^{(p)}r\right) + C_{Kh}^{m\ (p)} K_m\left(\nu^{(p)}r\right)\right]. \tag{1.57}$$

Matching at $r = a_1$

Firstly, from Ref. [56] we know that for any $m \geq 0$, $I_m(0)$ is finite while $K_m(z)$ goes to infinity when $|z| \to 0$. Therefore, for the first layer we have necessarily, for any m:

$$C_{Ke}^{m\ (0)} = C_{Kh}^{m\ (0)} = 0. \tag{1.58}$$

We also know (from e.g. Ref. [11, p. 18]) that the electric field component tangential to a boundary between media is always continuous, giving in particular at $r = a_1$

$$E_s^{(0)}(r = a_1, \theta, s;\omega) = E_s^{(1)}(r = a_1, \theta, s;\omega),$$

for any θ, s and ω. Thanks to the Fourier series decomposition from Eq. (1.22) together with Eq. (1.56), identifying each term, dropping the e^{-jks} factor and plugging the value of the radial propagation constant of vacuum $\nu^{(0)} = \nu^{(1)} = \frac{k}{\gamma}$ from Eq. (1.40) where $\gamma = \frac{1}{\sqrt{1-\beta^2}}$ is the relativistic mass factor, we get for any m

$$C_{Ie}^{m(0)} I_m\left(\frac{ka_1}{\gamma}\right) = C_{Ie}^{m(1)} I_m\left(\frac{ka_1}{\gamma}\right) + C_{Ke}^{m\ (1)} K_m\left(\frac{ka_1}{\gamma}\right). \tag{1.59}$$

Equation (1.35) is valid across $r = a_1$, and following what is done in Ref. [42], we can divide each side by r, use the identity $r\frac{d^2}{dr^2} + \frac{d}{dr} = \frac{d}{dr}\left(r\frac{d}{dr}\right)$, replace $R_E^{m,c}$ by $E_s^{m,c}e^{jks}$ and integrate over r between $a_1 - \delta a_1$

[5] To recover the results at any frequency we would simply need to replace $\frac{k}{\gamma}$ by $\frac{|k|}{\gamma}$ in the expression of the radial propagation constant of vacuum. See also the end of Section 1.2.

and $a_1+\delta a_1$, obtaining for any m

$$(a_1+\delta a_1)\left.\frac{\partial\left(E_s^{m,c}e^{jks}\right)}{\partial r}\right|_{a_1+\delta a_1} - (a_1-\delta a_1)\left.\frac{\partial\left(E_s^{m,c}e^{jks}\right)}{\partial r}\right|_{a_1-\delta a_1}$$
$$+\int_{a_1-\delta a_1}^{a_1+\delta a_1}\mathrm{d}r\left(-\frac{m^2}{r}-rk^2+r\omega^2\varepsilon_0\mu_0\right)E_s^{m,c}e^{jks} = \frac{jQ}{\pi a_1(1+\delta_{m0})}\left(\frac{-k}{\varepsilon_0 v}+\omega\mu_0\right)\int_{a_1-\delta a_1}^{a_1+\delta a_1}\mathrm{d}r\delta(r-a_1)r$$
$$= \frac{-jQ\omega\mu_0}{\pi\beta^2\gamma^2(1+\delta_{m0})},$$

where we have replaced ε_c and μ by their values in vacuum ε_0 and μ_0. When δa_1 goes to zero, the integral term in the left-hand side vanishes since $E_s^{m,c}$ is not infinite at $r=a_1$. Using again Eq. (1.56), we get then

$$\frac{ka_1}{\gamma}\left[C_{Ie}^{m\,(1)}I_m'\left(\frac{ka_1}{\gamma}\right)+C_{Ke}^{m\,(1)}K_m'\left(\frac{ka_1}{\gamma}\right)-C_{Ie}^{m\,(0)}I_m'\left(\frac{ka_1}{\gamma}\right)\right] = \frac{-jQ\omega\mu_0}{\pi\beta^2\gamma^2(1+\delta_{m0})}. \tag{1.60}$$

By virtue of Eq. (1.59) we obtain

$$\frac{ka_1}{\gamma}C_{Ke}^{m\,(1)}\left[K_m'\left(\frac{ka_1}{\gamma}\right)I_m\left(\frac{ka_1}{\gamma}\right)-I_m'\left(\frac{ka_1}{\gamma}\right)K_m\left(\frac{ka_1}{\gamma}\right)\right] = \frac{-jQ\omega\mu_0}{\pi\beta^2\gamma^2(1+\delta_{m0})}I_m\left(\frac{ka_1}{\gamma}\right).$$

The term between square brackets is equal to $-\frac{\gamma}{ka_1}$ from Eq. (C.6). Finally we get

$$C_{Ke}^{m\,(1)} = \frac{jQ\omega\mu_0}{\pi\beta^2\gamma^2(1+\delta_{m0})}I_m\left(\frac{ka_1}{\gamma}\right) = \frac{2\mathscr{C}}{1+\delta_{m0}}I_m\left(\frac{ka_1}{\gamma}\right), \tag{1.61}$$

with the definition

$$\mathscr{C} \equiv \frac{jQ\omega\mu_0}{2\pi\beta^2\gamma^2}. \tag{1.62}$$

Finally, in Eq. (1.34) there is no source of discontinuity at $r=a_1$, so no reason for $H_s^{m,s}$ to have different integration constants from one side to the other of $r=a_1$, such that

$$C_{Kh}^{m\,(1)} = C_{Kh}^{m\,(0)} = 0 \qquad \text{and} \qquad C_{Ih}^{m\,(1)} = C_{Ih}^{m\,(0)}. \tag{1.63}$$

Boundary conditions at the pipe wall inner surface and between each of its layers

We will now consider the boundary conditions for the subsequent layers, i.e. at each $r=b^{(p)}$ for $1\leq p\leq N-1$. There are no externally imposed surface charges or currents between each cylindrical layer, which means (see Ref. [11, p. 18]) that the tangential components of $\vec{E}$ and $\vec{H}$ are continuous. After decomposition according to Eqs. (1.22) and (1.23) and identification of each term, the constants in front of the modified Bessel functions in the expression of E_s and H_s in Eqs. (1.56) and (1.57) (four integration constants per layer) appear to be the solutions of a linear system. Instead of solving this system by "brute force" which turns out to be very time consuming even for a computer, we can actually find a recurrent matrix relation between the integration constants of a given layer and those of the adjacent one, which allows us to solve analytically the full system. The complete derivation is detailed in Appendix E.1.2, and we will show here only the resulting expressions.
Introducing the free space impedance Z_0, the field $\vec{G}$ that has the same dimension as the electric field $\vec{E}$,

and the corresponding integration coefficients for $\vec{G}$

$$\begin{aligned} Z_0 &= \frac{1}{\varepsilon_0 c} = \mu_0 c = \sqrt{\frac{\mu_0}{\varepsilon_0}}, \\ \vec{G} &= Z_0 \vec{H}, \\ C_{Ig}^{m\,(p)} &= Z_0 C_{Ih}^{m\,(p)}, \\ C_{Kg}^{m\ (p)} &= Z_0 C_{Kh}^{m\ (p)}, \end{aligned} \tag{1.64}$$

and letting

$$x^{p,p} = \nu^{(p)} b^{(p)} \qquad \text{and} \qquad x^{p+1,p} = \nu^{(p+1)} b^{(p)}, \tag{1.65}$$

the relation between the constants of adjacent layers can be written as

$$\begin{bmatrix} C_{Ie}^{m\,(p+1)} \\ C_{Ke}^{m\ (p+1)} \\ C_{Ig}^{m\,(p+1)} \\ C_{Kg}^{m\ (p+1)} \end{bmatrix} = M^{p+1,p} \cdot \begin{bmatrix} C_{Ie}^{m\,(p)} \\ C_{Ke}^{m\ (p)} \\ C_{Ig}^{m\,(p)} \\ C_{Kg}^{m\ (p)} \end{bmatrix} = \begin{bmatrix} P^{p+1,p} & Q^{p+1,p} \\ S^{p+1,p} & R^{p+1,p} \end{bmatrix} \cdot \begin{bmatrix} C_{Ie}^{m\,(p)} \\ C_{Ke}^{m\ (p)} \\ C_{Ig}^{m\,(p)} \\ C_{Kg}^{m\ (p)} \end{bmatrix}, \tag{1.66}$$

where $P^{p+1,p}$, $Q^{p+1,p}$, $R^{p+1,p}$ and $S^{p+1,p}$ are four 2×2 matrices given by

$$P^{p+1,p} = -\frac{\left(\nu^{(p+1)}\right)^2 b^{(p)}}{\varepsilon_1^{(p+1)}} \begin{bmatrix} \zeta_{IK}\left\{\frac{\varepsilon_1^{(p+1)}}{\nu^{(p+1)}}\kappa_p^{p+1} - \frac{\varepsilon_1^{(p)}}{\nu^{(p)}}\lambda_p^p\right\} & \zeta_{KK}\left\{\frac{\varepsilon_1^{(p+1)}}{\nu^{(p+1)}}\kappa_p^{p+1} - \frac{\varepsilon_1^{(p)}}{\nu^{(p)}}\kappa_p^p\right\} \\ \zeta_{II}\left\{-\frac{\varepsilon_1^{(p+1)}}{\nu^{(p+1)}}\lambda_p^{p+1} + \frac{\varepsilon_1^{(p)}}{\nu^{(p)}}\lambda_p^p\right\} & \zeta_{KI}\left\{-\frac{\varepsilon_1^{(p+1)}}{\nu^{(p+1)}}\lambda_p^{p+1} + \frac{\varepsilon_1^{(p)}}{\nu^{(p)}}\kappa_p^p\right\} \end{bmatrix}, \tag{1.67}$$

$$Q^{p+1,p} = -\left(\frac{\left(\nu^{(p+1)}\right)^2}{\left(\nu^{(p)}\right)^2} - 1\right) \frac{m}{\beta \varepsilon_1^{(p+1)}} \begin{bmatrix} -\zeta_{IK} & -\zeta_{KK} \\ \zeta_{II} & \zeta_{KI} \end{bmatrix}, \tag{1.68}$$

$$R^{p+1,p} = -\frac{\left(\nu^{(p+1)}\right)^2 b^{(p)}}{\mu_1^{(p+1)}} \begin{bmatrix} \zeta_{IK}\left\{\frac{\mu_1^{(p+1)}}{\nu^{(p+1)}}\kappa_p^{p+1} - \frac{\mu_1^{(p)}}{\nu^{(p)}}\lambda_p^p\right\} & \zeta_{KK}\left\{\frac{\mu_1^{(p+1)}}{\nu^{(p+1)}}\kappa_p^{p+1} - \frac{\mu_1^{(p)}}{\nu^{(p)}}\kappa_p^p\right\} \\ \zeta_{II}\left\{-\frac{\mu_1^{(p+1)}}{\nu^{(p+1)}}\lambda_p^{p+1} + \frac{\mu_1^{(p)}}{\nu^{(p)}}\lambda_p^p\right\} & \zeta_{KI}\left\{-\frac{\mu_1^{(p+1)}}{\nu^{(p+1)}}\lambda_p^{p+1} + \frac{\mu_1^{(p)}}{\nu^{(p)}}\kappa_p^p\right\} \end{bmatrix}, \tag{1.69}$$

$$S^{p+1,p} = \frac{\varepsilon_1^{(p+1)}}{\mu_1^{(p+1)}} Q^{p+1,p}, \tag{1.70}$$

with

$$\lambda_p^p = \frac{I'_m(x^{p,p})}{I_m(x^{p,p})}, \quad \lambda_p^{p+1} = \frac{I'_m(x^{p+1,p})}{I_m(x^{p+1,p})}, \quad \kappa_p^p = \frac{K'_m(x^{p,p})}{K_m(x^{p,p})}, \quad \kappa_p^{p+1} = \frac{K'_m(x^{p+1,p})}{K_m(x^{p+1,p})}, \tag{1.71}$$

and

$$\begin{aligned} \zeta_{II} &= I_m(x^{p,p}) I_m(x^{p+1,p}), & \zeta_{KK} &= K_m(x^{p,p}) K_m(x^{p+1,p}), \\ \zeta_{IK} &= I_m(x^{p,p}) K_m(x^{p+1,p}), & \zeta_{KI} &= K_m(x^{p,p}) I_m(x^{p+1,p}). \end{aligned} \tag{1.72}$$

The quotients involving modified Bessel functions and their derivatives can be computed accurately thanks to Eqs. (C.7) and (C.8):

$$\frac{I'_m(z)}{I_m(z)} = \frac{I_{m-1}(z)}{I_m(z)} - \frac{m}{z} \quad \text{and} \quad \frac{K'_m(z)}{K_m(z)} = -\frac{K_{m-1}(z)}{K_m(z)} - \frac{m}{z}, \tag{1.73}$$

and we can normalize the Bessel functions in the first quotient of these expressions with e^z for I_m and e^{-z} for K_m, which does not change the quotient value.
When successively applying the relation (1.66), we get

$$\begin{bmatrix} C_{Ie}^{m(N)} \\ C_{Ke}^{m\ (N)} \\ C_{Ig}^{m(N)} \\ C_{Kg}^{m\ (N)} \end{bmatrix} = M^{N,N-1} \cdot M^{N-1,N-2} \cdots M^{2,1} \cdot \begin{bmatrix} C_{Ie}^{m(1)} \\ C_{Ke}^{m\ (1)} \\ C_{Ig}^{m(1)} \\ C_{Kg}^{m\ (1)} \end{bmatrix} = \mathscr{M} \cdot \begin{bmatrix} C_{Ie}^{m(1)} \\ C_{Ke}^{m\ (1)} \\ C_{Ig}^{m(1)} \\ C_{Kg}^{m\ (1)} \end{bmatrix},$$

with the definition

$$\mathscr{M} = M^{N,N-1} \cdot M^{N-1,N-2} \cdots M^{2,1}. \tag{1.74}$$

Field matching for the outer layer and final solution for the integration constants

The outer layer goes to infinity, which can have two different implications in terms of the electromagnetic fields. If $\nu^{(N)}$ has a non zero real part, it must be strictly positive according to the definition of $\nu^{(N)}$ in Eq. (1.40) and that of the square root in Eq. (1.41). Then according to Eqs. (C.20) and (C.21), $I_m\left(\nu^{(N)} r\right)$ goes to infinity with r, while $K_m\left(\nu^{(N)} r\right)$ goes to zero. Since the electromagnetic fields cannot go to infinity, we must have $C_{Ie}^{m(N)} = C_{Ig}^{m(N)} = 0$.
The condition will be the same (but for a different reason) if $\nu^{(N)}$ is purely imaginary in the layer considered, which will happen if $\left(\nu^{(N)}\right)^2$ is real and strictly negative in that layer. In that situation Cherenkov radiation [11, p. 637] occurs in the outer layer, and since there is (in our geometrical model) no other material beyond the outer layer, we cannot have any incoming wave: there should be only outcoming radiation whose wave vector is directed toward the outside of the chamber. Due to our choice of convention for the Fourier transform – see e.g. Eq. (1.2) – an outcoming wave is represented by an exponential factor of the form $e^{-jk_r^{rad} r}$ in the field components, with $k_r^{rad} \geq 0$, because in time domain the factor $e^{j(\omega t - k_r^{rad} r)}$ represents outcoming propagation in these conditions only (this can also

be seen in Eq. (1.6) for the propagation along s). Since the imaginary part of the square root of a negative number is always positive according to Eq. (1.41), from Eq. (C.21) the term in $K_m\left(\nu^{(N)}r\right)$ asymptotically represents outcoming radiation, while from Eq. (C.22) we see that the term $I_m\left(\nu^{(N)}r\right)$ is asymptotically a superposition of incoming and outcoming waves, which is not physical here.
Therefore we have in any case:

$$C_{Ie}^{m\,(N)} = C_{Ig}^{m\,(N)} = 0. \tag{1.75}$$

Note that Cherenkov radiation can occur in the air due to its small dielectric susceptibility, for γ sufficiently high. The effect on the beam-coupling impedance was discussed for instance in Ref. [57].
Recalling, from Eqs. (1.61) and (1.63) that

$$\begin{aligned} C_{Ke}^{m\,(1)} &= \frac{2\mathscr{C}}{1+\delta_{m0}} I_m\left(\frac{ka_1}{\gamma}\right), \\ C_{Kg}^{m\,(1)} &= 0, \end{aligned} \tag{1.76}$$

we can write

$$\begin{bmatrix} 0 \\ C_{Ke}^{m\,(N)} \\ 0 \\ C_{Kg}^{m\,(N)} \end{bmatrix} = \mathscr{M} \cdot \begin{bmatrix} C_{Ie}^{m\,(1)} \\ \frac{2\mathscr{C}}{1+\delta_{m0}} I_m\left(\frac{ka_1}{\gamma}\right) \\ C_{Ig}^{m\,(1)} \\ 0 \end{bmatrix}, \tag{1.77}$$

leading finally to the linear equations

$$\begin{aligned} \mathscr{M}_{11} C_{Ie}^{m\,(1)} + \mathscr{M}_{13} C_{Ig}^{m\,(1)} &= -\mathscr{M}_{12} C_{Ke}^{m\,(1)}, \\ \mathscr{M}_{31} C_{Ie}^{m\,(1)} + \mathscr{M}_{33} C_{Ig}^{m\,(1)} &= -\mathscr{M}_{32} C_{Ke}^{m\,(1)}, \end{aligned}$$

and

$$\begin{aligned} C_{Ke}^{m\,(N)} &= \mathscr{M}_{21} C_{Ie}^{m\,(1)} + \mathscr{M}_{22} C_{Ke}^{m\,(1)} + \mathscr{M}_{23} C_{Ig}^{m\,(1)}, \\ C_{Kg}^{m\,(N)} &= \mathscr{M}_{41} C_{Ie}^{m\,(1)} + \mathscr{M}_{42} C_{Ke}^{m\,(1)} + \mathscr{M}_{43} C_{Ig}^{m\,(1)}, \end{aligned} \tag{1.78}$$

where $\mathscr{M}_{rs}$ is the component in row r and column s of the matrix $\mathscr{M}$. The first two equations above can be inverted easily using the inversion formula of a 2×2 matrix (see Appendix D.1), giving

$$\begin{aligned} C_{Ie}^{m\,(1)} &= -C_{Ke}^{m\,(1)} \frac{\mathscr{M}_{12}\mathscr{M}_{33} - \mathscr{M}_{32}\mathscr{M}_{13}}{\mathscr{M}_{11}\mathscr{M}_{33} - \mathscr{M}_{13}\mathscr{M}_{31}}, \\ C_{Ig}^{m\,(1)} &= C_{Ke}^{m\,(1)} \frac{\mathscr{M}_{12}\mathscr{M}_{31} - \mathscr{M}_{32}\mathscr{M}_{11}}{\mathscr{M}_{11}\mathscr{M}_{33} - \mathscr{M}_{13}\mathscr{M}_{31}}. \end{aligned} \tag{1.79}$$

As in Ref. [1] we define α^m_{TM} and α^m_{TE} as the proportionality constants respectively between $C^{m\,(1)}_{Ie}$ and $-C^{m\,(1)}_{Ke}$, and between $C^{m\,(1)}_{Ig}$ and $C^{m\,(1)}_{Ke}$:

$$\begin{aligned}\alpha^m_{\mathrm{TM}} &= \frac{\mathscr{M}_{12}\mathscr{M}_{33}-\mathscr{M}_{32}\mathscr{M}_{13}}{\mathscr{M}_{11}\mathscr{M}_{33}-\mathscr{M}_{13}\mathscr{M}_{31}},\\ \alpha^m_{\mathrm{TE}} &= \frac{\mathscr{M}_{12}\mathscr{M}_{31}-\mathscr{M}_{32}\mathscr{M}_{11}}{\mathscr{M}_{11}\mathscr{M}_{33}-\mathscr{M}_{13}\mathscr{M}_{31}}.\end{aligned} \tag{1.80}$$

Note that these two quantities do not depend on the offset of the source a_1 since the matrices $M^{p+1,p}$ do not depend on a_1. On the other hand, α^m_{TM} and α^m_{TE} depend on the angular frequency ω.
Finally, knowing from Eqs. (1.58), (1.59) and (1.63) that

$$\begin{aligned}C^{m\,(0)}_{Ke} &= C^{m\,(0)}_{Kg}=0,\\ C^{m\,(0)}_{Ig} &= C^{m\,(1)}_{Ig},\\ C^{m(0)}_{Ie} &= C^{m(1)}_{Ie}+C^{m\,(1)}_{Ke}\frac{K_m\left(\frac{ka_1}{\gamma}\right)}{I_m\left(\frac{ka_1}{\gamma}\right)},\end{aligned} \tag{1.81}$$

we can compute the constants for all the layers p, and therefore we completely solve the electromagnetic problem.
As an example, we plotted in Fig. 1.2 the electromagnetic fields components corresponding to a single azimuthal mode $m=1$, in a graphite tube, with respect to the radial position in the tube.
It is worth mentioning that the general multilayer analysis was performed long ago for $m=0$ and $m=1$ in Refs. [12, 13], using a different algorithm that was implemented in a computer program called LAWAT, later [15] converted to Mathematica®[58]. According to Ref. [14], the results seemed to lack accuracy due to numerical errors, so the code was modified to compute the solutions in a symbolic way before performing the numerical evaluation. Still, some problems remained as it was very long to perform the computation (for the $m=1$ mode) for 3 layers of different materials in the pipe wall, and impossible to perform it for a larger number of layers. Our method, which involves only multiplications of 4×4 matrices and a final simple formula to compute α_{TM} and α_{TE}, overcomes this difficulty. Similar matrix methods have also been developped independently in Refs. [18–21].

1.4.4 Electromagnetic force inside the chamber

One of the quantity of interest is the Lorentz electromagnetic force $\vec{F}$ on a given test particle inside the vacuum pipe. We assume such a particle has a charge of q and the same velocity v as the source, neglecting any transverse velocity. Dropping the superscript (p) for conciseness, the longitudinal component of the force is written

$$F_s = qE_s, \tag{1.82}$$

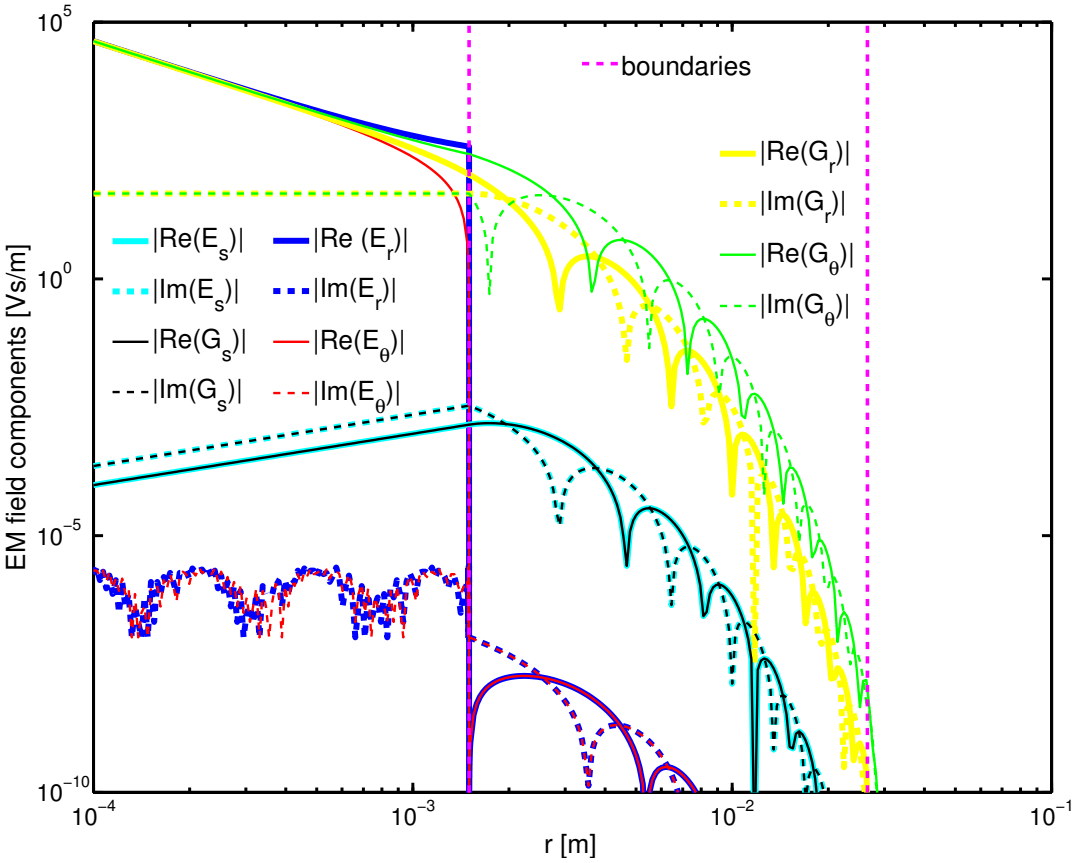

Figure 1.2: Electromagnetic fields along the direction $\theta = \frac{\pi}{4}$ for the $m = 1$ mode at a frequency of 1 MHz, in a graphite tube (actually made of CFC - see Chapter 2) of radius $b = 1.5$ mm and thickness 25 mm, surrounded by stainless steel (see materials parameters in Table F.4). The other parameters are $\gamma = 3730.26$, $Q = 1$ C and $a_1 = 10\,\mu$m.

while the transverse components are (using Eqs. (1.52) to (1.55) and recalling that $\nu = \frac{k}{\gamma}$ in vacuum)

$$F_r = q\left(E_r - v\mu_0 H_\theta\right) = \frac{jq\gamma^2}{k}\left(1-\beta^2\right)\frac{\partial E_s}{\partial r} = \frac{jq}{k}\frac{\partial E_s}{\partial r}, \tag{1.83}$$

$$F_\theta = q\left(E_\theta + v\mu_0 H_r\right) = \frac{jq\gamma^2}{k}\frac{1-\beta^2}{r}\frac{\partial E_s}{\partial \theta} = \frac{jq}{kr}\frac{\partial E_s}{\partial \theta}. \tag{1.84}$$

It appears here that the force does not depend on the longitudinal component of the magnetic field.

1.4.5 Total electric field longitudinal component in the vacuum region

Equations (1.46), (1.56) and (1.57) give, when reintroducing the Fourier series decomposition from Eqs (1.22) and (1.23) (recalling that $\vec{G} = Z_0\vec{H}$):

$$E_s^{(p)} = e^{-jks}\sum_{m=0}^{\infty}\cos(m\theta)\left[C_{Ie}^{m(p)} I_m\left(\nu^{(p)} r\right) + C_{Ke}^{m\,(p)} K_m\left(\nu^{(p)} r\right)\right], \tag{1.85}$$

and

$$G_s^{(p)} = e^{-jks} \sum_{m=0}^{\infty} \sin(m\theta) \left[C_{Ig}^{m\,(p)} I_m\left(\nu^{(p)} r\right) + C_{Kg}^{m\ (p)} K_m\left(\nu^{(p)} r\right) \right], \tag{1.86}$$

where the constants $C_{Ie}^{m(p)}$, $C_{Ke}^{m\ (p)}$, $C_{Ig}^{m(p)}$ and $C_{Kg}^{m\ (p)}$ (that depend on the angular frequency ω) are calculated thanks to the matrices defined in Eqs. (1.67) to (1.74), and the relations (1.66), (1.75), (1.76), (1.79) and (1.81).
Now we focus on E_s in the vacuum region inside the chamber, since only this component is needed to calculate the electromagnetic force that would affect a test particle. In the two vacuum regions indicated by the superscripts (0) and (1) (respectively for $r < a_1$ and $r \geq a_1$) we have, recalling that $\nu^{(0)} = \nu^{(1)} = \frac{k}{\gamma}$ and using Eqs. (1.76), (1.79), (1.81) and definitions (1.80):

$$\begin{aligned} E_s^{(0)} &= 2\mathscr{C} e^{-jks} \sum_{m=0}^{\infty} \frac{\cos(m\theta)}{1+\delta_{m0}} \left[K_m\left(\frac{ka_1}{\gamma}\right) - \alpha_{\mathrm{TM}}^m I_m\left(\frac{ka_1}{\gamma}\right) \right] I_m\left(\frac{kr}{\gamma}\right), \\ E_s^{(1)} &= 2\mathscr{C} e^{-jks} \sum_{m=0}^{\infty} \frac{\cos(m\theta)}{1+\delta_{m0}} \left[K_m\left(\frac{kr}{\gamma}\right) - \alpha_{\mathrm{TM}}^m I_m\left(\frac{kr}{\gamma}\right) \right] I_m\left(\frac{ka_1}{\gamma}\right). \end{aligned} \tag{1.87}$$

We will essentially identify two terms in E_s: one is the direct space charge term, that would be the only one present in the absence of any chamber (i.e. if the whole space were considered to be vacuum) and the other one will be called the wall term, entirely due to the cylindrical chamber's presence and properties.

Direct space charge term of the longitudinal electric field

If there is no pipe wall we must have $\alpha_{\mathrm{TM}}^m = 0$ since there can be no Bessel function I_m in the radial dependence of the field, this function going to infinity with r. We obtain exactly the first term of Eqs. (1.87):

$$\begin{aligned} E_s^{(0),SC} &= 2\mathscr{C} e^{-jks} \sum_{m=0}^{\infty} \frac{\cos(m\theta)}{1+\delta_{m0}} K_m\left(\frac{ka_1}{\gamma}\right) I_m\left(\frac{kr}{\gamma}\right), \\ E_s^{(1),SC} &= 2\mathscr{C} e^{-jks} \sum_{m=0}^{\infty} \frac{\cos(m\theta)}{1+\delta_{m0}} K_m\left(\frac{kr}{\gamma}\right) I_m\left(\frac{ka_1}{\gamma}\right), \end{aligned} \tag{1.88}$$

where the superscript "SC" stands for "direct space-charge". We can compute those two sums exactly using Eq. (C.27), giving the same result for both $r < a_1$ and $r \geq a_1$, so an expression valid in the whole vacuum region (we therefore drop the superscript (0) or (1)):

$$E_s^{vac,SC} = \mathscr{C} e^{-jks} K_0\left(\frac{k}{\gamma}\sqrt{a_1^2 + r^2 - 2a_1 r\cos\theta}\right), \tag{1.89}$$

where the superscript "vac" stands for the fields in the vacuum region. Note that $\sqrt{a_1^2 + r^2 - 2a_1 r\cos\theta}$ is, from the law of cosines, the distance (in the transverse plane) between the source and the point (r,θ)[6].

[6] This expression of the longitudinal electric field could have been derived in a simpler way: since we are in free space, it is the field created by a source particle at the origin of coordinates on a test particle at a distance r. The longitudinal electric field can be computed easily when knowing $E_s^{m,c}$ for $m = 0$ from Eq. (1.56), which is the electric field created by a cylindrically shaped source with charge density uniformly distributed on its surface $r = a_1$. By taking the limit $a_1 \to 0$ of $E_s^{0,c}$, removing the

We can generalize this formula for a source at $\theta = \theta_1$ instead of $\theta = 0$, which is straightforward from the continuous rotation invariance of the electromagnetic configuration about the s axis: we simply need to replace θ by $\theta - \theta_1$:

$$E_s^{vac,SC} = \mathscr{C} e^{-jks} K_0\left(\frac{k}{\gamma}\sqrt{a_1^2 + r^2 - 2a_1 r\cos(\theta - \theta_1)}\right). \tag{1.90}$$

Wall term of the longitudinal electric field

The wall term of the fields is the part of the fields due to the chamber, or in other words the total fields minus the direct space-charge term we have considered in the previous section. From Eqs. (1.87) and (1.88) the wall part of the field has the same expression in both regions 0 and 1, and we can write:

$$E_s^{vac,W} = -2\mathscr{C} e^{-jks} \sum_{m=0}^{\infty} \frac{\cos(m\theta)}{1+\delta_{m0}} \alpha_{\mathrm{TM}}^m I_m\left(\frac{ka_1}{\gamma}\right) I_m\left(\frac{kr}{\gamma}\right), \tag{1.91}$$

where the superscript "W" stands for the wall part of the field component. In the same way as above for the space-charge term, we can generalize to a source in $r = a_1$ and $\theta = \theta_1$ simply by replacing θ by $\theta - \theta_1$:

$$E_s^{vac,W} = -2\mathscr{C} e^{-jks} \sum_{m=0}^{\infty} \frac{\cos(m(\theta - \theta_1))}{1+\delta_{m0}} \alpha_{\mathrm{TM}}^m I_m\left(\frac{ka_1}{\gamma}\right) I_m\left(\frac{kr}{\gamma}\right). \tag{1.92}$$

The sum of Eqs. (1.90) and (1.92) gives the total general longitudinal electric field in the vacuum region due to the source in Eqs. (1.6) and (1.7), from which the total force and impedances can be derived.

1.4.6 Beam-coupling impedances

From now on we generalize our study to a source at $r = a_1$ and $\theta = \theta_1$ (instead of $\theta = 0$). We recall that in cartesian coordinates $x_1 = a_1\cos\theta_1$ and $y_1 = a_1\sin\theta_1$.

Definitions

We consider a test particle of charge q located at position $(r = a_2, \theta = \theta_2)$ in the transverse plane. Several definitions of the impedances exist in e.g. Refs. [42, 59, 60] and [7, p. 74]. We will here write the total longitudinal impedance in a general way, inspired by Ref. [60]:

$$Z_\parallel = -\frac{1}{Qq}\int \mathrm{d}V E_s J_t^*(a_2, \theta_2), \tag{1.93}$$

where the integration is performed over the volume of the structure considered, usually on a finite length L[7], and where E_s is given by the sum of Eqs. (1.90) and (1.92). The * stands for the complex conjugate

term in I_0 that goes to infinity with r, we obtain in that way

$$E_s = \mathscr{C} e^{-jks} K_0\left(\frac{kr}{\gamma}\right).$$

After a change of coordinates to put the source in $(r = a_1, \theta = 0)$, we get exactly the same as Eq. (1.89).

[7] This seems somehow in contradiction with our initial assumption on the infinite length of the chamber considered. First of all, if we were to integrate over an infinite length we would obtain an infinite result, as nothing depend on the position in the

and $\vec{J}_t = J_t \vec{e}_s$ is the density of the current flowing at the test particle position in frequency domain, whose expression is therefore (see Eq. (1.7))

$$J_t(a_2,\theta_2) = \frac{q}{a_2} e^{-jks} \delta(r-a_2)\delta_p(\theta-\theta_2). \tag{1.94}$$

With the same notations we define the total transverse impedances as [60]

$$Z_x = \frac{j}{Qq}\int \mathrm{d}V \left[\vec{E} + \beta\vec{e}_s \times \vec{G}\right]\cdot \vec{e}_x J_t^*(a_2,\theta_2) = \frac{j}{Qq}\int \mathrm{d}V \frac{F_x}{q} J_t^*(a_2,\theta_2), \tag{1.95}$$

$$Z_y = \frac{j}{Qq}\int \mathrm{d}V \left[\vec{E} + \beta\vec{e}_s \times \vec{G}\right]\cdot \vec{e}_y J_t^*(a_2,\theta_2) = \frac{j}{Qq}\int \mathrm{d}V \frac{F_y}{q} J_t^*(a_2,\theta_2). \tag{1.96}$$

These three definitions can be cast into a form involving only an integral over the length L, by plugging in Eqs. (1.83), (1.84), (1.94), and using $\vec{e}_x = \cos\theta\vec{e}_r - \sin\theta\vec{e}_\theta$ and $\vec{e}_y = \sin\theta\vec{e}_r + \cos\theta\vec{e}_\theta$:

$$Z_\parallel = -\frac{1}{Q}\int^L \mathrm{d}s E_s(a_2,\theta_2,s;\omega) e^{jks}, \tag{1.97}$$

$$Z_x = -\frac{1}{kQ}\int^L \mathrm{d}s \left[\cos\theta_2 \frac{\partial E_s}{\partial r}(a_2,\theta_2,s;\omega) - \frac{\sin\theta_2}{a_2}\frac{\partial E_s}{\partial \theta}(a_2,\theta_2,s;\omega)\right] e^{jks}, \tag{1.98}$$

$$Z_y = -\frac{1}{kQ}\int^L \mathrm{d}s \left[\sin\theta_2 \frac{\partial E_s}{\partial r}(a_2,\theta_2,s;\omega) + \frac{\cos\theta_2}{a_2}\frac{\partial E_s}{\partial \theta}(a_2,\theta_2,s;\omega)\right] e^{jks}. \tag{1.99}$$

Direct space-charge impedances

We find the direct space-charge impedances by injecting the longitudinal electric field due to the direct space charge from Eq. (1.90) in the impedance definitions from Eqs. (1.97) to (1.99). This requires some side calculations that are done in Appendix E.1.3. After conversion to cartesian coordinates, using the notations $x_2 = a_2\cos\theta_2$ and $y_2 = a_2\sin\theta_2$, we obtain

$$Z_\parallel^{SC,direct} = -\frac{j\omega\mu_0 L}{2\pi\beta^2\gamma^2} K_0\left(\frac{k\sqrt{(x_2-x_1)^2+(y_2-y_1)^2}}{\gamma}\right), \tag{1.100}$$

$$Z_x^{SC,direct} = \frac{j\omega\mu_0 L}{2\pi\beta^2\gamma^3} K_1\left(\frac{k\sqrt{(x_2-x_1)^2+(y_2-y_1)^2}}{\gamma}\right)\frac{x_2-x_1}{\sqrt{(x_2-x_1)^2+(y_2-y_1)^2}}, \tag{1.101}$$

$$Z_y^{SC,direct} = \frac{j\omega\mu_0 L}{2\pi\beta^2\gamma^3} K_1\left(\frac{k\sqrt{(x_2-x_1)^2+(y_2-y_1)^2}}{\gamma}\right)\frac{y_2-y_1}{\sqrt{(x_2-x_1)^2+(y_2-y_1)^2}}. \tag{1.102}$$

These expressions differ substantially from what can be found in Ref. [42] for instance, because we have summed all the azimuthal mode contributions in an exact way, which is required for that part of the impedance: even if both $\frac{ka_1}{\gamma}$ and $\frac{ka_2}{\gamma}$ are much smaller than unity, each mode contributes significantly to the sums in Eqs. (1.88). Indeed, it contains the product $I_m\left(\frac{ka_2}{\gamma}\right)K_m\left(\frac{ka_1}{\gamma}\right)$ (for e.g. $a_2 < a_1$) which is of order $\frac{1}{2m}\left(\frac{a_2}{a_1}\right)^m$ (i.e. of order unity) as can be seen from Eqs. (C.17) and (C.19).

integral. Besides, in practice one wants to compute the effect of the self-fields for a beam passing in a structure of finite length, which is the length L used here. Our initial assumption then simply states that we neglect all side effects due to the fact that the actual structure has some edges.

From Eqs. (C.18) and (C.19), it appears that when $\gamma \to \infty$, the direct space-charge impedances go to zero as $\frac{\ln(\gamma)}{\gamma^2}$ in longitudinal and as $\frac{1}{\gamma^2}$ in transverse. Therefore for ultrarelativistic beams the direct space-charge is often neglected, although it can still play a role in Landau damping even in the case of the LHC [61]. In any case direct space-charge effects constitute a field of study in itself, that can be well separated from the wall impedances defined below.

Wall impedances

The term of the impedance coming from the part of the fields due to the chamber presence is the so-called wall impedance, which is not exactly the same as the resistive-wall impedance and has been introduced in Ref. [9]. It contains both the impedance that we would have with a cylindrical chamber made of a perfect conductor (this part is usually called the indirect space-charge impedance) and the part of the impedance coming from the resistivity (or more generally the electromagnetic properties) of the layer(s).
The total wall impedances are therefore obtained when plugging the wall part of the longitudinal electric field from Eq. (1.92) into the definitions from Eqs. (1.97) to (1.99). After some additional algebra for the transverse wall impedances, which is detailed in Appendix E.1.4, we obtain

$$Z_{\parallel}^{Wall} = 2\frac{\mathscr{C}L}{Q}\sum_{m=0}^{\infty}\frac{\alpha_{\mathrm{TM}}^{m}\cos\left(m\left(\theta_2-\theta_1\right)\right)}{1+\delta_{m0}} I_m\left(\frac{ka_1}{\gamma}\right) I_m\left(\frac{ka_2}{\gamma}\right), \tag{1.103}$$

$$Z_{x}^{Wall} = 2\frac{\mathscr{C}L}{kQ}\sum_{m=0}^{\infty}\frac{\alpha_{\mathrm{TM}}^{m}}{1+\delta_{m0}} I_m\left(\frac{ka_1}{\gamma}\right)\left[\frac{k\cos\theta_2\cos\left(m\left(\theta_2-\theta_1\right)\right)}{\gamma} I_{m-1}\left(\frac{ka_2}{\gamma}\right) - \frac{m\cos\left(\theta_2+m\left(\theta_2-\theta_1\right)\right)}{a_2} I_m\left(\frac{ka_2}{\gamma}\right)\right], \tag{1.104}$$

$$Z_{y}^{Wall} = 2\frac{\mathscr{C}L}{kQ}\sum_{m=0}^{\infty}\frac{\alpha_{\mathrm{TM}}^{m}}{1+\delta_{m0}} I_m\left(\frac{ka_1}{\gamma}\right)\left[\frac{k\sin\theta_2\cos\left(m\left(\theta_2-\theta_1\right)\right)}{\gamma} I_{m-1}\left(\frac{ka_2}{\gamma}\right) - \frac{m\sin\left(\theta_2+m\left(\theta_2-\theta_1\right)\right)}{a_2} I_m\left(\frac{ka_2}{\gamma}\right)\right]. \tag{1.105}$$

These expressions give the general nonlinear wall impedances, but usually one is interested only in the first order terms in the source and test positions, so for small $\frac{ka_1}{\gamma}$ and $\frac{ka_2}{\gamma}$. These can be obtained by plugging the Taylor series of the modified Bessel functions in the above expressions. After some mathematical manipulations (also detailed in Appendix E.1.4), the wall impedances can be approximated up to second order by

$$Z_{\parallel}^{Wall} \approx \frac{\mathscr{C}L}{Q}\left[\alpha_{\mathrm{TM}}^{0} + \frac{k^2\alpha_{\mathrm{TM}}^{0}}{4\gamma^2}x_1^2 + \frac{k^2\alpha_{\mathrm{TM}}^{0}}{4\gamma^2}y_1^2 + \frac{k^2\alpha_{\mathrm{TM}}^{0}}{4\gamma^2}x_2^2 + \frac{k^2\alpha_{\mathrm{TM}}^{0}}{4\gamma^2}y_2^2 + \frac{k^2\alpha_{\mathrm{TM}}^{1}}{2\gamma^2}x_1x_2 + \frac{k^2\alpha_{\mathrm{TM}}^{1}}{2\gamma^2}y_1y_2\right], \tag{1.106}$$

$$Z_{x}^{Wall} \approx \frac{\mathscr{C}Lk}{2\gamma^2 Q}\left(\alpha_{\mathrm{TM}}^{1}x_1 + \alpha_{\mathrm{TM}}^{0}x_2\right), \tag{1.107}$$

$$Z_{y}^{Wall} \approx \frac{\mathscr{C}Lk}{2\gamma^2 Q}\left(\alpha_{\mathrm{TM}}^{1}y_1 + \alpha_{\mathrm{TM}}^{0}y_2\right). \tag{1.108}$$

The longitudinal wall impedance is often reduced to its zeroth order (constant) term, which is given by (with the definition of $\mathscr{C}$ in Eq. (1.62)):

$$Z_{\parallel}^{Wall,0} = \frac{j\omega\mu_0 L}{2\pi\beta^2\gamma^2}\alpha_{\mathrm{TM}}^0. \tag{1.109}$$

The terms usually considered for the transverse impedances are the linear ones, i.e. (since Z_x^{Wall} and Z_y^{Wall} have no constant term) proportional to x_1, y_1, x_2 or y_2, the coefficient of proportionality being called dipolar impedance (when considering a term proportional to the source particle coordinates) or quadrupolar impedance (when considering a term proportional to the test particle coordinates). We write therefore:

$$Z_x^{Wall,dip} = Z_y^{Wall,dip} = \frac{jk^2 Z_0 L}{4\pi\beta\gamma^4}\alpha_{\mathrm{TM}}^1, \tag{1.110}$$

$$Z_x^{Wall,quad} = Z_y^{Wall,quad} = \frac{jk^2 Z_0 L}{4\pi\beta\gamma^4}\alpha_{\mathrm{TM}}^0. \tag{1.111}$$

We notice here that, contrary to usual ultrarelativistic results (see e.g. Ref. [62]), we obtained a non zero quadrupolar impedance. It comes from the $m = 0$ mode, so from the fact that we considered together all azimuthal modes instead of treating separately the $m = 0$ and $m = 1$ modes and identifying the transverse impedances to those exclusively coming from the $m = 1$ mode, as is usually done.

Panofsky-Wenzel theorem on the derived impedances

In Appendix E.1.5, we check that the impedances derived above are in agreement with the Panofsky-Wenzel theorem as stated in Ref. [7, p. 90], namely

$$kZ_x^{Wall} = \frac{\partial Z_{\parallel}^{Wall}}{\partial x_2} \qquad \text{and} \quad kZ_y^{Wall} = \frac{\partial Z_{\parallel}^{Wall}}{\partial y_2}. \tag{1.112}$$

1.5 Case of a flat multilayer chamber

We study now the particular case of a flat multilayer chamber (typically a collimator), as shown in Fig. 1.3. The chamber is made of two infinitely thick (in the y direction) and large (in the x direction) plates with vertical separation of $2b$ between them, located at $y = \pm b$, where b is called the half gap. The space is thus divided into $N + M$ flat parallel layers, the outer boundary of each of them being located at $y = b^{(p)}$. N layers are located in the upper part of the chamber (including the vacuum layer between $y = y_1$ and $y = b = b^{(1)}$), and M layers are located in the lower part of the chamber (including the vacuum layer between $y = -b = b^{(-1)}$ and $y = y_1$). The superscript (p) is now added to all the quantities (material properties, electromagnetic fields, etc.) related to a particular layer (as in e.g. $\varepsilon_c^{(p)}$ and $\mu^{(p)}$), unless it is perfectly clear from the context which layer is being studied. In these, p is between $-M$ and N and is different from zero, and has a plus sign for the upper layers and a minus sign for the lower ones. Either M or N can be equal to one (case of a structure with no top or bottom plate).
To simplify the problem we can set the particle postion to $x = 0$ and $y = y_1$ without loss of generality since the geometry exhibits a continuous translational invariance along the x axis.
The approach followed here is equivalent but slightly different from that of Ref. [63]. To solve Maxwell

equations we will use cartesian coordinates and decompose the electromagnetic fields in the following way (omitting for now the superscript (p)):

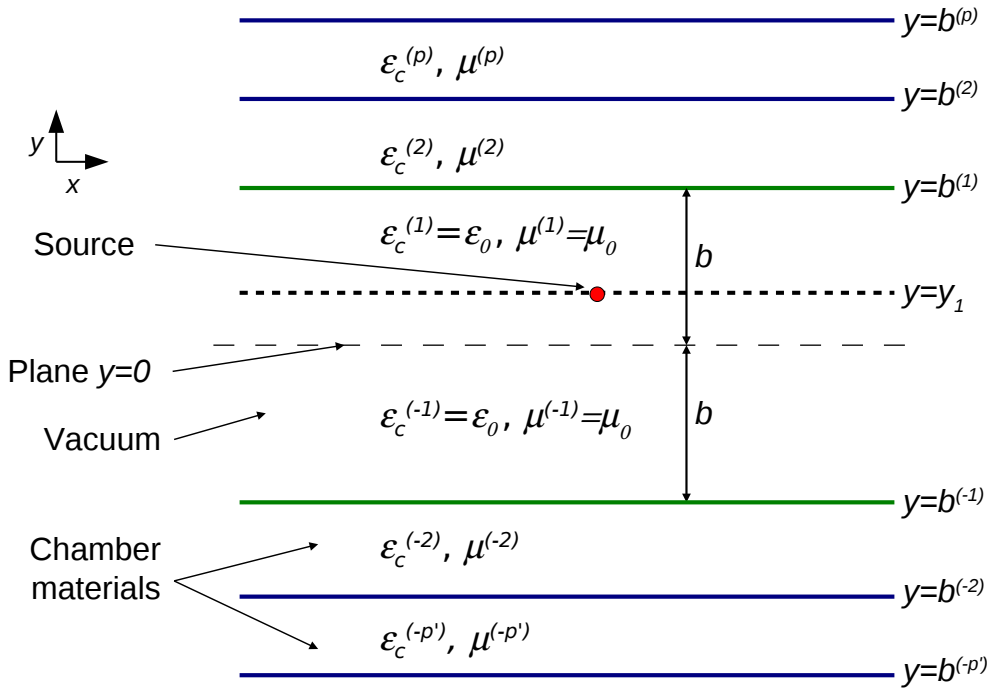

Figure 1.3: Cross section of the flat chamber. The regions denoted by the superscript (± 1) are the vacuum regions inside the structure, with the fictitious plane $y = y_1$ as a separation between them. Subsequent layers can be made of any medium. The last layers, denoted at the top by the superscript (N) and at the bottom by the superscript $(-M)$, go to infinity ($b^{(N)} = -b^{(-M)} = \infty$). We have also sketched in red the source particle at $x = 0$ and $y = y_1$.

$$\begin{aligned}\vec{E}(x,y,s;\omega) &= \int_{-\infty}^{\infty} \mathrm{d}k' e^{-jk's} \vec{\tilde{E}}(x,y;k',\omega) \\ &= \int_{-\infty}^{\infty} \mathrm{d}k' e^{-jk's} \int_0^{\infty} \mathrm{d}k_x \left[\cos(k_x x)\, \vec{\tilde{E}}^c(y;k_x,k',\omega) + \sin(k_x x)\, \vec{\tilde{E}}^s(y;k_x,k',\omega)\right], \end{aligned} \quad (1.113)$$

where $\vec{\tilde{E}}$ is the Fourier transform along the s axis of $\vec{E}$, while $\vec{\tilde{E}}^c$ and $\vec{\tilde{E}}^s$ are the Fourier cosine and sine transforms of $\vec{\tilde{E}}$ along the x axis (actually, the sine transform should have an additional $-j$ factor in front of $\sin(k_x x)$, but we prefer to include it in $\vec{\tilde{E}}^s$). We can decompose in the same way $\vec{H}$, introducing the quantities $\vec{\tilde{H}}$, $\vec{\tilde{H}}^c$ and $\vec{\tilde{H}}^s$:

$$\begin{aligned}\vec{H}(x,y,s;\omega) &= \int_{-\infty}^{\infty} \mathrm{d}k' e^{-jk's} \vec{\tilde{H}}(r,\theta;k',\omega) \\ &= \int_{-\infty}^{\infty} \mathrm{d}k' e^{-jk's} \int_0^{\infty} \mathrm{d}k_x \left[\cos(k_x x)\, \vec{\tilde{H}}^c(y;k_x,k',\omega) + \sin(k_x x)\, \vec{\tilde{H}}^s(y;k_x,k',\omega)\right]. \end{aligned} \quad (1.114)$$

We also define as $\vec{E}^c$, $\vec{E}^s$, $\vec{H}^c$ and $\vec{H}^s$ the horizontal cosine and sine Fourier transforms of $\vec{E}$ and $\vec{H}$, i.e.

$$\vec{E}\left(x,y,s;\omega\right) = \int_0^\infty \mathrm{d}k_x \left[\cos\left(k_x x\right)\vec{E}^c\left(y,s;k_x,\omega\right) + \sin\left(k_x x\right)\vec{E}^s\left(y,s;k_x,\omega\right)\right], \tag{1.115}$$

$$\vec{H}\left(x,y,s;\omega\right) = \int_0^\infty \mathrm{d}k_x \left[\cos\left(k_x x\right)\vec{H}^c\left(y,s;k_x,\omega\right) + \sin\left(k_x x\right)\vec{H}^s\left(y,s;k_x,\omega\right)\right], \tag{1.116}$$

such that

$$\vec{E}^c\left(y,s;k_x,\omega\right) = \int_{-\infty}^\infty \mathrm{d}k' e^{-jk's}\tilde{\vec{E}}^c\left(y;k_x,k',\omega\right), \quad \vec{E}^s\left(y,s;k_x,\omega\right) = \int_{-\infty}^\infty \mathrm{d}k' e^{-jk's}\tilde{\vec{E}}^s\left(y;k_x,k',\omega\right), \tag{1.117}$$

$$\vec{H}^c\left(y,s;k_x,\omega\right) = \int_{-\infty}^\infty \mathrm{d}k' e^{-jk's}\tilde{\vec{H}}^c\left(y;k_x,k',\omega\right), \quad \vec{H}^s\left(y,s;k_x,\omega\right) = \int_{-\infty}^\infty \mathrm{d}k' e^{-jk's}\tilde{\vec{H}}^s\left(y;k_x,k',\omega\right). \tag{1.118}$$

Finally, in a similar way as when we derived Eq. (1.2) we can rewrite the charge density from Eq. (1.4) thanks to the horizontal cosine Fourier transform of the $\delta(x)$ factor [30]:

$$\begin{aligned}\delta(x) &= \frac{1}{2\pi}\int_{-\infty}^\infty e^{-jk_x x}\mathrm{d}k_x \\ &= \frac{1}{2\pi}\int_0^\infty \left(e^{-jk_x x} + e^{jk_x x}\right)\mathrm{d}k_x \\ &= \frac{1}{\pi}\int_0^\infty \cos(k_x x)\mathrm{d}k_x.\end{aligned} \tag{1.119}$$

We then obtain for the charge density in frequency domain, recalling that here $x_1 = 0$:

$$\rho(x,y,s;\omega) = \frac{Q}{\pi\upsilon}\int_0^\infty \mathrm{d}k_x \cos(k_x x)\delta(y-y_1)e^{-jks}, \tag{1.120}$$

$$= \int_{-\infty}^\infty \mathrm{d}k' e^{-jk's}\delta(k'-k)\frac{Q}{\pi\upsilon}\int_0^\infty \mathrm{d}k_x \cos(k_x x)\delta(y-y_1). \tag{1.121}$$

1.5.1 Longitudinal components of the electromagnetic fields

In a given layer, using the expressions of the gradient and the laplacian in cartesian coordinates (see Eqs. (B.6), (B.9) and (B.10) of Appendix B.2), we can turn the wave equations (1.18) and (1.19) for the longitudinal field components into the following scalar Helmholtz equations (still omitting the superscript (p)):

$$\left[\frac{\partial^2}{\partial x^2} + \frac{\partial^2}{\partial y^2} + \frac{\partial^2}{\partial s^2} + \omega^2\varepsilon_c\mu\right]E_s = \frac{1}{\varepsilon_c}\frac{\partial\rho}{\partial s} + j\omega\mu\rho\upsilon, \tag{1.122}$$

$$\left[\frac{\partial^2}{\partial x^2} + \frac{\partial^2}{\partial y^2} + \frac{\partial^2}{\partial s^2} + \omega^2\varepsilon_c\mu\right]H_s = 0. \tag{1.123}$$

Similarly to what was done in the axisymmetric case, we can now rewrite those equations by introducing the decompositions from Eqs. (1.113), (1.114) and (1.121) of respectively $\vec{E}$, $\vec{H}$ and ρ. After identification of each cosine and sine term in the integrands, we get for the Fourier transforms of the fields longitudinal

components:

$$\frac{d^2\tilde{E}_s^c}{dy^2} - \left(k_x^2 + k'^2 - \omega^2\varepsilon_c\mu\right)\tilde{E}_s^c = \frac{jQe^{-jk's}\delta(y-y_1)\delta(k'-k)}{\pi}\left(\frac{-k'}{\varepsilon_c v} + \omega\mu\right), \tag{1.124}$$

$$\frac{d^2\tilde{E}_s^s}{dy^2} - \left(k_x^2 + k'^2 - \omega^2\varepsilon_c\mu\right)\tilde{E}_s^s = 0, \tag{1.125}$$

$$\frac{d^2\hat{H}_s^c}{dy^2} - \left(k_x^2 + k'^2 - \omega^2\varepsilon_c\mu\right)\hat{H}_s^c = 0, \tag{1.126}$$

$$\frac{d^2\hat{H}_s^s}{dy^2} - \left(k_x^2 + k'^2 - \omega^2\varepsilon_c\mu\right)\hat{H}_s^s = 0, \tag{1.127}$$

which is valid for any k_x, ω and k'. From the above system and the fact that the geometry studied does not allow any coupling between different wave numbers k' (from its translational invariance along the s axis), we can deduce that when $k' \neq k$, all the functions $\tilde{\vec{E}}^c$, $\tilde{\vec{E}}^s$, $\tilde{\vec{H}}^c$ and $\tilde{\vec{H}}^s$ are identically zero: they are solution of a system of differential equations with no right hand side, or, put in other words, without excitation of any external charge or current density. The only possibility for them not be zero is if some electromagnetic waves are present in the structure independently of the travelling beam, but this kind of solutions is not related to the beam-coupling impedance, therefore we will not consider them here. This means in particular that those functions have to be proportional to the only non zero right hand side term in the above system, so to $\delta(k'-k)$. We get then, from Eqs. (1.117) and (1.118):

$$\begin{aligned}
E_s^c\left(y,s;k_x,\omega\right) &= e^{-jks}Y_E^c\left(y;k_x,\omega\right),\\
E_s^s\left(y,s;k_x,\omega\right) &= e^{-jks}Y_E^s\left(y;k_x,\omega\right),\\
H_s^c\left(y,s;k_x,\omega\right) &= e^{-jks}Y_H^c\left(y;k_x,\omega\right),\\
H_s^s\left(y,s;k_x,\omega\right) &= e^{-jks}Y_H^s\left(y;k_x,\omega\right),
\end{aligned}$$

where Y_E^c, Y_E^s, Y_H^c and Y_H^s are independent of k'. After multiplication by $e^{-jk's}$ and integration over k', we get from Eqs. (1.124) to (1.127) the following differential equations for those functions of y:

$$\frac{d^2Y_E^c}{dy^2} - \left[k_x^2 + k^2 - \omega^2\varepsilon_c\mu\right]Y_E^c = \frac{jQ\delta(y-y_1)}{\pi}\left(\frac{-k}{\varepsilon_c v} + \omega\mu\right), \tag{1.128}$$

$$\frac{d^2Y_E^s}{dy^2} - \left[k_x^2 + k^2 - \omega^2\varepsilon_c\mu\right]Y_E^s = 0, \tag{1.129}$$

$$\frac{d^2Y_H^c}{dy^2} - \left[k_x^2 + k^2 - \omega^2\varepsilon_c\mu\right]Y_H^c = 0, \tag{1.130}$$

$$\frac{d^2Y_H^s}{dy^2} - \left[k_x^2 + k^2 - \omega^2\varepsilon_c\mu\right]Y_H^s = 0. \tag{1.131}$$

Now we define the radial propagation constant as in the cylindrical case – see Eqs. (1.39) and (1.40) (with the same convention for the square root):

$$\nu = |k|\sqrt{1-\beta^2\varepsilon_1\mu_1},$$

and the vertical wave number

$$k_y = \sqrt{k_x^2 + \nu^2}. \tag{1.132}$$

Equations (1.128) to (1.131) are harmonic differential equations, whose solutions are the exponentials $e^{k_y y}$ and $e^{-k_y y}$. Putting the integration constants into Y_E^c, Y_E^s, Y_H^c and Y_H^s, the horizontal cosine and sine Fourier transforms of the longitudinal components of the electromagnetic fields in frequency domain can be finally written

$$E_s^c\left(y,s;k_x,\omega\right) = e^{-jks}\left[C_{e+}^c(k_x)e^{k_y y} + C_{e-}^c(k_x)e^{-k_y y}\right], \tag{1.133}$$

$$E_s^s\left(y,s;k_x,\omega\right) = e^{-jks}\left[C_{e+}^s(k_x)e^{k_y y} + C_{e-}^s(k_x)e^{-k_y y}\right], \tag{1.134}$$

$$H_s^c\left(y,s;k_x,\omega\right) = e^{-jks}\left[C_{h+}^c(k_x)e^{k_y y} + C_{h-}^c(k_x)e^{-k_y y}\right], \tag{1.135}$$

$$H_s^s\left(y,s;k_x,\omega\right) = e^{-jks}\left[C_{h+}^s(k_x)e^{k_y y} + C_{h-}^s(k_x)e^{-k_y y}\right], \tag{1.136}$$

where the subscripts in the integration constants C_{e+}^c, C_{e-}^c, C_{h+}^c, C_{h-}^c, C_{e+}^s, C_{e-}^s, C_{h+}^s and C_{h-}^s have the following meaning: the letter (e or h) stands respectively for the electric or magnetic field, and the + or − sign stands for the sign in front of $k_y y$ in the exponential corresponding to the constant. Note that those integration constants are also functions of the horizontal wave number k_x.

1.5.2 Transverse components of the electromagnetic fields

When applying Maxwell equations in a region where ε_c and μ are constant, we can obtain relations for the electromagnetic fields transverse components in each region (p). These relations, derived in Appendix E.2.1, couple together $\tilde{E}_s^c$ and $\tilde{H}_s^s$, as well as $\tilde{E}_s^s$ and $\tilde{H}_s^c$, through the field matching between adjacent layers that will relate together only the same component of the fields $\vec{E}$ and $\vec{H}$ (i.e. it will relate horizontal components between them, vertical ones between them and longitudinal ones between them). It appears then that $\tilde{E}_s^c$ is never coupled to $\tilde{E}_s^s$ or $\tilde{H}_s^c$, and since no external excitation appears in Eqs. (1.125) and (1.126) we can use the same argument as in Section 1.5.1 to get

$$\tilde{E}_s^s = \tilde{H}_s^c = 0, \tag{1.137}$$

meaning obviously that E_s^s and H_s^c are zero as well. Finally, from the calculations done in Appendix E.2.1 we obtain for the transverse components

$$E_x^c = E_y^s = H_x^s = H_y^c = 0, \tag{1.138}$$

$$E_x^s = \frac{jk}{\nu^2}\left(-k_x E_s^c + \upsilon\mu\frac{dH_s^s}{dy}\right), \tag{1.139}$$

$$E_y^c = \frac{jk}{\nu^2}\left(\frac{dE_s^c}{dy} - k_x\upsilon\mu H_s^s\right), \tag{1.140}$$

$$H_x^c = \frac{jk}{\nu^2}\left(-\upsilon\varepsilon_c\frac{dE_s^c}{dy} + k_x H_s^s\right), \tag{1.141}$$

$$H_y^s = \frac{jk}{\nu^2}\left(-k_x\upsilon\varepsilon_c E_s^c + \frac{dH_s^s}{dy}\right). \tag{1.142}$$

We can also integrate over k_x thanks to Eqs. (1.115) and (1.116), obtaining for the total transverse components (reintroducing the superscript (p) for more generality):

$$E_x^{(p)} = \frac{jk}{\left(\nu^{(p)}\right)^2}\left(\frac{\partial E_s^{(p)}}{\partial x} + v\mu^{(p)}\frac{\partial H_s^{(p)}}{\partial y}\right), \tag{1.143}$$

$$E_y^{(p)} = \frac{jk}{\left(\nu^{(p)}\right)^2}\left(\frac{\partial E_s^{(p)}}{\partial y} - v\mu^{(p)}\frac{\partial H_s^{(p)}}{\partial x}\right), \tag{1.144}$$

$$H_x^{(p)} = \frac{jk}{\left(\nu^{(p)}\right)^2}\left(-v\varepsilon_c^{(p)}\frac{\partial E_s^{(p)}}{\partial y} + \frac{\partial H_s^{(p)}}{\partial x}\right), \tag{1.145}$$

$$H_y^{(p)} = \frac{jk}{\left(\nu^{(p)}\right)^2}\left(v\varepsilon_c^{(p)}\frac{\partial E_s^{(p)}}{\partial x} + \frac{\partial H_s^{(p)}}{\partial y}\right). \tag{1.146}$$

Note that we have implicitely assumed that $\nu^{(p)} \neq 0$ and will continue to make this assumption in all the following sections. This means we assume not to be at the onset of Cherenkov radiation (see footnote 3 at the end of Section 1.4.1).

1.5.3 Field matching

To specify the field components we need to express the boundary conditions between all the layers. For conciseness of the notations, we will assume from this section onward that the angular frequency ω is positive[8]. Since for E_s only the cosine Fourier transform is non zero while for H_s only the sine one is non zero, we can avoid using the superscript c or s in the integration constants C_{e+}^c, C_{e-}^c, C_{h+}^s and C_{h-}^s. Reintroducing then the superscript (p) for the quantities related to a certain layer p, we can rewrite Eqs. (1.133) and (1.136) in the following way:

$$E_s^{c(p)}\left(y, s; k_x, \omega\right) = e^{-jks}\left[C_{e+}^{(p)}(k_x)e^{k_y^{(p)}y} + C_{e-}^{(p)}(k_x)e^{-k_y^{(p)}y}\right], \tag{1.147}$$

$$H_s^{s(p)}\left(y, s; k_x, \omega\right) = e^{-jks}\left[C_{h+}^{(p)}(k_x)e^{k_y^{(p)}y} + C_{h-}^{(p)}(k_x)e^{-k_y^{(p)}y}\right], \tag{1.148}$$

with $k_y^{(p)}$ given by Eq. (1.132), i.e. with the (p) superscript added:

$$k_y^{(p)} = \sqrt{k_x^2 + \left(\nu^{(p)}\right)^2}. \tag{1.149}$$

Boundary conditions at $y = y_1$

We know (from e.g. Ref. [11, p. 18]) that the electric field components tangential to a boundary between media is always continuous, giving in particular at $y = y_1$

$$E_s^{(-1)}(x, y = y_1, s; \omega) = E_s^{(1)}(x, y = y_1, s; \omega),$$

[8] To recover the results at any frequency we would simply need to replace $\frac{k}{\gamma}$ by $\frac{|k|}{\gamma}$ in the expression of the propagation constant of vacuum. See also the end of Section 1.2.

for any x, s and ω. Thanks to the Fourier transform in Eq. (1.115), we get then from Eq. (1.147), identifying each term, dropping the e^{-jks} factor and noticing that $k_y^{(1)} = k_y^{(-1)}$ from $\nu^{(1)} = \nu^{(-1)}$ and Eq. (1.149):

$$C_{e+}^{(-1)} e^{k_y^{(1)} y_1} + C_{e-}^{(-1)} e^{-k_y^{(1)} y_1} = C_{e+}^{(1)} e^{k_y^{(1)} y_1} + C_{e-}^{(1)} e^{-k_y^{(1)} y_1} \iff C_{e-}^{(-1)} - C_{e-}^{(1)} = \left(C_{e+}^{(1)} - C_{e+}^{(-1)} \right) e^{2k_y^{(1)} y_1}, \quad (1.150)$$

for any k_x. Besides, Eq. (1.128) is valid across $y = y_1$, and following what is done in Ref. [42], we can replace Y_E^c by $E_s^c e^{jks}$ and integrate over y between $y_1 - \delta y_1$ and $y_1 + \delta y_1$, obtaining for any k_x

$$\left.\frac{\partial E_s^c}{\partial y}\right|_{y_1+\delta y_1} - \left.\frac{\partial E_s^c}{\partial y}\right|_{y_1-\delta y_1} + \int_{y_1-\delta y_1}^{y_1+\delta y_1} \mathrm{d}y \left(-k_x^2 - k^2 + \omega^2 \varepsilon_0 \mu_0\right) E_s^c = \frac{jQ}{\pi} \left(\frac{-k}{\varepsilon_0 v} + \omega \mu_0 \right) \int_{y_1-\delta y_1}^{y_1+\delta y_1} \mathrm{d}y \delta(y - y_1)$$
$$= \frac{-jQ\omega\mu_0}{\pi \beta^2 \gamma^2},$$

where we have replaced ε_c and μ by their values in vacuum ε_0 and μ_0. When δy_1 goes to zero, the integral term in the left-hand side vanishes since E_s^c is not infinite at $y = y_1$. Replacing E_s^c by its expression from Eq. (1.147) on each side of the boundary, we can rewrite the above equation as

$$k_y^{(1)} C_{e+}^{(1)} e^{k_y^{(1)} y_1} - k_y^{(1)} C_{e-}^{(1)} e^{-k_y^{(1)} y_1} - k_y^{(1)} C_{e+}^{(-1)} e^{k_y^{(1)} y_1} + k_y^{(1)} C_{e-}^{(-1)} e^{-k_y^{(1)} y_1} = -2\mathscr{C}, \quad (1.151)$$

with the definition $\mathscr{C} \equiv \frac{jQ\omega\mu_0}{2\pi\beta^2\gamma^2}$ already used in the axisymmetric case – see Eq. (1.62). Injecting then Eq. (1.150) into Eq. (1.151), we get

$$C_{e+}^{(1)} - C_{e+}^{(-1)} = -\mathscr{C} \frac{e^{-k_y^{(1)} y_1}}{k_y^{(1)}} \qquad \text{and} \qquad C_{e-}^{(1)} - C_{e-}^{(-1)} = \mathscr{C} \frac{e^{k_y^{(1)} y_1}}{k_y^{(1)}}. \quad (1.152)$$

Finally, in Eq. (1.127) there is no source of discontinuity at $y = y_1$, so no reason for H_s to have different integration constants from one side to the other of the plane $y = y_1$. We obtain then

$$C_{h+}^{(1)} = C_{h+}^{(-1)} \qquad \text{and} \qquad C_{h-}^{(1)} = C_{h-}^{(-1)}. \quad (1.153)$$

Boundary conditions at the flat chamber inner surfaces and between each of its layers

We will now consider the boundary conditions for the subsequent layers, i.e. at each $y = b^{(p)}$ for $1 \leq p \leq N-1$ and $-M+1 \leq p \leq -1$. There are no externally imposed surface charges or currents between each layer , which means (see Ref. [11, p. 18]) that the tangential components of $\vec{E}$ and $\vec{H}$ are continuous. When decomposing the continuity equations according to Eqs. (1.115) and (1.116) and identifying each term, the constants in front of the exponentials in the expression of E_s and H_s of Eqs. (1.147) and (1.148) appear to be the solutions of a linear system. Instead of solving this system by "brute force" we can, as in the axisymmetric case, find a recurrent matrix relation between the integration constants of a given layer and those of the adjacent one, which allows us to solve analytically the full system. The complete derivation is detailed in Appendix E.2.2, and we will show here only the resulting expressions.
With the free space impedance Z_0, the field $\vec{G}$ and the corresponding integration coefficients given as in

the cylindrical case by

$$Z_0 = \frac{1}{\varepsilon_0 c} = \mu_0 c = \sqrt{\frac{\mu_0}{\varepsilon_0}}, \qquad \vec{G} = Z_0 \vec{H},$$
$$C_{g+}^{(p)} = Z_0 C_{h+}^{(p)}, \qquad C_{g-}^{(p)} = Z_0 C_{h-}^{(p)},$$

we obtain for the upper part of the chamber (i.e. for $1 \le p \le N-1$)

$$\begin{bmatrix} C_{e+}^{(p+1)} \\ C_{e-}^{(p+1)} \\ C_{g+}^{(p+1)} \\ C_{g-}^{(p+1)} \end{bmatrix} = M^{p+1,p} \cdot \begin{bmatrix} C_{e+}^{(p)} \\ C_{e-}^{(p)} \\ C_{g+}^{(p)} \\ C_{g-}^{(p)} \end{bmatrix} = \begin{bmatrix} P^{p+1,p} & Q^{p+1,p} \\ S^{p+1,p} & R^{p+1,p} \end{bmatrix} \cdot \begin{bmatrix} C_{e+}^{(p)} \\ C_{e-}^{(p)} \\ C_{g+}^{(p)} \\ C_{g-}^{(p)} \end{bmatrix}, \tag{1.154}$$

with the four 2×2 matrices $P^{p+1,p}$, $Q^{p+1,p}$, $R^{p+1,p}$ and $S^{p+1,p}$ defined by

$$P^{p+1,p} = \frac{1}{2} \begin{bmatrix} \left(1+\psi_p^{p+1}\right) e^{\left(k_y^{(p)} - k_y^{(p+1)}\right) b^{(p)}} & \left(1-\psi_p^{p+1}\right) e^{\left(-k_y^{(p)} - k_y^{(p+1)}\right) b^{(p)}} \\ \left(1-\psi_p^{p+1}\right) e^{\left(k_y^{(p)} + k_y^{(p+1)}\right) b^{(p)}} & \left(1+\psi_p^{p+1}\right) e^{\left(k_y^{(p+1)} - k_y^{(p)}\right) b^{(p)}} \end{bmatrix}, \tag{1.155}$$

$$Q^{p+1,p} = \frac{k_x \left(\frac{\left(\nu^{(p+1)}\right)^2}{\left(\nu^{(p)}\right)^2} - 1 \right)}{2\beta k_y^{(p+1)} \varepsilon_1^{(p+1)}} \begin{bmatrix} -e^{\left(k_y^{(p)} - k_y^{(p+1)}\right) b^{(p)}} & -e^{\left(-k_y^{(p)} - k_y^{(p+1)}\right) b^{(p)}} \\ e^{\left(k_y^{(p)} + k_y^{(p+1)}\right) b^{(p)}} & e^{\left(k_y^{(p+1)} - k_y^{(p)}\right) b^{(p)}} \end{bmatrix}, \tag{1.156}$$

$$R^{p+1,p} = \frac{1}{2} \begin{bmatrix} \left(1+\phi_p^{p+1}\right) e^{\left(k_y^{(p)} - k_y^{(p+1)}\right) b^{(p)}} & \left(1-\phi_p^{p+1}\right) e^{\left(-k_y^{(p)} - k_y^{(p+1)}\right) b^{(p)}} \\ \left(1-\phi_p^{p+1}\right) e^{\left(k_y^{(p)} + k_y^{(p+1)}\right) b^{(p)}} & \left(1+\phi_p^{p+1}\right) e^{\left(k_y^{(p+1)} - k_y^{(p)}\right) b^{(p)}} \end{bmatrix}, \tag{1.157}$$

$$S^{p+1,p} = \frac{\varepsilon_1^{(p+1)}}{\mu_1^{(p+1)}} Q^{p+1,p}. \tag{1.158}$$

where

$$\psi_p^{p+1} = \frac{\left(\nu^{(p+1)}\right)^2 k_y^{(p)} \varepsilon_1^{(p)}}{\left(\nu^{(p)}\right)^2 k_y^{(p+1)} \varepsilon_1^{(p+1)}} \qquad \text{and} \quad \phi_p^{p+1} = \frac{\left(\nu^{(p+1)}\right)^2 k_y^{(p)} \mu_1^{(p)}}{\left(\nu^{(p)}\right)^2 k_y^{(p+1)} \mu_1^{(p+1)}}. \tag{1.159}$$

When successively applying the relation (1.154) for all the layers in the upper part of the chamber, we get

$$\begin{bmatrix} C_{e+}^{(N)} \\ C_{e-}^{(N)} \\ C_{g+}^{(N)} \\ C_{g-}^{(N)} \end{bmatrix} = M^{N,N-1} \cdot M^{N-1,N-2} \cdots M^{2,1} \cdot \begin{bmatrix} C_{e+}^{(1)} \\ C_{e+}^{(1)} \\ C_{g-}^{(1)} \\ C_{g-}^{(1)} \end{bmatrix} = \mathscr{M} \cdot \begin{bmatrix} C_{e+}^{(1)} \\ C_{e-}^{(1)} \\ C_{g+}^{(1)} \\ C_{g-}^{(1)} \end{bmatrix}, \tag{1.160}$$

with the definition

$$\mathscr{M} = M^{N,N-1} \cdot M^{N-1,N-2} \cdots M^{2,1}. \tag{1.161}$$

Very similarly we obtain for the lower part of the chamber (i.e. for $-M+1 \leq p \leq -1$)

$$\begin{bmatrix} C_{e+}^{(p-1)} \\ C_{e-}^{(p-1)} \\ C_{g+}^{(p-1)} \\ C_{g-}^{(p-1)} \end{bmatrix} = M^{p-1,p} \cdot \begin{bmatrix} C_{e+}^{(p)} \\ C_{e-}^{(p)} \\ C_{g+}^{(p)} \\ C_{g-}^{(p)} \end{bmatrix} = \begin{bmatrix} P^{p-1,p} & Q^{p-1,p} \\ S^{p-1,p} & R^{p-1,p} \end{bmatrix} \cdot \begin{bmatrix} C_{e+}^{(p)} \\ C_{e-}^{(p)} \\ C_{g+}^{(p)} \\ C_{g-}^{(p)} \end{bmatrix}, \tag{1.162}$$

with

$$P^{p-1,p} = \frac{1}{2} \begin{bmatrix} \left(1+\psi_p^{p-1}\right) e^{\left(k_y^{(p)} - k_y^{(p-1)}\right) b^{(p)}} & \left(1-\psi_p^{p-1}\right) e^{\left(-k_y^{(p)} - k_y^{(p-1)}\right) b^{(p)}} \\ \left(1-\psi_p^{p-1}\right) e^{\left(k_y^{(p)} + k_y^{(p-1)}\right) b^{(p)}} & \left(1+\psi_p^{p-1}\right) e^{\left(k_y^{(p-1)} - k_y^{(p)}\right) b^{(p)}} \end{bmatrix}, \tag{1.163}$$

$$Q^{p-1,p} = \frac{k_x \left(\frac{\left(\nu^{(p-1)}\right)^2}{\left(\nu^{(p)}\right)^2} - 1 \right)}{2\beta k_y^{(p-1)} \varepsilon_1^{(p-1)}} \begin{bmatrix} -e^{\left(k_y^{(p)} - k_y^{(p-1)}\right) b^{(p)}} & -e^{\left(-k_y^{(p)} - k_y^{(p-1)}\right) b^{(p)}} \\ e^{\left(k_y^{(p)} + k_y^{(p-1)}\right) b^{(p)}} & e^{\left(k_y^{(p-1)} - k_y^{(p)}\right) b^{(p)}} \end{bmatrix}, \tag{1.164}$$

$$R^{p-1,p} = \frac{1}{2} \begin{bmatrix} \left(1+\phi_p^{p-1}\right) e^{\left(k_y^{(p)} - k_y^{(p-1)}\right) b^{(p)}} & \left(1-\phi_p^{p-1}\right) e^{\left(-k_y^{(p)} - k_y^{(p-1)}\right) b^{(p)}} \\ \left(1-\phi_p^{p-1}\right) e^{\left(k_y^{(p)} + k_y^{(p-1)}\right) b^{(p)}} & \left(1+\phi_p^{p-1}\right) e^{\left(k_y^{(p-1)} - k_y^{(p)}\right) b^{(p)}} \end{bmatrix}, \tag{1.165}$$

$$S^{p-1,p} = \frac{\varepsilon_1^{(p-1)}}{\mu_1^{(p-1)}} Q^{p-1,p}, \tag{1.166}$$

where

$$\psi_p^{p-1} = \frac{\left(\nu^{(p-1)}\right)^2 k_y^{(p)} \varepsilon_1^{(p)}}{\left(\nu^{(p)}\right)^2 k_y^{(p-1)} \varepsilon_1^{(p-1)}} \quad \text{and} \quad \phi_p^{p-1} = \frac{\left(\nu^{(p-1)}\right)^2 k_y^{(p)} \mu_1^{(p)}}{\left(\nu^{(p)}\right)^2 k_y^{(p-1)} \mu_1^{(p-1)}}. \tag{1.167}$$

In the end, after successive application of Eq. (1.162) we get for the lower part of the chamber

$$\begin{bmatrix} C_{e+}^{(-M)} \\ C_{e-}^{(-M)} \\ C_{g+}^{(-M)} \\ C_{g-}^{(-M)} \end{bmatrix} = \mathscr{M}' \cdot \begin{bmatrix} C_{e+}^{(-1)} \\ C_{e-}^{(-1)} \\ C_{g+}^{(-1)} \\ C_{g-}^{(-1)} \end{bmatrix}, \tag{1.168}$$

with

$$\mathscr{M}' = M^{-M,-M+1} \cdot M^{-M+1,-M+2} \cdots M^{-2,-1}. \tag{1.169}$$

Finally, for reasons that will appear later in Section 1.5.5, it is better to rewrite Eqs. (1.160) and (1.168) in a form involving three constants of layer 1 ($C_{e+}^{(1)}$, $C_{g+}^{(1)}$ and $C_{g-}^{(1)}$) and one of layer -1 ($C_{e-}^{(-1)}$). We can do so using Eqs. (1.152) and (1.153):

$$\begin{bmatrix} C_{e+}^{(N)} \\ C_{e-}^{(N)} \\ C_{g+}^{(N)} \\ C_{g-}^{(N)} \end{bmatrix} = \mathscr{M} \cdot \begin{bmatrix} C_{e+}^{(1)} \\ C_{e-}^{(-1)} + \mathscr{C} \frac{e^{k_y^{(1)} y_1}}{k_y^{(1)}} \\ C_{g+}^{(1)} \\ C_{g-}^{(1)} \end{bmatrix} \quad \text{and} \quad \begin{bmatrix} C_{e+}^{(-M)} \\ C_{e-}^{(-M)} \\ C_{g+}^{(-M)} \\ C_{g-}^{(-M)} \end{bmatrix} = \mathscr{M}' \cdot \begin{bmatrix} C_{e+}^{(1)} + \mathscr{C} \frac{e^{-k_y^{(1)} y_1}}{k_y^{(1)}} \\ C_{e-}^{(-1)} \\ C_{g+}^{(1)} \\ C_{g-}^{(1)} \end{bmatrix}. \tag{1.170}$$

Field matching for the outer layers and final solution for the integration constants

The outer layers go to infinity in the y direction, which can have two different implications in terms of the electromagnetic fields at infinity. If in an outer layer $k_y^{(p)}$ has a non zero real part, this must be strictly positive according to the definition of $k_y^{(p)}$ in Eq. (1.149) and that of the square root in Eq. (1.41). Then in the layer considered the only possible exponential solution in y is the one with a sign in front of $k_y^{(p)}$ opposite to that of y in the layer (otherwise it would grow to infinity). In other words for the layer N we necessarily have $C_{e+}^{(N)} = C_{g+}^{(N)} = 0$ while for the layer $-M$ we get $C_{e-}^{(-M)} = C_{g-}^{(-M)} = 0$.
The condition will be the same (but for a different reason) if $k_y^{(p)}$ is purely imaginary in the layer considered, which can happen for sufficiently low k_x if $\left(\nu^{(p)}\right)^2$ is real and strictly negative in that layer. In that situation Cherenkov radiation [11, p. 637] occurs in the outer layer, and since there is (in our geometrical model) no other material beyond the outer layer, we cannot have any incoming wave: there should be only outcoming radiation whose wave vector is directed toward the outside of the chamber. Due to our choice of convention for the Fourier transform – see e.g. Eq. (1.2) – we must have an exponential term of

the form $e^{-jk_y^{rad}y}$ in the field components, with $k_y^{rad} \geq 0$ in the top layer N and $k_y^{rad} \leq 0$ in the bottom layer $-M$, because in time domain the factor $e^{j\left(\omega t - k_y^{rad} y\right)}$ represents outcoming propagation in these conditions only (this can also be seen in Eq. (1.4) for the propagation along s). Then, since the imaginary part of the square root of a negative number is always positive according to Eq. (1.41), we have in any case

$$\begin{aligned} C_{e+}^{(N)} = C_{g+}^{(N)} = 0 \qquad & \text{for the top layer,} \\ C_{e-}^{(-M)} = C_{g-}^{(-M)} = 0 \qquad & \text{for the bottom one.} \end{aligned} \tag{1.171}$$

From these conditions and Eqs. (1.170) we get the following system

$$\begin{bmatrix} \mathscr{M}_{11} & \mathscr{M}_{12} & \mathscr{M}_{13} & \mathscr{M}_{14} \\ \mathscr{M}_{31} & \mathscr{M}_{32} & \mathscr{M}_{33} & \mathscr{M}_{34} \\ \mathscr{M}'_{21} & \mathscr{M}'_{22} & \mathscr{M}'_{23} & \mathscr{M}'_{24} \\ \mathscr{M}'_{41} & \mathscr{M}'_{42} & \mathscr{M}'_{43} & \mathscr{M}'_{44} \end{bmatrix} \cdot \begin{bmatrix} C_{e+}^{(1)} \\ C_{e-}^{(-1)} \\ C_{g+}^{(1)} \\ C_{g-}^{(1)} \end{bmatrix} = -\frac{\mathscr{C}}{k_y^{(1)}} \begin{bmatrix} \mathscr{M}_{12} e^{k_y^{(1)} y_1} \\ \mathscr{M}_{32} e^{k_y^{(1)} y_1} \\ \mathscr{M}'_{21} e^{-k_y^{(1)} y_1} \\ \mathscr{M}'_{41} e^{-k_y^{(1)} y_1} \end{bmatrix}, \tag{1.172}$$

where e.g. $\mathscr{M}_{rs}$ is the component in row r and column s of the matrix $\mathscr{M}$. If we now call $\mathscr{P}$ the 4×4 matrix on the left hand side, we get the constants we look for as

$$\begin{bmatrix} C_{e+}^{(1)} \\ C_{e-}^{(-1)} \\ C_{g+}^{(1)} \\ C_{g-}^{(1)} \end{bmatrix} = -\frac{\mathscr{C}}{k_y^{(1)}} \mathscr{P}^{-1} \cdot \begin{bmatrix} \mathscr{M}_{12} e^{k_y^{(1)} y_1} \\ \mathscr{M}_{32} e^{k_y^{(1)} y_1} \\ \mathscr{M}'_{21} e^{-k_y^{(1)} y_1} \\ \mathscr{M}'_{41} e^{-k_y^{(1)} y_1} \end{bmatrix}, \tag{1.173}$$

or more explicitely:

$$\begin{aligned} C_{e+}^{(1)} &= -\frac{\mathscr{C}}{k_y^{(1)}} \left[\left\{ \left(\mathscr{P}^{-1}\right)_{11} \mathscr{M}_{12} + \left(\mathscr{P}^{-1}\right)_{12} \mathscr{M}_{32} \right\} e^{k_y^{(1)} y_1} \left\{ \left(\mathscr{P}^{-1}\right)_{13} \mathscr{M}'_{21} + \left(\mathscr{P}^{-1}\right)_{14} \mathscr{M}'_{41} \right\} e^{-k_y^{(1)} y_1} \right], \\ C_{e-}^{(-1)} &= -\frac{\mathscr{C}}{k_y^{(1)}} \left[\left\{ \left(\mathscr{P}^{-1}\right)_{21} \mathscr{M}_{12} + \left(\mathscr{P}^{-1}\right)_{22} \mathscr{M}_{32} \right\} e^{k_y^{(1)} y_1} + \left\{ \left(\mathscr{P}^{-1}\right)_{23} \mathscr{M}'_{21} + \left(\mathscr{P}^{-1}\right)_{24} \mathscr{M}'_{41} \right\} e^{-k_y^{(1)} y_1} \right], \\ C_{g+}^{(1)} &= -\frac{\mathscr{C}}{k_y^{(1)}} \left[\left\{ \left(\mathscr{P}^{-1}\right)_{31} \mathscr{M}_{12} + \left(\mathscr{P}^{-1}\right)_{32} \mathscr{M}_{32} \right\} e^{k_y^{(1)} y_1} + \left\{ \left(\mathscr{P}^{-1}\right)_{33} \mathscr{M}'_{21} + \left(\mathscr{P}^{-1}\right)_{34} \mathscr{M}'_{41} \right\} e^{-k_y^{(1)} y_1} \right], \\ C_{g-}^{(1)} &= -\frac{\mathscr{C}}{k_y^{(1)}} \left[\left\{ \left(\mathscr{P}^{-1}\right)_{41} \mathscr{M}_{12} + \left(\mathscr{P}^{-1}\right)_{42} \mathscr{M}_{32} \right\} e^{k_y^{(1)} y_1} + \left\{ \left(\mathscr{P}^{-1}\right)_{43} \mathscr{M}'_{21} + \left(\mathscr{P}^{-1}\right)_{44} \mathscr{M}'_{41} \right\} e^{-k_y^{(1)} y_1} \right]. \end{aligned} \tag{1.174}$$

From this all the constants for all the layers p can be computed thanks to Eqs. (1.152), (1.153), (1.154) and (1.162).

Note that the matrices $\mathscr{P}$, $\mathscr{M}$ and $\mathscr{M}'$ do not depend on y_1, the offset of the source, since the matrices

$M^{p+1,p}$ and $M^{p-1,p}$ do not depend on y_1. We can therefore define the following functions of k_x (that are also functions of ω, β and the materials properties, but independent of y_1):

$$\begin{aligned}
\chi_1(k_x) &= \left(\mathscr{P}^{-1}\right)_{11}\mathscr{M}_{12} + \left(\mathscr{P}^{-1}\right)_{12}\mathscr{M}_{32}, & \chi_2(k_x) &= \left(\mathscr{P}^{-1}\right)_{21}\mathscr{M}_{12} + \left(\mathscr{P}^{-1}\right)_{22}\mathscr{M}_{32}, \\
\eta_1(k_x) &= \left(\mathscr{P}^{-1}\right)_{13}\mathscr{M}'_{21} + \left(\mathscr{P}^{-1}\right)_{14}\mathscr{M}'_{41}, & \eta_2(k_x) &= \left(\mathscr{P}^{-1}\right)_{23}\mathscr{M}'_{21} + \left(\mathscr{P}^{-1}\right)_{24}\mathscr{M}'_{41},
\end{aligned} \tag{1.175}$$

such that we can write the constants for the electric fields in the following compact way

$$\begin{aligned}
C_{e+}^{(1)} &= -\frac{\mathscr{C}}{k_y^{(1)}}\left[\chi_1(k_x)e^{k_y^{(1)}y_1} + \eta_1(k_x)e^{-k_y^{(1)}y_1}\right], \\
C_{e-}^{(-1)} &= -\frac{\mathscr{C}}{k_y^{(1)}}\left[\chi_2(k_x)e^{k_y^{(1)}y_1} + \eta_2(k_x)e^{-k_y^{(1)}y_1}\right].
\end{aligned} \tag{1.176}$$

Therefore, to compute the constants of the electric field longitudinal component (which is the one needed to calculate the electromagnetic force and impedances as we will see below), we only need to perform multiplications of 4×4 matrices and one inversion of a 4×4 matrix. The final inversion can even be limited to the computation of only 8 coefficients of the inverted matrix, with the cofactor method for instance.

1.5.4 Electromagnetic force inside the chamber

To study the dynamics of a passing beam inside the chamber, we need to calculate the Lorentz electromagnetic force $\vec{F}$ on a given test particle. We assume such a particle has a charge of q and the same velocity as the source, namely $\vec{v} = v\vec{e}_s$. The longitudinal component of the force acting on this particle in the vacuum region is written (dropping the superscript (-1) or (1) for conciseness)

$$F_s = qE_s, \tag{1.177}$$

while the transverse components are (using Eqs. (1.143) to (1.146) and recalling that $\nu = \frac{k}{\gamma}$ in vacuum)

$$F_x = q\left(E_x - v\mu_0 H_y\right) = \frac{jq\gamma^2}{k}\left(1-\beta^2\right)\frac{\partial E_s}{\partial x} = \frac{jq}{k}\frac{\partial E_s}{\partial x}, \tag{1.178}$$

$$F_y = q\left(E_y + v\mu_0 H_x\right) = \frac{jq\gamma^2}{k}\left(1-\beta^2\right)\frac{\partial E_s}{\partial y} = \frac{jq}{k}\frac{\partial E_s}{\partial y}. \tag{1.179}$$

It appears here that the force components can be computed with the knowledge of the longitudinal component of the electric field only, as in the axisymmetric case.

1.5.5 Total electric field longitudinal component in the vacuum region

Equations (1.137), (1.147) and (1.148) give, when reintroducing the horizontal Fourier transform from Eqs. (1.115) and (1.116) (recalling that $\vec{G} = Z_0\vec{H}$):

$$E_s^{(p)} = e^{-jks}\int_0^\infty \mathrm{d}k_x \cos(k_x x)\left[C_{e+}^{(p)}(k_x)e^{k_y^{(p)}y} + C_{e-}^{(p)}(k_x)e^{-k_y^{(p)}y}\right], \tag{1.180}$$

and

$$G_s^{(p)} = e^{-jks}\int_0^\infty \mathrm{d}k_x \sin(k_x x)\left[C_{g+}^{(p)}(k_x)e^{k_y^{(p)}y} + C_{g-}^{(p)}(k_x)e^{-k_y^{(p)}y}\right], \tag{1.181}$$

where the integration contants $C_{e+}^{(p)}$, $C_{e-}^{(p)}$, $C_{g+}^{(p)}$ and $C_{g-}^{(p)}$ (functions of k_x and ω) are calculated thanks to the matrices defined in Eqs. (1.155) to (1.161), Eqs. (1.163) to (1.169), and the relations (1.152), (1.153), (1.154), (1.162) and (1.174),.
Now we focus on E_s in the vacuum region inside the chamber, since only this component is needed to calculate the electromagnetic force that would affect a test particle. In the two vacuum regions indicated by the superscripts (-1) and (1) (respectively for $y < y_1$ and $y \geq y_1$) we have, recalling that $\nu^{(-1)} = \nu^{(1)} = \frac{k}{\gamma}$ and using Eqs. (1.152):

$$\begin{aligned}
E_s^{(1)} &= e^{-jks}\int_0^\infty \mathrm{d}k_x \cos(k_x x)\left[C_{e+}^{(1)}e^{k_y^{(1)}y} + C_{e-}^{(-1)}e^{-k_y^{(1)}y} + \frac{\mathscr{C}}{k_y^{(1)}}e^{k_y^{(1)}(y_1-y)}\right],\\
E_s^{(-1)} &= e^{-jks}\int_0^\infty \mathrm{d}k_x \cos(k_x x)\left[C_{e+}^{(1)}e^{k_y^{(1)}y} + C_{e-}^{(-1)}e^{-k_y^{(1)}y} + \frac{\mathscr{C}}{k_y^{(1)}}e^{k_y^{(1)}(y-y_1)}\right].
\end{aligned} \tag{1.182}$$

As in the axisymmetric case, we will identify two terms in E_s: one is the direct space charge term, that would be the only one present in the absence of any chamber (i.e. if the whole space were considered to be vacuum) and the other one will be called the wall term, entirely due to the flat chamber's presence.

Direct space charge term of the longitudinal electric field

If there were no chamber around the beam, the finiteness of the fields for $y \to \pm\infty$ prevents any growing exponential in y in the expression of E_s. Therefore, since $k_y^{(1)} = \sqrt{k_x^2 + \frac{k^2}{\gamma^2}}$ is real and strictly positive, we must have $C_{e+}^{(1)} = C_{e-}^{(-1)} = 0$. From the above Eqs. (1.182) we clearly have

$$\begin{aligned}
E_s^{(1),SC} &= e^{-jks}\int_0^\infty \mathrm{d}k_x \frac{\mathscr{C}}{k_y^{(1)}}\cos(k_x x)\, e^{k_y^{(1)}(y_1-y)},\\
E_s^{(-1),SC} &= e^{-jks}\int_0^\infty \mathrm{d}k_x \frac{\mathscr{C}}{k_y^{(1)}}\cos(k_x x)\, e^{k_y^{(1)}(y-y_1)},
\end{aligned} \tag{1.183}$$

where the superscript "SC" stands for "direct space-charge". Recalling that $k_y^{(1)} = \sqrt{k_x^2 + \frac{k^2}{\gamma^2}}$ from Eq. (1.149) and noticing that in the layer 1 we have $y_1 - y < 0$ while in the layer -1, $y - y_1 < 0$, we can integrate those formulae using Eq. (C.29). This gives the same result for both regions:

$$E_s^{vac,SC} = \mathscr{C}\, e^{-jks} K_0\left(\frac{k}{\gamma}\sqrt{x^2 + \left(y-y_1\right)^2}\right), \tag{1.184}$$

where K_0 is the modified Bessel function of the second kind of order 0, and the superscript "vac" stands for the fields in the vacuum region.
We can generalize this formula for a source at $x = x_1$ instead of $x = 0$, which is straightforward from the continuous translation invariance of the electromagnetic configuration along the x axis, or in other words the fact that the place of the source along the horizontal axis does not change the problem: only the difference between the test and the source x coordinates matters, which means that we simply need

to replace x by $x - x_1$:

$$E_s^{vac,SC} = \mathscr{C} e^{-jks} K_0\left(\frac{k}{\gamma}\sqrt{(x-x_1)^2 + \left(y-y_1\right)^2}\right). \tag{1.185}$$

Note that this is the same result, written in cartesian coordinates, as what was found earlier in Section 1.4.5, Eq. (1.90), as it should be.

Wall term of the longitudinal electric field

The wall term of the fields is the part of the fields due to the chamber, or in other words the total fields minus the direct space-charge term we have considered in the previous section. From Eqs. (1.182) and (1.183) the wall part of the field has the same expression in both regions 1 and −1, and we can write:

$$E_s^{vac,W} = e^{-jks}\int_0^\infty \mathrm{d}k_x \cos(k_x x)\left[C_{e+}^{(1)} e^{k_y^{(1)} y} + C_{e-}^{(-1)} e^{-k_y^{(1)} y}\right], \tag{1.186}$$

where the superscript "W" stands for the wall part of the field component. A direct analytical integration of this equation in the general case (given the very complicated expression of $C_{e+}^{(1)}(k_x)$ and $C_{e-}^{(-1)}(k_x)$, see Section 1.5.3) looks like an impossible task, or at least very difficult. Nevertheless, it turns out that several algebraic manipulations detailed in Appendix E.2.3 allow us to identify the dependences in the test particle coordinates as well as in the source particle offset y_1. The final formula obtained is thus written

$$E_s^{vac,W} = -4\mathscr{C} e^{-jks} \sum_{m,n=0}^{\infty} \frac{\alpha_{mn}\cos\left[n\left(\theta - \frac{\pi}{2}\right)\right]}{(1+\delta_{m0})(1+\delta_{n0})} I_m\left(\frac{ky_1}{\gamma}\right) I_n\left(\frac{kr}{\gamma}\right), \tag{1.187}$$

where α_{mn} are constants defined by the integral

$$\alpha_{mn} = \int_0^\infty \mathrm{d}u \cosh(mu)\cosh(nu)\left[\chi_1\left(\frac{k}{\gamma}\sinh u\right) + (-1)^m \eta_1\left(\frac{k}{\gamma}\sinh u\right) + (-1)^n \chi_2\left(\frac{k}{\gamma}\sinh u\right) + (-1)^{m+n}\eta_2\left(\frac{k}{\gamma}\sinh u\right)\right]. \tag{1.188}$$

The coefficients α_{mn} depend only on the functions η_1, η_2, χ_1 and χ_2 so only on the chamber properties and on ω and β (see Section 1.5.3). The infinite integrals involved are fastly converging in most cases, so even though it does not seem to be possible to compute them analytically in the general case, they can be calculated numerically.
The decomposition into azimuthal modes of $E_s^{vac,W}$ in Eq. (1.187) has a similar form as the one that arises in the case of the axisymmetric structure – see Eq. (1.92). The clear advantage of this formula is that $I_m\left(\frac{ky_1}{\gamma}\right)$ and $I_n\left(\frac{kr}{\gamma}\right)$ are fastly decaying with m or n when the argument is small (see Eq. (C.17)). Therefore only the first few terms of the series will be sufficient in most applications.
In cartesian coordinates, $E_s^{vac,W}$ can be written (see Appendix E.2.3)

$$E_s^{vac,W} = -2\mathscr{C} e^{-jks} \sum_{m,n=0}^{\infty} \frac{\alpha_{mn}\left[(y-jx)^n + (y+jx)^n\right]}{\left(x^2+y^2\right)^{\frac{n}{2}}(1+\delta_{m0})(1+\delta_{n0})} I_m\left(\frac{ky_1}{\gamma}\right) I_n\left(\frac{k\sqrt{x^2+y^2}}{\gamma}\right). \tag{1.189}$$

As we did for the direct space charge in the previous section, we can generalize this formula for a source at $x = x_1$ instead of $x = 0$, by replacing x with $x - x_1$:

$$E_s^{vac,W} = -2\mathscr{C}e^{-jks}\sum_{m,n=0}^{\infty}\frac{\alpha_{mn}\left[\left\{y-j(x-x_1)\right\}^n+\left\{y+j(x-x_1)\right\}^n\right]}{\left\{(x-x_1)^2+y^2\right\}^{\frac{n}{2}}(1+\delta_{m0})(1+\delta_{n0})}I_m\left(\frac{ky_1}{\gamma}\right)I_n\left\{\frac{k\sqrt{(x-x_1)^2+y^2}}{\gamma}\right\}. \tag{1.190}$$

The sum of Eqs. (1.185) and (1.190) gives the total general longitudinal electric field in the vacuum region due to the source in Eqs. (1.4) and (1.7), from which the total force and impedances can be derived.

1.5.6 Beam-coupling impedances

Definitions

We consider a test particle of charge q located at position (x_2, y_2) in the transverse plane, while the source is at (x_1, y_1) as stated in the Section 1.1. We define the impedances in exactly the same way as in Section 1.4.6, but replace the cylindrical coordinates by the cartesian coordinates. This gives for the current density flowing at the position of the test particle in Eq. (1.94) (in frequency domain)

$$J_t(x_2, y_2) = qe^{-jks}\delta(x-x_2)\delta(y-y_2), \tag{1.191}$$

which can be injected into the impedances definitions from Eqs. (1.93), (1.95) and (1.96), giving, thanks to Eqs. (1.178) and (1.179):

$$Z_\parallel = -\frac{1}{Q}\int^L \mathrm{d}s E_s(x_2, y_2, s;\omega)e^{jks}, \tag{1.192}$$

$$Z_x = -\frac{1}{kQ}\int^L \mathrm{d}s \frac{\partial E_s}{\partial x}(x_2, y_2, s;\omega)e^{jks}, \tag{1.193}$$

$$Z_y = -\frac{1}{kQ}\int^L \mathrm{d}s \frac{\partial E_s}{\partial y}(x_2, y_2, s;\omega)e^{jks}, \tag{1.194}$$

L being the length of the element considered (see also footnote 7).

Direct space-charge impedances

When plugging in the above definitions the longitudinal electric field due to the direct space charge from Eq. (1.185) together with the value of $\mathscr{C}$ in Eq. (1.62), one gets exactly the space-charge impedances of the axisymmetric case, i.e. Eqs. (1.100), (1.101) and (1.102). This was expected since the direct space-charge is the part of the impedance due to the direct interaction between the source and test particles without the mediation of the surrounding structure, so must be independent of it.

Wall impedances

The term of the impedance coming from the part of the fields due to the flat chamber's presence is the wall impedance (see Section 1.4.6). It contains both the impedance that we would have with a flat cham-

ber made of a perfect conductor (this part is usually called the indirect space-charge impedance) and the part of the impedance coming from the resistivity (or more generally the electromagnetic properties) of the layer(s). We will discuss more the indirect space-charge impedance taken alone in Section 1.5.7. The general nonlinear impedances are found by injecting the electric field of Eq. (1.187) into the definitions from Eqs. (1.192) to (1.194). Then, usually one is interested only in the first order terms in the source and test positions, so for small $\frac{ky_1}{\gamma}$ and $\frac{kr_2}{\gamma}$. They can be obtained through Taylor expansion of the modified Bessel functions, knowing that the first few terms of the sum in Eq. (1.187) are sufficient. The corresponding derivations are performed in Appendix E.2.4. We obtain for the general nonlinear impedances in the particular case when $x_1 = 0$

$$Z_{\parallel}^{Wall} = 4\frac{\mathscr{C}L}{Q}\sum_{m,n=0}^{\infty}\frac{\alpha_{mn}\cos\left(n\phi_2\right)}{\left(1+\delta_{m0}\right)\left(1+\delta_{n0}\right)}I_m\left(\frac{ky_1}{\gamma}\right)I_n\left(\frac{kr_2}{\gamma}\right), \tag{1.195}$$

$$Z_x^{Wall} = 4\frac{\mathscr{C}L}{kQ}\sum_{m,n=0}^{\infty}\frac{\alpha_{mn}}{\left(1+\delta_{m0}\right)\left(1+\delta_{n0}\right)}I_m\left(\frac{ky_1}{\gamma}\right)\frac{1}{r_2}\left[\frac{ny_2\sin\left(n\phi_2\right)}{r_2}I_n\left(\frac{kr_2}{\gamma}\right) + \frac{kx_2\cos\left(n\phi_2\right)}{\gamma}I_n'\left(\frac{kr_2}{\gamma}\right)\right], \tag{1.196}$$

$$Z_y^{Wall} = 4\frac{\mathscr{C}L}{kQ}\sum_{m,n=0}^{\infty}\frac{\alpha_{mn}}{\left(1+\delta_{m0}\right)\left(1+\delta_{n0}\right)}I_m\left(\frac{ky_1}{\gamma}\right)\frac{1}{r_2}\left[-\frac{nx_2\sin\left(n\phi_2\right)}{r_2}I_n\left(\frac{kr_2}{\gamma}\right) + \frac{ky_2\cos\left(n\phi_2\right)}{\gamma}I_n'\left(\frac{kr_2}{\gamma}\right)\right], \tag{1.197}$$

where $r_2 = \sqrt{x_2^2+y_2^2}$ and ϕ_2 is such that $x_2 = -r_2\sin\phi_2$ and $y_2 = r_2\cos\phi_2$ (see Appendix E.2.3). In Appendix E.2.4 the approximations of the above expressions up to second order are obtained, and from the continuous translation invariance of the problem along the x axis, we can generalize these results to the general case $x_1 \neq 0$, simply by replacing x_2 with the difference between the test and source horizontal coordinates $x_2 - x_1$. This gives, when plugging the value of the constant $\mathscr{C}$ from Eq. (1.62):

$$Z_{\parallel}^{Wall} \approx \frac{jkZ_0L}{2\pi\beta\gamma^2}\left[\alpha_{00} + \frac{k\alpha_{10}}{\gamma}y_1 + \frac{k\alpha_{01}}{\gamma}y_2 + k^2\left(\frac{\alpha_{00}-\alpha_{02}}{4\gamma^2}\right)x_1^2 + k^2\left(\frac{\alpha_{00}+\alpha_{20}}{4\gamma^2}\right)y_1^2 + k^2\left(\frac{\alpha_{00}-\alpha_{02}}{4\gamma^2}\right)x_2^2 + k^2\left(\frac{\alpha_{00}+\alpha_{02}}{4\gamma^2}\right)y_2^2 - k^2\left(\frac{\alpha_{00}-\alpha_{02}}{2\gamma^2}\right)x_1x_2 + \frac{k^2\alpha_{11}}{\gamma^2}y_1y_2\right], \tag{1.198}$$

$$Z_x^{Wall} \approx \frac{jk^2Z_0L}{4\pi\beta\gamma^4}\left[-\left(\alpha_{00}-\alpha_{02}\right)x_1 + \left(\alpha_{00}-\alpha_{02}\right)x_2 - k\frac{\alpha_{10}-\alpha_{12}}{\gamma}x_1y_1 - k\frac{\alpha_{01}-\alpha_{03}}{2\gamma}x_1y_2 + k\frac{\alpha_{10}-\alpha_{12}}{\gamma}y_1x_2 + k\frac{\alpha_{01}-\alpha_{03}}{2\gamma}x_2y_2\right], \tag{1.199}$$

$$Z_y^{Wall} \approx \frac{jkZ_0L}{2\pi\beta\gamma^3}\left[\alpha_{01} + \frac{\alpha_{11}k}{\gamma}y_1 + k\frac{\alpha_{00}+\alpha_{02}}{2\gamma}y_2 + k^2\frac{\alpha_{01}-\alpha_{03}}{8\gamma^2}x_1^2 + k^2\frac{\alpha_{01}+\alpha_{21}}{4\gamma^2}y_1^2 + k^2\frac{\alpha_{01}-\alpha_{03}}{8\gamma^2}x_2^2 + k^2\frac{3\alpha_{01}+\alpha_{03}}{8\gamma^2}y_2^2 - k^2\frac{\alpha_{01}-\alpha_{03}}{4\gamma^2}x_1x_2 + k^2\frac{\alpha_{10}+\alpha_{12}}{2\gamma^2}y_1y_2\right]. \tag{1.200}$$

Finally, the longitudinal wall impedance is often reduced to its zeroth order (constant) term, and the transverse impedances to the linear terms. All those terms are given by

$$Z_{\parallel}^{Wall,0} = \frac{jkZ_0L}{2\pi\beta\gamma^2}\alpha_{00}, \tag{1.201}$$

$$Z_{y}^{Wall,0} = \frac{jkZ_0L}{2\pi\beta\gamma^3}\alpha_{01}, \tag{1.202}$$

$$Z_{x}^{Wall,dip} = -\frac{jk^2Z_0L}{4\pi\beta\gamma^4}(\alpha_{00}-\alpha_{02}), \tag{1.203}$$

$$Z_{y}^{Wall,dip} = \frac{jk^2Z_0L}{2\pi\beta\gamma^4}\alpha_{11}, \tag{1.204}$$

$$Z_{x}^{Wall,quad} = \frac{jk^2Z_0L}{4\pi\beta\gamma^4}(\alpha_{00}-\alpha_{02}), \tag{1.205}$$

$$Z_{y}^{Wall,quad} = \frac{jk^2Z_0L}{4\pi\beta\gamma^4}(\alpha_{00}+\alpha_{02}). \tag{1.206}$$

Z_x^{Wall} has no constant term due to the left-right symmetry (see Fig. 1.3) but we can notice that Z_y^{Wall} has a non-zero constant term due to the absence of top-bottom symmetry: the layers at the bottom can be different from those at the top so the electromagnetic vertical force has no reason to be zero for $y_1 = y_2 = 0$. Concerning the dipolar and quadrupolar terms (defined as in Section 1.4.6), we note here that $Z_x^{Wall,dip} = -Z_x^{Wall,quad}$ which is a direct consequence of the continuous translation invariance along the x axis of the configuration. On the other hand, contrary to ultrarelativistic results (see e.g. Ref. [62]), we see that $Z_x^{Wall,quad} \neq -Z_y^{Wall,quad}$, which is due to the term proportional to α_{00} (it is actually similar to the quadrupolar term found for the impedance in an axisymmetric structure, see Section 1.4.6).
Finally, one can check without much difficulty that Eq. (1.198) and the linear terms of Z_x^{Wall} and Z_y^{Wall} in Eq. (1.199) and (1.200) are in agreement with the Panofsky-Wenzel theorem given in Eqs. (1.112).

1.5.7 Some particular cases

We apply here our formalism to several particular configurations.

General simplifications in case of top-bottom symmetry

Typically flat chamber have a symmetry between the top and bottom parts, which simplifies the analysis. The top-bottom symmetry means in particular that if we replace y_1 by $-y_1$, we should obtain the same results provided we switch the roles of $C_{e+}^{(1)}$ and $C_{e-}^{(-1)}$. Therefore in Eqs. (1.176) we should have

$$\chi_2 = \eta_1 \qquad \text{and} \qquad \eta_2 = \chi_1. \tag{1.207}$$

So we only need to compute the functions η_1 and χ_1. Note that the matrices $\mathscr{M}$ and $\mathscr{M}'$ defined in Eqs. (1.161) and (1.169) are not identical, since $M^{p+1,p} \neq M^{-p-1,-p}$ because $b^{(p)}$ changes sign in Eqs. (1.163) to (1.166) with respect to Eqs. (1.155) to (1.158). So one still needs to compute both $\mathscr{M}$ and $\mathscr{M}'$ to get χ_1 and η_1.

We can write now a simpler formula for the α_{mn} from Eq. (1.188):

$$\alpha_{mn} = \left[(-1)^{m+n}+1\right]\int_0^\infty \mathrm{d}u \cosh(mu)\cosh(nu)\left[\chi_1\left(\frac{k}{\gamma}\sinh u\right)+(-1)^m\eta_1\left(\frac{k}{\gamma}\sinh u\right)\right]. \tag{1.208}$$

This means in particular that $\alpha_{mn}=0$ whenever $m+n$ is odd, so in particular $\alpha_{01}=\alpha_{03}=\alpha_{10}=\alpha_{12}=\alpha_{21}=0$. For the wall linear terms in the beam-coupling impedances, this has for consequence to cancel out the constant term in Z_y^{Wall}, as expected:

$$Z_y^{Wall,0}=0. \tag{1.209}$$

On the other hand the impedances used most often, namely $Z_\parallel^{Wall,0}$ from Eq. (1.201) and the dipolar and quadrupolar transverse impedances from Eqs. (1.203) to (1.206) remain with the same expressions. More generally the second order approximation of the longitudinal and transverse total wall impedance become:

$$\begin{aligned} Z_\parallel^{Wall} \approx \frac{jkZ_0L}{2\pi\beta\gamma^2}\Bigg[&\alpha_{00}+k^2\left(\frac{\alpha_{00}-\alpha_{02}}{4\gamma^2}\right)x_1^2+k^2\left(\frac{\alpha_{00}+\alpha_{20}}{4\gamma^2}\right)y_1^2+k^2\left(\frac{\alpha_{00}-\alpha_{02}}{4\gamma^2}\right)x_2^2\\ &+k^2\left(\frac{\alpha_{00}+\alpha_{02}}{4\gamma^2}\right)y_2^2-k^2\left(\frac{\alpha_{00}-\alpha_{02}}{2\gamma^2}\right)x_1x_2+\frac{k^2\alpha_{11}}{\gamma^2}y_1y_2\Bigg], \end{aligned} \tag{1.210}$$

$$Z_x^{Wall} \approx \frac{jk^2Z_0L}{4\pi\beta\gamma^4}\left[-(\alpha_{00}-\alpha_{02})x_1+(\alpha_{00}-\alpha_{02})x_2\right], \tag{1.211}$$

$$Z_y^{Wall} \approx \frac{jk^2Z_0L}{4\pi\beta\gamma^4}\left[2\alpha_{11}y_1+(\alpha_{00}+\alpha_{02})y_2\right], \tag{1.212}$$

where we see that the nonlinear terms in the transverse impedances are at least of third order.

Case of two perfectly conducting plates

Now we consider that at $y=\pm b$ we have plates of infinite conductivity, assuming for simplicity $x_1=0$ (without loss of generality thanks to the horizontal translation invariance). In this case (where the results above on top-bottom symmetry apply), we must have $\vec{E}=\vec{0}$ all along the plates so in particular, from Eqs. (1.182):

$$\begin{aligned} C_{e+}^{(1)}e^{k_y^{(1)}b}+C_{e-}^{(-1)}e^{-k_y^{(1)}b}+\frac{\mathscr{C}}{k_y^{(1)}}e^{k_y^{(1)}(y_1-b)}=0,\\ C_{e+}^{(1)}e^{-k_y^{(1)}b}+C_{e-}^{(-1)}e^{k_y^{(1)}b}+\frac{\mathscr{C}}{k_y^{(1)}}e^{k_y^{(1)}(-b-y_1)}=0, \end{aligned}$$

or, in matrix form:

$$\begin{bmatrix} e^{k_y^{(1)}b} & e^{-k_y^{(1)}b}\\ e^{-k_y^{(1)}b} & e^{k_y^{(1)}b}\end{bmatrix}\cdot\begin{bmatrix} C_{e+}^{(1)}\\ C_{e-}^{(-1)}\end{bmatrix}=-\frac{\mathscr{C}}{k_y^{(1)}}\begin{bmatrix} e^{k_y^{(1)}(y_1-b)}\\ e^{-k_y^{(1)}(y_1+b)}\end{bmatrix}.$$

Using the inversion formula of a 2×2 matrix (see Appendix D.1) we obtain for $C_{e+}^{(1)}$:

$$C_{e+}^{(1)} = -\frac{\mathscr{C}}{2\sinh\left(2k_y^{(1)}b\right)k_y^{(1)}}\left[e^{k_y^{(1)}y_1} - e^{-k_y^{(1)}(y_1+2b)}\right],$$

which gives for χ_1 and η_1, from Eqs. (1.149) and (1.176)

$$\chi_1 = \frac{1}{2\sinh\left(2b\sqrt{k_x^2+\frac{k^2}{\gamma^2}}\right)} \qquad \text{and} \qquad \eta_1 = \frac{-e^{-2b\sqrt{k_x^2+\frac{k^2}{\gamma^2}}}}{2\sinh\left(2b\sqrt{k_x^2+\frac{k^2}{\gamma^2}}\right)}, \tag{1.213}$$

which can be plugged into Eq. (1.208):

$$\alpha_{mn}^{PC} = \left[(-1)^{m+n}+1\right]\int_0^\infty \mathrm{d}u \frac{\cosh(mu)\cosh(nu)}{2\sinh\left(2\frac{kb}{\gamma}\cosh u\right)}\left[1-(-1)^m e^{-2\frac{kb}{\gamma}\cosh u}\right], \tag{1.214}$$

where the superscript PC stands for "perfect conductor". Then, the linear part of the wall impedances for such perfectly conducting plates (also called indirect space-charge) are given by Eq. (1.201) and Eqs. (1.203) to (1.206).
As a verification of the theory, we can check that the longitudinal electric field (and therefore the electromagnetic force and impedances) given by our approach would have been identical if we had used instead the method of images [64, chap. 4] to impose the boundary conditions. This is done in Appendix E.2.5.

A note on the case of a single plate

The case of a single plate is included in our formalism and can be treated with the same equations as those for a flat chamber with two plates. If for instance there is a plate only on the top part, we simply notice that $M = 1$ (number of layers in the lower part of the chamber) and that the matrix $\mathscr{M}'$ in Eq. (1.169) is the identity matrix, as can be readily seen in Eq. (1.168).

1.6 Wake functions

1.6.1 Definitions

In the previous sections, all the computations were done in frequency domain, which enabled us to obtain analytical expressions for the electromagnetic fields and impedances. Generally speaking, to get the elctromagnetic fields in time domain, we need to put back the factor $\frac{1}{2\pi}\int_{-\infty}^{\infty}\mathrm{d}\omega e^{j\omega t}$ that has been dropped in Section 1.1. More specifically, the time domain counterparts of the beam-coupling

impedances defined in Sections 1.4.6 and 1.5.6 are called the wake functions and defined by [10, p. 70]

$$W_\parallel(\tau) = \frac{1}{2\pi}\int_{-\infty}^{\infty} \mathrm{d}\omega e^{j\omega\tau} Z_\parallel(\omega), \tag{1.215}$$

$$W_x(\tau) = -\frac{j}{2\pi}\int_{-\infty}^{\infty} \mathrm{d}\omega e^{j\omega\tau} Z_x(\omega), \tag{1.216}$$

$$W_y(\tau) = -\frac{j}{2\pi}\int_{-\infty}^{\infty} \mathrm{d}\omega e^{j\omega\tau} Z_y(\omega). \tag{1.217}$$

To give a physical meaning to the time τ at which the wake functions are computed, we inject in those expressions the impedances definitions from Eqs. (1.93), (1.95) and (1.96), together with the expressions of J_t from Eq. (1.191) and of the wave number $k \equiv \frac{\omega}{v}$:

$$W_\parallel(\tau) = -\frac{1}{2\pi Qq}\int_{-\infty}^{\infty} \mathrm{d}\omega \int^{L} \mathrm{d}s e^{j\omega\left(\tau+\frac{s}{v}\right)} F_s(x_2, y_2, s; \omega) = -\frac{1}{Qq}\int^{L} \mathrm{d}s F_s\left(x_2, y_2, s; \tau + \frac{s}{v}\right), \tag{1.218}$$

$$W_x(\tau) = \frac{1}{2\pi Qq}\int_{-\infty}^{\infty} \mathrm{d}\omega \int^{L} \mathrm{d}s e^{j\omega\left(\tau+\frac{s}{v}\right)} F_x(x_2, y_2, s; \omega) = \frac{1}{Qq}\int^{L} \mathrm{d}s F_x\left(x_2, y_2, s; \tau + \frac{s}{v}\right), \tag{1.219}$$

$$W_y(\tau) = \frac{1}{2\pi Qq}\int_{-\infty}^{\infty} \mathrm{d}\omega \int^{L} \mathrm{d}s e^{j\omega\left(\tau+\frac{s}{v}\right)} F_y(x_2, y_2, s; \omega) = \frac{1}{Qq}\int^{L} \mathrm{d}s F_y\left(x_2, y_2, s; \tau + \frac{s}{v}\right). \tag{1.220}$$

It appears that to a multiplicative sign, the wake functions are actually the components of the electromagnetic force in time domain created by a point-like particle on a test particle, normalized by the charges of both particles and integrated over a certain distance L (typically the length of the structure surrounding the beam and inducing the electromagnetic force – see also Section 1.4.6 and footnote 7). The force is taken at the position around the ring s and at the time $\tau + \frac{s}{v}$, which is τ seconds after the time at which the source particle passes at the same point s, from Eq. (1.1). In other words, the time τ at which the wake functions are computed is the time interval between the source and test particles, counted positively if the test is behind the source. Equivalently, we will also often consider the wakes as functions of $z \equiv \beta c\tau$, i.e. the distance between the source and test particles.
Note that the concept of wake functions is slightly different from the one of wake potentials, which are created by a distribution of particles of finite size, instead of point-like.

Using the parity properties of the impedances, one can make a first simplification of the definitions of the wake functions. From Eqs. (1.192) to (1.194), using the parity property of E_s and therefore of $\frac{\partial E_s}{\partial x}$ and $\frac{\partial E_s}{\partial y}$ from Eq. (1.17), we have for any ω

$$Z_\parallel(-\omega) = Z_\parallel(\omega)^*, \tag{1.221}$$

$$Z_x(-\omega) = -Z_x(\omega)^*, \tag{1.222}$$

$$Z_y(-\omega) = -Z_y(\omega)^*, \tag{1.223}$$

and therefore

$$W_{\parallel}(\tau) = \frac{1}{\pi}\Re\left[\int_0^{\infty} \mathrm{d}\omega e^{j\omega t} Z_{\parallel}(\omega)\right], \tag{1.224}$$

$$W_x(\tau) = \frac{1}{\pi}\Im\left[\int_0^{\infty} \mathrm{d}\omega e^{j\omega t} Z_x(\omega)\right], \tag{1.225}$$

$$W_y(\tau) = \frac{1}{\pi}\Im\left[\int_0^{\infty} \mathrm{d}\omega e^{j\omega t} Z_y(\omega)\right], \tag{1.226}$$

where $\Re$ denotes the real part and $\Im$ the imaginary part of a complex number. Note that impedances and wake functions are actually also functions of (x_1, y_1) (transverse position of the source particle) and of (x_2, y_2) (transverse position of the test particle).
The beam-coupling impedances computed in Sections 1.4 and 1.5 and used in the above definitions are in general very complicated functions of the angular frequency ω, such that an analytical computation of the wake functions does not seem to be feasible, and we have to resort to a numerical computation. Probably the most intuitive way to compute numerically Fourier integrals such as in Eqs. (1.224) to (1.226) is to use a discretized Fast Fourier transform (FFT). However, as we will see below, this method has severe shortcomings, both in terms of accuracy and computation time. Therefore we will develop here another approach based on a idea of Filon [65], using an uneven frequency sampling.
To describe both methods, the problem being similar for all three wake functions $W_{\parallel}$, W_x and W_y, we will consider in the following sections the general problem of computing the Fourier integral of a continuous, infinitely derivable and integrable complex function f of the real variable ω:

$$I_{\omega_{min}}(t) = \int_{\omega_{min}}^{\infty} \mathrm{d}\omega e^{j\omega t} f(\omega), \tag{1.227}$$

where ω_{min} can be any real number (for wake functions integration, ω_{min} will be zero or close enough to zero).

1.6.2 Overview of the usual discrete Fourier transform method

To compute $I_{\omega_{min}}(t)$, one can perform a discretization on N evenly separated points $\omega_k = \omega_{min} + \Delta\omega(k-1)$ in frequency domain, up to a frequency cutoff $\omega_{max} = \omega_N$ that needs to be chosen large enough to span most of the frequency spectrum of the function f. Then we can compute the Fourier integral $I_{\omega_{min}}(t_i)$ on certain times $t_i = t_1 + \Delta t(i-1)$ (with Δt depending on $\Delta\omega$ and N as we will see below) thanks to a fast

(discrete) Fourier transform (FFT):

$$\begin{aligned} I_{\omega_{min}}(t_i) \approx I_{\omega_{min}}^{\omega_{max}}(t_i) &\equiv \int_{\omega_{min}}^{\omega_{max}} \mathrm{d}\omega e^{j\omega t_i} f(\omega) \\ &= \sum_{k=1}^{N-1} \int_{\omega_k}^{\omega_{k+1}} \mathrm{d}\omega e^{j\omega t_i} f(\omega) \\ &\approx \sum_{k=1}^{N-1} \Delta\omega f(\omega_k) e^{j(\omega_{min}+\Delta\omega(k-1))(t_1+\Delta t(i-1))} \\ &\approx \Delta\omega e^{j\omega_{min}(t_1+\Delta t(i-1))} \sum_{k=1}^{N-1} f(\omega_k) e^{j\Delta\omega(k-1)t_1} e^{j\Delta\omega\Delta t(k-1)(i-1)} \\ &\approx \Delta\omega e^{j\omega_{min}t_i}(N-1)\mathrm{IFFT}[g](i), \end{aligned} \tag{1.228}$$

where $g(k) = f(\omega_k)e^{j\Delta\omega(k-1)t_1}$ is an array of $N-1$ values, and IFFT$[g]$ is the inverse fast Fourier transform of this array using Matlab® [66] convention, i.e.

$$\mathrm{IFFT}[g](i) = \frac{1}{N-1}\sum_{k=1}^{N-1} g(k) e^{2\pi j \frac{(i-1)(k-1)}{N-1}}. \tag{1.229}$$

It is seen here that Δt needs then to be set to

$$\Delta t = \frac{2\pi}{(N-1)\Delta\omega}. \tag{1.230}$$

We will not discuss here details on the implementation of the fast Fourier transform. Abondant litterature can be found on the subject, among which we can indicate Refs. [67, 68] and Ref. [69, p. 504].
The above derivation is similar to that of Ref. [69, pp. 584-585], where it is clearly stated that this procedure is not recommended for use to compute Fourier integrals, especially when the function $f(\omega)$ is smooth. As explained in this reference, the problem comes from the oscillatory nature of the integrand in $I_{\omega_{min}}^{\omega_{max}}(t)$, i.e. $e^{j\omega t_i} f(\omega)$, for which the period in ω of the factor $e^{j\omega t_i}$ is given by

$$\frac{2\pi}{t_i} = \frac{2\pi}{t_1 + \Delta t(i-1)} \leq \frac{2\pi}{\Delta t(i-1)} = \frac{N-1}{i-1}\Delta\omega,$$

from Eq. (1.230), assuming $t_1 \geq 0$. This means that for large t_i (i close to N) the integrand oscillates significantly in ω between ω_k and ω_{k+1}. For instance if $i \geq \frac{N}{2} + \frac{1}{2}$ we have at least half a period in ω between ω_k and ω_{k+1}. This effect is even stronger if the offset t_1 is well above 0. Therefore the approximation made above in the derivation of Eq. (1.228), namely $\int_{\omega_k}^{\omega_{k+1}} \mathrm{d}\omega e^{j\omega t_i} f(\omega) \approx \Delta\omega f(\omega_k) e^{j\omega_k t_i}$ which means that we assume the oscillating factor to be flat between ω_k and ω_{k+1}, might be quite wrong. As a practical example we take the function $f(\omega) = \frac{1}{\sqrt{\omega}}$ which is proportional to the classic thick wall formula (see next chapter, in particular Eq. (2.1)) and therefore a typical wall impedance. In this case we know that the integral from 0 to ∞ defined in Eq. (1.227) can be analytically computed: from Ref. [70] we have $\Re[I_0(t)] = \sqrt{\frac{\pi}{2t}}$ for $t > 0$. In Fig. 1.4 we show the real part of $I_0(t)$ from the method described above and from the analytical formula. The usual FFT method can give accurate results on a certain scale but not up to arbitrary large times, even with ten millions frequencies in the sampling. This example also highlights another practical limitation related to the FFT method described above, namely the number of evenly spaced frequencies required. This kind of frequency sampling is indeed not appropriate to

wall impedances spanning a large frequency range. This is also why we cannot use the more accurate method proposed in Ref. [69, pp. 585-587] where an even frequency sampling is also used.

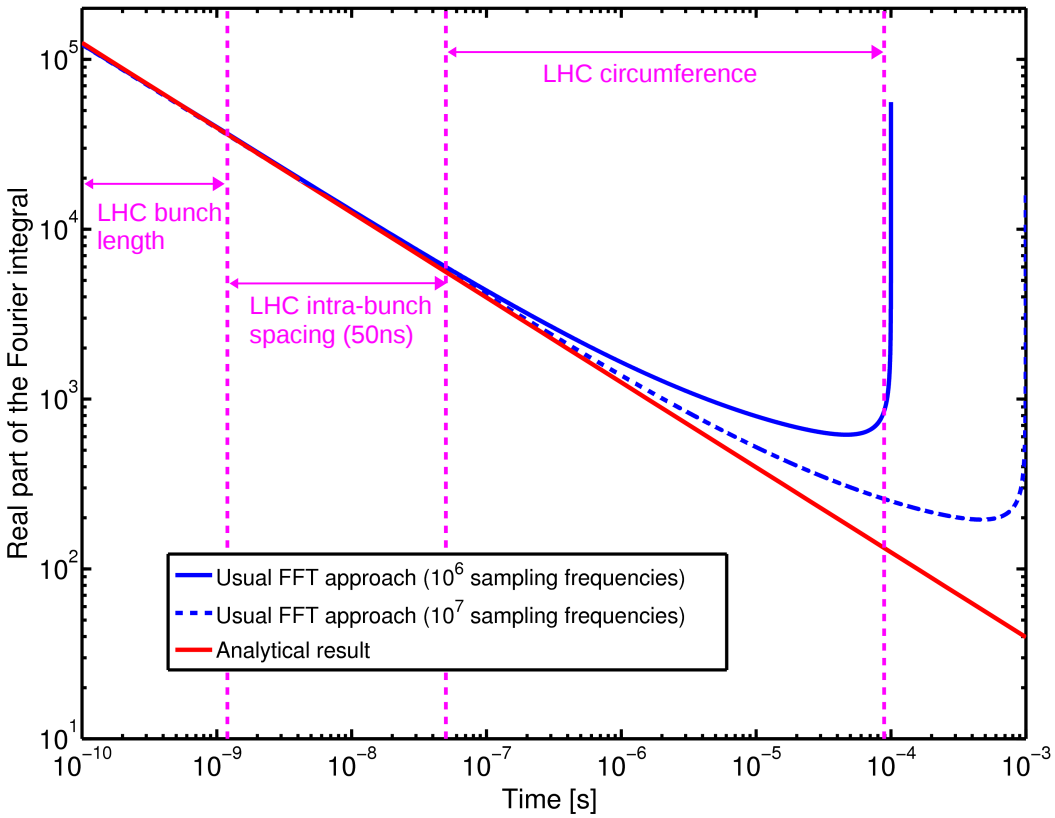

Figure 1.4: Real part of the Fourier integral from 0 to ∞ of $f(\omega) = \frac{1}{\sqrt{\omega}}$, obtained using the usual FFT method with two different frequency samplings, and from the analytical formula.

1.6.3 A general approach to compute Fourier integrals

We indicate in the following a general method to compute accurately Fourier integrals of the form given in Eq. (1.227) using an uneven sampling and a piecewise polynomial interpolation scheme, by taking advantage of the smoothness of the function we want to transform. The original idea of this method dates back from 1928 [65] and was extended later until recently [71–74]. We introduce here a few novelties with respect to those works, combining several methods and the use of a piecewise cubic interpolation, the aim being to render the method more practical and to avoid the use of complicated derivatives. The objective here is to present a single algorithm that proved to work in many different cases.

The first step is to decompose the integral $I_{\omega_{min}}(t)$ into two parts:

$$I_{\omega_{min}}(t) = \int_{\omega_{min}}^{\omega_{max}} \mathrm{d}\omega e^{j\omega t} f(\omega) + \int_{\omega_{max}}^{\infty} \mathrm{d}\omega e^{j\omega t} f(\omega), \tag{1.231}$$

where $\omega_{max} > \omega_{min}$ is a real number chosen sufficiently high such that $f(\omega)$ becomes small enough for $\omega \geq \omega_{max}$. For instance, in the case when f is an impedance we can choose $\omega_{max} = 10\frac{\beta c \gamma}{b}$, b being

the half gap or radius of the chamber (see previous sections). Indeed at such high frequencies the space-charge electric field from Eq. (1.185) – which is the source of the induced currents so of the wall impedance – begins to decrease exponentially with frequency at the position of the chamber walls, as can be seen in Eq. (C.21). In other words the walls do not feel anymore the beam's electromagnetic fields, so the impedances vanish.
The second and semi-infinite part of the integral in Eq. (1.231) can then be treated thanks to a Taylor's expansion of the function f around ω_{max}. After some algebra described in Appendix E.3.1 and taking only the first term of the expansion, one obtains an asymptotic approximation for $I_{\omega_{max}}(t)$ as

$$I_{\omega_{max}}(t) \equiv \int_{\omega_{max}}^{\infty} \mathrm{d}\omega e^{j\omega t} f(\omega) \approx e^{j\omega_{max} t} \frac{j f(\omega_{max})}{t}. \tag{1.232}$$

This approximation has the advantage that no derivatives of f are needed.
The first part of the integral $I_{\omega_{min}}(t)$ as written in Eq. (1.231) can be treated with a Filon's type method. To do so we cut the interval $[\omega_{min}, \omega_{max}]$ into several subintervals, not necessarily equidistant, delimited by the angular frequencies ω_i with i from 0 to N, $\omega_0 = \omega_{min}$ and $\omega_N = \omega_{max}$. Then, for any i between 0 and $N-1$

$$f(\omega) \approx p_i(\omega) \quad \text{for } \omega_i \leq \omega \leq \omega_{i+1}, \tag{1.233}$$

where p_i ($0 \leq i \leq N-1$) is an interpolating polynomial on the interval $[\omega_i, \omega_{i+1}]$. The main idea of Filon's method is in principle quite simple: on each subinterval we replace f by its interpolating polynomial

$$I_{\omega_{min}}^{\omega_{max}}(t) \equiv \int_{\omega_{min}}^{\omega_{max}} \mathrm{d}\omega e^{j\omega t} f(\omega) \approx \sum_{i=0}^{N-1} \int_{\omega_i}^{\omega_{i+1}} \mathrm{d}\omega e^{j\omega t} p_i(\omega). \tag{1.234}$$

The key aspect of this approach is that each term in the above sum can be computed analytically when p_i is a polynomial. In the case of the linear interpolation, we have

$$p_i(\omega) = f_i + \left(f_{i+1} - f_i\right) \frac{\omega - \omega_i}{\Delta_i} = f_i \frac{\omega_{i+1} - \omega}{\Delta_i} + f_{i+1} \frac{\omega - \omega_i}{\Delta_i}, \tag{1.235}$$

with $f_i = f(\omega_i)$ and $\Delta_i = \omega_{i+1} - \omega_i$. The integral on each subinterval is computed in Appendix E.3.2, obtaining

$$I_i(t) \equiv \int_{\omega_i}^{\omega_{i+1}} \mathrm{d}\omega e^{j\omega t} p_i(\omega) = \Delta_i \left[f_i e^{j\omega_{i+1} t} \Lambda\left(-\Delta_i t\right) + f_{i+1} e^{j\omega_i t} \Lambda\left(\Delta_i t\right) \right], \tag{1.236}$$

with Λ a function defined in Eq. (E.136). In Appendix E.3.2 we also provide its Taylor's expansion for the case when the argument of Λ is very small compared to unity, as well as a way to bound the error when truncating this expansion.
Rather than a linear interpolation, we can also choose a cubic Hermite interpolation, in which case the polynomial can be written [75]

$$p_i(\omega) = f_i \phi\left(\frac{\omega_{i+1} - \omega}{\Delta_i}\right) + f_{i+1} \phi\left(\frac{\omega - \omega_i}{\Delta_i}\right) - d_i \Delta_i \psi\left(\frac{\omega_{i+1} - \omega}{\Delta_i}\right) + d_{i+1} \Delta_i \psi\left(\frac{\omega - \omega_i}{\Delta_i}\right), \tag{1.237}$$

for i between 0 and $N-1$, with

$$d_i = p_i'(\omega_i), \quad \phi(h) = 3h^2 - 2h^3 \quad \text{and} \quad \psi(h) = h^3 - h^2. \tag{1.238}$$

The slopes of the interpolating polynomial d_i are found by the interpolation algorithm; in the case of spline interpolation [69, p. 113-114], they are found by imposing conditions of continuity at ω_i of the first and second derivatives of the final interpolating function. We prefer to use here a monotone piecewise cubic Hermite interpolation [75], where the slopes d_i are determined by a continuity condition of the first derivative only, and by forcing monotonicity between two adjacent points. This can give different results from the spline cubic Hermite interpolation [69, p. 113], in particular in preventing unphysical wiggles to appear in the interpolation polynomial, since monotonicity on each subinterval is forced. We anyway assume here that the slopes d_i are given by a certain algorithm which can be anything, such that we can choose e.g. the spline or monotonic interpolation without affecting the remainder of the section. For such a cubic interpolation, as with the linear interpolation one can compute analytically the Fourier integral on each subinterval. This is done in Appendix E.3.3, obtaining

$$\begin{aligned} I_i(t) &= \int_{\omega_i}^{\omega_{i+1}} \mathrm{d}\omega e^{j\omega t} p_i(\omega) \\ &= \Delta_i \left[f_i e^{j\omega_{i+1} t} \Phi(-\Delta_i t) + f_{i+1} e^{j\omega_i t} \Phi(\Delta_i t) - d_i \Delta_i e^{j\omega_{i+1} t} \Psi(-\Delta_i t) + d_{i+1} \Delta_i e^{j\omega_i t} \Psi(\Delta_i t) \right], \end{aligned} \tag{1.239}$$

where the functions Φ and Ψ are defined in Eqs. (E.142) and (E.143). In Appendix E.3.3 we also provide their Taylor's expansions for the case when the argument of Φ or Ψ is very small compared to unity, as well as a way to bound the error when truncating these expansions.
The final approximation of $I_{\omega_{min}}^{\omega_{max}}(t)$ is then

$$I_{\omega_{min}}^{\omega_{max}}(t) \approx \sum_{i=0}^{N-1} I_i(t), \tag{1.240}$$

where on each subinterval either Eq. (1.236) or Eq. (1.239) is chosen to compute $I_i(t)$, depending on which interpolation (linear or cubic) has been used. We can even vary the interpolation on each subinterval, choosing the one giving the best approximation of f at the mid-point of the interval, for instance.
One crucial aspect of the method is the choice of the sampling points used for the interpolation. For the integral $I_{\omega_{min}}^{\omega_{max}}(t)$, the approximation lies in the replacement of $f(\omega)$ by the interpolating piecewise polynomial $p(\omega)$ equal to $p_i(\omega)$ on each subinterval $[\omega_i, \omega_{i+1}]$. Control of the accuracy can then be made thanks to the following inequality:

$$\left| \int_{\omega_{min}}^{\omega_{max}} \mathrm{d}\omega e^{j\omega t} f(\omega) - \int_{\omega_{min}}^{\omega_{max}} \mathrm{d}\omega e^{j\omega t} p(\omega) \right| \leq \int_{\omega_{min}}^{\omega_{max}} \mathrm{d}\omega \left| f(\omega) - p(\omega) \right|. \tag{1.241}$$

Therefore, we can refine in an automatic manner the uneven sampling until the integral on the right hand side is smaller than a certain required tolerance: at each step we compute the integral of $\left| f(\omega) - p(\omega) \right|$ on the whole interval $[\omega_{min}, \omega_{max}]$ and we bisect the subinterval with the highest portion of the total integral. Note that the bisection of an interval $[\omega_i, \omega_{i+1}]$ can be either in terms of the absolute frequencies (i.e. we add the point $\frac{\omega_{i+1}+\omega_i}{2}$ to get two smaller intervals) or in terms of their logarithms (i.e. we add the point $e^{\frac{\ln(\omega_{i+1})+\ln(\omega_i)}{2}}$). In the case when f is an impedance, it exhibits a power-law behaviour at low frequencies, and we can choose the logarithmic bisection, while at high frequency the "normal" bisection is usually better.
Finally, only the choices of ω_{min} and ω_{max} remain arbitrary. A practical way to make sure than those two values are respectively close enough to zero and high enough, is to make several trials: typically the

procedure would be to choose ω_{min} and ω_{max} and then to try to choose a lower ω_{min} and a higher ω_{max} and see if the resulting wake gets very different.
As a practical example of the method, we go back to the case of Fig. 1.4, i.e. with the function $f(\omega) = \frac{1}{\sqrt{\omega}}$. In Fig. 1.5 we show the real part of $I_0(t)$ from Eq. (1.227) obtained using the usual method described in Section 1.6.2, our new approach and the analytical formula. Our method can give accurate results on various time scales with as low as 61 frequencies in the sampling.

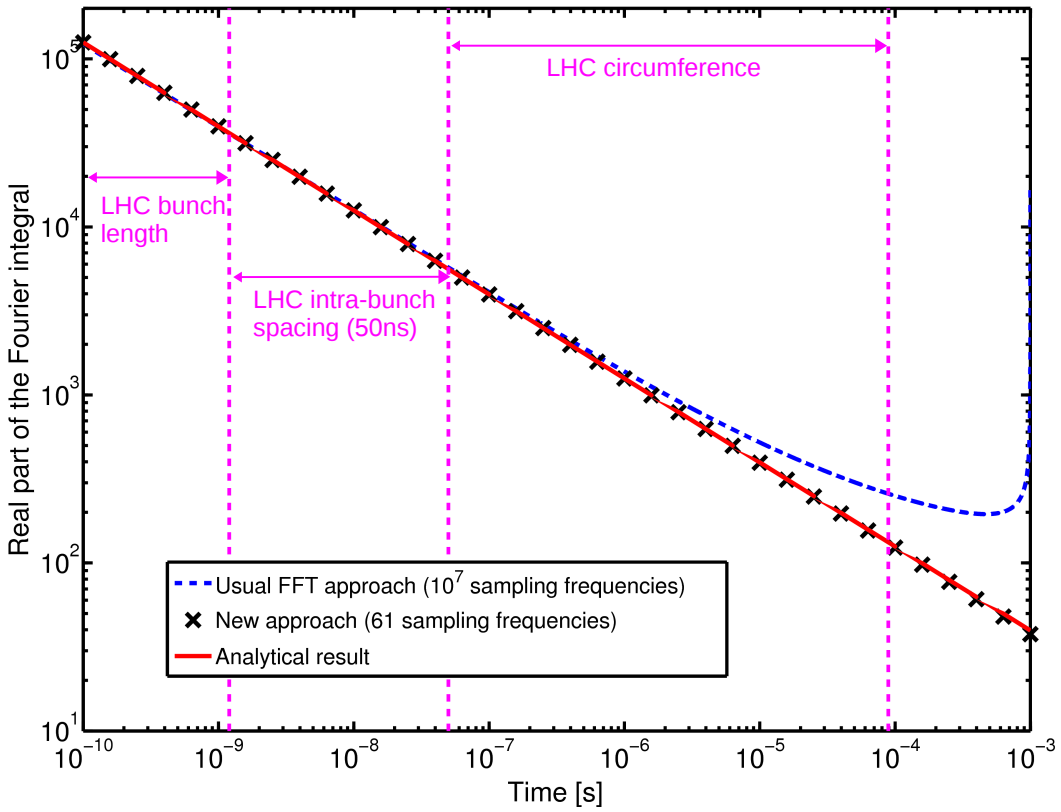

Figure 1.5: Real part of the Fourier integral from 0 to ∞ of $f(\omega) = \frac{1}{\sqrt{\omega}}$, obtained using the usual FFT method, the new general method proposed in this work, and the analytical formula.

Advantages of the method described here, with respect to the usual Fourier transform performed on evenly separated frequencies, are its accuracy and the ability to compute Fourier integrals at any point (no limitation to a given sampling depending on the frequency domain function sampling). This method is particularly useful for functions such as the analytical impedances computed in the previous sections, which are spanning a large number of decades. If the function f is smooth enough, the method proved to use much less memory and to be much less computationally intensive than the usual discretized fast Fourier transform scheme where a huge number of points have to be used to get accurate results.

1.7 Conclusion

In this chapter we described a general method to compute beam-coupling impedances and wake functions for infinitely long multilayer structures, either axisymmetric (see Fig. 1.1) or made of two infinitely large parallel plates (see Fig. 1.3). We gave the detailed analytical derivation of the electromagnetic fields

in frequency domain and impedances created by an offset point charge travelling at any velocity in those two kinds of structures, assuming only the linearity, isotropy and homogenity of the layers' materials together with the validity of local Ohm's law (thus neglecting magnetoresitance and the anomalous skin effect). New results obtained from this general approach in the axisymmetric case are the matrix method applied for the first time to Zotter's formalism, thus allowing much faster computation than was previously the case [76], and the general nonlinear (or "multimode", in the sense that all the azimuthal modes have been considered) beam-coupling impedances in Eqs. (1.103), (1.104) and (1.105). In the flat chamber case, such a general multilayer formalism applying to any linear materials and both in longitudinal and transverse has been derived, to the best of our knowledge, for the first time here; we also give the impedances in their full nonlinear expansion in Eqs. (1.195), (1.196) and (1.197).
The way to use this formalism in the cylindrical case is to first use the matrix formulae in Section 1.4.3, namely Eqs. (1.66) to (1.74), with the definitions from Eqs. (1.12), (1.13) and (1.40). This gives a 4×4 matrix $\mathscr{M}$ that we finally used in Eqs. (1.80) to compute the α_{TM}^{m} constant. The latter is then plugged into the beam-coupling impedances from Eqs. (1.103) to (1.108), or (1.109) to (1.111) for the first linear terms.
For the case of a flat chamber, the way to proceed is to first use the matrix formulae in Section 1.5.3, namely Eqs. (1.154) to (1.169), with the definitions from Eqs. (1.12), (1.13), (1.40) and (1.149). This gives two 4×4 matrices $\mathscr{M}$ and $\mathscr{M}'$, each depending on the horizontal wave number k_x, from which we can construct the matrix $\mathscr{P}$ on the left hand side of Eq. (1.172), that we finally used in Eqs. (1.175) to compute the $\eta_{1,2}$ and $\chi_{1,2}$ functions. The latter are then plugged into Eq. (1.188) to get the α_{mn} constants, before computing the beam-coupling impedances from Eqs. (1.195) to (1.200), or (1.201) to (1.206) for the first linear terms. In the case of a structure with top-bottom symmetry one can use the results of Section 1.5.7 to reduce the number of computations to be performed.
Note that the implementation of both the axisymmetric and flat formalisms required the use of high precision floating point numbers, as was already needed in the previous implementation of Zotter's formalism [76].
Finally, we described an original method to obtain numerically and accurately the wake functions from these analytically computed impedances, based on a set of known techniques and on a uneven frequency sampling.
These theories and numerical implementations are now available in several codes [77]. We will use them extensively in the next chapter for the LHC impedance model computation. Other applications of the flat chamber beam-coupling formalism shown above can be found in Refs. [78–80], with comparisons with other approaches. In particular, form factors between the impedances in an axisymmetric structure and the impedances in a flat chamber have been computed in Refs. [78, 79] and compared with the limiting case of the Yokoya factors [23].

2 The LHC impedance and wake function model

To compute transverse instability rise times and tune shifts in the LHC, one has first to estimate its impedance through a model that should take into account the most important impedance contributors. In the case of transverse coupled-bunch instabilities, long-ranged contributions are looked for in priority, and among those the (resistive-)wall impedance of the machine elements is assumed to be the dominant contributor. In principle, parasitic trapped modes and higher order modes from the RF cavities should have been considered as well. The former are difficult to evaluate (it requires extensive three dimensional electromagnetic simulations of each machine element) and should be in most cases damped thanks to appropriate impedance reduction techniques; even if this were not the case, their effect is thought to be small, as was seen for instance for the trapped modes in the CMS chamber that were evaluated and proved to have little impact at least on the longitudinal instabilities [2]. Concerning the higher order modes of the RF cavities, a previous study [81] has shown their very small effect on the transverse coupled-bunch instabilities with respect to the other impedance contributors described in this chapter.
To identify some basic criteria to select a priori the elements contributing the most to the wall impedance, we can use the classic thick wall formula for the transverse dipolar impedance of an axisymmetric and infinitely long structure in the ultrarelativistic case [10, p. 71], even if we know this formula is approximate and does not hold in the general case (see the beginning of the previous chapter and Refs. [9, 82]):

$$Z_x^{W,dip} \approx \left(1+j\right)\frac{LZ_0\delta_s}{2\pi b^3}, \tag{2.1}$$

where $\delta_s = \sqrt{\frac{2}{\mu_0\mu_r\sigma_{DC}\omega}}$ [11, p. 354] is the skin-depth of the material the closest to the beam (with the notations of Section 1.2). It appears that the three main parameters affecting the impedance are, by order of significance, the proximity to the beam (the radius b in the above formula), the length L and the resistivity $\rho_{DC} = \frac{1}{\sigma_{DC}}$ of the first material of the wall.
In the LHC, the elements the nearest to the beam are the 44 collimators, which are devices put in several places around the ring to cut the beam halo that could otherwise quench [83] or even damage the superconducting magnets (see Refs. [84, chap. 18] and [85, 86] for more details on the design and layout of the collimation system). Their rather small length (usually around one meter for each collimator) is compensated by a very narrow half gap (down to the millimeter range). Among them, the graphite collimators[1] have in addition a relatively high resistivity; actually, as already mentioned, for them the

[1] The expression "graphite collimator" is slightly inappropriate since the jaws of most of the collimators are actually made of a so called "carbon-carbon" material (also called CFC or carbon fiber-reinforced carbon), which is not the same as graphite (see Table F.4). Still, for the sake of conciseness we will use all along the thesis the expression "graphite collimators" as a general

formula above does not hold.
The next wall impedance contributor we will consider are the cold beam screens that are inside the vacuum pipe on all the cold sections of the ring, and that are used to protect the superconducting magnets against the synchrotron radiation. Even if their resistivity is very low thanks to their low temperature (less than 20K), their total length (86% of the total circumference) compensates.
Finally, the vacuum pipe outside of the cold sections is also quite long (14% of the total LHC circumference), and since its resistivity is at least twenty times higher than that of the beam screens, one has to consider them as well.
We will not totally neglect the short-ranged wake fields, because we are also interested in coupled-bunch instabilities with intrabunch motion. The wall impedance contributors considered above also exhibit short-ranged wake fields and we will naturally include them in the model. In addition, a broad-band impedance coming from previous estimates [84, chap. 5] will also be taken into account.
In this chapter we will describe from the impedance point of view those four kinds of impedance contribution: collimators, beam screens, warm vacuum pipe and broad-band model. We will then explain how to assemble together the wake functions and impedances computed for each of them, in order to get a single-kick impedance and wake-function model.

2.1 Wall impedances and wake functions of individual machine elements

2.1.1 Collimators

Generally speaking, collimators are devices consisting of two parallel jaws which are arranged at each side of the beam orbit (except for the TCDQs which have only one jaw) in order to cut particles that are far from the orbit. Primary collimators (TCP) are scattering particles directly from the beam halo, i.e. from the tail of the distribution profile (longitudinal and/or transverse), secondary collimators (TCSG) are deflecing particles scattered at the primaries, and absorbers (TCLA, TCT, TCL) are catching particles previously scattered by collimators, or debris from the collisions at the interaction points [86]. There are also dump protection collimators (TCSG and TCDQ in point 6), and injection protection collimators (TDI and TCLI) to protect the superconducting magnets against mis-kicked beams. Each of the two beams in the LHC have their own collimators, and all the collimators have only one of the two beams passing through them, except for the TDI, TCLIA and TCTVB (8 collimators in total) which are "two-beams" collimators, i.e. both beams get through the vacuum tank of the collimator, but actually only one of the two beams is travelling between the jaws, meaning that the other beam does not "see" the jaws from the electromagnetic point of view.
We show in Fig. 2.1a a graphite collimator during construction, where one jaw only had been installed yet. The flat jaw itself can be seen in Fig. 2.1b, and the two jaws seen from the beam orbit at the entrance of the collimator in Fig. 2.1c. The width of the jaws is 80 mm [88] so much larger than the beam size[2], and one can reasonably assume that the jaws can be considered, from the beam point of view, as infinitely large. Moreover, the non-flatness of the jaws is estimated not to exceed $\sim 40\mu m$ [86]. Therefore, neglecting also the anisotropy of certain carbon materials (see footnote [b] in Appendix F, Table F.4), the theory developped in Section 1.5 applies.

name for all collimators whose jaws are made of a carbon material.

[2]With a normalized RMS emittance of 3.75 mm.mrad, the beam RMS size is at the highest 2 mm at injection energy, at the collimator with the highest beta function, i.e. the TCSG in point 6 (see Table F.1).

(a) Assembly (only one jaw installed). (b) A graphite collimator jaw. (c) Jaws as seen from their entrance.

Figure 2.1: Parts of a graphite collimator, during construction. Courtesy of the LHC collimation project [87].

We define the cartesian coordinates $(Oxys)$ as in Chapter 1, with (Os) the axis tangent to the beam orbit and in the direction of movement of the beam, (Oxs) the orbit plane, (Oy) toward the top and $(Oxys)$ chosen direct[3]. The jaws are not necessarily parallel to the horizontal plane as in Fig. 1.3, they can be oriented with a certain skew angle α, defined as the angle between the jaw and the (Oy) axis, counted positively counter-clockwise [91], as shown in Fig. 2.2 (see also Ref. [89, p. 51]). We have $\alpha = 0$ for an horizontal collimator (i.e. with jaws parallel to (Oy), so intercepting the halo in the horizontal direction), $\alpha = \frac{\pi}{2}$ for a vertical collimator (with jaws parallel to (Ox)), and any other values of α for skew collimators. In Fig. 2.2, b is the half gap between the two parallel jaws, as in Section 1.5. The collimator is in our model made of several flat layers of materials, which are, from the inside to the outside:

- a coating (i.e. a very thin surface layer), only in the case of the hBN block of the TDI (see Table F.3),
- the jaw material (several possibilities), of thickness (or depth) $d = 25$ mm, except for the TDI ($d = 54$ mm) and the TCLIA ($d = 33$ mm),
- stainless steel (type 304L), of infinite thickness. In reality, beyond the jaw the collimator is made of many different pieces (mainly metallic) that are very different from a multilayer flat chamber as shown in Fig. 1.3. Still, since those pieces are far from the beam, we can model them with a infinitely large and thick layer of stainless steel (we chose arbitrarily the stainless steel 304L, which is one of the most used). The alternative would have been to choose vacuum as the last layer, but this is slightly less realistic than choosing a conductive layer since there is probably not a complete electrical insulation between the jaws and the vacuum tank. Also, choosing vacuum proved to lower the low frequency impedance, and we preferred to take the most pessimistic approach.

The jaws of each collimator have a certain length L (neglecting the tapering at each end, whose wall impedance cannot be calculated with the theory of Section 1.5).
Note that the half gaps b of the collimators vary between injection, flat top and (for some collimators) after squeezing the beams at the interaction points, because, roughly speaking, they need to follow the beam size. The jaws are indeed able to move thanks to motors that are precise within $\sim 20\mu m$ [86]. The

[3]Note that since the two colliding beams move in opposite directions, their respective set of coordinates are different. According to Ref. [89, p. 16], in the optics program MAD-X [90] the x axis is toward the outside of the LHC ring for beam 1, and the inside for beam 2, and we choose the same convention here.

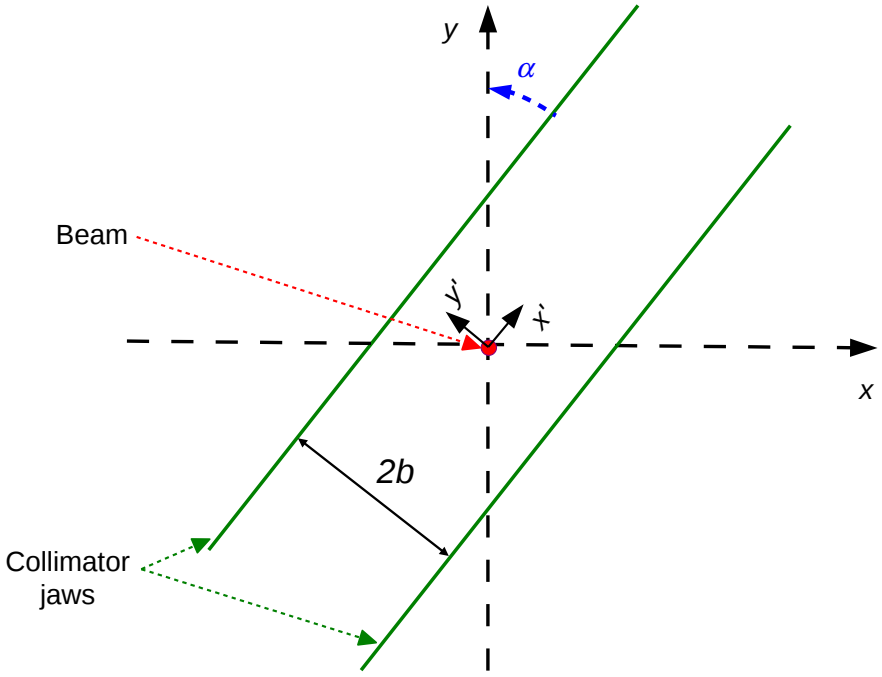

Figure 2.2: Representation of the cross section of a collimator for the impedances and wake functions calculation. b is the half gap.

half gaps of all the collimators are set up by the collimation team during specific campaigns.
The parameters defined above (jaw material, length L, half gap b, skew angle α) are summarized in Appendix F, Tables F.1 for the beam 1 collimators and F.2 for the beam 2 ones, plus some additional parameters for the TDI collimator in Table F.3. The half gaps indicated at injection and collision (3.5 TeV/c) are those measured during normal operation of the machine in 2011, the beta functions (see Section 2.3.1) at the CMS and ATLAS interaction points being $\beta^* = 1.5$ m, i.e. before the decrease of β^* to 1 m that took place in September 2011.
The TCDQ collimators are particular in the sense that they have only one jaw, parallel to (Oy), and located toward the outside of the ring for beam 1 and the inside for beam 2 [84, 92, chap. 17], i.e. at positive x in each case [89, p. 16]. The definitions above still hold, b being defined as the position between the reference orbit and the jaw, and the theory of Section 1.5 is also valid in this particular case.
The impedances and wake functions of a general skew collimator as shown in Fig. 2.2 can be obtained from the ones of a flat chamber with walls parallel to the (Oxs) plane as in Fig. 1.3, thanks to a simple change in coordinates. If we call (x', y', s) the coordinate system associated to the jaws of a particular skew collimator of angle α, with (Ox') parallel to the jaws and (Oy') perpendicular to them as shown in Fig. 2.2, we see that the collimator geometry corresponds to the one analysed in Section 1.5 (in particular Fig. 1.3) in the new coordinates (x', y', s). Using the same definitions as in Section 1.5.6 but replacing x by x' and y by y', we have, when taking into account only the constant and linear terms of the total

transverse wall impedances (see Eqs. (1.199) and (1.200)):

$$\begin{aligned} Z_{x'}^{Wall} &\approx Z_{x'}^{Wall,dip} x_1' + Z_{x'}^{Wall,quad} x_2', \\ Z_{y'}^{Wall} &\approx Z_{y'}^{Wall,0} + Z_{y'}^{Wall,dip} y_1' + Z_{y'}^{Wall,quad} y_2'. \end{aligned} \tag{2.2}$$

The change of coordinates corresponds to a rotation of angle $\frac{\pi}{2} - \alpha$. After some algebra detailed in Appendix E.4, the constant, dipolar and quadrupolar impedances as defined in Section 1.4.6 and 1.5.6 are finally given, in the initial coordinate system (x, y, s), by

$$Z_x^{Wall,0} = -\cos\alpha Z_{y'}^{Wall,0}, \tag{2.3}$$

$$Z_y^{Wall,0} = \sin\alpha Z_{y'}^{Wall,0}, \tag{2.4}$$

$$Z_x^{Wall,dip} = Z_{x'}^{Wall,dip} \sin^2\alpha + Z_{y'}^{Wall,dip} \cos^2\alpha, \tag{2.5}$$

$$Z_y^{Wall,dip} = Z_{x'}^{Wall,dip} \cos^2\alpha + Z_{y'}^{Wall,dip} \sin^2\alpha, \tag{2.6}$$

$$Z_x^{Wall,quad} = Z_{x'}^{Wall,quad} \sin^2\alpha + Z_{y'}^{Wall,quad} \cos^2\alpha, \tag{2.7}$$

$$Z_y^{Wall,quad} = Z_{x'}^{Wall,quad} \cos^2\alpha + Z_{y'}^{Wall,quad} \sin^2\alpha, \tag{2.8}$$

and we need to add two additional "coupled terms", which are giving impedance terms in the x direction proportional to y_1 (dipolar) or y_2 (quadrupolar) as well as terms in the y direction proportional to x_1 (dipolar) or x_2 (quadrupolar):

$$Z_{xy}^{Wall,dip} = \cos\alpha \sin\alpha \left(Z_{x'}^{Wall,dip} - Z_{y'}^{Wall,dip} \right), \tag{2.9}$$

$$Z_{xy}^{Wall,quad} = \cos\alpha \sin\alpha \left(Z_{x'}^{Wall,quad} - Z_{y'}^{Wall,quad} \right). \tag{2.10}$$

Note that there is no need to define $Z_{yx}^{Wall,dip}$ and $Z_{yx}^{Wall,quad}$ because here their values would be identical to respectively $Z_{xy}^{Wall,dip}$ and $Z_{xy}^{Wall,quad}$. Also, the constant term of the longitudinal impedance $Z_{\parallel}^{Wall,0}$ (from Eq. (1.201)) remains unaffected by the change of coordinates, so is independent of the skew angle.
Similar relations hold for the wake functions associated to the above impedances, respectively $W_{\parallel}^{Wall,0}$, $W_x^{Wall,0}$, $W_y^{Wall,0}$, $W_x^{Wall,dip}$, $W_y^{Wall,dip}$, $W_x^{Wall,quad}$, $W_y^{Wall,quad}$, $W_{xy}^{Wall,dip}$ and $W_{xy}^{Wall,quad}$, defined from the impedances thanks to Eqs. (1.215) to (1.217).
To compute the impedances in the coordinate system associated to the jaws, i.e. $Z_{x'}^{Wall,dip}$, $Z_{y'}^{Wall,dip}$, etc., different theories can be used:

1. the multilayer flat chamber theory of Section 1.5, which is, to the best of our knowledge, the most general two-dimensional theory for a multilayer flat chamber,

2. the multilayer flat chamber theory from Ref. [31],

3. the multilayer axisymmetric chamber theory from B. Zotter, rederived in Section 1.4, with constant form factors that enable the computation of the impedances and wake functions of the flat

geometry in the following way:

$$\begin{aligned} Z_{x'}^{Wall,dip}(\text{flat}) &= \mathscr{F}_{x'}^{dip} Z_{x'}^{Wall,dip}(\text{cyl.}), & Z_{y'}^{Wall,dip}(\text{flat}) &= \mathscr{F}_{y'}^{dip} Z_{y'}^{Wall,dip}(\text{cyl.}), \\ Z_{x'}^{Wall,quad}(\text{flat}) &= \mathscr{F}_{x'}^{quad} Z_{x'}^{Wall,dip}(\text{cyl.}), & Z_{y'}^{Wall,quad}(\text{flat}) &= \mathscr{F}_{y'}^{quad} Z_{y'}^{Wall,dip}(\text{cyl.}), \\ Z_{\parallel}^{Wall,0}(\text{flat}) &= \mathscr{F}_{\parallel} Z_{\parallel}^{Wall,0}(\text{cyl.}). \end{aligned} \tag{2.11}$$

Here we apply Yokoya's (or Laslett's) form factors for a flat geometry, obtained assuming a single metallic layer in the two parallel horizontal walls, and a certain frequency range [22, 23]:

$$\mathscr{F}_{\parallel}(\text{Yok.}) = 1,\ \mathscr{F}_{x'}^{dip}(\text{Yok.}) = \frac{\pi^2}{24},\ \mathscr{F}_{y'}^{dip}(\text{Yok.}) = \frac{\pi^2}{12},\ \mathscr{F}_{x'}^{quad}(\text{Yok.}) = -\frac{\pi^2}{24},\ \mathscr{F}_{y'}^{quad}(\text{Yok.}) = \frac{\pi^2}{24}. \tag{2.12}$$

For the single-jaw TCDQs, form factors are different and we use Burov-Danilov ones [62], obtained for a single resistive layer in the ultrarelativistic case under certain frequency conditions:

$$\mathscr{F}_{x'}^{dip}(\text{BD}) = \frac{1}{4},\quad \mathscr{F}_{y'}^{dip}(\text{BD}) = \frac{1}{4},\quad \mathscr{F}_{x'}^{quad}(\text{BD}) = -\frac{1}{4},\quad \mathscr{F}_{y'}^{quad}(\text{BD}) = \frac{1}{4}, \tag{2.13}$$

4. the multilayer axisymmetric chamber theory from Ref. [17] with Yokoya (or Burov-Danilov) form factors,
5. the single-layer axisymmetric classic thick wall formula of Eq. (2.1) with Yokoya (or Burov-Danilov) form factors.

In all those variants except for the last one where an analytical formula exists [10, p. 59], the wake functions have to be computed numerically, which we do using the method described in Section 1.6.3. In Figs. 2.3a, 2.3b and 2.4, we applied all these different theories, except for the second one whose implementation is unfortunately not available, to get the vertical dipolar impedance $Z_{y'}^{Wall,dip}$ of respectively a graphite (CFC) collimator, a tungsten one and the titanium-coated hBN block of the TDI (see Table F.3). We used the smallest half gaps occuring during normal operation (see Tables F.1 and F.2) and the material parameters of Table F.4.
These plots show that the first and third methods enumerated above give very similar vertical dipolar impedances except at very high frequencies (above at least ~ 20 GHz for the CFC collimator, ~ 100 GHz for the tungsten one and ~ 1 GHz for the TDI), meaning that Yokoya factors seem to give the correct impedances of the flat geometry at low and intermediate frequencies. The fourth method (Burov-Lebedev round chamber's theory with Yokoya factors) is also very similar[4] except again at very high frequencies, which is expected from the fact that this theory explicitely assumes that $\omega \ll \frac{c}{b}$ [17]. Around THz frequencies, with Zotter's theory a peak appears in all three cases, due to a resonance caused by the interaction between the relativistic particle and waveguide modes propagating down the chamber [32]. This resonance is also visible with the new flat chamber theory but is much weaker and has a slightly different frequency. For the TDI with Zotter's round chamber theory, other resonances appear around GHz frequencies, due to a coupling with waveguide modes inside the hBN layer which is a dielectric material (see Table F.4). The frequency of such resonances can be approximately computed by assuming that the TDI is a circular waveguide completely filled with the hBN of dielectric constant $\varepsilon_b = 4$ (see Table F.4), neglecting its resistivity, with a perfect conductor on its outer surface of radius $b^{(2)} = b + d = 58$ mm

[4] Note that the double-layer formula in Ref. [17] is valid only at intermediate frequencies, and one has to use the more general method described in this reference to get an accurate result at low frequencies.

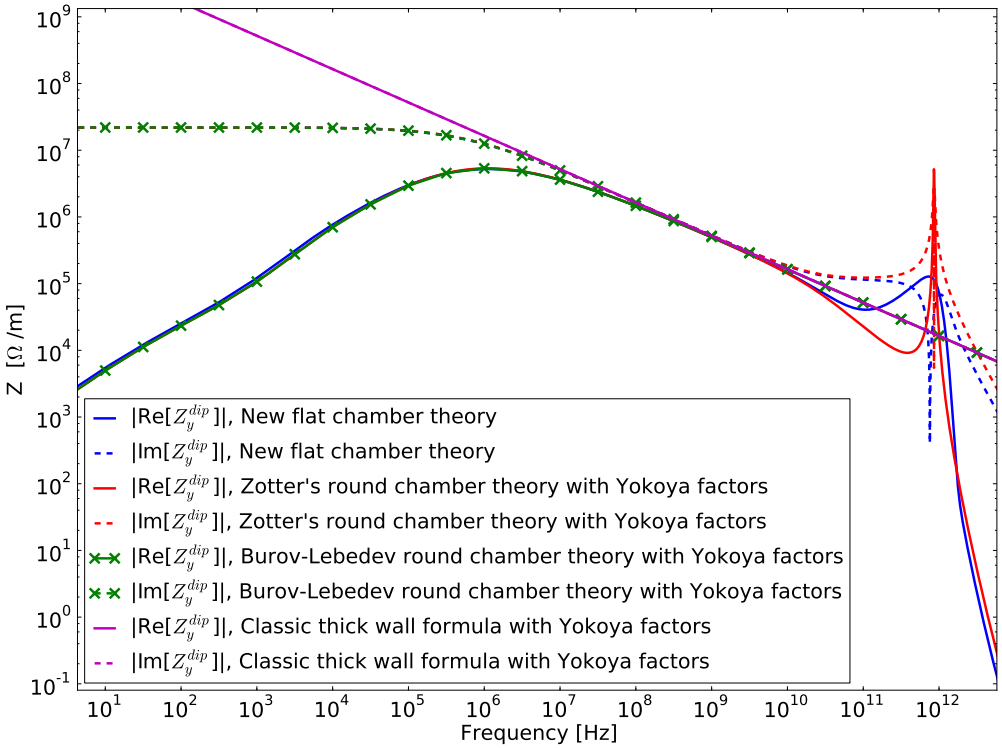

(a) CFC collimator with 1.5 mm half gap.

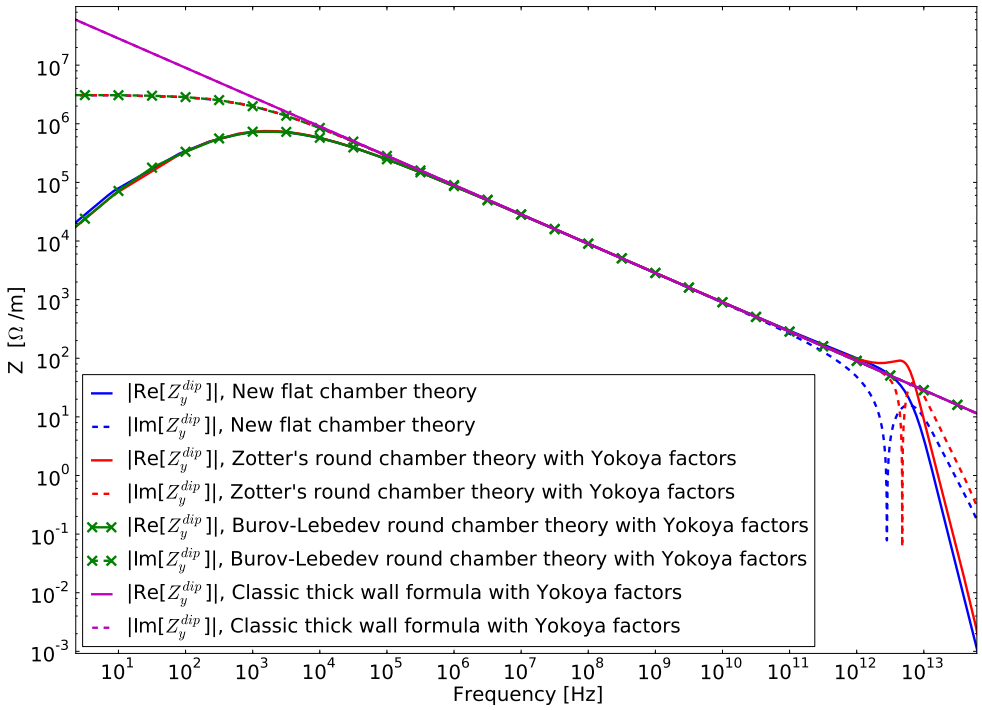

(b) Tungsten collimator with 4 mm half gap.

Figure 2.3: Vertical dipolar impedance of 1m-long CFC and tungsten collimators (see parameters in Table F.4) at 3.5 TeV/c ($\gamma = 3730.26$). We compare the theories 1, 3, 4 and 5 enumerated in Section 2.1.1.

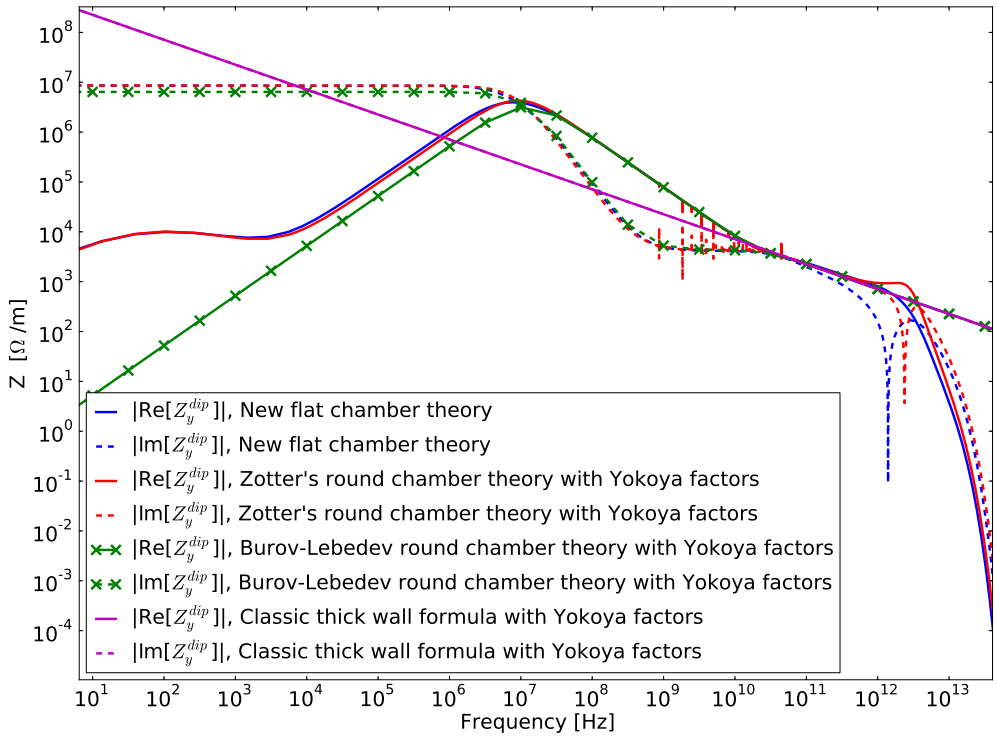

Figure 2.4: Vertical dipolar impedance of the titanium-coated hBN block of the TDI (see parameters in Tables F.3 and F.4), with a half gap of 4 mm, at injection energy ($\gamma = 479.6$). We compare the methods 1, 3, 4 and 5 enumerated in Section 2.1.1. Note that for Burov-Lebedev round chamber theory, only two layers have been taken into account and the hBN replaced by vacuum.

(with the notations of Chapter 1). The dispersion relation of such a dielectric waveguide is then given by $k = \frac{\omega\sqrt{\varepsilon_b}}{c}\sqrt{1-\frac{\omega_\lambda^2}{\omega^2}}$ from Ref. [11, p. 364], with ω_λ the lowest possible angular frequency achievable by the mode λ ("cut-off" angular frequency). We choose the mode with the lowest possible cut-off frequency, namely the first TE mode for which $\omega_\lambda = \frac{j'_{11}c}{\sqrt{\varepsilon_b}b^{(2)}}$ [93] where $j'_{11} \approx 1.84$ is the first zero of J'_1 (derivative of the Bessel function J_1). Resonances in the impedances appear when the source particle wave number $k = \frac{\omega}{v} = \frac{\omega}{\beta c}$ crosses the dispersion relation of the waveguide mode. The resulting equation in ω can be solved, obtaining for the first resonance

$$f_{resonance} = \frac{\omega_{resonance}}{2\pi} = \frac{j'_{11}c}{2\pi b^{(2)}\sqrt{\varepsilon_b - \frac{1}{\beta^2}}}. \tag{2.14}$$

One obtains $f_{resonance} \approx 874$ MHz, which is very close to the frequency of the lowest peak visible in Fig. 2.4, found at 866 MHz. Note that these resonances are not visible in the case of the calculation using Burov-Lebedev's approach because the dielectric constant of hBN has been neglected. This, together with the absence of the third layer in stainless steel when using Burov-Lebedev's approach (up to now only the case of two layers has been implemented), explans also the discrepancy between this approach and Zotter's one at low frequencies.
Finally, the classic thick wall formula almost does not apply at all for the hBN block of the TDI, while it applies only between ~ 10 MHz and ~ 10 GHz for the CFC collimator, and on most of the range of interest

for the tungsten collimator. In the case of CFC collimators (or more generally, graphite collimators), the fact that the transverse dipolar impedance is well below the classic thick wall formula (in particular for the real part of the impedance) at the first unstable betatron line (8 kHz) was historically a very important discovery during the LHC design, since the predicted instabilities growth rates were then reduced by several order of magnitudes.

Using the approaches shown in Chapter 1, i.e. the first and third methods enumerated above, we can also compute generalized frequency dependent form factors between the flat and cylindrical geometries, obtained using the same definitions as above in Eqs. (2.11). Thanks to Eqs. (1.109) to (1.111) and Eqs. (1.201) to (1.206), those generalized form factors are obtained by

$$\mathscr{F}_{x'}^{dip} \equiv \frac{Z_{x'}^{Wall,dip}(\text{flat})}{Z_{x'}^{Wall,dip}(\text{cyl.})} = \frac{\alpha_{02}-\alpha_{00}}{\alpha_{\text{TM}}^{1}}, \qquad \mathscr{F}_{y'}^{dip} \equiv \frac{Z_{y'}^{Wall,dip}(\text{flat})}{Z_{y'}^{Wall,dip}(\text{cyl.})} = \frac{2\alpha_{11}}{\alpha_{\text{TM}}^{1}}, \tag{2.15}$$

$$\mathscr{F}_{x'}^{quad} \equiv \frac{Z_{x'}^{Wall,quad}(\text{flat})}{Z_{x'}^{Wall,dip}(\text{cyl.})} = \frac{\alpha_{00}-\alpha_{02}}{\alpha_{\text{TM}}^{1}}, \qquad \mathscr{F}_{y'}^{quad} \equiv \frac{Z_{y'}^{Wall,quad}(\text{flat})}{Z_{y'}^{Wall,dip}(\text{cyl.})} = \frac{\alpha_{00}+\alpha_{02}}{\alpha_{\text{TM}}^{1}}, \tag{2.16}$$

$$\mathscr{F}_{\parallel} \equiv \frac{Z_{\parallel}^{Wall,0}(\text{flat})}{Z_{\parallel}^{Wall,0}(\text{cyl.})} = \frac{\alpha_{00}}{\alpha_{\text{TM}}^{0}}, \tag{2.17}$$

with α_{TM}^{m} and α_{mn} given respectively by Eqs. (1.80) and (1.188). To check the validity of the third method enumerated above (i.e. Zotter's axisymmetric theory with Yokoya factors), we can compare these form factors to Yokoya's ones [23], or for the TCDQs to Burov-Danilov ones [62]. This is shown is Figs. 2.5a, 2.5b, 2.6a and 2.6b for respectively TCDQ, graphite (CFC), tungsten and hBN collimators. For the TCDQs, Burov-Danilov form factors are in good agreement with our generalized factors, from very low to quite high frequencies. For the tungsten and CFC collimators, our form factors are very similar to Yokoya's ones, except again at very high frequencies. For the titanium-coated ceramic block of the TDI, some differences in the transverse form factors appear around MHz frequencies and for frequencies above $\sim$ 1 GHz (in particular for the resonant peaks between $\sim$ 1 GHz and $\sim$ 100 GHz), while in longitudinal the form factor calculated from our theories is on most of the frequency range significantly different from the Yokoya factor.

Similar form factors can be computed for the wake functions, and compared to the same Yokoya factors. This is shown in Figs. 2.7a, 2.7b and 2.8, for the transverse wake functions. Very short-ranged wakes (up to 4 cm for the CFC collimator, and up to 0.1 mm for the tungsten collimator and the hBN block) significantly deviate from Yokoya factors, with a limiting value for zero distance behind the source, that seems to reach ~ 0.4 in all these cases and for all transverse impedances (except of course for $W_{x'}^{Wall,quad}$ which is always the opposite of $W_{x'}^{Wall,dip}$, see Section 1.5.6). For tungsten, no other significant discrepancy appears, whereas CFC and hBN long-ranged wake functions also exhibit a behaviour different from Yokoya's factors, between 1 km and 100 km for CFC and above 10 m for the TDI. Short-ranged wakes even up to 4 cm are of little relevance for the LHC where the total bunch length should be at the shortest around 30 cm at 7 TeV/c [84, chap. 1, p. 3]. On the contrary, long-ranged wakes, from 7.5 m (bunch spacing for bunches separated by 25 ns) up to several turns, are obviously much more important in the case of coupled-bunch instabilities.

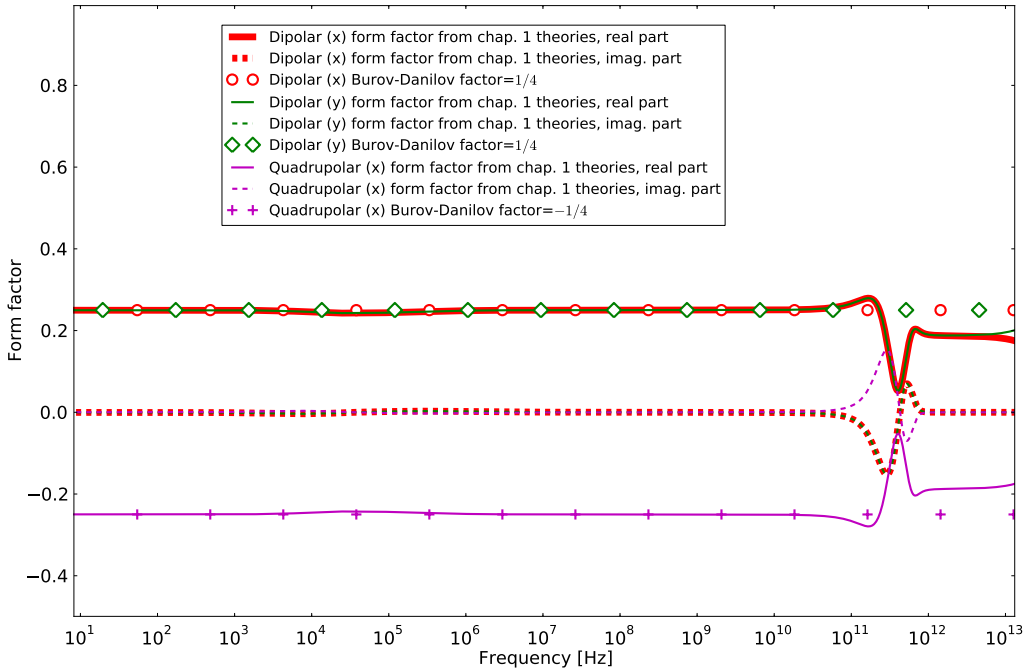

(a) TCDQ collimator with 6.5 mm half gap. The vertical quadrupolar form factor has not been plotted because it turns out to be the same as the vertical dipolar one.

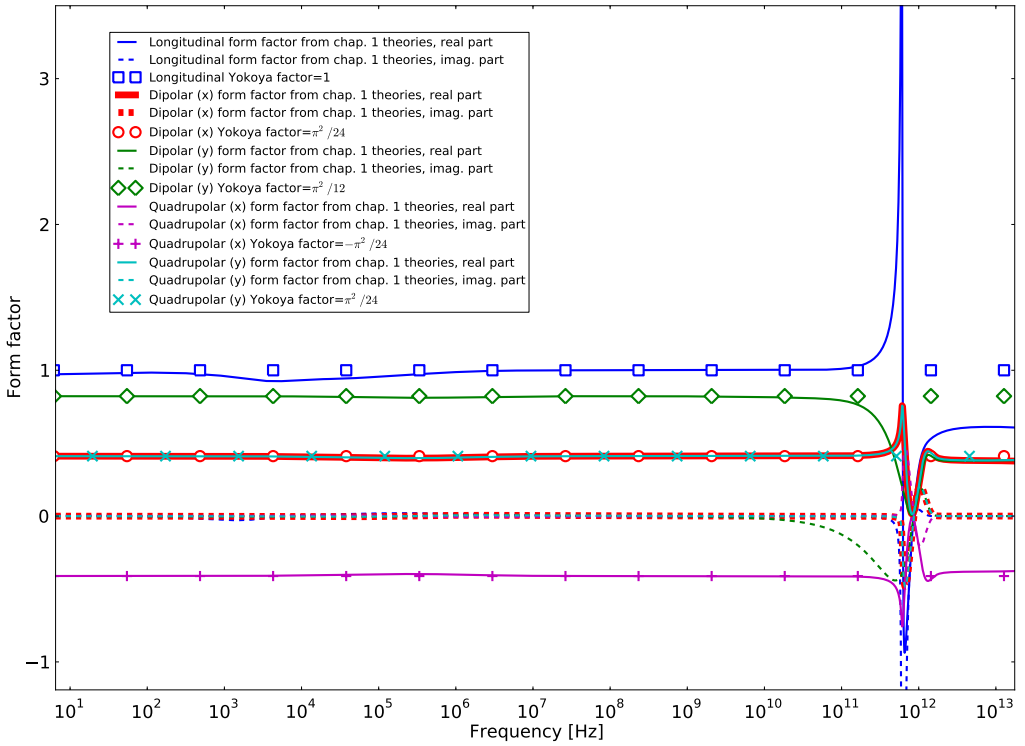

(b) CFC collimator with 1.5 mm half gap.

Figure 2.5: Form factors between the flat and cylindrical geometries, for the impedances of a single-jaw TCDQ collimator and a 1m-long CFC collimator (see parameters in Appendix F.3) at 3.5 TeV/c ($\gamma = 3730.26$).

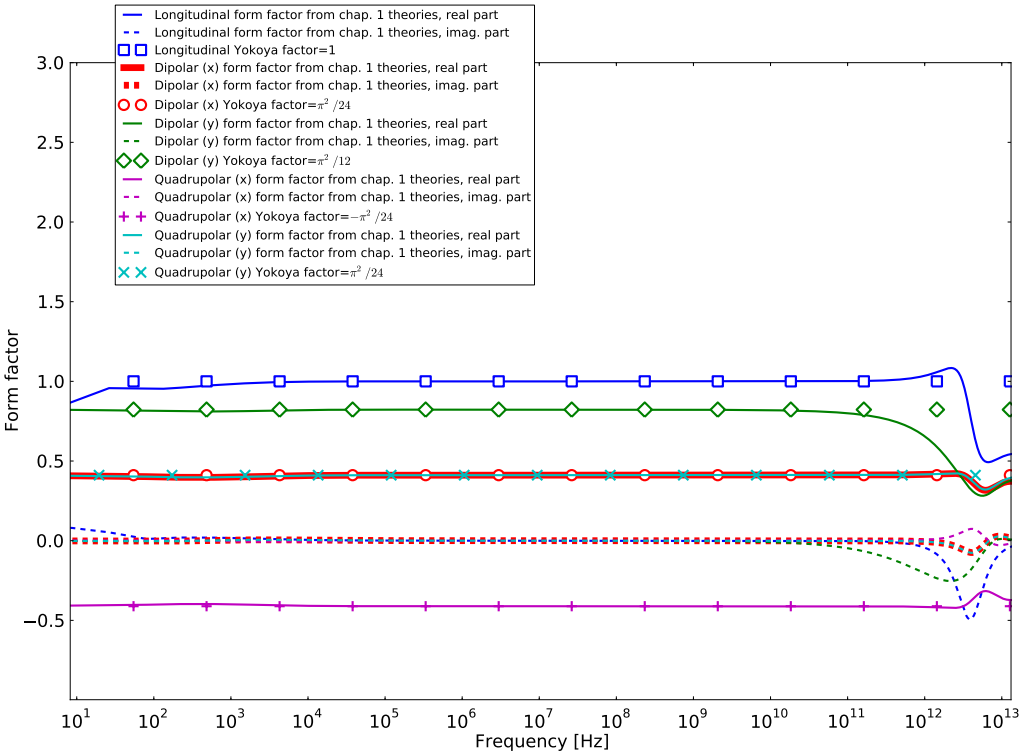

(a) Tungsten collimator with 4 mm half gap, at 3.5 TeV/c ($\gamma = 3730.26$).

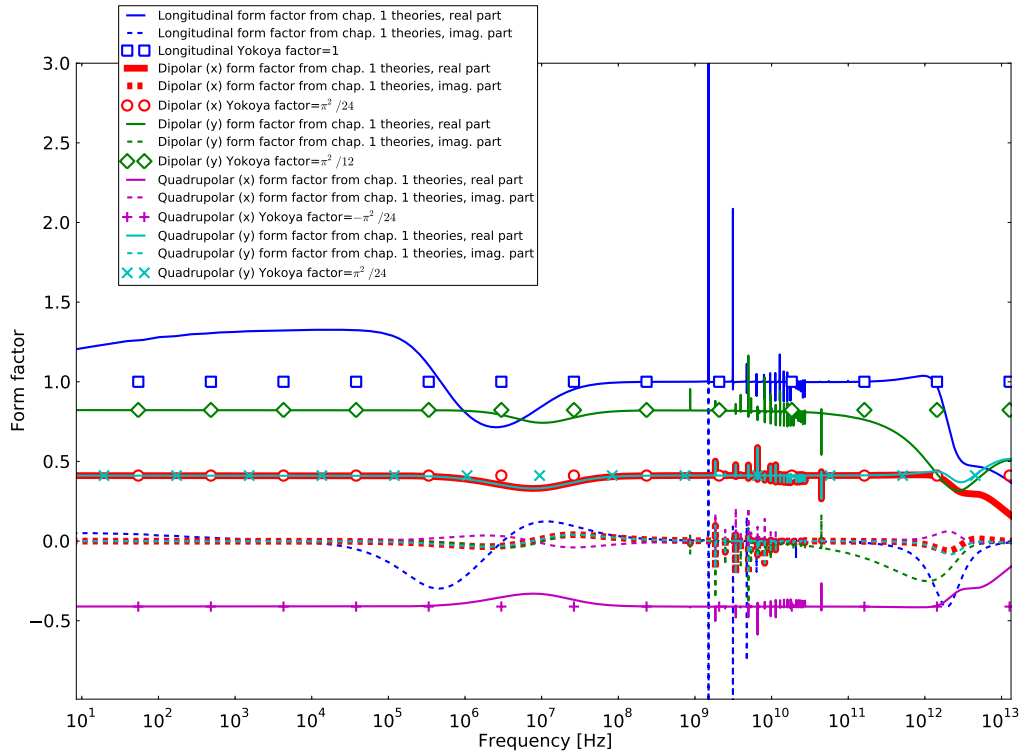

(b) TDI with 4 mm half gap, at injection energy ($\gamma = 479.6$).

Figure 2.6: Form factors between the flat and cylindrical geometries, for the impedances of a 1m-long tungsten collimator and the titanium-coated hBN block of the TDI (see parameters in Appendix F.3).

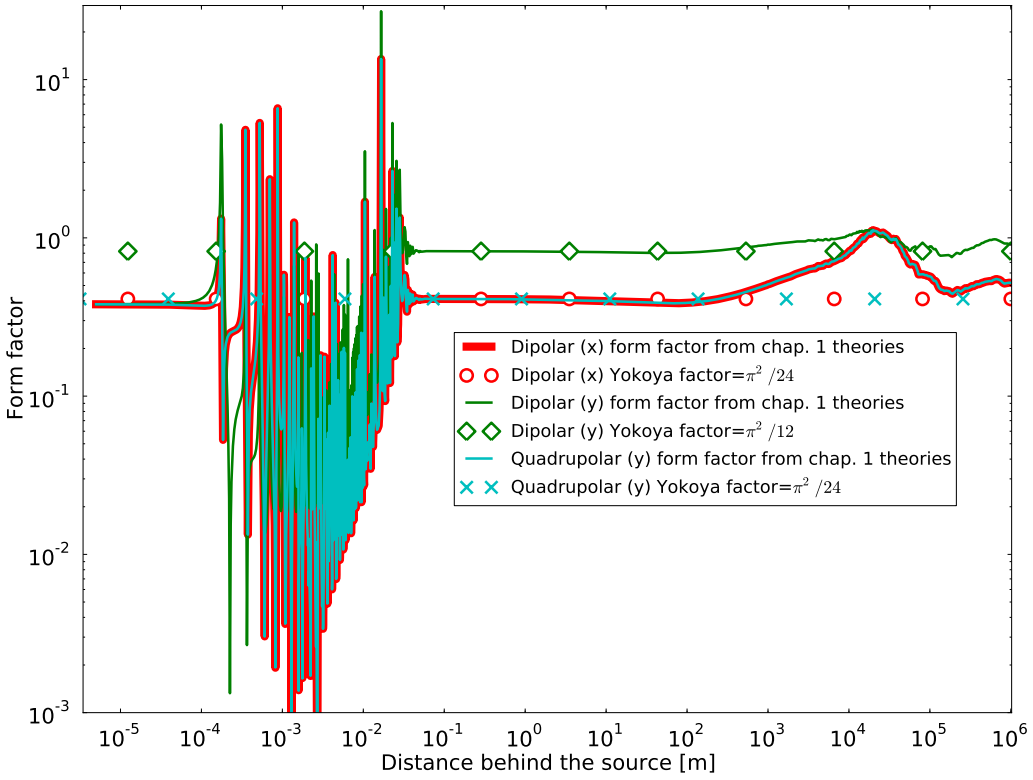

(a) CFC collimator with 1.5 mm half gap. Form factors are taken in absolute value.

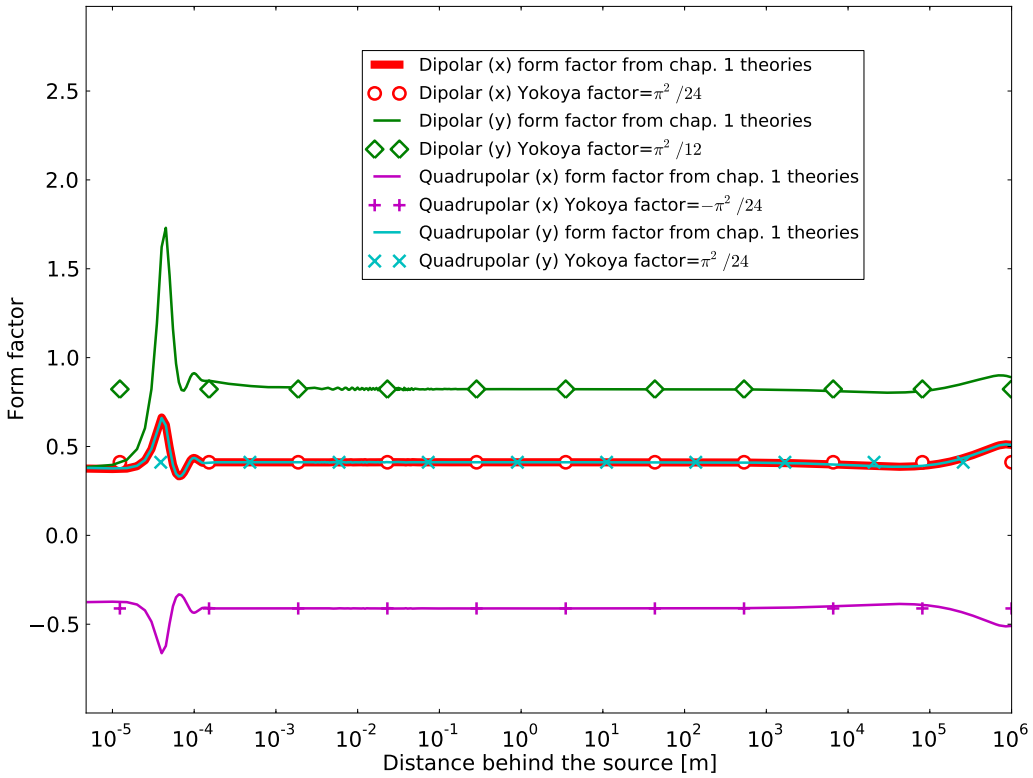

(b) Tungsten collimator with 4 mm half gap.

Figure 2.7: Form factors between the flat and cylindrical geometries, for the wake functions of 1m-long CFC and tungsten collimators (see parameters in Table F.4) at 3.5 TeV/c ($\gamma = 3730.26$).

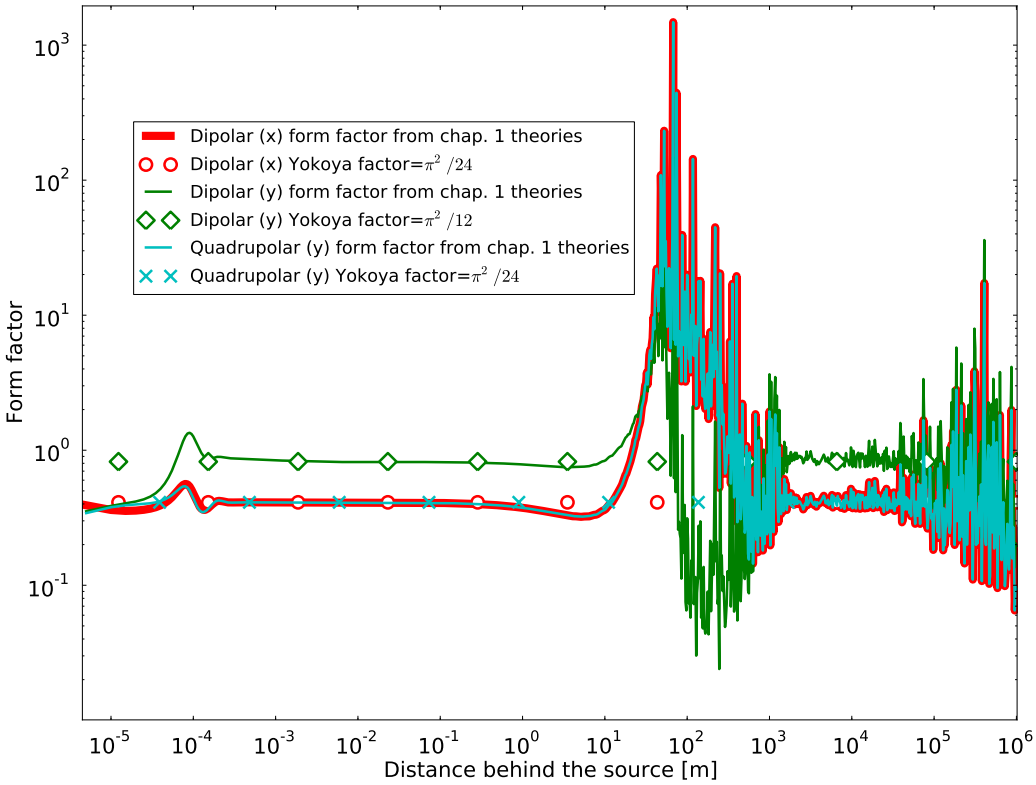

Figure 2.8: Form factors between the flat and cylindrical geometries, for the wake functions of the titanium-coated hBN block of the TDI (see parameters in Tables F.3 and F.4), with a half gap of 4 mm, at injection energy ($\gamma = 479.6$). Form factors are taken in absolute value.

The large difference between the Yokoya factors and the generalized ones for the CFC collimator wake functions below 4 cm is due the quite different high frequency peak at the THz level in the two flat and cylindrical theories, that was already visible in Fig. 2.3a. In particular, in the flat chamber theory the peak is much less sharp, translating into a faster damping of the time domain oscillations, visible in Fig. 2.9a where we have plotted $W_{x'}^{Wall,dip}$ obtained from the flat chamber theory, the cylindrical chamber's one with Yokoya factors and the classic thick wall formula with Yokoya factors. This then turns into strong oscillations in the form factors below 4 cm in Fig. 2.7a, because the wake oscillations in the flat and cylindrical cases are very different. The discrepancy between 1 km and 100 km is also clearly visible in Fig. 2.9a. The long-ranged discrepancy between the flat chamber theory and Zotter's one with Yokoya factors, for the TDI, is shown on $W_{x'}^{Wall,dip}$ in Fig. 2.9b. Note that the erratic behaviour above 10 m of the wake function in Zotter's theory does not seem to be due to numerical errors (the wake seems well converged – with the algorithm of Section 1.6.3 – at least up to 1 km) but looks like a long-ranged oscillation. This also explains the strong oscillations above 10 m in the form factors of Fig. 2.8.
In conclusion, Zotter's theory with Yokoya factors seems to be sufficient to calculate the impedances and wake functions of all collimators, except for the long-ranged behaviour of the CFC and TDI collimators. Since those kinds of collimators are high impedance contributors (see e.g. the magnitude of the impedances in Figs. 2.3a and 2.4 with respect to that of the tungsten collimator in Fig. 2.3b), we chose the apply the new flat chamber theory to maximize accuracy.

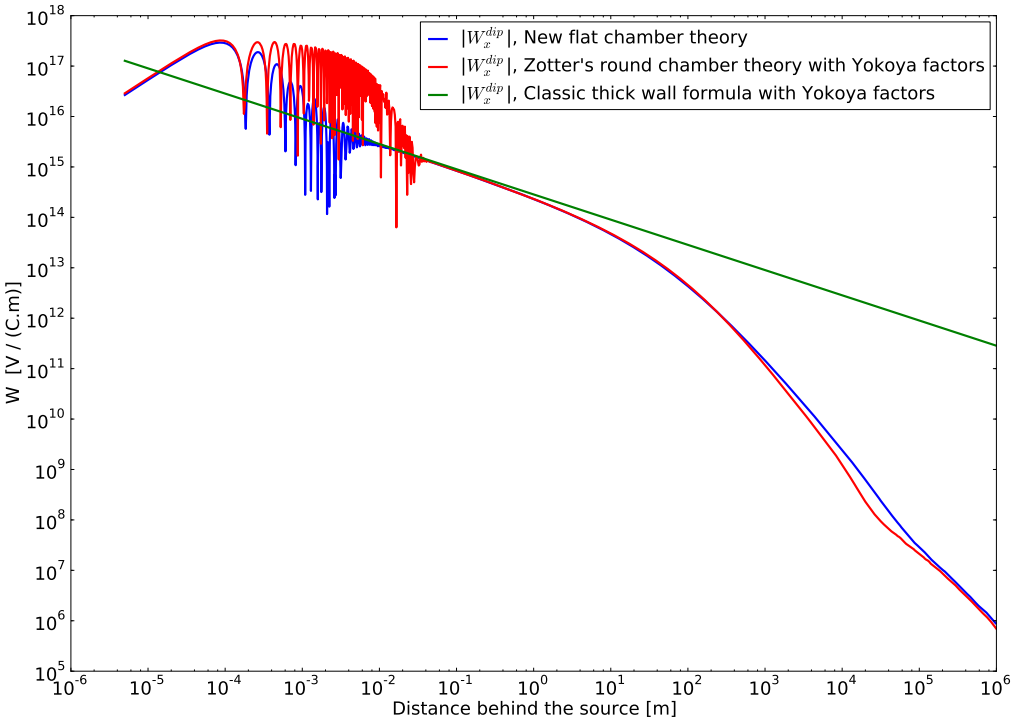

(a) CFC collimator with 1.5 mm half gap, at 3.5 TeV/c ($\gamma = 3730.26$).

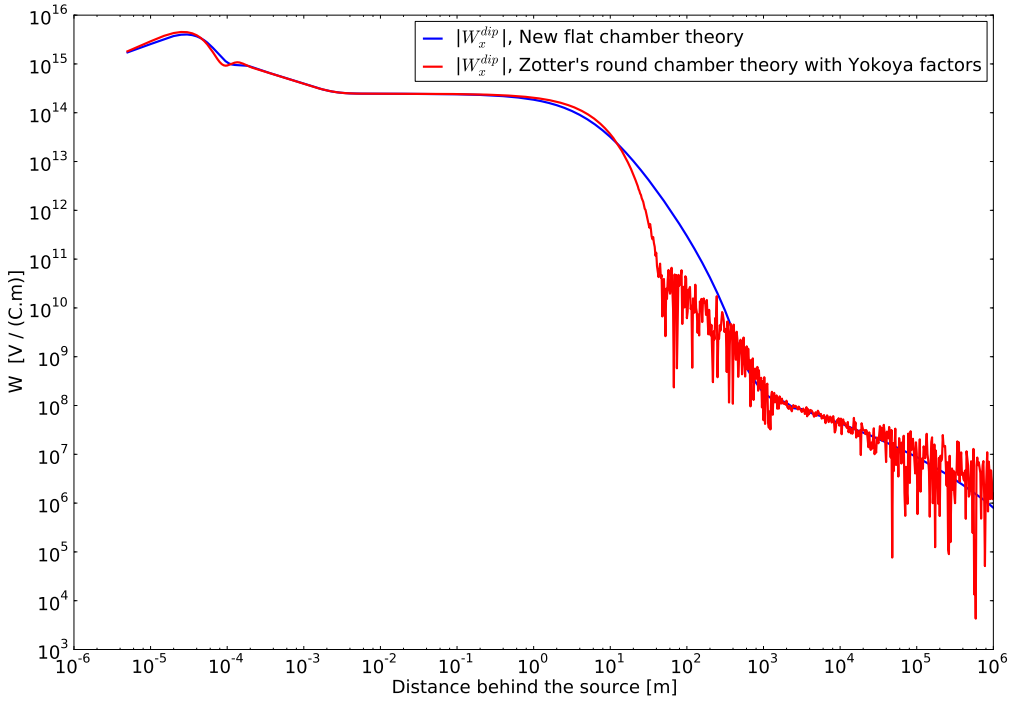

(b) Titanium-coated hBN block of the TDI, with 4 mm half gap, at injection energy ($\gamma = 479.6$).

Figure 2.9: Horizontal dipolar wake function of a 1m-long CFC collimator and the titanium-coated hBN block of the TDI (see parameters in Tables F.3 and F.4). We compare the theories 1, 3 and 5 enumerated in Section 2.1.1.

2.1.2 Beam screens

Beam screens are perforated tubes inside the superconducing magnets, protecting the cold bore against synchrotron radiation and ion bombardment [84, p. 7 & 343]. They are made of copper-coated stainless steel [84, chap. 5, p. 98] maintained at a temperature between 5 and 20 K [94], and exhibit several geometrical particularities making their impedance a priori difficult to compute:

- a cross section partly round and partly flat (the sides perpendicular to the plane of the bending – usually the horizontal plane – are round while the others are flat),
- pumping slots, i.e. holes on the flat sides that permit vacuum pumping inside the beam screens,
- an uncoated stainless-steel weld on one of the round sides of the wall (the one toward the inside of the LHC ring),
- saw teeth on the other round side of the wall: these are a series of 30 μm-high steps spaced by 500 μm in the longitudinal direction, that reduce the forward reflectivity of photons from synchrotron radiation and therefore the build up of electron clouds [84, chap. 5, p. 116].

Those geometrical features are visible in Figs. 2.10a and 2.10b. Beam-coupling impedances for such particular cross-sections cannot be computed with two-dimensional analytical models, at least up to now. Consequently we have approximated this geometry by an elliptical one, the axes of which correspond to the actual beam screen dimensions, as shown in Fig. 2.11. The pumping slots are geometrical features assumed to give essentially an additive broad-band impedance contribution (see the discussion at the beginning of Chapter 1). Therefore we neglect them when computing the wall impedance of the beam screens, and will consider them instead later in Section 2.2.

The uncoated weld, of about 2 mm width [95, 96], creates an azimuthal inhomogeneity that in principle should be taken into account for the wall-impedance computation. The impact of the weld proved indeed to be significant in the resistive power loss related to the longitudinal impedance, as shown in Refs. [95, 97]. In the transverse plane, to date no complete evaluation of its effect was performed on the correct geometry, which require the use of electromagnetic codes that, up to now, cannot easily provide the wake functions on a long enough range as needed by our multibunch and multiturn computations (see Chapter 3). Moreover, strong difficulties arise when one wants to take into account properly the coating and the round part of the cross-section. Reference [98] give results for a rectangular geometry and shows that at 8 kHz (first unstable betatron line [2]) the weld induces in the studied geometry an increase of the real part of the dipolar impedance by a factor 1.2, and of the imaginary part by a factor 1.5, whereas at 40 MHz the factor becomes 2 for both real and imaginary parts. But in this reference calculations do not take into account the coating thickness outside the weld (i.e. assume that the wall is only made of copper apart from the weld), which is probably a too strong approximation for long-ranged wakes since image currents will go beyond the copper, inside the stainless steel, below a certain frequency (around 28 kHz at injection energy and 78 kHz at 7 TeV/c, from the parameters of Table F.7, the skin depth formula and taking 50 μm as the copper coating thickness, see below). Therefore, at very low frequencies the impact of the weld might be overestimated there. Since the impedance of the beam screens is significant with respect to the other contributions only at low frequencies (see Section 2.3.3), we have therefore chosen not to use the results from this reference and not to take the weld into account at all in our study.

Finally, the effect of the saw teeth on the wall impedance have been neglected as well, as measurements [99] show that at low temperature the surface resistance of copper is not affected by such ribbed

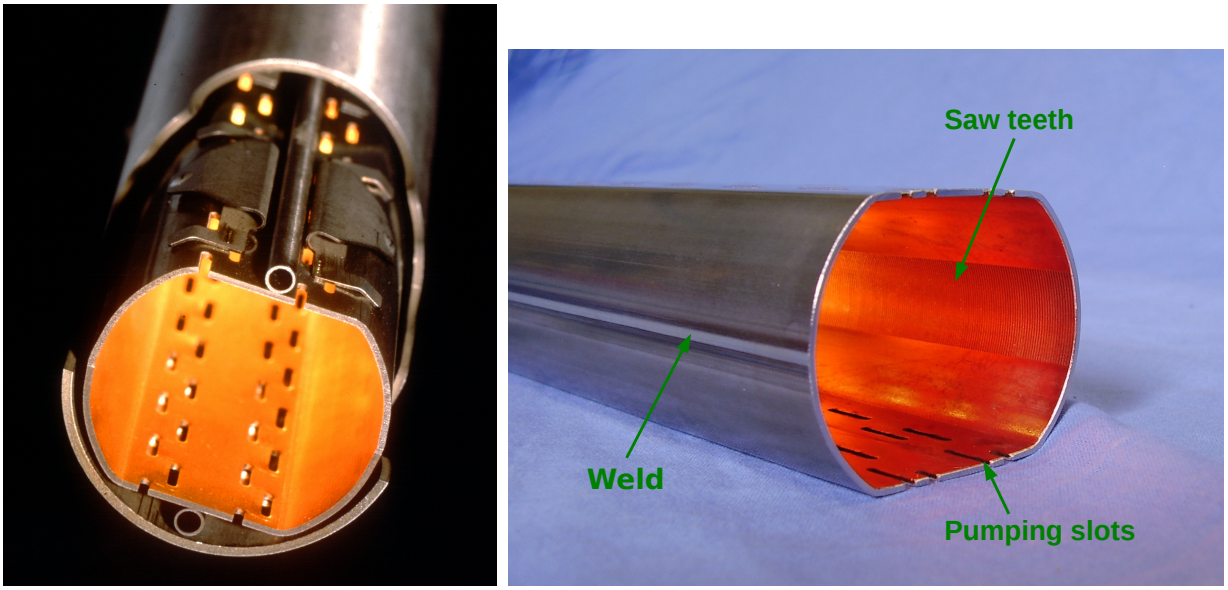

(a) The beam screen and its surroundings. Source: CERN.

(b) Some details of the beam screen itself. Courtesy of N. Kos.

Figure 2.10: An LHC beam screen.

structures (contrary to the room temperature surface resistance [99]). Their contribution to the broad-band impedance has also been neglected (see Section 2.2): only the longitudinal broad-band contribution was evaluated, in Ref. [97], giving $\left|Z_{\parallel}/n\right| \approx 2\,\mathrm{m}\Omega$ (with $n = \omega/\omega_{rev}$, ω_{rev} being the angular revolution frequency) which is about fourty times less than the total broad-band budget.
Beam screens are made of stainless steel of grade P506 and thickness 0.6 mm (except for the beam screen of type 50A which are 1 mm thick), co-laminated with a surface layer of copper of thickness 75 μm [100]. Due to the fabrication process, copper gets contaminated with elements from the stainless steel [101], creating an heterogeneous layer. This is approximately taken into account in the model by reducing artificially the copper layer to 50 μm, as done in Ref. [84, chap. 5, p. 98].
An important remark is that in the presence of such high fields and low temperatures, copper is magneto-resistant and suffers from the anomalous skin effect [52]. While those effects do not fit in the theories of Chapter 1, one can still take them into account approximately by choosing the resistivity values in an appropriate manner. In particular, copper resistivity strongly depends on the B field in the magnets around the beam screen, so on the beam energy, as shown in Table F.7.

As a consequence of all the above considerations, the beam screens impedances are computed thanks to Zotter's theory as presented in Section 1.4, taking the radius equal to the semi-axis b in Table F.5, and assuming the structure is made of two layers, both at 20 K: one layer of copper of thickness 50 μm and an infinite layer of stainless steel (we chose it infinite for the same reason as we did for collimators, see previous section). Then, Yokoya factors for an elliptical shape [23] are applied, to get the impedances of an elliptic structure approximating the beam screen cross-section, as shown in Fig. 2.11. Those factors are assumed to be reasonably valid in most of the frequency regime of interest, since the skin depth in the copper layer is below 50 μm for any frequency above 78 kHz. Still, for very low frequencies (i.e. very long-ranged wakes) Yokoya factors might not apply anymore. Experience on the collimators (see previous section) seems to indicate that at low frequencies they are still valid for conductive walls, but

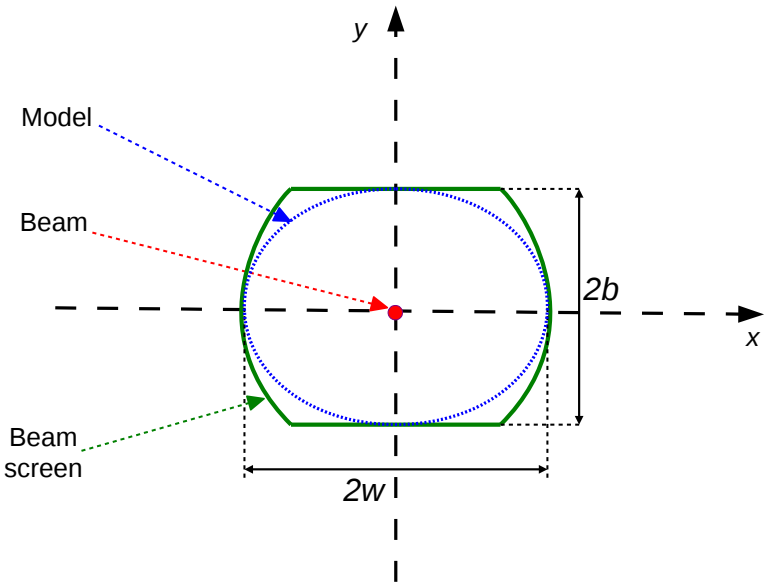

Figure 2.11: Representation of the cross section of a vertical beam screen for the impedances and wake functions calculation. In blue is sketched the elliptical shape used to get the impedance model, b being the vertical semi-axis and w the horizontal one.

this remains unverified for the beam screens.
Details of the transverse dimensions, lengths and Yokoya factors of each kind of beam screen are shown in Appendix F, Table F.5. The materials parameters used in the impedance calculations can be found in Table F.7. We show in Fig. 2.12 the vertical dipolar impedance per unit length of the beam screen that is by far the most present (type 50A, of almost 22 km of cumulated length), together with the classic thick wall approximation of Eq. (2.1) for a single layer of copper, applying also the Yokoya factors of Table F.5 in both cases. In the same figure we also show the vertical dipolar impedance of the warm vacuum pipe (see next section). These plots show that from ~ 100 kHz up to ~ 100 GHz (which is well beyond the frequency spectrum of LHC bunches that are on the order of 1 ns length), the classic thick wall approximation is valid for the LHC beam screens. However, at low frequencies, induced currents penetrate the stainless steel and the impedances become much larger. This is also clearly visible in the long-ranged behaviour of the dipolar vertical wake function per unit length (computed thanks to the approach of Section 1.6.3) which is shown in Fig. 2.13.

2.1.3 Vacuum pipe in the warm sections

The vacuum pipe goes obviously around the whole LHC ring circumference, but its impedance has to be considered only in the parts of the ring where there are neither collimators nor beam screens, since in those parts the vacuum pipe is farther away from the beam than elements already taken into account. Therefore, we focus here only on the warm sections of the vacuum pipe, where beam screens are absent. In those sections there are essentially four types of vacuum pipes, with different cross-sections, which are summarized in Appendix F, Table F.8. Those are inside the MBW magnets (twin aperture warm

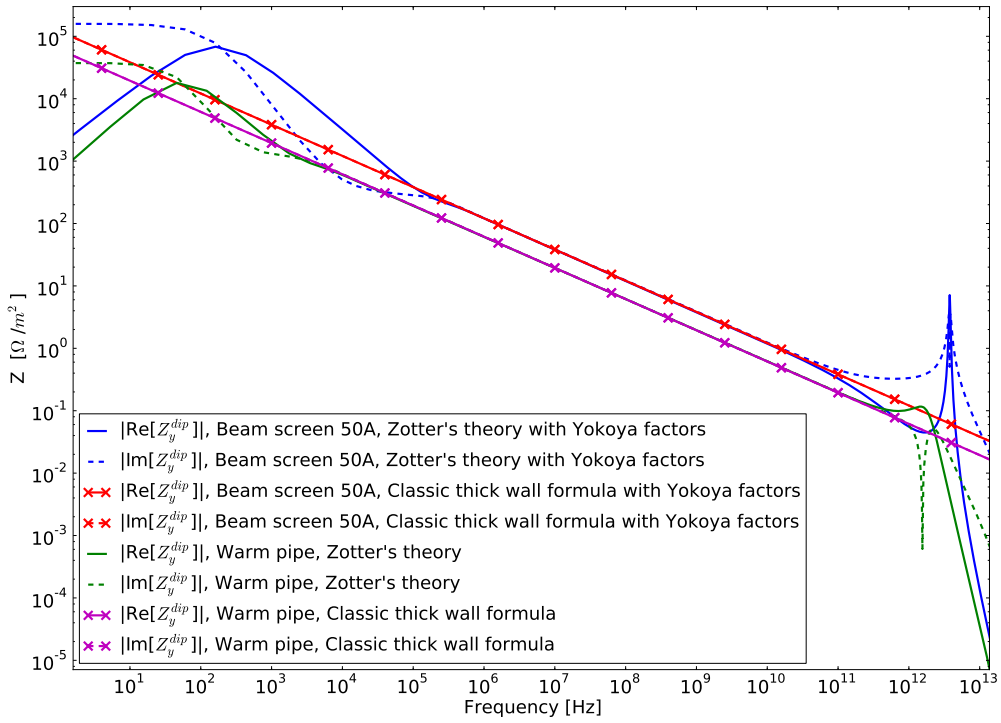

Figure 2.12: Vertical dipolar impedance, per unit length, of the beam screen of type 50A and the main part of the warm pipe (see Section 2.1.3). We used the parameters in Tables F.4, F.5, F.7 and F.8 at 7 TeV/c ($\gamma = 7460.52$). We compare the theory exposed in Section 1.4 and the classic thick wall formula, both with Yokoya factors in the case of the beam screen.

dipole module in the cleaning insertions IR3 and IR7), inside the MQW magnets (twin aperture warm quadrupole module in IR3 and IR7, with two different shapes – horizontal or vertical), and in the rest of the warm sections, taking out the part that is around the collimators which accounts for a cumulated length of 49.5 m per beam (see Tables F.1 and F.2). The pipe wall thickness is 2 mm [84, chap. 5, p. 98], and we assumed in the model that it is surrounded by infinite vacuum. Indeed, contrary to the collimator jaws and the beam screens (see previous sections), taking stainless steel behind the copper would give a slightly lower impedance at low frequencies, so we prefer to choose the most pessimistic approach. From Ref. [84, chap. 5, p. 98], the pipe's cross-section is circular except in the MQWs, where an elliptical shape is assumed (either vertical or horizontal).

Therefore, to compute the impedances we used the theory presented in Section 1.4 with two layers (copper and vacuum), using the copper material properties from Table F.4 and the Yokoya factors [23] of an elliptic shape for the MQWs (see Table F.8). Those factors are assumed to be reasonably valid in most of the frequency regime of interest, since the skin depth in the copper layer is below 2 mm for any frequency above 1 kHz.

We showed in Fig. 2.12 the vertical dipolar impedances per unit length of the warm vacuum pipe of radius 40 mm (by far the most present kind of pipe, see Table F.8), together with the classic thick wall approximation of Eq. (2.1) for a single layer of copper. This figure shows that from $\sim$ 1 kHz up to hundreds of GHz (well beyond the frequency spectrum of LHC bunches), the classic thick wall approximation is valid for this kind of pipe. Per unit length and at intermediate frequencies, the impedance is about half

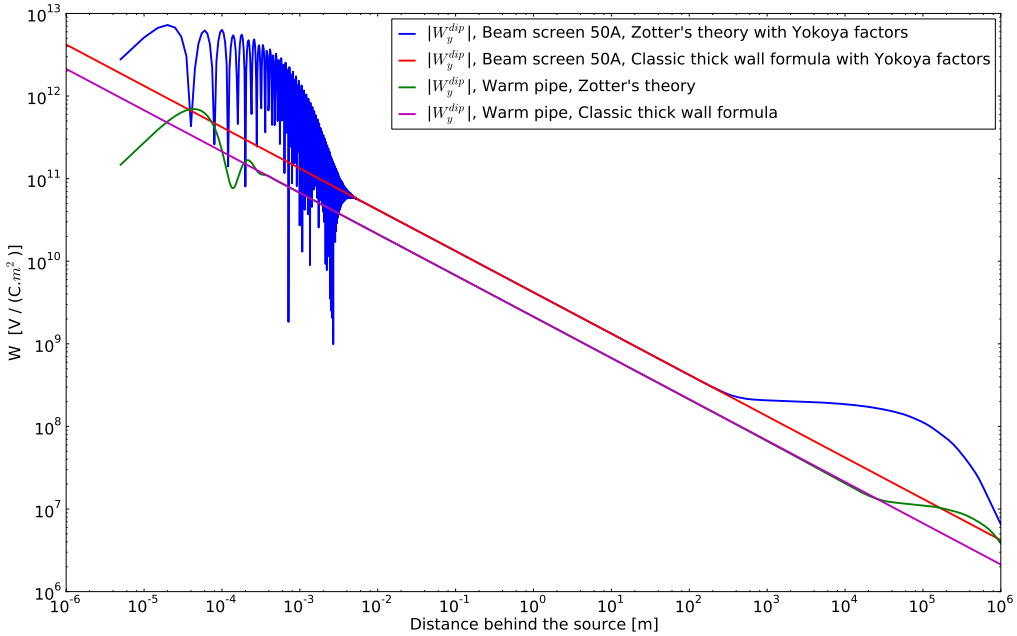

Figure 2.13: Vertical dipolar wake function, per unit length, of the beam screen of type 50A and the main part of the warm pipe (see Section 2.1.3). We used the parameters in Tables F.4, F.5, F.7 and F.8 at 7 TeV/c ($\gamma = 7460.52$). We compare the theory exposed in Section 1.4 and the classic thick wall formula, both with Yokoya factors in the case of the beam screen.

that of the beam scren of type 50A: the much higher resistivity of the warm copper with respect to the cold one of the beam screens, is compensated by a much larger radius. For the same kind of pipe, the dipolar vertical wake function (computed thanks to the approach of Section 1.6.3) is shown in Fig. 2.13, where one can see that the beam screen multiturn wake function per unit length (i.e. for a distance behind the bunch equal to the ring circumference of ~ 27 km) is much higher than the warm pipe one by about one order of magnitude .

2.2 Broad-band impedance model

Reference [84, chap. 5, p. 101] gives a first estimate of the broad-band impedance in the LHC. In the transverse plane, it is assumed to be an axisymmetric, dipolar and purely imaginary impedance, constant up to around the cut-off frequency f_r of the vacuum chamber (i.e. the frequency above which electromagnetic waves can propagate down the beam pipe). In longitudinal, the broad-band impedance is also purely imaginary and $\frac{Z_\parallel}{n}$ is also constant up to around f_r, with $n = \omega/\omega_{rev}$.
The cut-off frequency is obtained in principle from [93, slide 111]

$$f_r \approx 0.3\frac{c}{b}, \tag{2.18}$$

with b the half gap of the beam screens type 50A, covering most of the LHC circumference (see Table F.5). We get as in Ref. [84, chap. 5, p. 100], namely

$$f_r \approx 5 \text{ GHz}.$$

Then, the broad-band impedances and wakes functions are obtained thanks to a resonator model [93, slides 95-96], assuming a very low quality factor $Q = 1$

$$Z_x^{BB,dip}(\omega) = Z_y^{BB,dip}(\omega) = Z_\perp^{BB,dip}(\omega) = \frac{\omega_r}{\omega} \frac{R_\perp}{1 - jQ\left(\frac{\omega_r}{\omega} - \frac{\omega}{\omega_r}\right)}, \tag{2.19}$$

$$W_x^{BB,dip}(\tau) = W_y^{BB,dip}(\tau) = W_\perp^{BB,dip}(\tau) = \frac{\omega_r^2 R_\perp}{Q\overline{\omega}_r} e^{-\alpha\tau} \sin\left(\overline{\omega}_r \tau\right) \quad \text{for } \tau > 0, \quad (W_\perp^{BB,dip}(\tau) = 0 \text{ if } \tau < 0), \tag{2.20}$$

$$Z_\parallel^{BB}(\omega) = \frac{R_\parallel}{1 - jQ\left(\frac{\omega_r}{\omega} - \frac{\omega}{\omega_r}\right)}, \tag{2.21}$$

$$W_\parallel^{BB}(\tau) = \frac{\omega_r R_\parallel}{Q} e^{-\alpha\tau} \left[\cos\left(\overline{\omega}_r \tau\right) - \frac{\alpha}{\overline{\omega}_r} \sin\left(\overline{\omega}_r \tau\right)\right] \quad \text{for } \tau > 0 \quad (W_\parallel^{BB}(\tau) = 0 \text{ if } \tau < 0), \tag{2.22}$$

where the superscript "BB" stands for "broad-band", and with $R_\parallel$ the longitudinal shunt impedance (in Ω), $R_\perp$ the transverse one (in Ω/m), $\omega_r = 2\pi f_r$ the cut-off angular frequency, $\overline{\omega}_r = \omega_r \sqrt{1 - \frac{1}{4Q^2}}$ and $\alpha = \frac{\omega_r}{2Q}$.
With $Q = 1$, taking the limiting case $\frac{\omega}{\omega_r} << 1$ in Eq (2.19), it is clear that the value chosen for the transverse shunt impedance $R_\perp$ has to be the constant value of the imaginary part of the transverse impedance one wants to obtain below the cut-off frequency. In longitudinal, since the broad-band model gives a constant $\frac{Z_\parallel}{n}$, we see from Eq. (2.21) taken at the limit $\frac{\omega}{\omega_r} << 1$ that the value chosen for the longitudinal shunt impedance has to be $R_\parallel = \Im\left[\frac{Z_\parallel}{n}\right] \frac{\omega_r}{\omega_{rev}}$ (for $Q = 1$).
Using (as a first estimate) the broad-band model of Ref. [84, chap. 5, p. 101], which takes into account beam screens pumping slots, beam position monitors (BPM), shielded and unshielded bellows, vacuum valves, experimental chambers, RF cavities, Y-chambers, beam instrumentation other than BPM, space-charge and broad-band contributions from the collimators, giving

$$\Im\left[\frac{Z_\parallel}{n}\right] = 0.07\,\Omega \quad \text{and} \quad \Im[Z_\perp] = 1.34\ \text{M}\Omega/\text{m} \quad \text{for injection optics,} \tag{2.23}$$

$$\Im\left[\frac{Z_\parallel}{n}\right] = 0.076\,\Omega \quad \text{and} \quad \Im[Z_\perp] = 2.67\ \text{M}\Omega/\text{m} \quad \text{for squeezed optics,} \tag{2.24}$$

we get the shunt impedances as

$$R_\parallel = 31.1\ \text{k}\Omega \quad \text{and} \quad R_\perp = 1.34\ \text{M}\Omega/\text{m} \quad \text{for injection optics,} \tag{2.25}$$

$$R_\parallel = 33.8\ \text{k}\Omega \quad \text{and} \quad R_\perp = 2.67\ \text{M}\Omega/\text{m} \quad \text{for squeezed optics.} \tag{2.26}$$

Note that in the transverse plane those values have already been weighted (see Section 2.3.2) by the beta functions over the average beta functions from the smooth approximation (taken approximately as $< \beta^{smooth} > \sim 70$ m both in horizontal and vertical, see Appendix F.1). In the case of squeeze optics (i.e. optics with a lower beta at the interaction points), $\beta^* = 0.55$ m is assumed in both ATLAS and CMS

interaction points, which is not consistent with what is done for all the other elements for which we have chosen the case $\beta^* = 1.5$ m, corresponding to normal operation in 2011, at least until September (see Appendix F). Since lower β^* means higher beta functions on average, our broad-band impedance model for squeezed optics is probably slightly pessimistic for the 2011 situation.
In Fig. 2.14 we show the longitudinal (over n) and transverse broad-band impedances and wake functions obtained from Eqs. (2.19) to (2.22), when injecting the above values for the squeezed optics. We can see in Figs. 2.14a and 2.14c that $\frac{Z_\parallel}{n}$ and $Z_\perp$ are indeed constant and purely imaginary up to the cut-off frequency. In Figs. 2.14b and 2.14d the short-ranged nature of the broad-band wake functions appears clearly: it is significant only for a distance less than the bunch length (which is of the order of 0.36 m at 3.5 TeV/c).

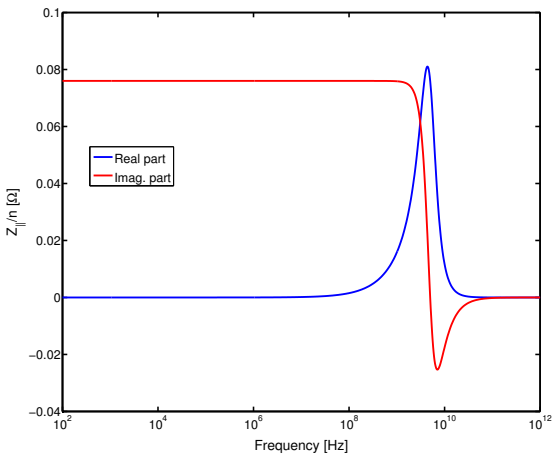

(a) Longitudinal impedance (over n).

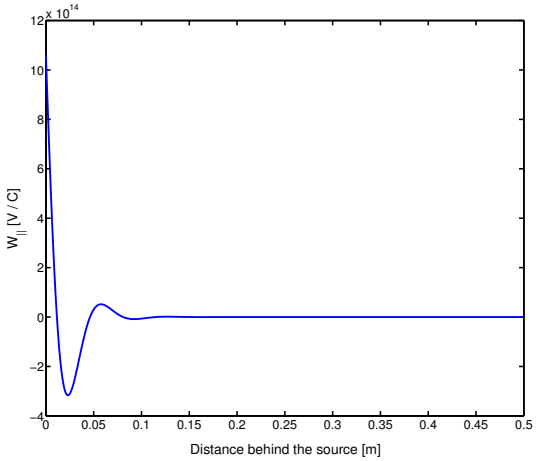

(b) Longitudinal wake function.

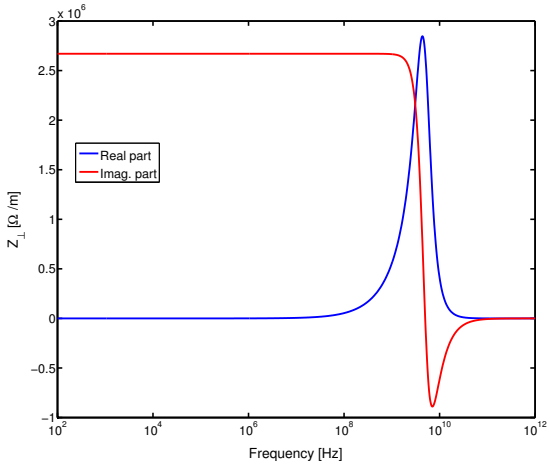

(c) Transverse dipolar impedance.

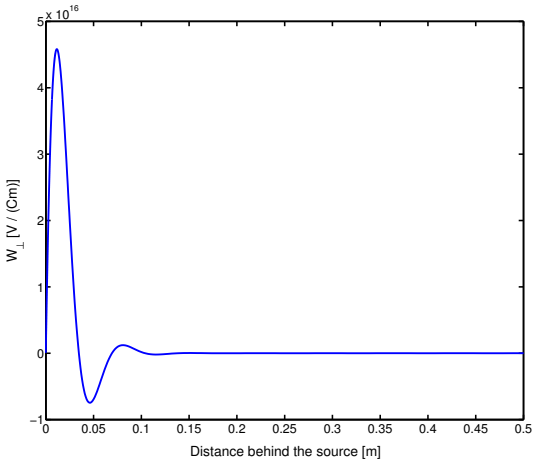

(d) Transverse dipolar wake function.

Figure 2.14: Broad-band impedances and wake functions at squeezed optics ($\beta^* = 0.55$m at CMS and ATLAS interaction points).

2.3 Summing the element contributions into a single-kick model

The previous sections showed how we obtained the impedances and wake functions of each machine element considered in the impedance model. Those individual impedances and wakes need now to be assembled into a single model for the full machine. We will here first make a few reminders about linear dynamics of individual particles in an accelerator, before explaining how we weight and sum all impedance contributions into a single-kick model, i.e. impedances or wake functions applied only once per turn in a certain point of the ring.

2.3.1 Some reminders on 2D linear beam dynamics in the transverse plane

For a given particle of cartesian coordinates $\big(x(t), y(t), s(t)\big)$, the equation of motion in the particle accelerator is governed by Newton's second law of motion, namely:

$$\frac{d\vec{p}}{dt} = \vec{F} \tag{2.27}$$

where $\vec{p}$ is the momentum and $\vec{F}$ the total force acting on the particle. In the framework of special relativity, one gets in the horizontal plane, with m_0 the rest mass of the particle:

$$F_x = m_0\gamma\frac{dv_x}{dt} = m_0\gamma\frac{dv_x}{ds}\frac{ds}{dt} \approx m_0\gamma v\frac{d}{ds}\left(\frac{dx}{dt}\right) \approx m_0\gamma v^2 x'', \tag{2.28}$$

with $x'' = \frac{d^2x}{ds^2}$, and γ and v defined as in Chapter 1 (respectively relativistic mass factor and velocity along the orbit). Note that we assumed that there is no energy deviation from the design energy, and that $\frac{ds}{dt} \approx v$, which is strictly speaking the case only if the orbit on which the particle is travelling is exactly the design (or reference) orbit along which the longitudinal coordinate s is constructed. More rigourous calculations [102] show that the above equation can be obtained as a linearization of the exact equation of motion of a particle following an orbit a priori different from the design one.
We neglect then the weak focusing from the dipoles [102], and we assume that $\vec{F}$ comes only from the linear (transverse) magnetic field in the quadrupoles around the ring and that there is no skew quadrupoles so no coupling ($\frac{\partial B_x}{\partial x} = \frac{\partial B_y}{\partial y} = 0$ [102]), so we write $\vec{F}$ as (neglecting transverse velocities with respect to the longidutinal one v)

$$\vec{F} = qv\left(-B_y\vec{e_x} + B_x\vec{e_y}\right) = -qv\left(\frac{\partial B_y}{\partial x}x\vec{e_x} - \frac{\partial B_x}{\partial y}y\vec{e_y}\right) = -qv\frac{\partial B_y}{\partial x}\left(x\vec{e_x} - y\vec{e_y}\right),$$

with q the particle charge, and where the last equality was obtained from Maxwell equation $\vec{\text{curl}}\vec{B} = 0$ (the field is static in the magnets). In the above, $\frac{\partial B_y}{\partial x}$ is the constant gradient in the quadrupoles. We can then obtain the well-known equation of motion [102]

$$x'' + K(s)x = 0, \tag{2.29}$$

with

$$K(s) \equiv \frac{-F_x}{m_0\gamma v^2 x} = \frac{q}{p_0}\frac{\partial B_y}{\partial x},$$

where $p_0 \equiv m_0 \gamma v$ is the momentum of the particles.
Equation (2.29) is a Floquet differential equation since $K(s)$ is periodic of period the ring circumference. In Ref. [102] one proves that the general solution is an oscillation around the design orbit $x(s) = 0$, called betatron oscillation, which can be written

$$x(s) = \sqrt{\varepsilon_x \beta_x(s)} \cos\left(\mu_x(s) - \mu_{x0}\right), \tag{2.30}$$

where $\beta_x(s)$ is a positive and periodic function called the horizontal beta function (of periodicity the ring circumference), $\mu_x(s) = \int_{s_0}^{s} \frac{\mathrm{d}\sigma}{\beta_x(\sigma)}$ is the phase function, and ε_x the constant single-particle horizontal emittance. A very similar equation can be written for the vertical coordinate of the particle:

$$y(s) = \sqrt{\varepsilon_y \beta_y(s)} \cos\left(\mu_y(s) - \mu_{y0}\right), \tag{2.31}$$

with similar definitions of $\beta_y(s)$, $\mu_y(s)$ and ε_y.
We can note here that an additional external force $\vec{F}^{ext}$ (such as the wake fields from other particles) can be added to Eq. (2.29) quite easily thanks to Eq. (2.28):

$$x'' + K(s)x = \frac{F_x^{ext}}{m_0 \gamma v^2}. \tag{2.32}$$

The tune is defined as the total phase over a full circumference divided by 2π, and represents the number of betatron oscillations done by the particle, per turn:

$$Q_x = \frac{1}{2\pi} \int_{s_0}^{s_0+C} \frac{\mathrm{d}s}{\beta_x(s)} \qquad \text{and} \qquad Q_y = \frac{1}{2\pi} \int_{s_0}^{s_0+C} \frac{\mathrm{d}s}{\beta_y(s)}, \tag{2.33}$$

where C is the machine circumference. Note that the tunes are independent on the location s_0 at which the integral is computed (from the periodicity of the beta functions).
Two important properties need to be emphasized concerning the beta functions:

- from Eqs. (2.30) and (2.31), the particles transverse coordinates around the ring are proportional to the square root of the beta functions,
- if a kick (i.e. an instantaneous transverse momentum change) is given to all particles every turn at the same location s_0 around the ring (due for instance to a dipole field error), the new closed orbit around which particles will perform betation oscillations will be different from $x(s) = 0$ and will be proportional to the square root of the beta functions at the position of the kick [103, slide 7]. This means that the square root of the beta function at a certain location around the ring measures the "sensitivity" of the beam to a kick at this location, or in other words the amplitude of the effect of any transverse kick around the ring is likely to be proportional to the square root of the beta function at the kick position.

2.3.2 Weighting by the beta functions

The most intuitive way to use in a tracking program all the wake functions computed for individual machine elements would be to track a particle around the ring in such a way that at each location where one of those elements is present, the wake fields coming from particles ahead of the particle tracked should be applied through a kick. However, depending on the number of elements to be taken into

account, this could be very time consuming as the ring would have to be subdivided into as many parts as there are locations with elements creating impedances. Also, such an accurate tracking seems somehow irrelevant because the effects of wake fields begin to appear usually on a slow basis (after several hundreds or thousands of turns), meaning that an "averaged" tracking at each turn should be sufficient. One widespread way to simplify the tracking is therefore to consider that all the wake functions are concentrated at a single location around the ring, and we only need to apply one kick there and track the particle for the full turn, which decreases a lot the number of operations to be performed each turn. To assemble all the wake functions and apply them at a single location, an heuristic approach is to consider that as far as the wake functions and their effects are concerned, the only significant parameters that depend on the location of a machine element, are the beta functions. Indeed, according to what was said in the previous section, the particles transverse coordinates are proportional to the square root of the beta functions, and the total transverse wake functions as well since they are proportional to those coordinates when we neglect constant and nonlinear terms (see e.g. Sections 1.4.6 and 1.5.6). Moreover, the effect of a kick being also proportional to the square root of the beta function in the direction of the kick (see previous section), the square root of the beta function appears twice.
In other words, to get the effect at a given location around the ring, of a certain transverse wake function due an element located elsewhere, we have to weight it by the square root of the beta function at its real location, in the same direction as the source (or test) particle coordinate it is multiplied by, times the square root of the beta function at its real location in the direction of the wake component considered, all of this being divided by the same beta functions taken at the point where the kick is applied. In doing so we totally neglect the effect of the phase advance between different locations. Note that we can take any point around the ring as the final kick location, so any value for the beta functions there. Therefore, without loss of generality we can consider that at the point chosen the beta functions have the values coming from the smooth approximation (see Appendix F.1). The final weighting formulae are then

$$W_x^{Wall,dip} = \sum_j \frac{\beta_x(s_j)\, W_{j,x}^{Wall,dip}}{<\beta_x^{smooth}>}, \qquad W_y^{Wall,dip} = \sum_j \frac{\beta_y(s_j)\, W_{j,y}^{Wall,dip}}{<\beta_y^{smooth}>}, \tag{2.34}$$

$$W_x^{Wall,quad} = \sum_j \frac{\beta_x(s_j)\, W_{j,x}^{Wall,quad}}{<\beta_x^{smooth}>}, \qquad W_y^{Wall,quad} = \sum_j \frac{\beta_y(s_j)\, W_{j,y}^{Wall,quad}}{<\beta_y^{smooth}>}, \tag{2.35}$$

$$W_{xy}^{Wall,dip} = \sum_j \frac{\sqrt{\beta_x(s_j)\beta_y(s_j)}\, W_{j,xy}^{Wall,dip}}{\sqrt{<\beta_x^{smooth}><\beta_y^{smooth}>}}, \qquad W_{xy}^{Wall,quad} = \sum_j \frac{\sqrt{\beta_x(s_j)\beta_y(s_j)}\, W_{j,xy}^{Wall,quad}}{\sqrt{<\beta_x^{smooth}><\beta_y^{smooth}>}}, \tag{2.36}$$

where $<\beta_x^{smooth}>$ (resp. $<\beta_y^{smooth}>$) is the average beta function in x (resp. y) from the smooth approximation, and where the sums run over all the impedance contributors j located at s_j, for which the individual wake functions are $W_{j,x}^{Wall,dip}$, $W_{j,x}^{Wall,quad}$, etc. Note that for the coupling terms one has to weight by the square root of the beta functions in both directions: one for the component of the wake considered, and the other for the transverse coordinate this term is multiplied by. Also, for the transverse constant terms (not considered here), only one beta function square root would have to be applied as the weighting factor. No weighting has to be done in longitudinal, and simply summing all the longitudinal wake functions provides the total longitudinal model.
An important remark is that in doing this weighting we assumed a purely 2D motion, i.e. no linear coupling between x and y. Different formulae should be used in the case of linear coupling [104].

Finally, the same weighting procedure can be applied to impedances, to get the total impedance model that can be used in instability theories such as Sacherer's [5] or Laclare's [6] ones, that are also essentially applying impedances of the full ring at a single location. We obtain:

$$Z_x^{Wall,dip} = \sum_j \frac{\beta_x(s_j)\, Z_{j,x}^{Wall,dip}}{<\beta_x^{smooth}>}, \qquad Z_y^{Wall,dip} = \sum_j \frac{\beta_y(s_j)\, Z_{j,y}^{Wall,dip}}{<\beta_y^{smooth}>}, \tag{2.37}$$

$$Z_x^{Wall,quad} = \sum_j \frac{\beta_x(s_j)\, Z_{j,x}^{Wall,quad}}{<\beta_x^{smooth}>}, \qquad Z_y^{Wall,quad} = \sum_j \frac{\beta_y(s_j)\, Z_{j,y}^{Wall,quad}}{<\beta_y^{smooth}>}, \tag{2.38}$$

$$Z_{xy}^{Wall,dip} = \sum_j \frac{\sqrt{\beta_x(s_j)\beta_y(s_j)}\, Z_{j,xy}^{Wall,dip}}{\sqrt{<\beta_x^{smooth}><\beta_y^{smooth}>}}, \quad Z_{xy}^{Wall,quad} = \sum_j \frac{\sqrt{\beta_x(s_j)\beta_y(s_j)}\, Z_{j,xy}^{Wall,quad}}{\sqrt{<\beta_x^{smooth}><\beta_y^{smooth}>}}, \tag{2.39}$$

This way of weighting the impedances, used originally in Refs. [105, 106], has been rigorously proven by Scott Berg [107].

2.3.3 Total impedances and wake functions in the LHC

In the final model, we took into account all the collimators calculated in Section 2.1.1, all the beam screens from Section 2.1.2 and all the warm sections of the vacuum pipe from Section 2.1.3, summing all these contributions thanks to the formulae of Section 2.3.2 and the beta functions that can be found in Appendix F, Tables F.1, F.2, F.6 and F.9, taking the values from Eqs. (F.3) (at injection energy) or (F.4) (at collision energies) as the beta functions at the location of the final kick. We neglect the rather small constant term in the transverse impedances of the asymmetric TCDQs. The broad-band model of Section 2.2 (already weighted by the beta functions) is then added to the full model.
The full transverse impedance model obtained this way is plotted at injection energy in Fig. 2.15a, and at 3.5 TeV/c in Fig. 2.15b. The corresponding wake functions are respectively in Figs. 2.15c and 2.15d. In these plots are showns all the components of the transverse impedances or wake functions (dipolar, quadrupolar and coupled terms), excluding only the constant transverse impedances from the TCDQs. It appears that both for the impedances and the wake functions, the dipolar terms are dominant with respect to the quadrupolar terms and even more with respect to the coupled terms.
The longitudinal impedance has been calculated as well and is shown in Figs. 2.16a and 2.16b, but it will be neglected in the simulations performed in the following chapters.
It is of interest to know the respective contributions of each element around the LHC, in terms of percentage of the total impedance or wake functions versus frequency or distance behind the source, taking into account the weighting by the beta functions when calculating each contribution. This is shown for the vertical dipolar impedance in Fig. 2.17, for the vertical dipolar wake in Fig. 2.18, and for the longitudinal impedance in Fig. 2.19.
These plots show that the beam screen contribution is the dominant one at low frequencies and for the long-ranged wake functions. This is particularly true for the real part of the impedances, up to more than 10 kHz. At intermediate frequencies and distances, the collimators are dominant in the transverse plane, and this is more the case at 3.5 TeV/c than at injection. In longitudinal, the different contributions of the warm vacuum pipe, the beam screens and the collimators are almost equal at intermediate frequencies. Finally, at high frequencies the broad-band impedance dominate, above a few GHz for the real part of the impedances, above ~ 100 MHz for the imaginary part of the vertical dipolar impedances, and above

~ 10 MHz for the imaginary part of the longitudinal impedance.
Note finally that the repartition of the contributions to the horizontal dipolar impedance and wake function (not represented here) is very similar to the vertical case.

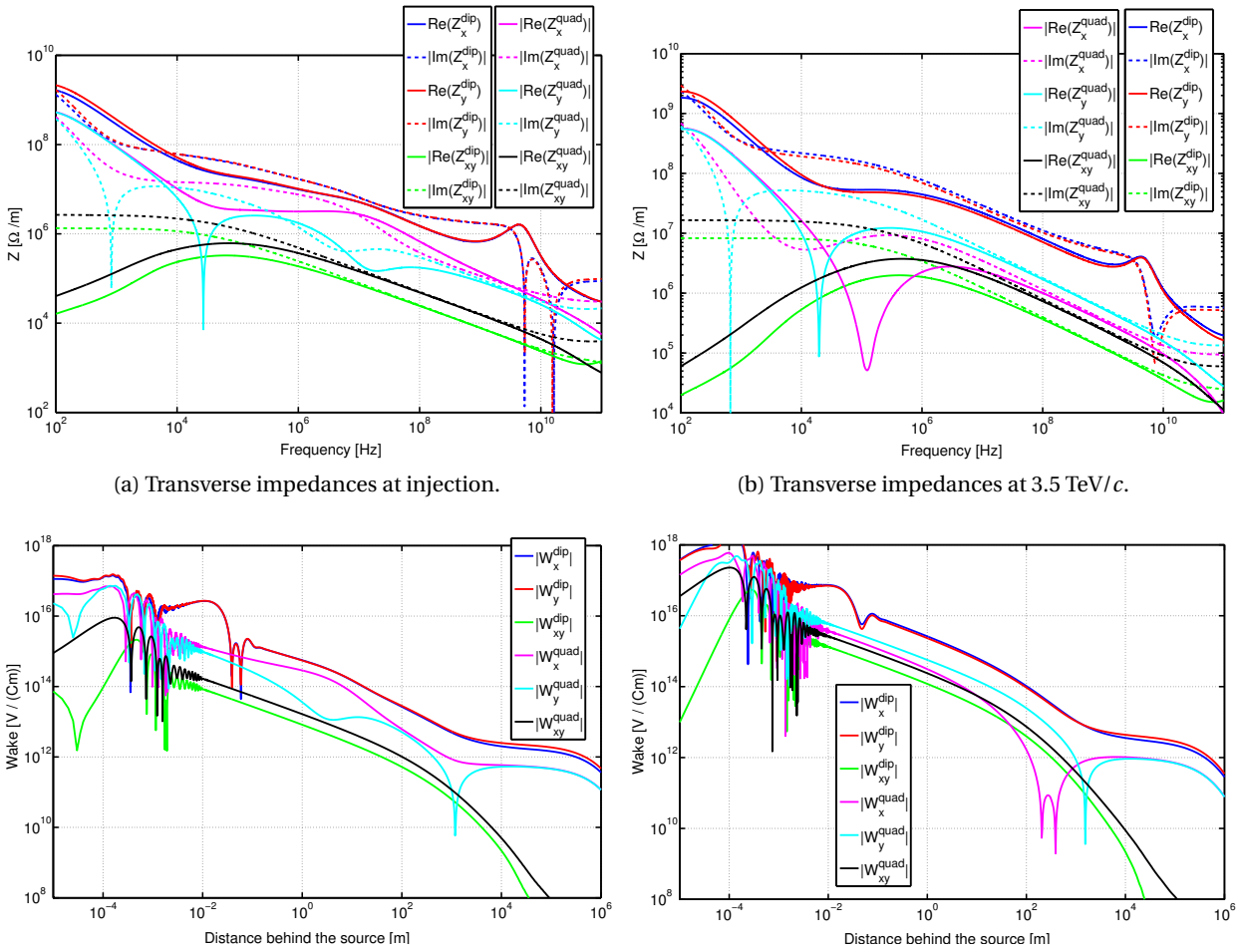

(a) Transverse impedances at injection.

(b) Transverse impedances at 3.5 TeV/c.

(c) Transverse wake functions at injection.

(d) Transverse wake functions at 3.5 TeV/c.

Figure 2.15: The LHC impedance and wake function model in the transverse plane (beam 1).

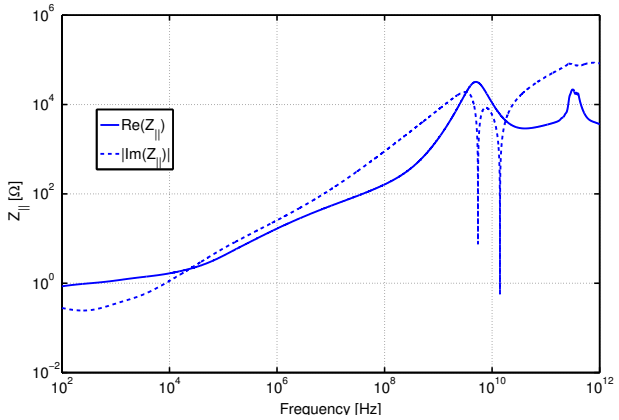

(a) Longitudinal impedance at injection.

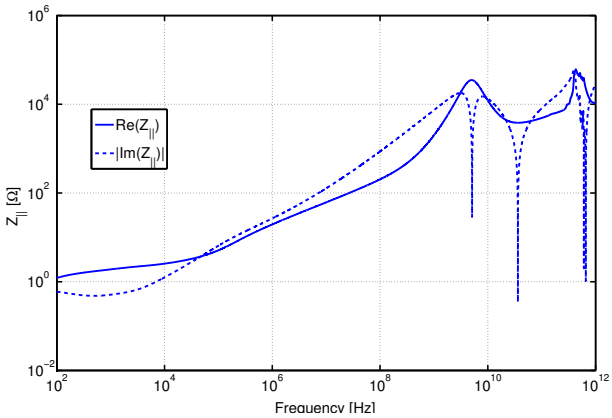

(b) Longitudinal impedance at 3.5 TeV/c.

Figure 2.16: The LHC impedance model in longitudinal (beam 1).

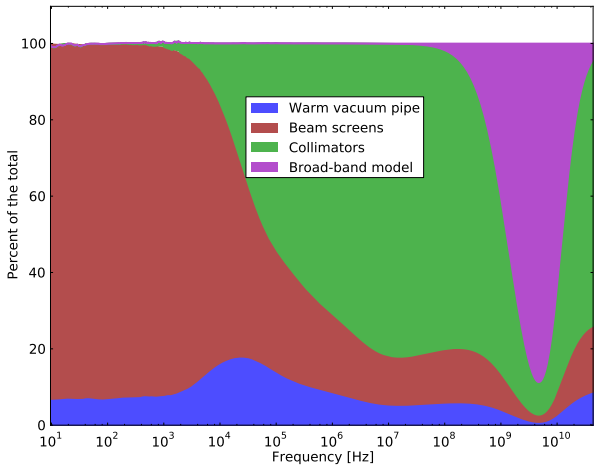

(a) At injection, real part.

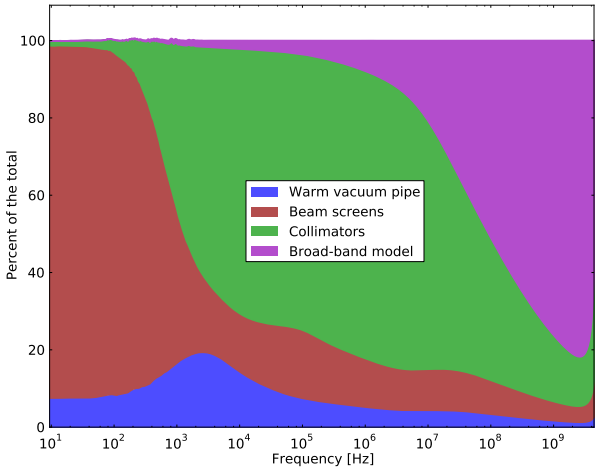

(b) At injection, imaginary part.

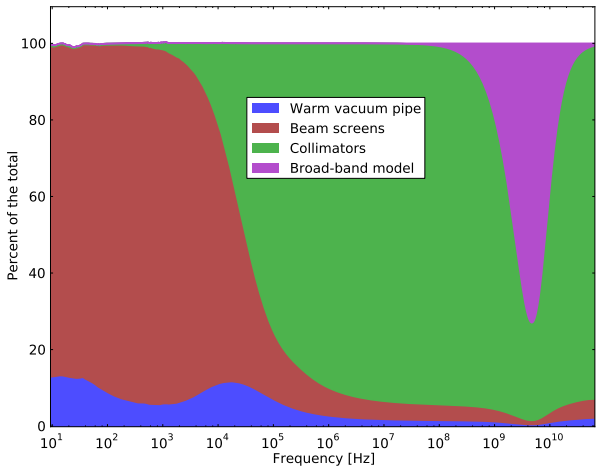

(c) At 3.5 TeV/c, real part.

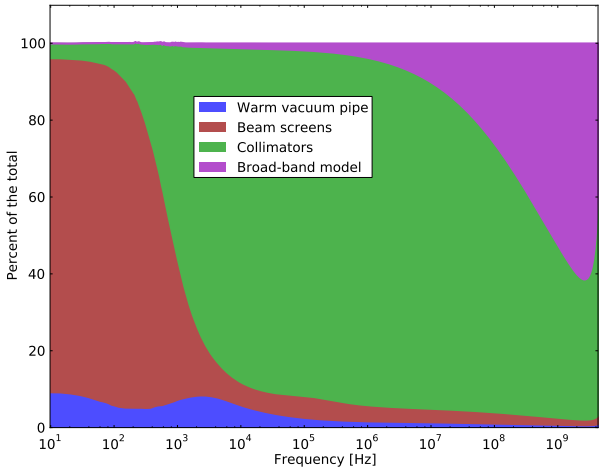

(d) At 3.5 TeV/c, imaginary part.

Figure 2.17: Repartition of the various contributions to the LHC total vertical dipolar impedance.

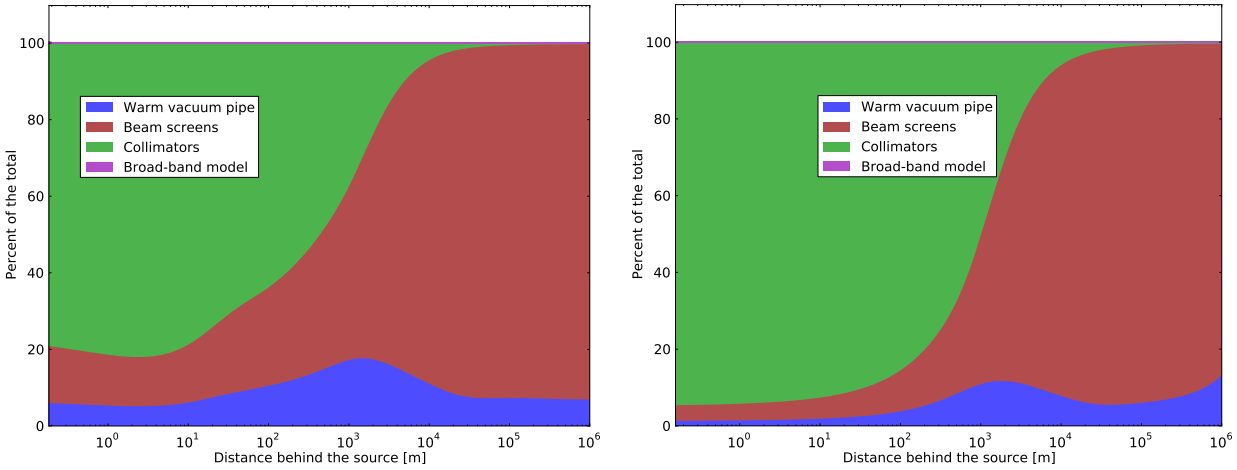

(a) At injection.

(b) At 3.5 TeV/c.

Figure 2.18: Repartition of the various contributions to the LHC total vertical dipolar wake function.

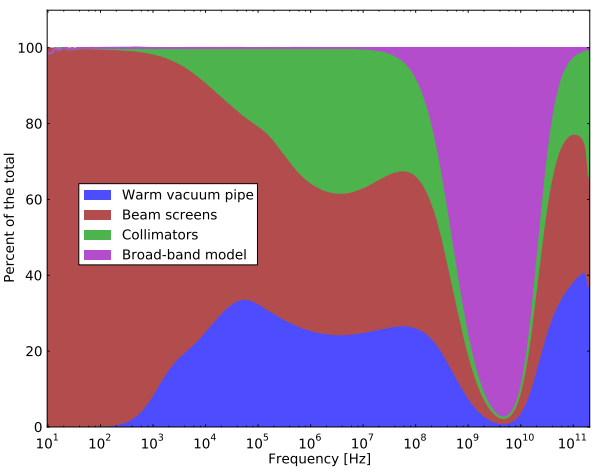

(a) At injection, real part.

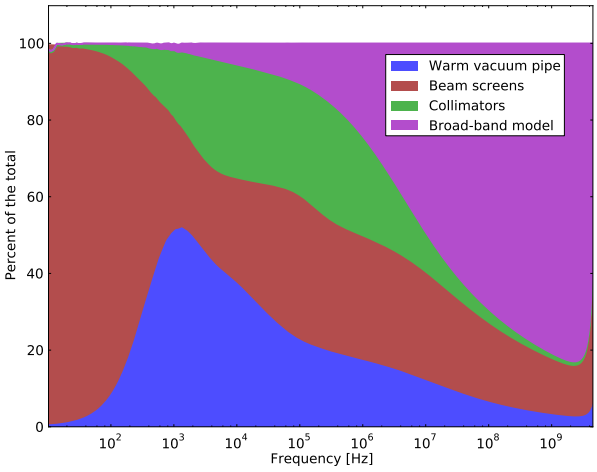

(b) At injection, imaginary part.

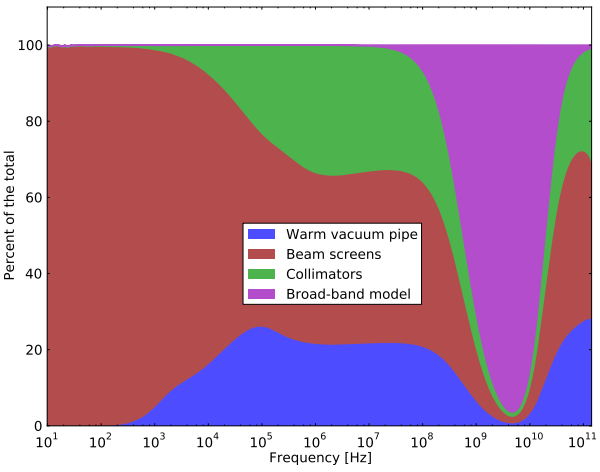

(c) At 3.5 TeV/c, real part.

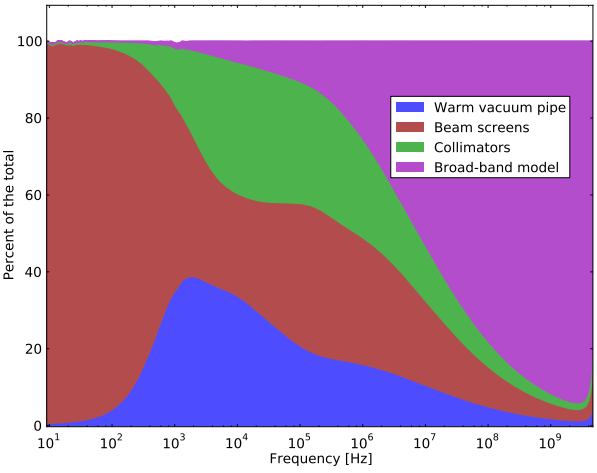

(d) At 3.5 TeV/c, imaginary part.

Figure 2.19: Repartition of the various contributions to the LHC total longitudinal impedance.

2.4 Conclusion

In this chapter we have fully described the impedance and wake functions model we use for the LHC. We took into account the wall impedances of all the collimators, of the beam screens and of the warm part of the vacuum pipe. For the collimators, to compute the impedances we used extensively the new flat chamber theory presented in Section 1.5, benchmarking it with the usual approach consisting in applying constant form factors to the results of an axisymmetric theory. For the beam screens and warm part of the pipe we got the impedances thanks to Zotter's theory with Yokoya factors, using the approach of Section 1.4, in particular the matrix formalism that speeds up the computations by at least two orders of magnitude, with respect to previous implementations of Zotter's formalism [76]. The wake functions of all these impedances were computed thanks to the technique of Section 1.6.3 that proved to be efficient and accurate.
Finally, to these wall impedances was added a broad-band impedance model from the LHC design report [84], as a first estimate of geometrical and short-ranged wake fields.
The full LHC wake function and impedance model can be computed in a few hours time for any collimator settings, any of the two beams, and at injection, intermediate (3.5 TeV/c) or top (7 TeV/c) energy. With settings used during the physics runs in 2011, the long-ranged wake functions (and low frequency impedances) are dominated by the ones of the beam screens, the intermediate range by the collimators, while the high frequency impedances are dominated by the broad-band contributions.

3 A new simulation tool for coupled-bunch impedance-related instabilities

Transverse coupled-bunch instabilities occur in general when several bunches interact with the machine impedance, creating some wake fields that act back on the bunch train in such a way as to give rise to an exponentially growing oscillation. The ability to compute the complex tune shift associated to such instabilities is critical for the machine operation, as one wants to make sure that the means installed in the machine to prevent such instabilities – typically the transverse feedback and/or octupoles providing Landau damping – are sufficient to suppress them.
To evaluate the rise times of such instabilities, several theories exist, such as those from Sacherer [5, 59], Laclare [6] and Scott Berg [107], as well as a macroparticle simulation code, MTRISM [81]. The latter has several limitations, in particular the absence of quadrupolar impedance, the impossibility to load wake functions tables which can reflect the complexity of the machine impedance, and the rigid bunch approximation for the wake fields computation. All the theories cited rely on strong assumptions: Sacherer's formula assumes certain predefined eigenvectors, i.e. predefined intrabunch oscillation modes; both Sacherer's and Laclare's formalisms assume a machine entirely filled with equidistant bunches, which is not the case in the LHC; Sacherer's formalism also assumes no transverse mode coupling. On the other hand Scott Berg's theory is much more general and includes in principle lattice non-linearities, chromaticity, mode coupling, and any kind of bunch filling scheme. Still, wake fields from a cylindrical structure are assumed there, which is a strong asumption in many machines with non axisymmetric elements, in particular in the case of the LHC (see Chapter 2); also in practical cases this very general theory has been simplified to study only equidistant bunches, which is again too restrictive. Implementation of the full theory seems a quite challenging task.
Therefore, to be able to study multibunch instabilities due to wake fields, the most straightforward and general way was to extend the single-bunch code HEADTAIL [3, 4]. A first simplified version, accounting only for rigid bunch oscillations with no longitudinal motion, was already developped in Ref. [108]. We present here a new extension that can in principle handle multibunch behaviour without neglecting intrabunch motion.

3.1 Algorithm

HEADTAIL is a macroparticle simulation code where each individual macroparticle i is tracked through a ring subdivided into several kick sections. The macroparticles' transverse positions (x_i, y_i) and their derivatives (x_i', y_i') with respect to s (the curvilinar coordinate along the ring) are initialized according to Gaussian distributions, while their longitudinal position in the bunch z_i and their relative momentum

deviation $\delta_i = \frac{p_i - p_0}{p_0}$ (with p_0 the reference momentum and p_i the momentum of the macroparticle i) can have either Gaussian or uniform distribution, confined to a certain bunch length in the latter case. The longitudinal components can also be confined to a linear or nonlinear bucket – all those different possible options are set in input. Then, one simulates the collective behaviour of the macroparticles around the ring in the following way:

1. At each kick section, every bunch (which all contain the same number of elementary particles) is sliced longitudinally according to a predefined number of slices n_{sl}, all of them having the same thickness. The average offsets (x_S, y_S) from the beam orbit and the number of elementary particles (protons or electrons) n_S in each slice S are computed. The slicing goes up to a given number of σ_z (RMS standard deviation) of the longitudinal distribution (typically from $-2\sigma_z$ to $+2\sigma_z$, which is what we will always choose here), i.e. all macroparticles out of this extension are not part of the slices so do not give or receive any wake fields kicks, but are still transported through the lattice.

2. Then, at the same kick section, each macroparticle receives a kick in all three directions, i.e. $\Delta x'_i$ is added to x'_i, $\Delta y'_i$ to y'_i and $\Delta\delta_i$ to δ_i, with[1]

$$\begin{aligned}
\Delta x'_i &= \frac{e^2}{m_0 \gamma v^2} \sum_{z_S > z_{S_i}} n_S W_x\left(z_S - z_{S_i}, x_S, y_S, x_{S_i}, y_{S_i}\right), \\
\Delta y'_i &= \frac{e^2}{m_0 \gamma v^2} \sum_{z_S > z_{S_i}} n_S W_y\left(z_S - z_{S_i}, x_S, y_S, x_{S_i}, y_{S_i}\right), \\
\Delta\delta_i &= -\frac{e^2}{m_0 \gamma v^2} \sum_{z_S \geq z_{S_i}} n_S W_{||}\left(z_S - z_{S_i}\right),
\end{aligned} \tag{3.1}$$

   with the same conventions as in the previous chapters (v is the beam velocity, γ its relativistic mass factor, m_0 the rest mass of the elementary particles), and with e the elementary charge, S_i the slice containing the macroparticle i, and z_S the longitudinal position of each slice (the reference being the first slice of the first bunch, at the head of the bunch train, with decreasing z when going toward the tail of the bunches). In the above expressions the sums run over all slices and bunches before the slice of the macroparticle considered, neglecting thus any possible wake in front of any given slice (which is an ultrarelativistic approximation). The sum continues up to a certain number of turns, n_{wake} (specified in input), i.e. the wakes of preceding turns are taken into account. $W_{||}(z)$ is the longitudinal wake function, while $W_x(z)$ and $W_y(z)$ are the total transverse wake functions given by (see previous chapters)

$$W_x(z, x_S, y_S, x_{S_i}, y_{S_i}) = W_x^{dip}(z) x_S + W_{xy}^{dip}(z) y_S + W_x^{quad}(z) x_{S_i} + W_{xy}^{quad}(z) y_{S_i}, \tag{3.2}$$

$$W_y(z, x_S, y_S, x_{S_i}, y_{S_i}) = W_y^{dip}(z) y_S + W_{xy}^{dip}(z) x_S + W_y^{quad}(z) y_{S_i} + W_{xy}^{quad}(z) x_{S_i}, \tag{3.3}$$

   where the superscript dip stands for "dipolar wake" and $quad$ for "quadrupolar wake". Note that the coupled terms (linear wakes in the x direction but proportional to the y position, and vice versa) are taken into account. The wake functions above ($W_x^{dip}(z)$, $W_x^{quad}(z)$, etc.) are provided

[1] In transverse, these expressions can be found by integrating Eq. (2.32), without the focusing term, over the length of an element creating the wake function, with the force expressed thanks to Eqs. (1.219) and (1.220) summed over the slices that are before the particle considered (taking $q = e$ and $Q = en_S$), and replacing $\int^L \mathrm{d}s x''(s)$ by $\Delta x'_i$ and $\int^L \mathrm{d}s y''(s)$ by $\Delta y'_i$. In longitudinal, one can obtain the result directly from Eq. (2.27), with the same procedure (note the sign change, due to Eq. (1.218)).

in a table given in input, and should contain the single-kick model of the machine, so weighted by the actual beta functions around the ring if several machine elements are considered (see Section 2.3.2). When there are several kick sections per turn, the single-kick wake functions are simply divided by the number of kick sections.
The sums in Eqs. (3.1) are quite time consuming for large number of slices, of bunches and/or of preceding turns taken into account, so we actually replace them by sums where contiguous slices (or even bunches) are grouped together when the wake functions do not change by more than 0.1% inside one group, which is usually the case for large distances from the macroparticle i. The groups of slices (or bunches) such defined are considered as single slices for the sums in Eqs. (3.1), meaning that the wake functions are computed only for one distance $z_S - z_{S_i}$ (taken as the average of the $z_S - z_{S_i}$ of all the slices of the group). To know how to form such groups of slices (or bunches) where the wake do not changes by more than 0.1%, once at the beginning of the simulation we scan the full wake functions and identify distances such that in-between them the wakes do not change by more than this value.

3. The transverse components of each macroparticle are transported to the next kick section with a 4D linear map (including coupling), assuming that at each kick section the beta functions β_x and β_y (see Section 2.3.1) are at an extremum and all equal, therefore taking into account only the phase advance between the kick sections and the beta functions. The chromaticity and the transverse amplitude detuning due to the octupoles are included by modifying for each macroparticle the phase advances μ_x and μ_y from this kick section to the next, according to the momentum deviation and transverse components of the macroparticle:

$$\mu_x = \frac{2\pi}{n_{kick}}\left(Q_x + Q'_x\delta_i + a_x J_{x,i} + a_{xy} J_{y,i}\right), \quad \mu_y = \frac{2\pi}{n_{kick}}\left(Q_y + Q'_y\delta_i + a_{xy} J_{x,i} + a_y J_{y,i}\right) \tag{3.4}$$

with n_{kick} the number of kick sections per turn, and Q'_x (resp. Q'_y) the derivative of the horizontal (resp. vertical) tune with respect to the momentum deviation δ. The action variables are defined as $J_{x,i} \equiv \frac{\varepsilon_{x,i}}{2} = \frac{x_i^2+\beta_x^2 x_i'^2}{2\beta_x}$ and $J_{y,i} \equiv \frac{\varepsilon_{y,i}}{2} = \frac{y_i^2+\beta_y^2 y_i'^2}{2\beta_y}$ [109], with $\varepsilon_{x,i}$ and $\varepsilon_{y,i}$ the single particle emittances from Eqs. (2.30) and (2.31) and assuming again a zero derivative with respect to s of the beta functions. The coefficients a_x, a_{xy} and a_y represent the detuning due to the octupoles and are obtained through [109]

$$\begin{aligned} a_x &= \frac{3}{8\pi}\int_{s_0}^{s_0+C} \mathrm{d}s\beta_x^2(s)\frac{O_3(s)}{\frac{p_0}{e}}, & a_y &= \frac{3}{8\pi}\int_{s_0}^{s_0+C} \mathrm{d}s\beta_y^2(s)\frac{O_3(s)}{\frac{p_0}{e}}, \\ a_{xy} &= -\frac{3}{4\pi}\int_{s_0}^{s_0+C} \mathrm{d}s\beta_x(s)\beta_y(s)\frac{O_3(s)}{\frac{p_0}{e}}, \end{aligned} \tag{3.5}$$

where C is the machine circumference and $O_3 \equiv \frac{1}{6}\frac{\partial^3 B_y}{\partial x^3}$ the octupolar strength. In the specific case of the LHC, they are two kinds of octupoles, focusing and defocusing, with different beta functions and polarities, such that [110]

$$a_x = \frac{3e}{8\pi p_0}\left(N_{oct}^F \beta_x^{F2} O_3^F l + N_{oct}^D \beta_x^{D2} O_3^D l\right), \qquad a_y = \frac{3e}{8\pi p_0}\left(N_{oct}^F \beta_y^{F2} O_3^F l + N_{oct}^D \beta_y^{D2} O_3^D l\right),$$

$$a_{xy} = -\frac{3e}{4\pi p_0}\left(N_{oct}^F \beta_x^F \beta_y^F O_3^F l + N_{oct}^D \beta_x^D \beta_y^D O_3^D l\right),$$

with $l = 0.32$ m [111] the length of the octupole magnets, $\beta_x^F = 175.5$ m, $\beta_y^F = 33.6$ m, $\beta_x^D = 30.1$ m, $\beta_y^D = 178.8$ m (from MAD-X with the LHC optics – see Appendix F.1; those values are independent on the beam or the squeeze), $N_{oct}^F = N_{oct}^D = 84$ [111, p. 84] the number of focusing and defocusing octupoles[2], and with the octupolar strength given in T.m^{-3} by [110] $O_3^F = 63100\frac{I_{oct}^F}{550}$ and $O_3^D = -63100\frac{I_{oct}^D}{550}$ where I_{oct}^F and I_{oct}^D are the currents (in A) in the focusing and defocusing octupoles (the maximum being 550 A in the LHC). In the end, one obtains for the LHC (in m^{-1})

$$a_x \approx \frac{7000}{p_0[\text{GeV}/c]}\left(267065\frac{I_{oct}^F[\text{A}]}{550} - 7856\frac{I_{oct}^D[\text{A}]}{550}\right), \quad a_y \approx \frac{7000}{p_0[\text{GeV}/c]}\left(9789\frac{I_{oct}^F[\text{A}]}{550} - 277203\frac{I_{oct}^D[\text{A}]}{550}\right),$$

$$a_{xy} \approx \frac{7000}{p_0[\text{GeV}/c]}\left(-102261\frac{I_{oct}^F[\text{A}]}{550} + 93331\frac{I_{oct}^D[\text{A}]}{550}\right), \tag{3.6}$$

with I_{oct}^F and I_{oct}^D set in input.

4. For the first kick section of the ring and after it has been dealt with as explained previously, the synchrotron motion is treated (separately for each bunch) solving the 2D longitudinal equations of motions (linearized or not) thanks to a Runge-Kutta algorithm or a kick approximation. Various options are possible for this longitudinal behaviour.

5. Depending on the input options, lost macroparticles (out of the vacuum pipe transversely, or out of the bucket longitudinally) are taken away at each kick section.

In all the practical applications of the code presented in the following sections, only one kick section per turn was used.
The code has been parallelized over the number of bunches, i.e. in a multiprocessor architecture each processor will be assigned a certain number of bunches. Such a parallelization is quite efficient since all the bunches can be treated almost independently, the only requirement being that after each slicing (see above) the processors exchange for all the bunches the positions and number of particles of each slice, such that the wakes can be computed in all bunches. This represents a quite limited amount of data, since the number of slices is usually restricted to a few hundreds at most. Indeed, Fig. 3.1 shows that the computational time is inversely proportional to the number of processors used, i.e. the parallelization is linear with the number of processors.

3.2 Postprocessing tools to analyse coupled-bunch instabilities

3.2.1 Single-bunch analysis

In the case of multibunch simulations or measurements, each bunch can always be considered individually, or the average of the centroids of all bunches can be computed in order to get the average beam motion. In that case, one can apply single-bunch techniques to analyse data, such as frequency domain analysis thanks to a one dimensional Fast Fourier Transform (FFT) or to the program SUSSIX [112] which gives the same kind of output as the FFT except that the frequency domain spectrum obtained is

[2]Actually, in 2010-2011 two octupoles per LHC ring were not present (both defocusing for beam 1, and both focusing for beam 2) [110]. This represents a change of the detuning coefficients of about 1%, which we neglect.

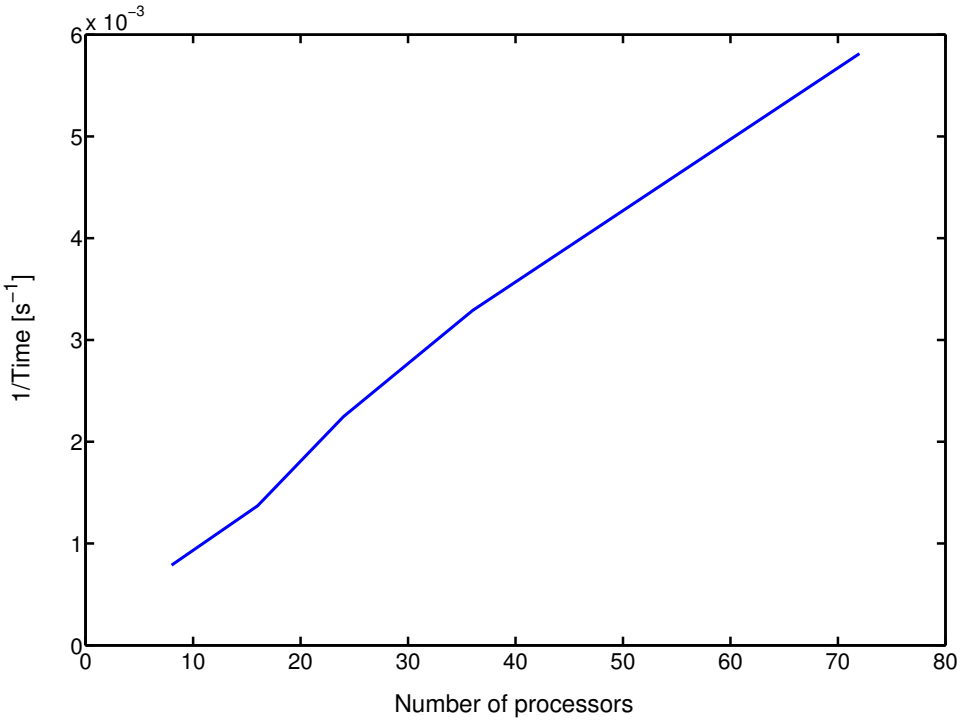

Figure 3.1: Inverse of the computational time vs. number of processors used, in the case of a HEADTAIL simulation on 72 bunches with 10 slices per bunch.

usually much finer. In particular, intrabunch headtail modes are often much more visible with a SUSSIX analysis than with a standard FFT analysis [76, p. 147]. Also, SUSSIX gives much higher precision on the tunes obtained, in particular one can get accurate tune shifts between the unperturbed tune (or the unperturbed spectrum line of a synchrotron sideband) and the growing peak due to the impedances.
Another important quantity that one wants to get both from simulation and measurements data is the rise time (or, equivalently, the growth rate, or imaginary tune shift) of a certain instability. One straightforward and intuitive way to obtain it is simply to fit the maxima of the turn by turn centroid positions data of the bunch (or of the full beam) by an exponential (which is a linear fit of the logarithm of the data). However, this can be relatively inaccurate, in particular for measurements, where artificial peaks may pollute the data and make it difficult to extract the maxima. Another way to obtain such rise time is to compute the SUSSIX spectra over a "sliding window" along the simulation, i.e. over a fixed number of turns that we move from the beginning toward the end of the data. This way one obtains spectrum amplitudes varying with turn number, which we can fit with an exponential in order to get the rise time. This technique is very reliable and gives quite accurate results provided the size of the window is set appropriately (not too small to get enough resolution on the peaks, but not too long to get enough spectra to do the final fit). One shortcoming is that one can get this way only one rise time (the lowest one of all present modes), because it happens to be the same for all the peaks of the spectrum, i.e. all the peaks grow according to the most critical mode. This is probably due to the fact that frequency domain analysis (FFT or SUSSIX) is not really good at analysing data with growing exponentials in it.
If one wants to get the rise time of modes that are not the most critical one, we need to perform another kind of spectral analysis that takes into account not only oscillating exponentials (i.e. with an

imaginary argument) but also growing (or damped) exponentials (i.e. with a real argument). In other words, one would need to get a spectral decomposition over complex frequencies. A promising and still experimental way to do such a spectral decomposition is to adopt the following procedure, inspired from Ref. [113]:

1. Given the signal $x(n)$ between $n = 0$ to $n = N-1$, we can compute for any real number σ

$$\tilde{x}_\sigma(k) = \mathrm{FFT}[e^{-\sigma n} x(n)], \qquad \varepsilon_\sigma = \frac{1}{N}\sum_{n=0}^{N-1} e^{-2\sigma n}\,|x(n)|^2, \qquad \text{and} \quad P_\sigma[x](k) = \frac{|\tilde{x}_\sigma(k)|^2}{\varepsilon_\sigma}, \tag{3.7}$$

   where $\mathrm{FFT}[f]$ denotes the FFT of a certain function f. The key result of Ref. [113] is that $P_\sigma[x]$ turns out to be maximum for the growth rate σ_0 and the frequency k_0 of the most growing mode. One can take the maximum line of $P_\sigma[x]$, namely $max_k(P_\sigma[x](k))$, and maximize it versus σ with a standard optimization algorithm, getting a first estimate σ_0 of the highest growth rate.

2. To get a more accurate frequency of the line with the highest growth rate, we can multiply $x(n)$ by an exponential factor in the following way:

$$x_\alpha(n) = e^{2\pi j \alpha n} x(n).$$

   A first estimate of the highest peak is then obtained from the maximization versus α of the highest peak in the FFT of $x_\alpha(n)$, thus obtaining α_0. Then

$$x(n) = e^{-2\pi j \alpha_0 n} x_{\alpha_0}(n) = \frac{1}{N} e^{-2\pi j \alpha_0 n} \sum_{k=0}^{N-1} \mathrm{FFT}[x_{\alpha_0}](k) e^{2\pi j \frac{kn}{N}} = \frac{1}{N}\sum_{k=0}^{N-1} \mathrm{FFT}[x_{\alpha_0}](k) e^{2\pi j (\frac{k}{N} - \alpha_0) n}$$

   such that the corresponding frequency (or tune) of the highest peak is given by $Q_0 = \frac{k_0}{N} - \alpha_0$ with k_0 the maximum line of the spectrum (i.e. such that $max_k \left|\mathrm{FFT}[x_{\alpha_0}](k)\right| = \left|\mathrm{FFT}[x_{\alpha_0}](k_0)\right|$).

3. From the two previous steps we can initialize with σ_0 and α_0 a two dimensional maximisation of $max_k\,(P_\sigma[x_\alpha](k))$ over both α and σ, where the power spectrum $P_\sigma[x_\alpha]$ is defined as above but with x replaced by x_α. One then gets σ_1 (growth rate) and α_1, from which the tune Q_1 is obtained by the same procedure as in the previous step.

4. Finally, the amplitude of the exponential of complex angular frequency $\sigma_1 + j2\pi Q_1$ is obtained from the amplitude (divided by N) of the zeroth line of the FFT of $x(n)e^{-(\sigma_1 + j2\pi Q_1)n}$:

$$A(\sigma_1 + 2\pi j Q_1) = \frac{\mathrm{FFT}[x(n)e^{-(\sigma_1 + j2\pi Q_1)n}](0)}{N}.$$

5. We can then take out the exponential term obtained from the full signal, i.e. replace the initial $x(n)$ by $x(n) - A(\sigma_1 + j2\pi Q_1)e^{(\sigma_1 + j2\pi Q_1)n}$, and reiterate the full procedure several times.

In such a way a set of harmonics with complex frequencies can be obtained. Note that for the initial signal $x(n)$ we can take the bunch (or beam) centroid horizontal (resp. vertical) position, or the quantity $x(n) - j\beta_x x'(n)$ (resp. $y(n) - j\beta_y y'(n)$) as is done in SUSSIX [112], provided that the data of x' is available as well as the beta functions and that the derivative of the beta functions is zero at the location where x and x' (resp. y and y') are observed. These conditions are true in the case of HEADTAIL simulations.

This technique is quite simple and straightforward to implement, and gives a quite accurate complex tune shift of the most critical mode observed in a given set of data (see later in Section 3.3). With respect to the SUSSIX method with the sliding window, this method has the asset that no window width has to be chosen, the turn by turn data being processed in its entirety. For the other modes possibly present in the data, less critical than the main mode, results of this procedure are up to now subject to caution and improvements are probably possible.

3.2.2 Coupled-bunch analysis

Simulations data as well as measurements will often give us the centroid position of each bunch versus number of turns, i.e. $x(n,b)$ with n the turn number (from 1 to n_{turn}) and b the bunch number (from 1 to n_{bunch}). This two-dimensional data can be analysed thanks to one dimensional FFT, either along a bunch train at a given turn, or along the number of turns for a given bunch. Also, two dimensional FFT can be used to analyse at the same time the coupled-bunch mode number (the mode along the bunch train) and the tune.
Another two-dimensional technique that we will sometimes use is the Singular Value Decomposition (SVD), useful in particular when bunch trains are not composed of equidistant bunches, such that the mode number that the standard FFT could provide would have little meaning. We do here SVD in time domain and base our analysis on the technique described in Refs. [114, 115].
The idea is that the set of data $x(n,b)$ can be put into a matrix X of size $(n_{turn} \times n_{bunch})$, and of elements $x_{nb} \equiv x(n,b)$. X can in turn be decomposed thanks to the SVD as

$$X = U^T \cdot W \cdot V, \tag{3.8}$$

where U and V are two orthonormal matrices of size respectively $(n_{bunch} \times n_{turn})$ and $(n_{bunch} \times n_{bunch})$, ^{T} denotes the transposition, and W is a diagonal matrix of size $(n_{bunch} \times n_{bunch})$. This decomposition can be rewritten

$$x(n,b) = \sum_{k=1}^{n_{bunch}} \lambda_k u_k(n) v_k(b), \tag{3.9}$$

with $\lambda_k = W_{kk}$, $u_k(n) = U_{kn}$ and $v_k(b) = V_{kb}$. The orthonormality conditions are that for any k and l between 1 and n_{bunch} we have

$$\sum_{n=1}^{n_{turn}} u_k(n) u_l(n) = \delta_{kl} \quad \text{and} \quad \sum_{b=1}^{n_{bunch}} v_k(b) v_l(b) = \delta_{kl},$$

with $\delta_{kl} = 1$ if $k = l$, 0 otherwise. In the form given by Eq. (3.9), the SVD gives for each k a "time pattern" $u_k(n)$ and a "spatial pattern" $v_k(b)$. Selecting the k with the highest λ_k will give the patterns of the dominant oscillations both in time domain and along the bunch train. In turn, both $u_k(n)$ and $v_k(b)$ can be analysed thanks to one-dimensional techniques such as the FFT, or for the time pattern the SUSSIX analysis [112] or the decomposition over complex frequencies (see previous section).

3.3 Benchmarking the code with Laclare's theory for dipolar impedance and a fully filled machine

3.3.1 Short description of Laclare's results on transverse instabilities

Laclare's formalism is fully described in Ref. [6]. References [116, 117] also give a synthetic description of the theory. Here we will summarize the main aspects and results of the theory.
This theory is two-dimensional (i.e. no coupling with the other transverse plane or with the longitudinal coordinates is considered), and studies the dynamics of one or several equidistant and equipopulated bunches in a ring. Each bunch has initially a stationary distribution. In longitudinal, this translates into a phase space density $g_0(\hat{\tau})$, normalized by the total number of bunch particles ($\hat{\tau}$ being the amplitude of the longitudinal motion). With τ_b the total bunch length in seconds (or four times the standard deviation for Gaussian bunches), we have

$$\text{for a Gaussian distribution:} \quad g_0(\hat{\tau}) = \frac{8}{\pi\tau_b^2} e^{-8\frac{\hat{\tau}^2}{\tau_b^2}} \qquad \text{for } 0 \le \hat{\tau} < \infty,$$

$$\text{for a parabolic distribution:} \quad g_0(\hat{\tau}) = \frac{8}{\pi\tau_b^2}\left(1 - 4\frac{\hat{\tau}^2}{\tau_b^2}\right) \qquad \text{for } 0 \le \hat{\tau} < \frac{\tau_b}{2},$$

$$\text{for an elliptical distribution:} \quad g_0(\hat{\tau}) = \frac{6}{\pi\tau_b^2}\sqrt{1 - 4\frac{\hat{\tau}^2}{\tau_b^2}} \qquad \text{for } 0 \le \hat{\tau} < \frac{\tau_b}{2},$$

$$\text{for a "water-bag" distribution:} \quad g_0(\hat{\tau}) = \frac{4}{\pi\tau_b^2} \qquad \text{for } 0 \le \hat{\tau} < \frac{\tau_b}{2}.$$

To make comparisons with the HEADTAIL code we will also use a Gaussian distribution cut at the bunch length, i.e. non-zero for $0 \le \hat{\tau} < \frac{\tau_b}{2}$ only.
The theory (here written for the horizontal plane) consists in solving the linearized Vlasov equation for a given dipolar impedance Z_x^{dip}, assuming the distribution of particles is perturbed by a term of angular frequency close to a synchrotron satellite, i.e. close to $(Q_x + mQ_s)\omega_{rev}$ with ω_{rev} the angular frequency of revolution, Q_s the synchrotron tune and m an integer (headtail – or azimuthal – mode number). In the low intensity version of the theory (the only one we will use in this chapter), each headtail mode m is considered independently and cannot couple to another mode. Note that the headtail mode is assumed to be the same in all bunches.
The final solution of the Vlasov equation appears in terms of the solution of an eigenvalue problem:

$$\Delta\omega_c^m \sigma^m(l) = \sum_{p=-\infty}^{\infty} K_{lp}^m \sigma^m(p), \tag{3.10}$$

with $\Delta\omega_c^m$ the angular frequency shift with respect to $(Q_x + mQ_s)\omega_{rev}$ for the coherent mode looked for, σ^m the eigenvalue associated with this mode, and K^m a matrix of components

$$K_{lp}^m = \frac{je^2 M N_b \omega_{rev}}{4\pi\gamma m_0 c Q_x} Z_x^{dip}\left[\left(n + pM + [Q_x] + mQ_s\right)\omega_{rev}\right] \cdot \int_0^{\frac{\tau_b}{2}} J_m\left\{\left[\left(n + lM + [Q_x]\right)\omega_{rev} - \omega_{\xi_x}\right]\hat{\tau}\right\} J_m\left\{\left[\left(n + pM + [Q_x]\right)\omega_{rev} - \omega_{\xi_x}\right]\hat{\tau}\right\} g_0(\hat{\tau})\hat{\tau}\,\mathrm{d}\hat{\tau}, \tag{3.11}$$

where N_b is the number of elementary particles per bunch, M the number of bunches, n the coupled-bunch mode number (which here includes the integer part of the tune), J_m the Bessel function of order m, $[Q_x]$ the fractional part of the tune, and where the chromaticity is taken into account approximately [107, p. 92] by an angular frequency shift of value $\omega_{\xi_x} = \frac{\xi_x Q_x \omega_{rev}}{\eta}$ with $\eta = \alpha_p - \frac{1}{\gamma^2}$ the slip factor, $\xi_x = Q'_x/Q_x$ the chromaticity and α_p the momentum compaction factor. Note that for an infinite Gaussian longitudinal distribution, the integral in the matrix term above goes up to ∞ instead of $\frac{\tau_b}{2}$.
The eigensystem has to be solved for each coupled-bunch mode number n and each headtail mode number m. The main results are the angular frequency shifts $\Delta\omega_c^m$ from which one can deduce the complex tune shifts (dividing by ω_{rev}), or, equivalently, the real tune shifts and the rise (or damping) times of the modes. The most critical instability is then the one whose $\Delta\omega_c^m$ has the lowest (and negative) imaginary part.
We recall finally the assumptions under which this theory is valid:

- low intensity (well below the transverse mode coupling regime [106, 118]). Note that in Ref. [6], a more complicated high-intensity formalism is also developped,
- absence of non-linearities,
- absence of transverse linear coupling or coupling with the longitudinal plane,
- purely dipolar impedance,
- equidistant and equipopulated bunches in the ring,
- same intrabunch motion in all bunches,
- the effect of the chromaticity can be approximated through the chromatic frequency shift.

The formalism has been implemented in a code that automatically checks that the necessary matrix truncation to solve the system still gives accurate eigenvalues (within 0.1%) by testing convergence with respect to the matrix size.

3.3.2 Case of 924 equidistant and equipopulated bunches in the SPS

We study first the SPS filled with a 25 ns beam, i.e. containing 924 equidistant bunches. We consider here the vacuum pipe of the SPS as the only impedance contributor, assuming it has the same cross section all around the ring. To compute its impedance we use Zotter's theory as presented in Section 1.4, assuming the pipe has 2 cm radius and is made of stainless steel (resistivity $\rho = 7.2 \cdot 10^{-7}\Omega$m, dielectric constant $\varepsilon_r = 1.5$, permeability $\mu_r = 1.01$, thickness 2 mm [76]) surrounded by vacuum. The wake function is then obtained thanks to the technique seen in Section 1.6.3. Since the beam pipe is actually of elliptical cross section with the horizontal demi-axis significantly larger than the vertical one (2 cm), to get the dipolar impedances and wake functions for this geometry we multiply by the Yokoya factors [23] for a flat chamber, namely $\frac{\pi^2}{24}$ in x and $\frac{\pi^2}{12}$ in y.
The theory assumes a purely transverse dipolar impedance and a linear longitudinal bucket; we used then the same conditions in HEADTAIL. Also, in the simulations the longitudinal parameters were initially matched. The beam parameters used in both the simulation and the theory can be found in Table 3.1. Note that the normalized RMS emittances are different from the single-particle emittances ε_x

and ε_y considered up to know: they are defined as the average ε_x or ε_y of all the particles of the beam multiplied by $\beta\gamma$, and can be written [84, p. 13]

$$\varepsilon_x^n = \beta\gamma\sqrt{< x^2 >< x'^2 > - < xx' >^2}, \qquad \varepsilon_y^n = \beta\gamma\sqrt{< y^2 >< y'^2 > - < yy' >^2}, \tag{3.12}$$

where $< . >$ indicates the average value.

We show first in Fig. 3.2a the average horizontal beam position versus turn number for various chro-

Table 3.1: SPS with 924 bunches: parameters. Perfect longitudinal matching was assumed.

Number of protons per bunch N_b	$5 \cdot 10^{10}$
Total bunch length= $4\sigma_z$	0.76 m
Longitudinal momentum spread σ_δ	0.002
RF voltage V_{rf}	3 MV
Harmonic number h	4620
Synchrotron tune Q_s	$7.25 \cdot 10^{-3}$
Bunch spacing	25 ns
Number of equidistant bunches	924
Circumference	6911 m
Horizontal / vertical tune Q_x / Q_y	26.129 / 26.164
Horizontal / vertical beta function β_x / β_y	42 / 42 m
Horizontal / vertical normalized RMS emittance ε_x^n / ε_y^n	4 / 4 mm.mrad
Relativistic γ	27.7
Momentum compaction factor α_p	$1.92 \cdot 10^{-3}$
Number of slices per bunch n_{sl}	50
Number of macroparticles per bunch n_{MP}	250000
Number of turns of memory for the wakes n_{wake}	19

maticities, together with the fit of the maxima of the curves. The beam clearly becomes unstable, with a rise time of a few ms.

The bunch centroid vertical coordinates versus turns are also analysed thanks to the two-dimensional FFT in Fig. 3.2b, in the case of zero chromaticity. The most critical multibunch mode appears to be $n = 923$ (which is equivalent to $n = -1$), both in horizontal and vertical and for any of the chromaticities studied. The same mode was found when using Laclare's theory, provided one adds the integral part of the tune to the mode number as was done in the previous section.

To benchmark our code, we show in Fig. 3.3 a comparison, in terms of the complex tune shifts, between Laclare and HEADTAIL for various chromaticities. For HEADTAIL simulations, the complex tune shift has been computed thanks to the decomposition over complex frequencies of the average beam positions (method given in Section 3.2.1). We chose the headtail mode $m = 0$, and the most critical coupled-bunch mode for Laclare's theory. The agreement between HEADTAIL and Laclare's theory is quite good, in particular for the imaginary part of the tune shift. For the real part, there seems to be a constant offset for all the chromaticities studied, which might be due to the fact that the wake fields from a given slice do not affect the slice itself (see Eq. (3.1)).

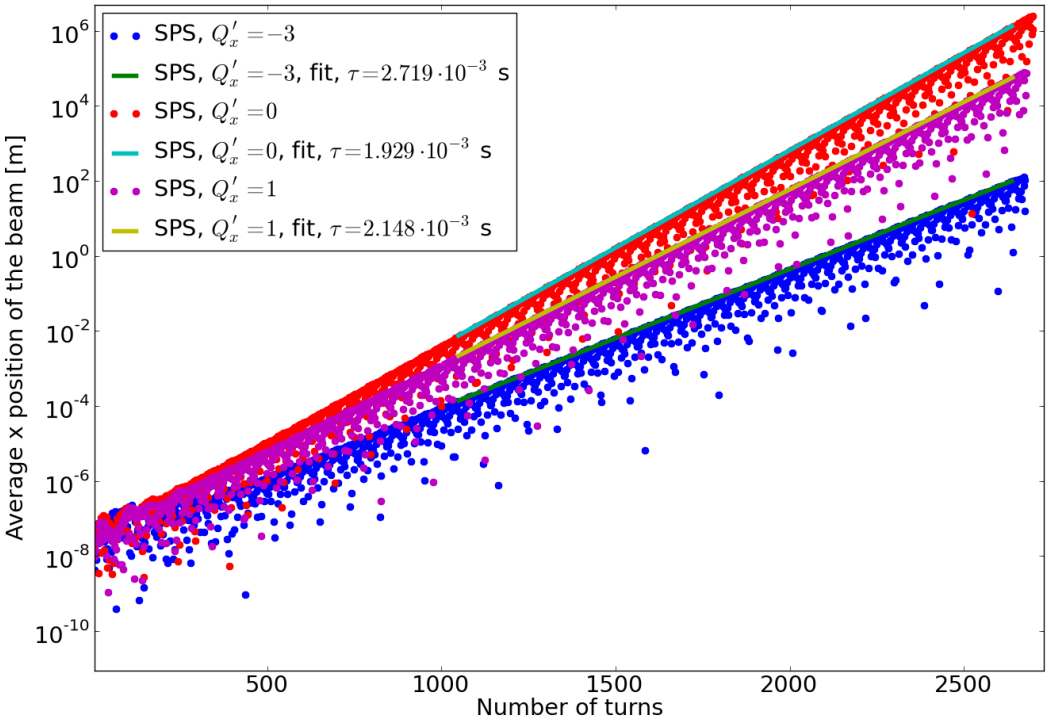

(a) Horizontal beam position vs. turn number, for various chromaticities.

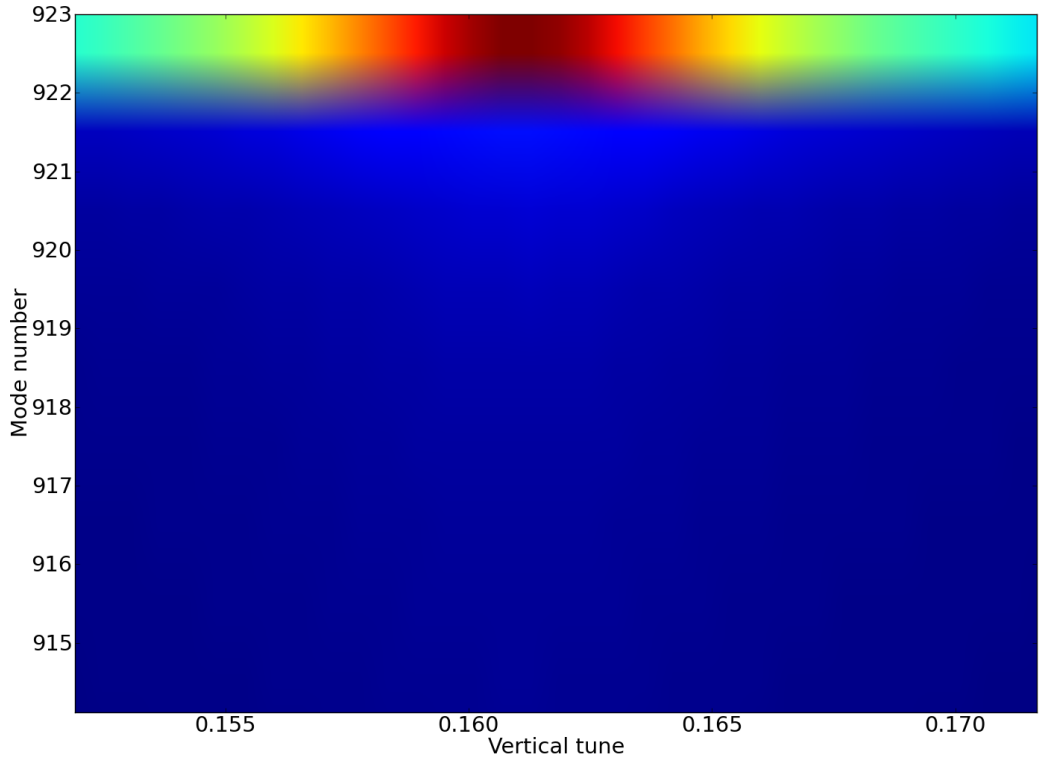

(b) 2D-FFT of the bunch centroid position vs. turns, zoomed around high mode numbers (vertical plane, zero chromaticity). The color represents the amplitude of the FFT (red for high amplitudes).

Figure 3.2: HEADTAIL simulations of 924 bunches in the SPS.

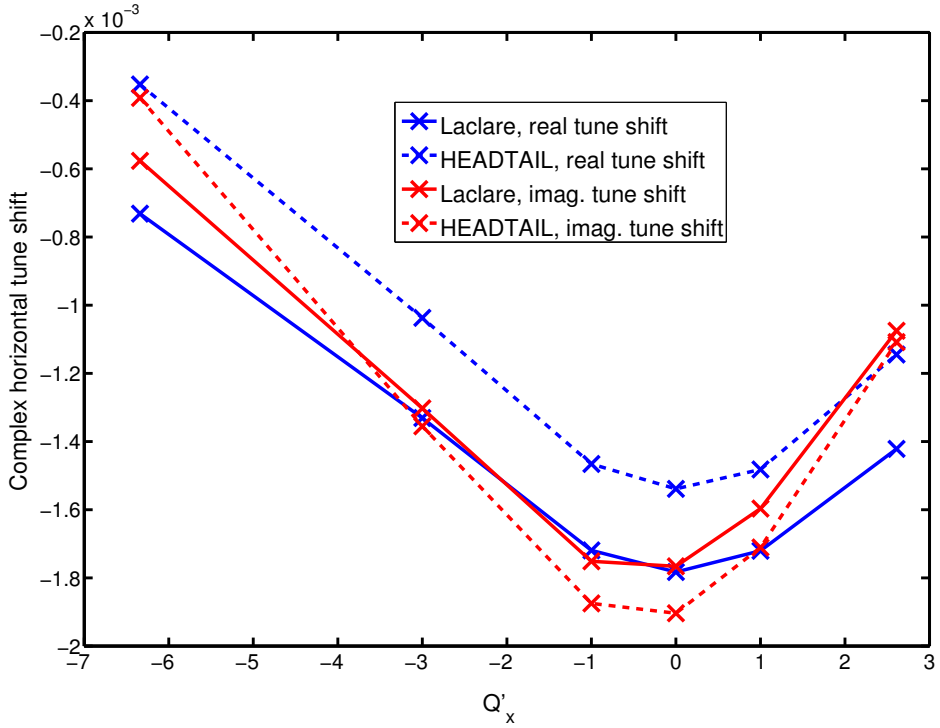

(a) Horizontal plane.

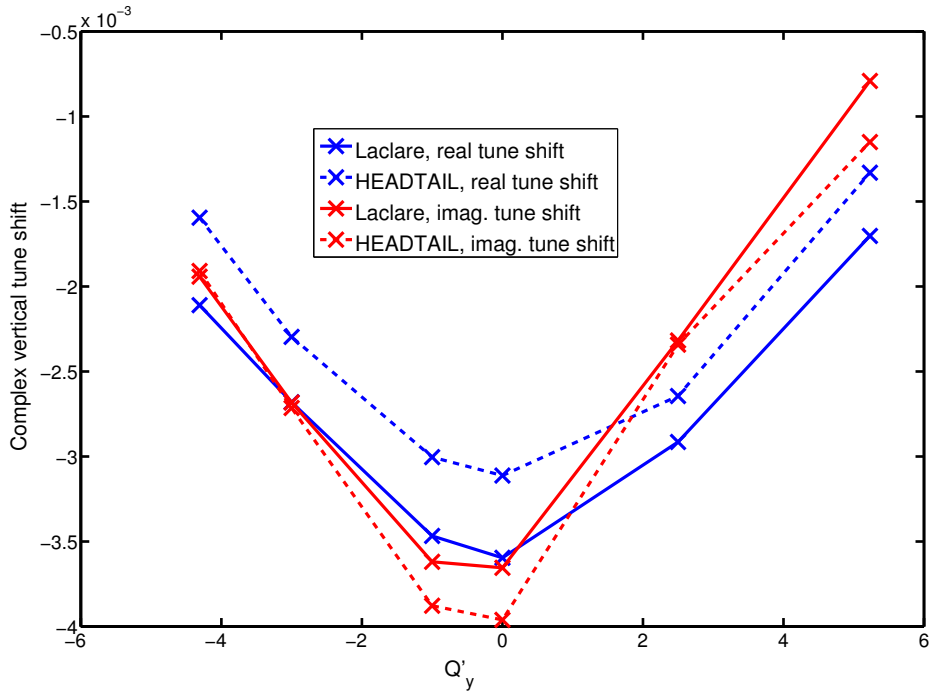

(b) Vertical plane.

Figure 3.3: Case of 924 bunches in the SPS: comparison between Laclare's theory and HEADTAIL multibunch for the complex tune shift vs. Q' (headtail mode $m = 0$).

For the highest vertical chromaticity simulated ($Q'_y = 5.23$), in the simulation the most unstable mode is actually a headtail mode with $m = -1$, rather than the $m = 0$ mode plotted in Fig. 3.3. Indeed, Fig. 3.4a shows the vertical profile (i.e. the number of particles of each slice multiplied by their offset) of one of the bunch of the train, on 100 successive turns, where one can clearly see a node which is the signature of a headtail mode with $|m| = 1$. The spectral decomposition over complex frequencies shows that the highest amplitude is obtained for the $m = -1$ mode, with a rise time of 3.2 ms and a real tune shift (with respect to $Q_y - Q_s$) of $-6.7 \cdot 10^{-4}$. In comparison, Laclare's theory gives the headtail mode $m = 1$ as the most critical (actually it has very little difference with respect to the $m = -1$ one, in terms of both rise time and real tune shift), with a rise time of 4.5 ms and a real tune shift of $-9.6 \cdot 10^{-4}$. The discrepancy remains therefore reasonable (around 30%). Note that even though intrabunch activity appears in this case, a coupled-bunch motion is also clearly visible, as can be seen from the SVD of the bunch positions (see Section 3.2.2) in Fig. 3.4b.

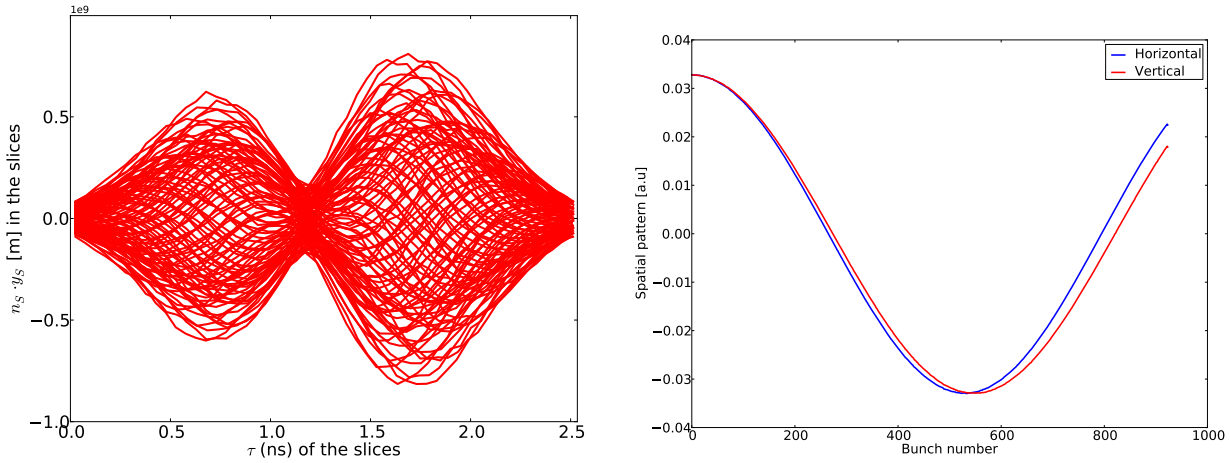

(a) Vertical bunch profile for the 500$^{\text{th}}$ bunch of the train.

(b) Spatial pattern of the highest λ_k from the SVD.

Figure 3.4: HEADTAIL simulation of 924 bunches in the SPS, with $Q'_y = 5.23$: intrabunch and coupled-bunch motion.

3.3.3 Case of 1782 equidistant and equipopulated bunches in the LHC

We study now the LHC with a 50 ns beam, i.e. 1782 equidistant bunches. The impedance model used is the one presented in Chapter 2. As for the SPS case, we used only the transverse dipolar impedances and a linear longitudinal bucket (initially matched in HEADTAIL).The beam parameters used in both the simulation and the theory are shown in Table 3.2.
We show first in Fig. 3.5 the average horizontal beam position versus turn number for various chromaticities, together with the fit of the maxima of the curves. The beam is clearly unstable, with rise times between 0.2 and 0.4 s. We apply also the two-dimensional FFT to the bunch vertical positions versus turns in Fig. 3.6, in the case of $Q'_y = 2$. The most critical multibunch mode appears to be $n = 1781$ (which is equivalent to $n = -1$), both in horizontal and vertical and for any of the chromaticities studied. The same mode was found when using Laclare's theory.

Table 3.2: LHC with 1782 bunches: parameters. Perfect longitudinal matching was assumed.

Number of protons per bunch N_b	$1.2 \cdot 10^{11}$
Total bunch length= $4\sigma_z$	0.36 m
Longitudinal momentum spread σ_δ	$1.9 \cdot 10^{-4}$
RF voltage V_{rf}	16 MV
Harmonic number h	35640
Synchrotron tune Q_s	$2.891 \cdot 10^{-3}$
Bunch spacing	50 ns
Number of bunches	1782
Circumference	26658.883 m
Horizontal / vertical tune Q_x / Q_y	64.31 / 59.32
Horizontal / vertical beta function β_x / β_y	65.976 / 71.538 m
Horizontal / vertical normalized RMS emittance ε_x^n / ε_y^n	3.75 / 3.75 mm.mrad
Relativistic γ	3730.26
Momentum compaction factor α_p	$3.225 \cdot 10^{-4}$
Number of slices per bunch n_{sl}	20
Number of macroparticles per bunch n_{MP}	80000
Number of turns of memory for the wakes n_{wake}	19

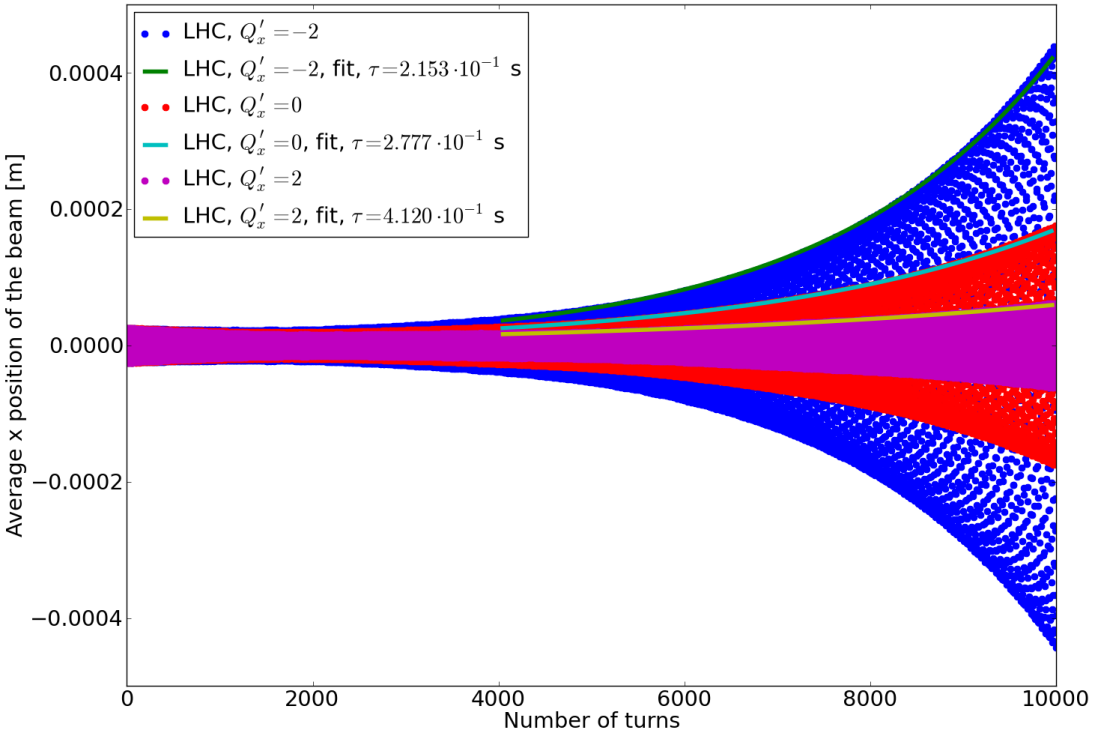

Figure 3.5: HEADTAIL simulations of 1782 bunches in the LHC: vertical beam position vs. turn number, for various chromaticities.

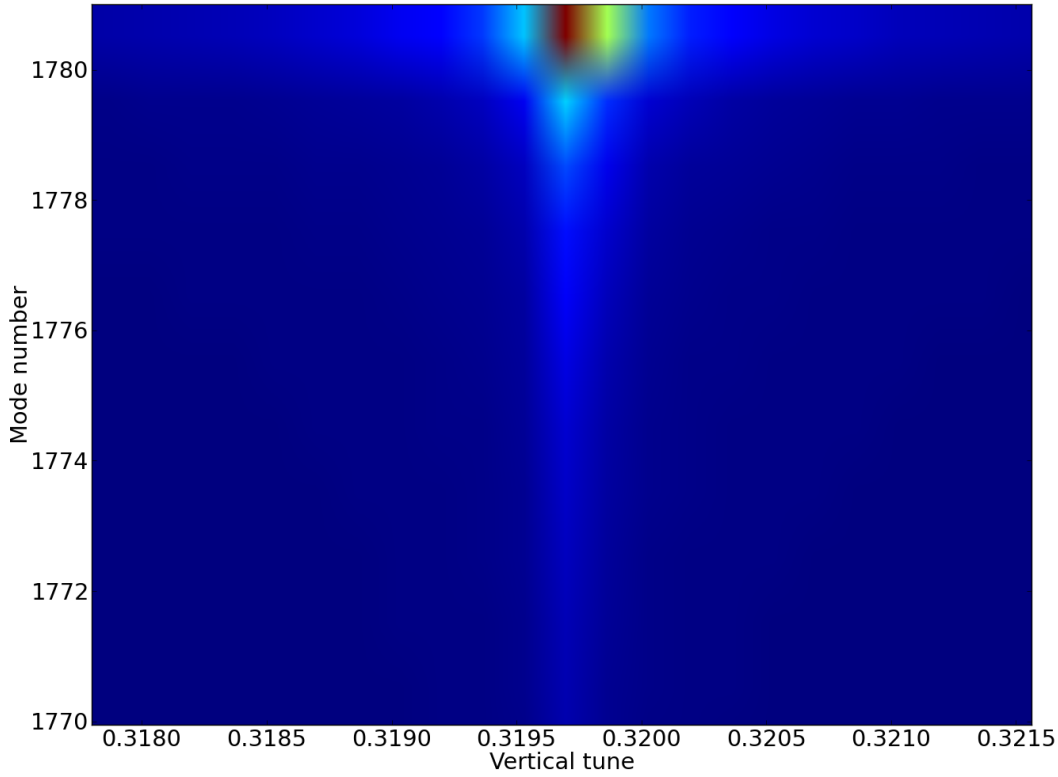

Figure 3.6: HEADTAIL simulation of 1782 bunches in the LHC: 2D-FFT of the bunch centroid position vs. turns, zoomed around high mode numbers (vertical plane, $Q'_y = 2$). The color represents the amplitude of the FFT (red for high amplitudes).

In Fig. 3.7 is shown a comparison between HEADTAIL simulations and Laclare's most critical coupled-bunch mode, in terms of the complex tune shift of the headtail mode $m = 0$ vs. Q'. For HEADTAIL the complex tune shifts were obtained through spectral decomposition of the beam average position over complex frequencies (see Section 3.2.1). The agreement is very good, in particular for the imaginary tune shift.

3.4 Conclusion

The wake fields simulation code HEADTAIL is now fully multibunch and includes all the features present in the previous version of the code (intrabunch motion, amplitude detuning from the octupoles and chromaticity), at the notable exception of the possibility to simulate the effect of electron cloud. It proved to be effective in simulating large number of bunches, and reliable since in simple cases agreement with Laclare's theory is rather good, for both "rigid-bunch" modes (i.e. headtail mode $m = 0$) and modes with intrabunch motion.

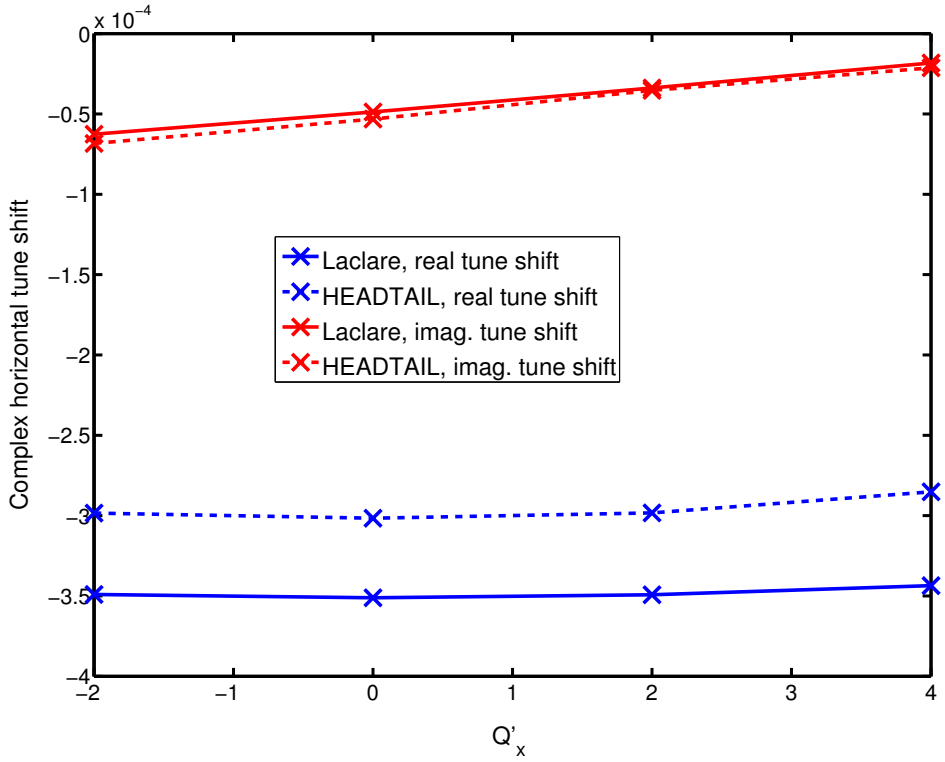

(a) Horizontal plane.

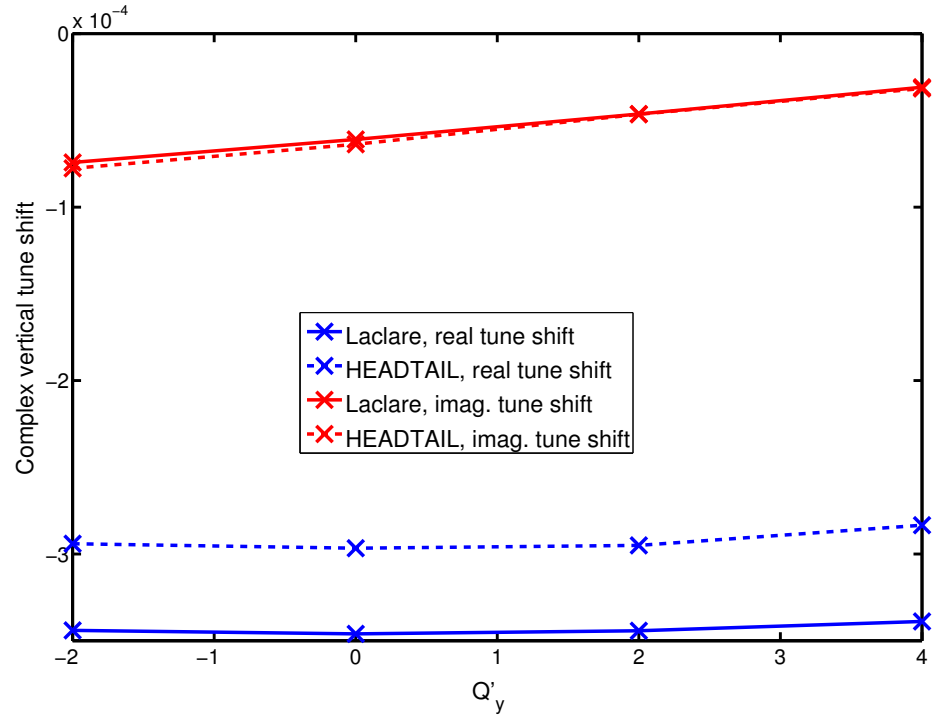

(b) Vertical plane.

Figure 3.7: Case of 1782 bunches in the LHC: comparison between Laclare's theory and HEADTAIL multibunch for the complex tune shift vs. Q' (headtail mode $m = 0$).

4 Simulation results and comparison with experiments

In this chapter, simulations results for the transverse coupled-bunch instabilities of the LHC are presented. We use the code HEADTAIL in its new multibunch version as shown and benchmarked in Chapter 3, and the LHC transverse impedance model of Chapter 2.
We study first the case of small bunch trains, comparing them to a fully filled machine. Then we present a case of coupled-bunch instability with intrabunch (headtail) activity, comparing it to a single-bunch headtail instability. We then make a comparison between simulation results and actual beam-based measurements in the LHC. Finally, we give predictions for the future operation of the machine at 7 TeV/c.

4.1 Comparison between small trains and a completely filled machine

In the LHC, the beams are made of several bunches, separated by a distance not lower than 7.5 m (corresponding to 25 ns, or 10 RF buckets). When all the bunches have the same separation between them, they are said to be equidistant; this was the situation studied in Section 3.3. In reality, more complex situations arise where all the bunches are not equidistant. In the LHC, one has at maximum 3564 possible slots of 25 ns, some of them being empty while others contain one bunch. A filling pattern is then a particular way to fill the machine, i.e. to assign slots to the bunches.
To maximize the machine collision rate, it would be best to have all the slots occupied by one bunch, i.e. a completely filled machine. This is not possible because of several constraints, among which one can mention the limited capacity of the injectors, which forces the bunches to be grouped into batches containing 72 bunches separated by 25 ns, or 36 with 50 ns spacing. Another constraint is the injection kicker magnets rise time, which is the time needed by the injection kicker magnets to reach the magnetic field required to bend the particles trajectory when they are transfered from one ring or line to another one (rise time of 225 ns [119] for the injection into the SPS, and 900 ns – although more than this value is used most often – for the injection into the LHC [84, chap. 16, p. 422]). The LHC dump system – which protects the machine in case of unwanted events such as beam losses by deviating the beam away from the main ring – additionally requires an interval of 3 μs with empty slots [84, chap. 17, p. 460], for the rise time of its kicker magnet. All those constraints (plus several others) end up into the following filling scheme (written in standard form), which contains the maximum possible number of bunches one can

inject and collide into the LHC [119]:

$$\{[(72(b)+8(e))\times 2+30(e)]+[(72(b)+8(e))\times 3+30(e)]+[(72(b)+8(e))\times 4+31(e)]\}$$
$$+\{[(72(b)+8(e))\times 3+30(e)]+[(72(b)+8(e))\times 3+30(e)]+[(72(b)+8(e))\times 4+31(e)]\}\times 3$$
$$+\{80(e)\} \quad (4.1)$$

where (b) indicates a 25 ns slot occupied by a bunch and (e) an empty slot. One obtains this way a total of 2808 bunches (out of 3564 slots). In this filling scheme, the elementary batches contain 72 equidistant bunches spaced by 25 ns. One can do a very similar filling scheme with instead 50 ns bunch spacing in those batches, obtaining 36 bunches per batch and a total of 1404 bunches. In the present configuration of the LHC, up to 1380 bunches with 50 ns spacing were injected and brought into collision at 3.5 TeV/c; this is sligthly lower than 1404 because of an additional constraint on the injection system, requiring a low intensity pilot bunch plus a batch of 12 bunches to be injected before the batches of 36 bunches.
The multibunch HEADTAIL code presented in Chapter 3 now allows to study any filling pattern. This is particularly interesting for small trains which are in principle far from the situation of a completely filled machine accessible to theories such as the ones from Sacherer [5, 59] or Laclare [6] (see also Section 3.3). We study here the case of a train of 36 bunches spaced between them by 50 ns, filling on the whole only 2% of the total circumference, and compare it to the case of 1782 equidistant bunches with the same 50 ns spacing, which completely fill the machine. We show in Table 4.1 the parameters used in the simulations, which are close to those of normal operation at 3.5 TeV/c, the only difference being in the tunes (64.28 instead of 64.31 and 59.31 instead of 59.32 – this is of little importance in the case of multibunch instabilities). In Fig. 4.1 the average x and y positions of the full beam are shown. Clearly,

Table 4.1: LHC parameters for the comparison between 36 and 1782 bunches. Perfect longitudinal matching was assumed.

Number of protons per bunch N_b	$1.2\cdot 10^{11}$
Total bunch length= $4\sigma_z$	0.36 m
Longitudinal momentum spread σ_δ	$1.6\cdot 10^{-4}$
RF voltage V_{rf}	12 MV (non linear bucket)
Harmonic number h	35640
Synchrotron tune Q_s	$2.504\cdot 10^{-3}$
Bunch spacing	50 ns
Circumference	26658.883 m
Horizontal / vertical tune Q_x / Q_y	64.28 / 59.31
Horizontal / vertical beta function β_x / β_y	66.006 / 71.538 m
Horizontal / vertical normalized RMS emittance ε_x^n / ε_y^n	2 / 2 mm.mrad
Horizontal / vertical Q'_x / Q'_y	0 / 0
Relativistic γ	3730.26
Momentum compaction factor α_p	$3.225\cdot 10^{-4}$
Number of slices per bunch n_{sl}	20
Number of macroparticles per bunch n_{MP}	200000
Number of turns of memory for the wakes n_{wake}	19

the beam with 1782 bunches gets unstable more quickly than the other one, but the rise time is only about a factor 2.5 higher in horizontal and 4 in vertical. The spatial pattern of the instability, obtained

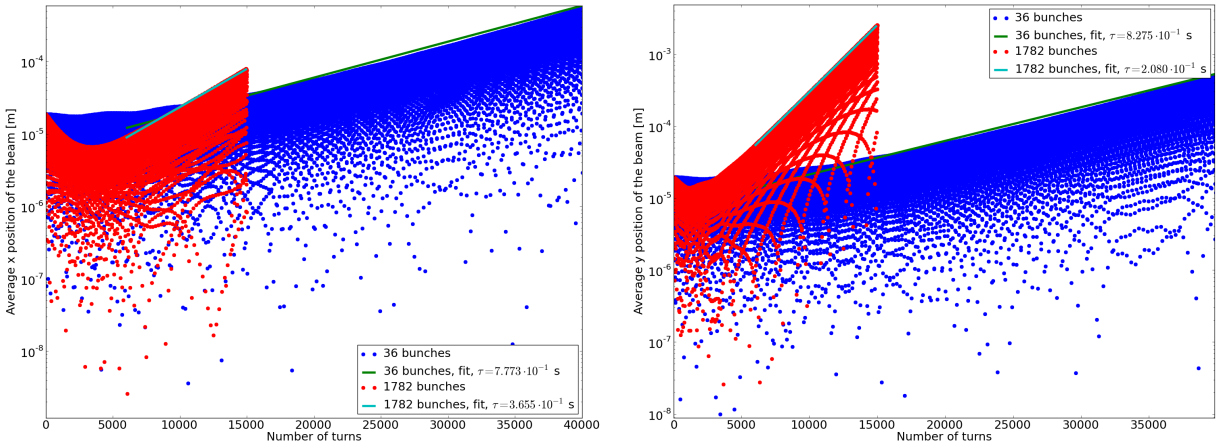

(a) Average horizontal position of the beam.

(b) Average vertical position of the beam.

Figure 4.1: Beam position vs. turns for 36 bunches and 1782 bunches with 50 ns spacing.

thanks to the SVD technique [114] described in Section 3.2.2, is shown for both cases in Fig. 4.2. It appears that the spatial pattern of the instability with 1782 bunches has a larger wavelength than the one with 36 bunches. In Fig. 4.3 we also compare the rise times (computed thanks to an exponential

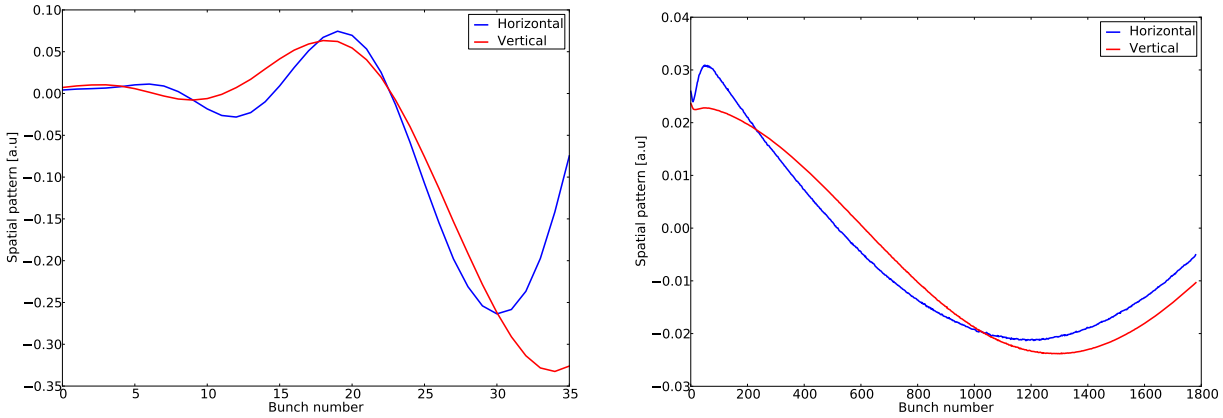

(a) Case with 36 bunches.

(b) Case with 1782 bunches.

Figure 4.2: SVD spatial pattern along the bunches for 36 bunches and 1782 bunches with 50 ns spacing.

fit of the maxima of the average bunch positions) of the first bunches of the train (in the case of 1782 bunches, all the bunches after the 100$^{\text{th}}$ one have almost the same rise time). The first bunch is unstable as well because of the multiturn wake functions (i.e. wakes coming from the previous turns), which makes the difference between beam break-up (present in linear accelerators) and instabilities that can be found in circular rings. Indeed, if in the simulation we suppress the multiturn wakes, the first bunch of the 36-bunches train recovers stability, as can be seen in Fig. 4.4. Another interesting feature visible in Fig. 4.3 is the fact that the first bunches of the train seems to exhibit a much higher rise time than the

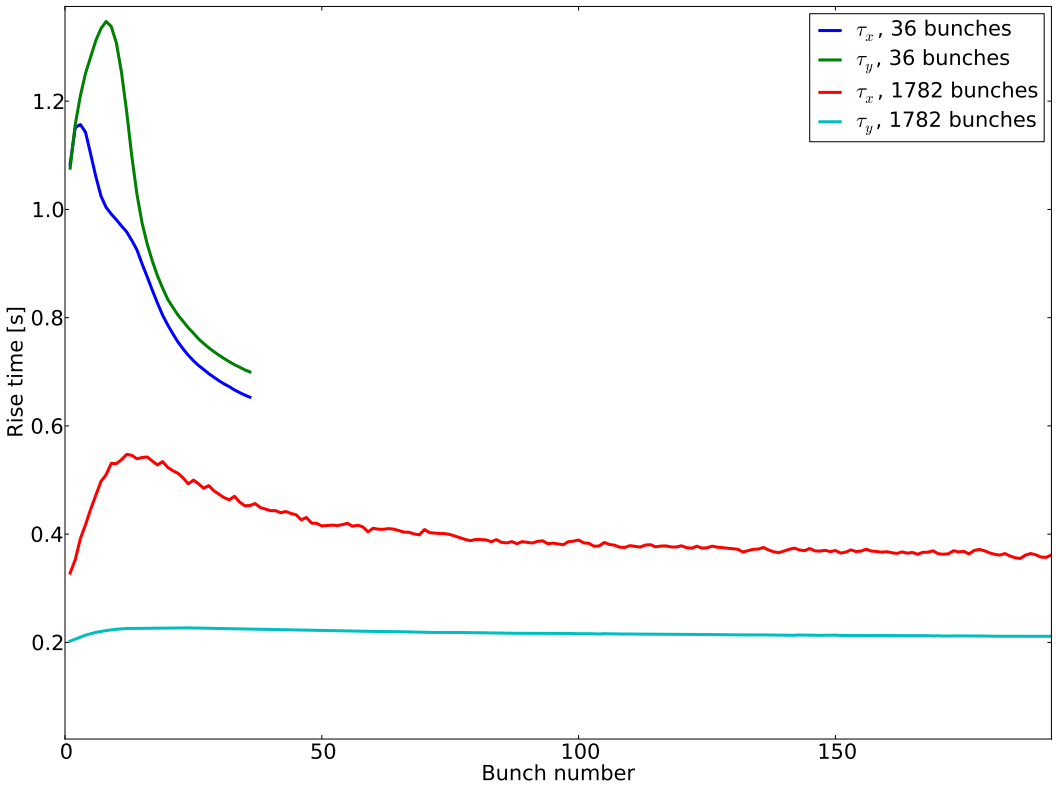

Figure 4.3: Rise times vs. bunch number (low numbers correspond to the head of the train) for 36 bunches and 1782 bunches with 50 ns spacing.

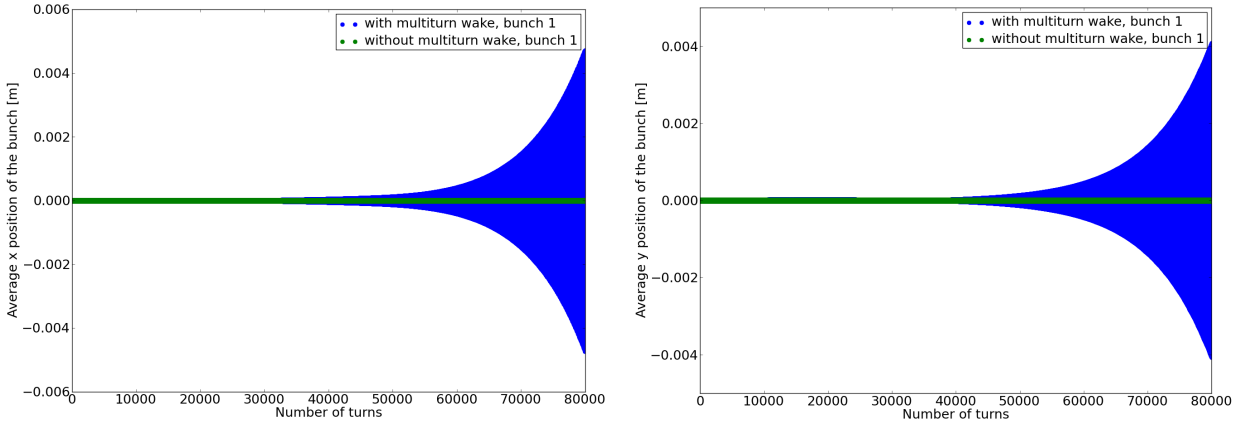

(a) Horizontal position.

(b) Vertical position.

Figure 4.4: Case of 36 bunches with 50 ns spacing: effect of the multiturn wake on the first bunch position vs. turns.

others, in particular in vertical for the 36-bunches train. As can be seen in the case of the 7th bunch in Fig. 4.5, this behaviour is actually due to a kind of decoherence happening after a high number of turns, which prevents an accurate fitting of the rise time when the number of turns is too low. This effect seems related to the presence of quadrupolar wake functions as it disappears when only the dipolar terms are used in the simulations (note that the coupled-terms are less likely to be responsible for this effect, as they are much smaller than the quadrupolar terms – see Fig. 2.15 in Section 2.3.3). Indeed, as can be seen in Fig. 2.15d, the vertical quadrupolar wake function is higher than the horizontal one for intermediate distances behind the source (in particular for the bunch spacing which is of 15 m), which would explain why this effect is higher in the vertical plane. A tentative explanation of this effect could be the fact that the detuning due the quadrupolar impedance is dependent on the z position of the macroparticle in the bunch, so on the longitudinal motion, and therefore entails the same kind of decoherence as the chromaticity. Then, after several bunches the z-independent detuning due to the previous bunches becomes dominant with respect to the z-dependent intrabunch detuning, which could explain why this effect disappears after several bunches.

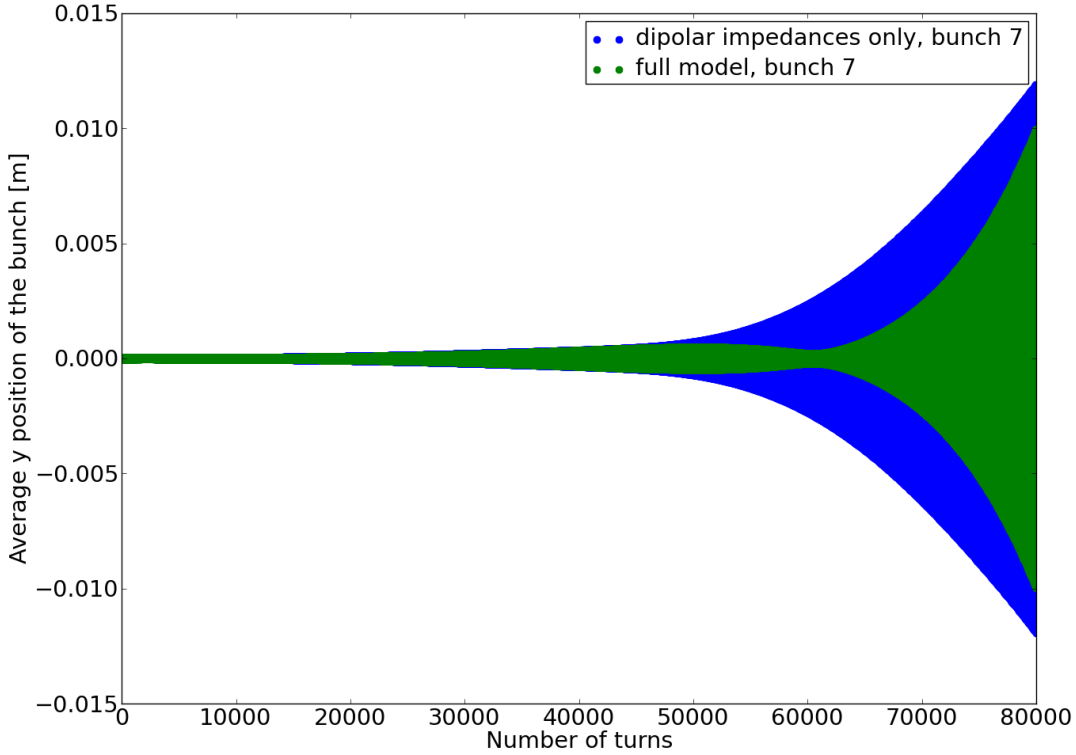

Figure 4.5: Case of 36 bunches with 50 ns spacing: position of the seventh bunch vs. turns, with the full impedance model and with dipolar impedances only.

4.2 Coupled-bunch instabilities with intrabunch activity

Intrabunch coherent modes (called headtail modes) cause instabilities even with a single-bunch in the machine, in particular if the chromaticity is positive. In May 2010 [110], such modes were found to be

responsible for instabilities developping during the first ramp performed with a high intensity bunch (i.e. $N_b \approx 1 \cdot 10^{11}$), and were suppressed thanks to the octupole magnets, which create some artificial non-linearity that damp instabilities through the mechanism of Landau damping. Basically, Landau damping (often considered schematically as the "immune system" of a beam) damp any instability that is not too strong, or more precisely that is such that the complex tune shift associated with the instability is not outside of a certain region in the complex plane called the stability diagram [120]. In the present state of the LHC, headtail modes can be suppressed only through Landau damping, as their intrabunch motion cannot be detected and damped by the current transverse feedback system.
When many bunches are in the machine, one needs to know if the coupled-bunch counterparts of those headtail modes (in other words coupled-bunch modes with intrabunch motion) could be stronger than the single-bunch headtail modes. Using the parameters of Table 4.1 except for Q', set to 6 in both planes, the intensity N_b, set to $3 \cdot 10^{11}$ protons per bunch (to artificially enhance the instability and be able to observe it in much less number of turns than at nominal intensity), and the number of slices and of macroparticles set to $n_{sl} = 50$ and $n_{MP} = 250000$ (taking higher values because intrabunch motion needs to be more accurately simulated), we compare for the horizontal plane a train of 36 bunches with a single-bunch in Fig. 4.6. The rise time of the train is slightly lower than the single-bunch one, in this case.

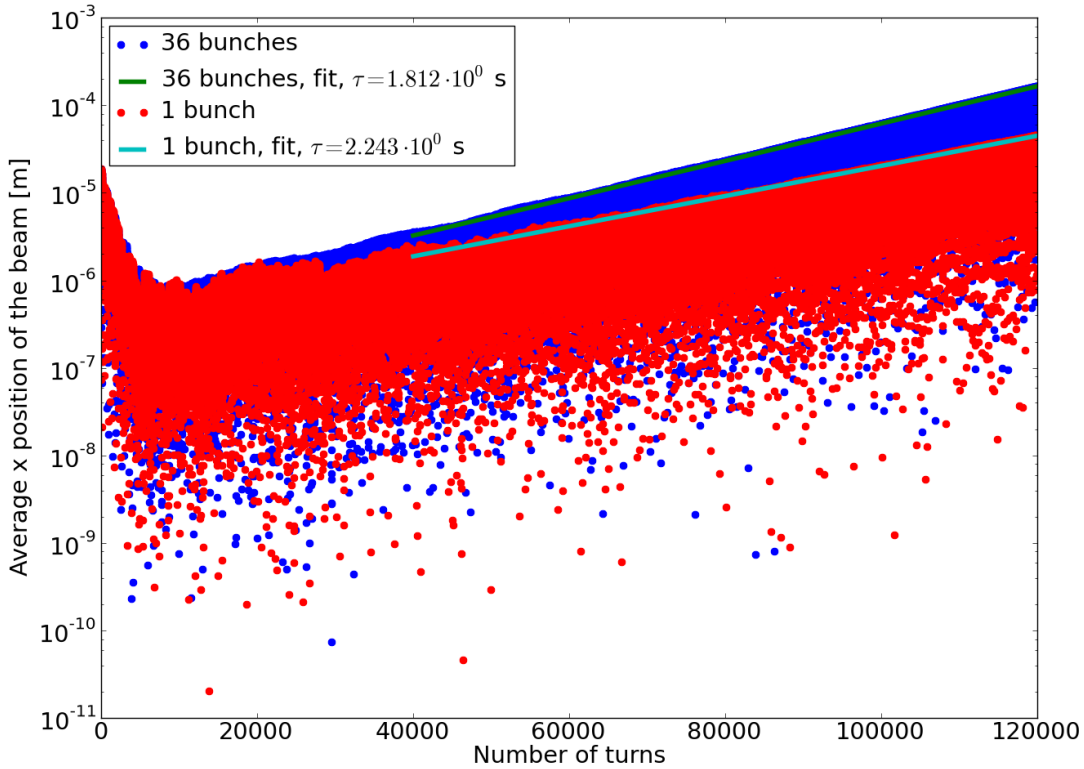

Figure 4.6: Horizontal beam average position vs. turns for a single bunch and for 36 bunches with 50 ns spacing at 3.5 TeV/c, with $Q'_x = 6$ and $N_b = 3 \cdot 10^{11}$.

An intrabunch mode with one node (i.e. a headtail mode with $|m| = 1$) is clearly visible in Fig. 4.7a, and the coupled-bunch nature of the spatial pattern from the SVD in Fig. 4.7b. It is interesting to note that the coupled-bunch spatial pattern has a much smaller wave-length in vertical than in horizontal. Finally, the spectrum, computed with SUSSIX, of the horizontal and vertical time pattern from the SVD is shown in Fig. 4.8, and it clearly appears that the main peaks are located at $-Q_s$ from the tune, indicating a $m = -1$ headtail mode.

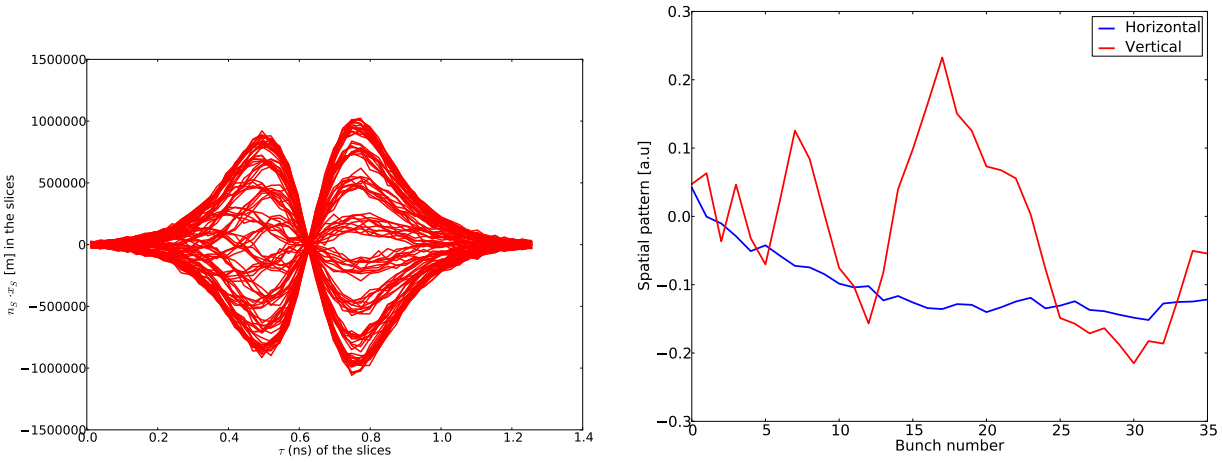

(a) Horizontal bunch profile of the last bunch.

(b) SVD spatial pattern of the highest λ_k.

Figure 4.7: Case of 36 bunches with 50 ns spacing at 3.5 TeV/c, with $Q'_x = Q'_y = 6$ and $N_b = 3 \cdot 10^{11}$: intrabunch and coupled-bunch motion.

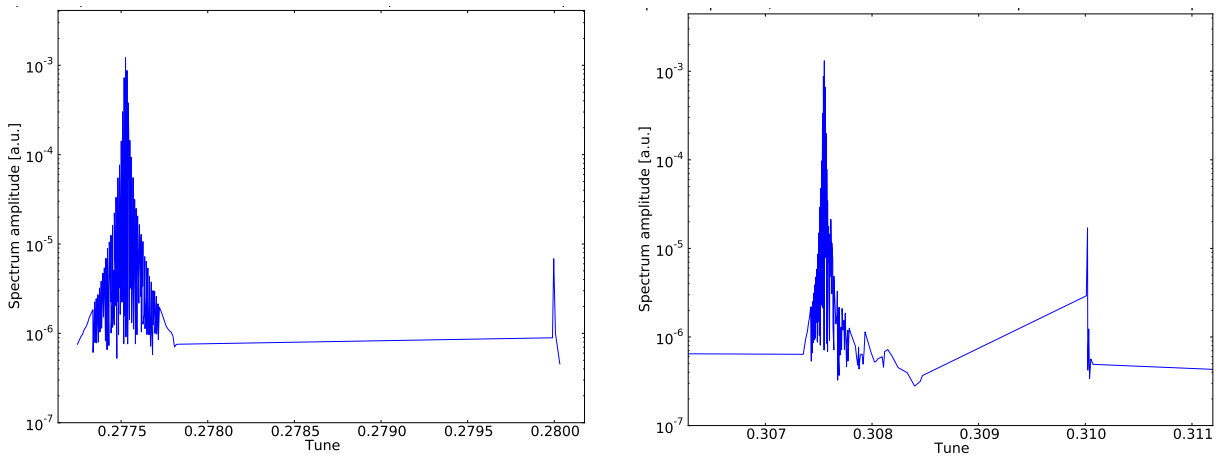

(a) Horizontal plane.

(b) Vertical plane.

Figure 4.8: Tune spectrum, computed with SUSSIX [112], of the SVD time pattern of the highest λ_k, for 36 bunches with 50 ns spacing at 3.5 TeV/c, with $Q'_x = Q'_y = 6$ and $N_b = 3 \cdot 10^{11}$.

In Table 4.2 we compare the tune shifts (with respect to $Q - Q_s$) and the rise times for the single-

bunch and 36-bunches cases. The values were obtained thanks to the spectral analysis on complex frequencies described in Section 3.2.1, performed on the time pattern from the SVD decomposition seen in Section 3.2.2 for the 36-bunches case. Clearly, the rise times are lower and the tune shifts significantly higher in the 36-bunches case with respect to the single-bunch one. Therefore, enhancement of the headtail modes with many bunches has to be expected, and higher current in the octupoles needed to damp them.

Table 4.2: Rise times and tune shifts for the single-bunch and 36 bunches cases (50 ns spacing) at 3.5 TeV/c, with $Q' = 6$ and $N_b = 3 \cdot 10^{11}$.

	τ_x [s]	τ_y [s]	ΔQ_x	ΔQ_y
1 bunch	2.25	2.45	$4.1 \cdot 10^{-6}$	$4.1 \cdot 10^{-5}$
36 bunches	1.74	1.95	$2.9 \cdot 10^{-5}$	$5.7 \cdot 10^{-5}$

4.3 Experimental results vs. simulations

To validate the full process (theory, LHC impedance model and wake fields multibunch simulation code), a beam-based experiment was performed in the LHC on May 8th, 2011. The idea was to trigger coupled-bunch instabilities and measure their rise times, at both injection energy and 3.5 TeV/c, with nominal bunch intensities and 50 ns spaced bunches. As it was seen in the previous section, small trains give rise to instabilities only a few times weaker than those of a fully filled machine, so the measurements were performed on a quite small number of bunches: a single batch of 36 bunches spaced by 50 ns, preceded by 12 bunches (also 50 ns spaced), as required by the injection system.
The advantage of using such small number of bunches is first to minimize the potential danger for the machine when triggering instabilities with a high intensity beam (although in principle the dump system of the LHC [84, chap. 17] is able in any case to prevent any incident by deviating the beam out of the ring, when too high losses around the machine are seen, in particular in the case of such slow instabilities). Moreover, if we had been using many more bunches, an electron cloud could appear (i.e. electrons created through secondary emission of the beam pipe surface receiving some primary electrons from e.g. photoemission), which also gives rise to instabilities. Actually, at the time when the experiment was performed, the LHC had been "scrubbed" [121], i.e. the beam pipe surface had been treated in such a way as to emit much less secondary electrons, thanks to long periods of operation with many bunches at injection energy. This means that a relatively small amount of electron cloud is created even when many batches of 36 bunches are circulating in the machine, without detrimental effects on the beam. In the case of our experiment, the fact that the machine had been scrubbed added to the small number of bunches clearly minimized the chance to get effects from the electron cloud, which have therefore been totally neglected in our analysis.
As already demonstrated in the previous sections and chapter, coupled-bunch instabilities are in principle always developping, whatever the chromaticity, if there are no or too weak non-linearities in the machine. During normal operation, they are prevented by a transverse feedback system which gives kicks conteracting any detected oscillation of the bunch centroids. The way to observe instabilities is therefore simply to switch off the feedback system during a certain amount of time. In addition, to allow instabilities to develop at top energy (3.5 TeV/c), Landau damping had to be reduced by decreasing the current in the octupoles.

4.3.1 Description of the experiment

Three measurements sequences took place during the experiment: two at injection energy (450 GeV/c), and one at top energy (3.5 TeV/c). At injection energy, the main manipulations done during each measurement sequence were the following:

- for each beam (except for the first measurement sequence where only beam 2 could be injected), injection of 48 bunches from the SPS: a first batch a 12 bunches separated by 50 ns, followed 925 ns later by a second batch of 36 bunches, also separated by 50 ns[1],
- adjustment of the chromaticities to values close to zero, or to slightly negative values,
- switching off the transverse feedback (both beams and both planes) during a time window long enough to allow an instability to develop, but not too long to avoid high beam losses.

The last two steps were repeated several times in order to get measurements of the instability rise times for several values of the chromaticities.
For the measurement at top energy, after injection (first step above), the ramp to 3.5 TeV/c was done, followed by the measurement and adjustment of the chromaticity. The octupole currents were then put to a high value before reducing them by steps until some instability develops during the time window when the feedback is switched off (see last step above). Note that the defocusing octupoles are set to a positive current and the focusing ones to its opposite.
Several data acquisitions processes were triggered during the time window when the feedback was off, acquiring in particular the beam position monitors (BPM) data, the headtail monitor signal and the transverse feedback pickups (called ADT in the following) data. The BPMs acquire the positions of the individual bunch centroids for the last 36 bunches of the train during 1000 successive turns (i.e. 89 ms), the headtail monitor acquire the individual horizontal or vertical profile of all the bunches for 100 successive turns (i.e. 8.9 ms), and the ADT acquire individual bunch centroid positions of the 8 last bunches of the train for 32768 turns (i.e 2.9 s). The most reliable of those instruments were the ADT pickups, because of their better resolution as well as their ability to record a high number of turns, which was required for coupled-bunch instabilities developping with rise times of the order of the second. Note that in the data analyses that will follow, the position data from the ADT have been pretreated, eliminating some isolated and artificial peaks and subtracting the sliding average over 20 turns to avoid high amplitude low frequency noise that caused the observation to be much less clear.
In addition to these three kinds of measurements specifically set up for the experiment, other data were continuously logged in the measurement database as during any LHC run. In particular, we will use in the following the FBCT (fast beam current transformer) which gives the individual bunch intensity (i.e. number of particles), and the BQM (beam quality monitor) for the individual bunch lengths. Collimator half gaps were also continuously monitored; at injection and flat top their measured values are those of Tables F.1 and F.2. A few wirescans measurements were also done, to get the beams normalized emittances along the experiment.
All the parameters used in the HEADTAIL simulations to calculate the rise times corresponding to the measurements are based on actual data and can be found in Table 4.3.

[1] A so-called “pilot bunch” was also injected before those 48 bunches, but its number of particles is ten times lower than each of the other bunches so it has been neglected in the simulations.

Table 4.3: LHC parameters during the measurements and in HEADTAIL simulations, for all the cases studied. For the simulations, perfect longitudinal matching was assumed as well as a non-linear RF bucket.

Beam	2	2	1	2	1	2	1	2
Q'_x / Q'_y	2 / 2	1 / −0.5	0.4 / 0.3	0.1 / −0.6	−0.6 / −0.7	−0.9 / −1.6	0 / 2	0 / 1
N_b	$1.2\cdot10^{11}$	$1.2\cdot10^{11}$	$1.21\cdot10^{11}$	$1.21\cdot10^{11}$	$1.18\cdot10^{11}$	$1.2\cdot10^{11}$	$1.22\cdot10^{11}$	$1.18\cdot10^{11}$
σ_z [m]	0.105	0.105	0.097	0.097	0.103	0.103	0.085	0.091
σ_δ	$3.8\cdot10^{-4}$	$3.8\cdot10^{-4}$	$3.4\cdot10^{-4}$	$3.5\cdot10^{-4}$	$3.7\cdot10^{-4}$	$3.7\cdot10^{-4}$	$1.6\cdot10^{-4}$	$1.7\cdot10^{-4}$
ε_x^n / ε_y^n [mm.mrad]	2.5 / 2.7	2.5 / 2.7	2.5 / 2.3	2.9 / 3	2.5 / 2.3	2.9 / 3	2 / 1.9	2.3 / 2.8
γ	479.6						3730.26	
V_{rf} [MV]	6						12	
Q_s	$4.905\cdot10^{-3}$						$2.504\cdot10^{-3}$	
h	35640							
Circ. [m]	26658.883							
Q_x / Q_y	64.28 / 59.31							
β_x / β_y [m]	66.006 / 71.538							
α_p	$3.225\cdot10^{-4}$							
n_{sl}	50							
n_{MP}	250000							
n_{wake}	19							

4.3.2 Results at injection

Several instabilities were observed with the ADT during the time windows when the transverse feedback was off, for both beams and both planes. We show in Fig. 4.9 exemples of such instabilites, in terms of the turn by turn position of the last bunch of the train measured with the ADT.
From the spectral analysis of the individual bunches, no particular tune shift trend was observed along the 8 bunches. For a given chromaticity, and neglecting the small differences in bunch length and bunch intensities (of at most 8%) between different measurements, we put together all the available ADT measurements showing clear instabilities, fitting them with two different methods (fit of the curve maxima and of the amplitude of the largest spectrum line obtained with SUSSIX [112]), obtaining then the average rise times for each of the 8 last bunches of the train, and the standard deviation due to both the fitting and the data repetition. We show the results in Fig. 4.10, together with the results of HEADTAIL simulations with the same parameters as in the measurements (in particular bunch length, bunch intensities, tunes and chromaticities – see Table 4.3). In those cases, the agreement between simulations and experimental data is very good. For those 8 bunches, a small trend on the rise times is visible in the simulation data, the rise times decreasing slightly toward the tail of the bunch train, but this is not visible in the measurements for which the accuracy is clearly not good enough to see such a small trend.
Averaging then the rise times of the 8 bunches obtained from the ADT data, we can give for each chromaticity an average measured rise time, together with its standard deviation coming from the fact that many different measurements and even ways of fitting the data were taken into account. We compare in Figs. 4.11 and 4.12 those to the rise times obtained at the same chromaticities thanks to HEADTAIL simulations, where the instability comes from rigid-bunch (headtail mode $m = 0$) coupled-bunch motion. Note that in the case of HEADTAIL simulations, the three different methods to obtain the rise time presented in Section 3.2.1 give very similar rise times. The agreement between the measurements and HEADTAIL simulations with 48 bunches is remarkable for negative chromaticities and chromaticities

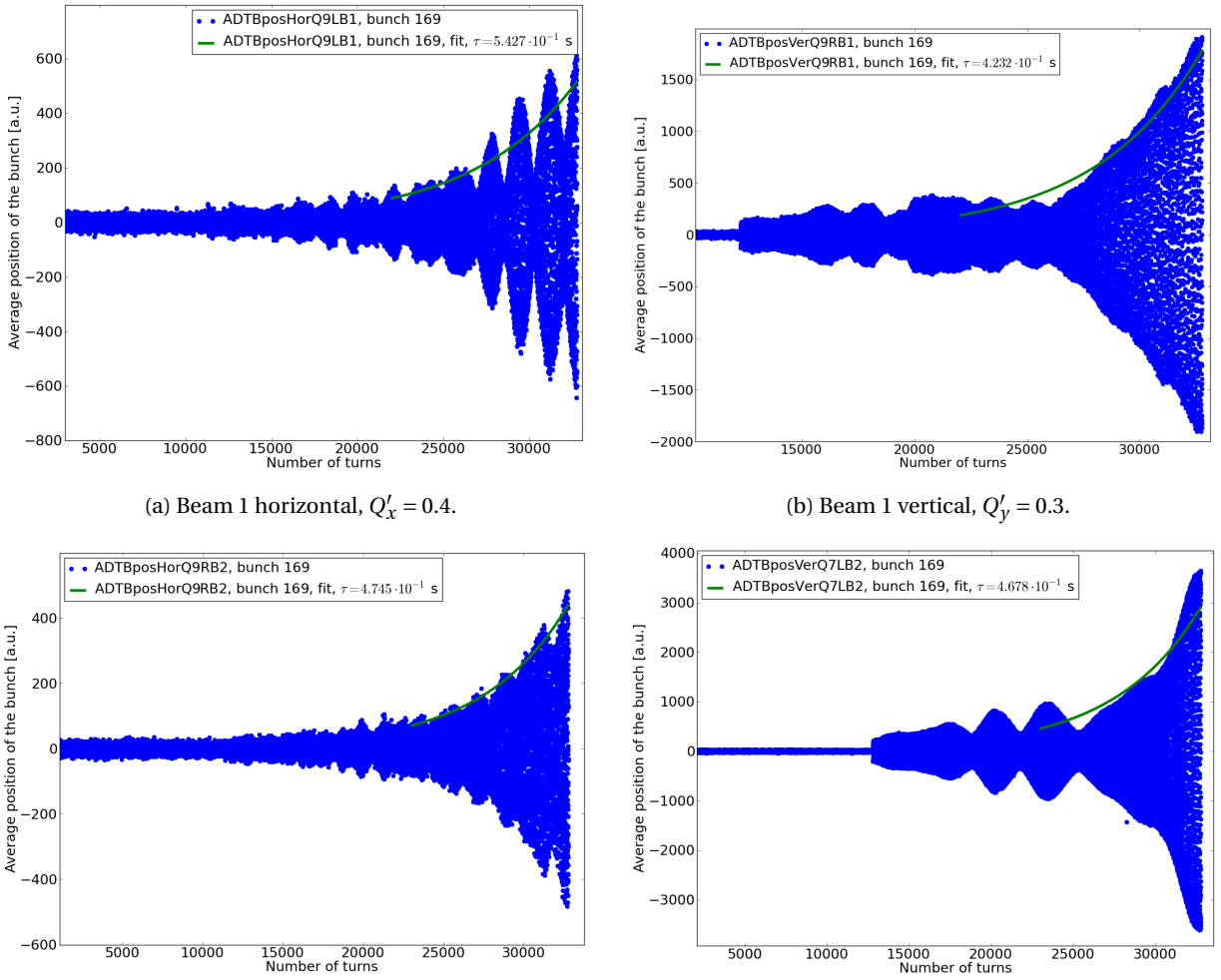

(a) Beam 1 horizontal, $Q'_x = 0.4$.

(b) Beam 1 vertical, $Q'_y = 0.3$.

(c) Beam 2 horizontal, $Q'_x = 0.1$.

(d) Beam 2 vertical, $Q'_y = -0.6$.

Figure 4.9: Signal from the ADT pickups during an instability measured at 14h46 (local time), for the last bunch of the train. In the legend are indicated the name of the pickup measuring this signal, and the slot occupied by the last bunch (in terms of 25 ns slots).

close to zero, for both beams and both planes. The only significant discrepancy appears for beam 2 in vertical when $Q'_y = 2$. Note that in this case the error bar on the measurement does not reflect the real error, as only one set of data and one fitting method could be used to get the measured rise time.
Comparison between the single-bunch and coupled-bunch rise times from the simulations seems to rule out the possibility that the instabilities observed are actually single-bunch. For beam 1, only the cases with negative chromaticities reveals some instabilities (at least with simulations of 200000 turns, i.e. 17.8 s), with rise times far above the coupled-bunch rise times as can be seen in Fig. 4.11. For beam 2, the single-bunch rise times of the cases where an instability is detectable in 200000 turns, are shown in Fig. 4.12, and again are much higher than the coupled-bunch ones.
Also, in certain cases the spatial pattern of the most critical λ_k from the singular value decomposition of the BPM data (see Section 3.2.2) clearly exhibit a coupled-bunch motion along the batch containing 36 bunches. This is shown in Fig. 4.13 in the particular case of the vertical plane of beam 1 for $Q'_y = 0.3$.

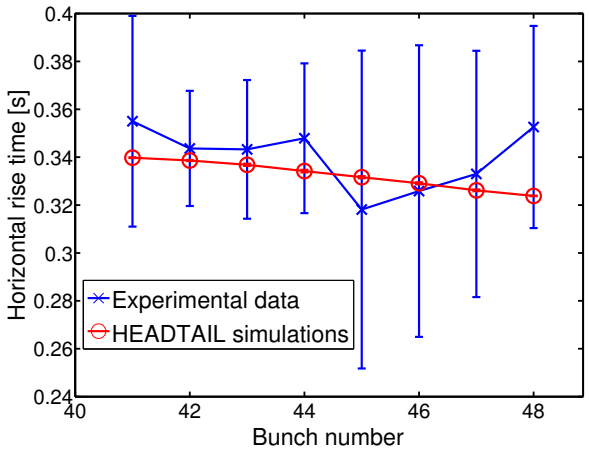

(a) Beam 1 horizontal, $Q'_x = -0.6$.

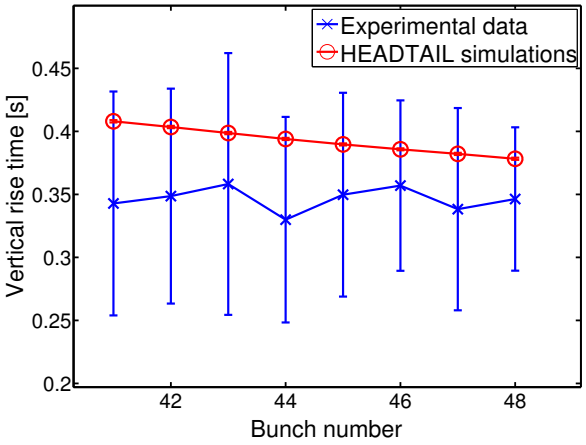

(b) Beam 1 vertical, $Q'_y = 0.3$.

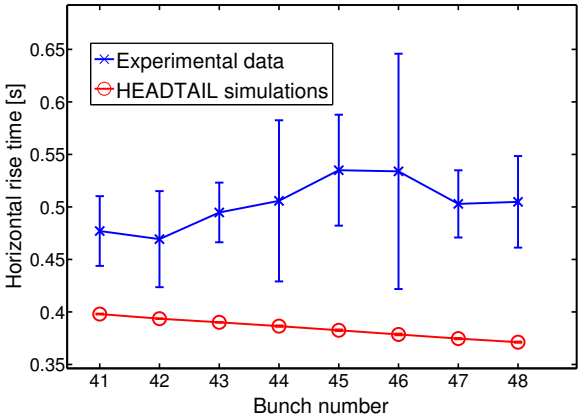

(c) Beam 2 horizontal, $Q'_x = 0.1$.

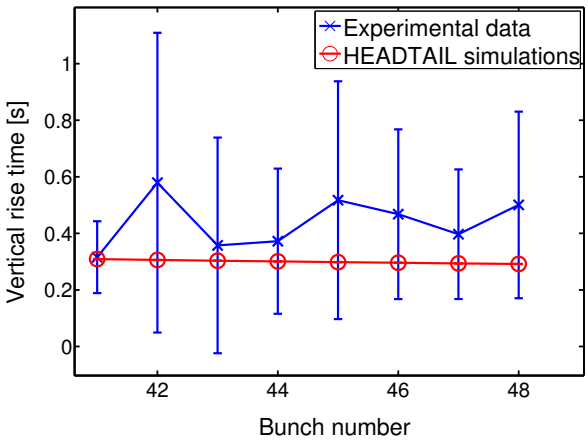

(d) Beam 2 vertical, $Q'_y = -0.5$.

Figure 4.10: Rise times of the last 8 bunches of the train at injection energy, for various chromaticities, and comparison with HEADTAIL simulations.

Unfortunately, not all the BPM data exhibit such a clear coupled-bunch behaviour, probably because of the rather poor precision of the measurement as well as the lack of turns (only 1000 turns are recorded).

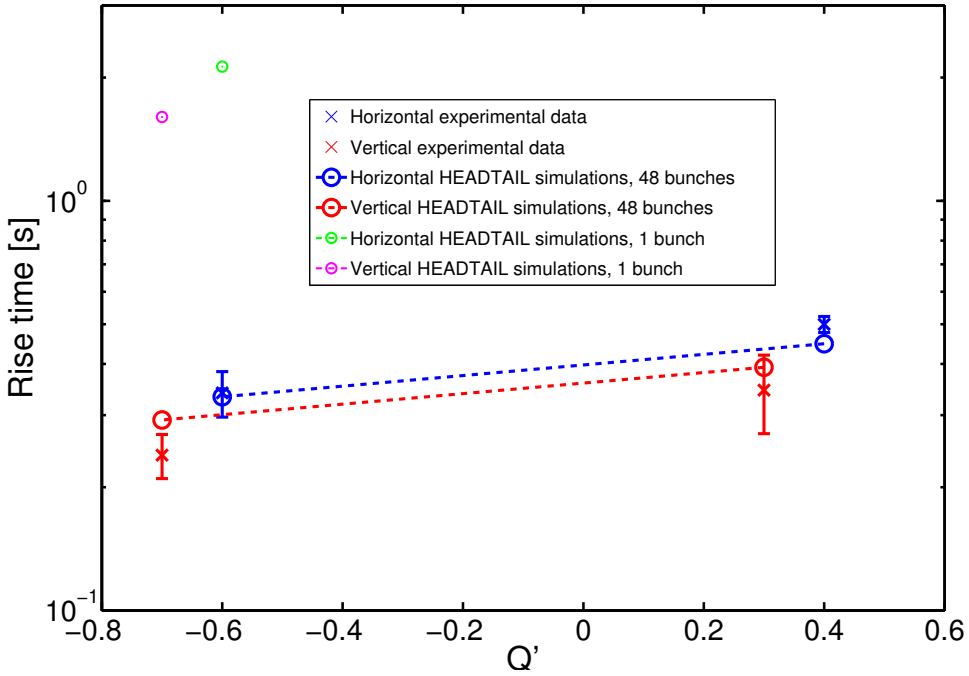

Figure 4.11: Rise times vs. Q' for beam 1 at injection: measurements and HEADTAIL simulations. Simulation results in the single-bunch case are also shown.

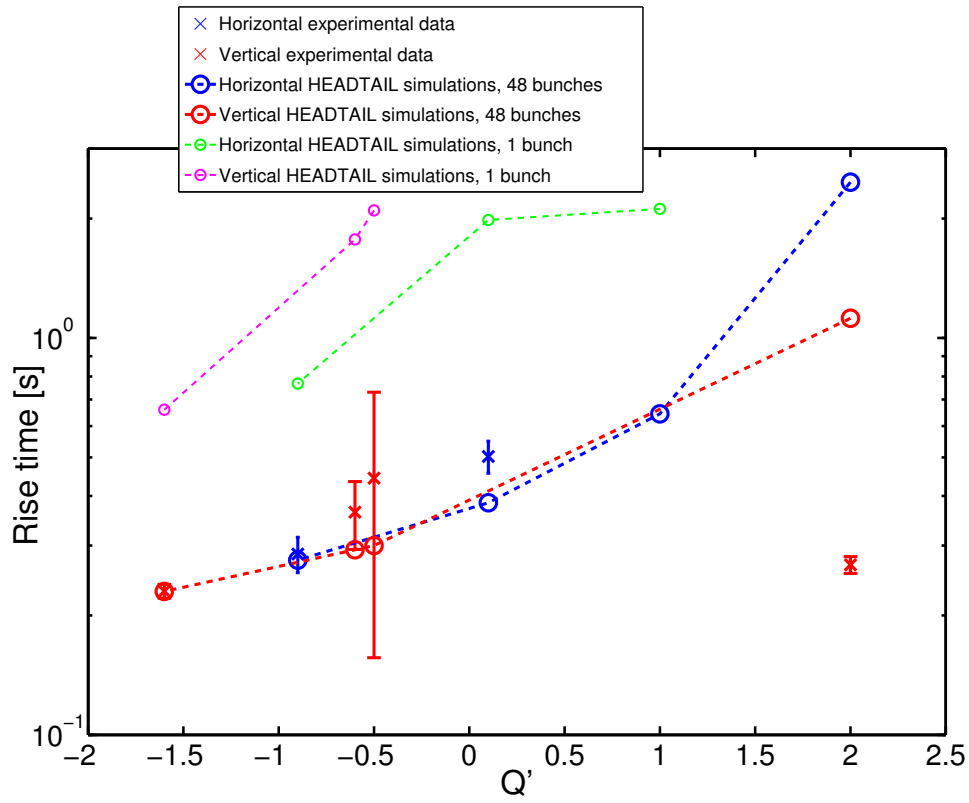

Figure 4.12: Rise times vs. Q' for beam 2 at injection: measurements and HEADTAIL simulations. Simulation results in the single-bunch case are also shown.

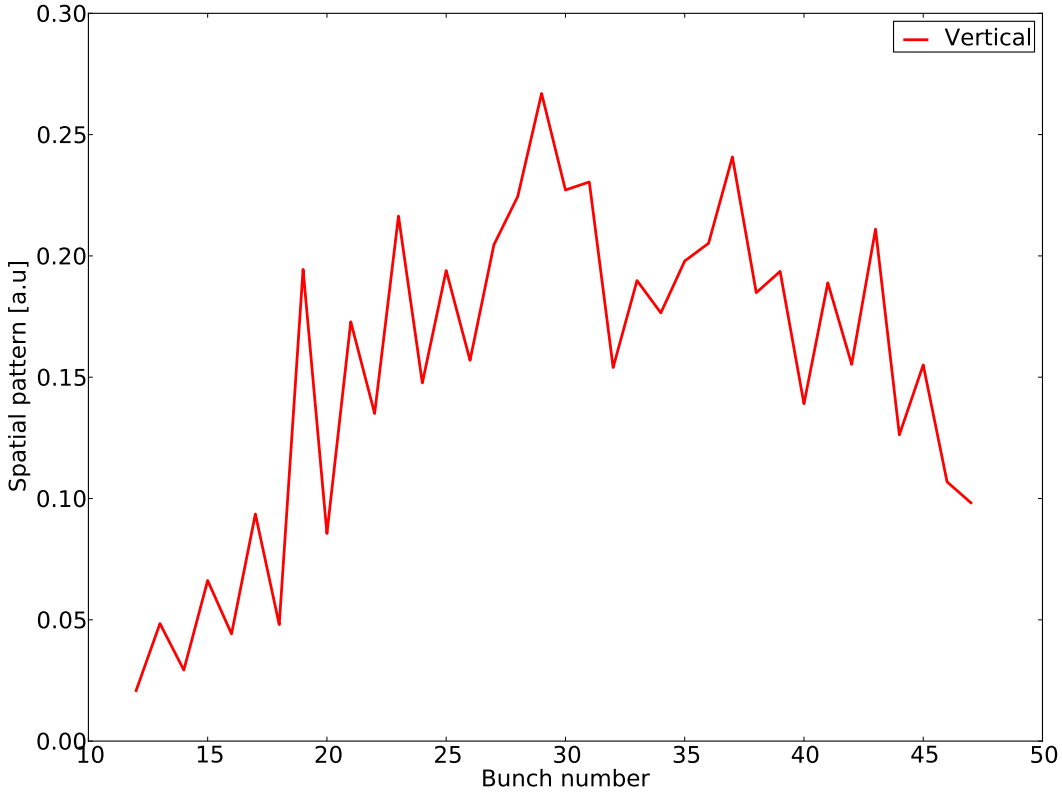

Figure 4.13: Spatial pattern of the highest λ_k in the singular value decomposition of the LHC-BPMs data, for the vertical plane of beam 1 with $Q'_y = 0.3$, at injection.

4.3.3 Results at flat top

After the ramp to 3.5 TeV/c, decreasing the octupole currents enabled us to observe instabilities on the ADT during the time window when the feedback was off, as shown in Fig. 4.14. All the instabilities observed occurred in the vertical plane.
HEADTAIL simulations were performed in the same conditions as the measurements (see parameters in Table 4.3). For octupole currents close to the stabilization value, the average beam position versus turns is shown in Fig. 4.15, for the horizontal plane as only this plane got unstable when the octupole currents were different from zero. This can be explained by the fact that $Q'_x = 0$ while $Q'_y \geq 1$ for both beams, such that instabilities in the horizontal plane are more critical than in the vertical plane (given the fact that the dipolar wake functions are quite similar for both planes at this energy, see Fig. 2.15). Then, as soon as the horizontal plane gets unstable, the beam average positions grow and the vertical plane gets stabilized by the action of the octupoles which couple both planes, thus preventing any unstable mode to grow in vertical except for $I^D_{oct} = I^F_{oct} = 0$. The fact that in the measurement it is on the contrary the vertical plane which is the most unstable means either that the impedance model in the vertical plane should contain additional contributions, or that the chromaticity measured during the experiment (which is the critical factor here) is incorrect, which could be the case as it is quite difficult to measure the chromaticity at 3.5 TeV/c.

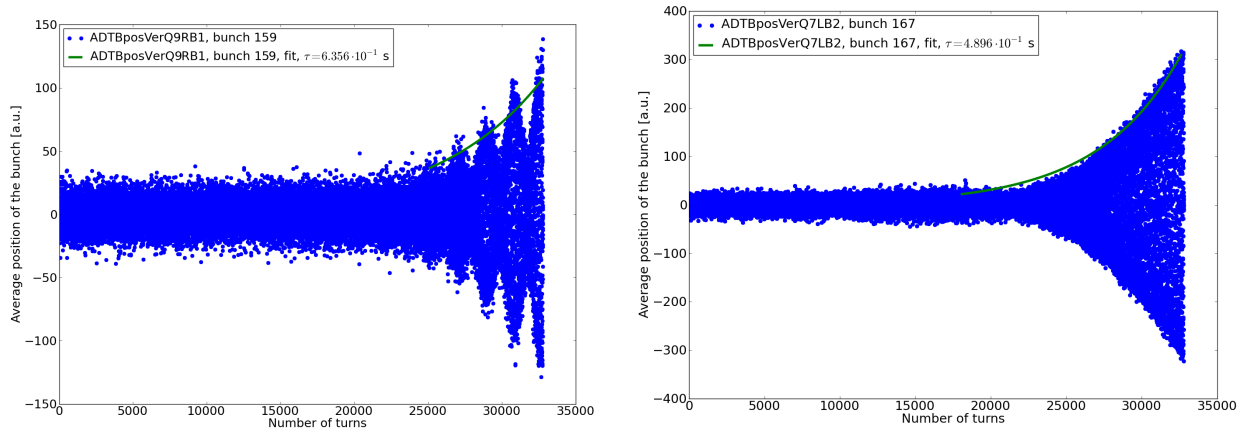

(a) Beam 1 vertical, $I^D_{oct} = -I^F_{oct} = 20$ A.

(b) Beam 2 vertical, $I^D_{oct} = I^F_{oct} = 0$ A.

Figure 4.14: Average bunch position vs. turns in the ADT at 3.5 TeV/c.

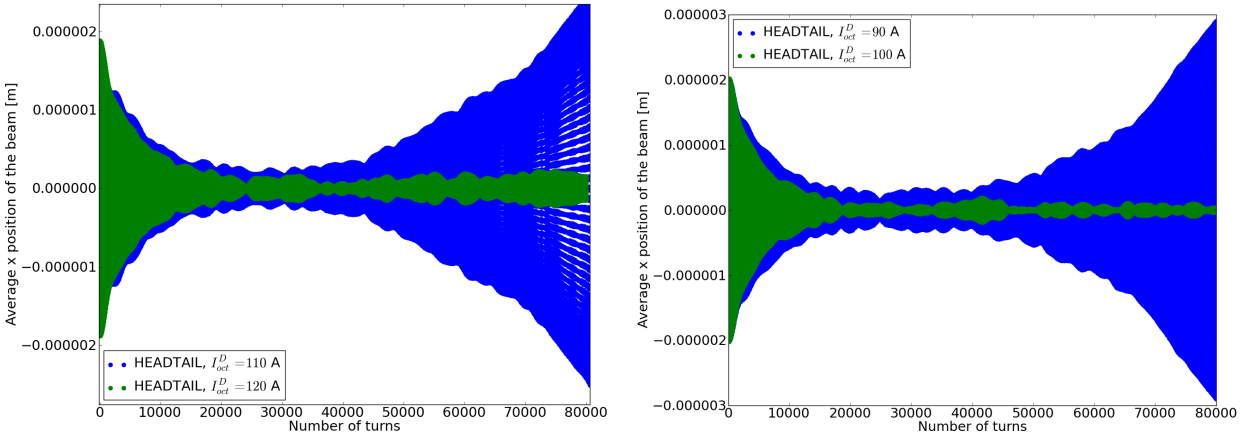

(a) Beam 1 horizontal.

(b) Beam 2 horizontal.

Figure 4.15: Average beam position vs. turns according to HEADTAIL, with octupoles and at 3.5 TeV/c.

Results concerning the stabilization currents, both in the measurements and with HEADTAIL simulations, are summarized in Table 4.4. HEADTAIL simulations require more currents in the octupoles to stabilize the beams than in the ADT measurements, meaning either that the impedance model is too pessimistic, or that Landau damping is more efficient than foreseen. The latter case could be explained by the fact that we neglected in the simulations some sources of non-linearity providing damping such as Q'' (second derivative of the tune with respect to the momentum deviation) or the direct space-charge, or that the transverse bunch profile is quite different from a Gaussian profile.
For the cases when the octupoles were completely switched off, comparison between HEADTAIL simulations (where the instability comes from rigid-bunch coupled-bunch motion) and the rise times on the 8 last bunches of the train obtained with the ADT, is shown in Fig. 4.16. The HEADTAIL simulations bunch positions were fitted with each of the three methods described in Section 3.2.1, except for the beam 1

case where only two methods could be used, because the one consisting in fitting the amplitude of the main spectrum line failed. Note the quite large error bars on the simulation data, indicating probably that a higher number of turns would be better to fit the data with a better accuracy. The measurements and simulations have a significant discrepancy of a factor between 2 and 3, which might well be due to the uncertainty on the chromaticity value in the vertical plane. On the other hand, a similar trend along the bunch train is visible in both the measurements and the simulations data, the rise time decreasing when going toward the tail of the train.
Finally, all the vertical rise times that could be obtained from the ADT data were collected and are shown in Figs. 4.17 and 4.18, together with HEADTAIL simulations results when the octupoles are switched off. The discrepancy already mentioned appears clearly. If instead a chromaticity of zero is assumed in the vertical plane, this discrepancy is much reduced. Its seems that for both beams the measured rise times increase with higher octupole currents, although this trend stays within the error bars.

Table 4.4: Currents in the defocusing octupoles required to stabilize the beam at 3.5 TeV/c, according to the ADT data and HEADTAIL simulations. The focusing octupoles are set to the opposite of this current.

	Beam 1	Beam 2
ADT	60 A	70 A
HEADTAIL	120 A	100 A

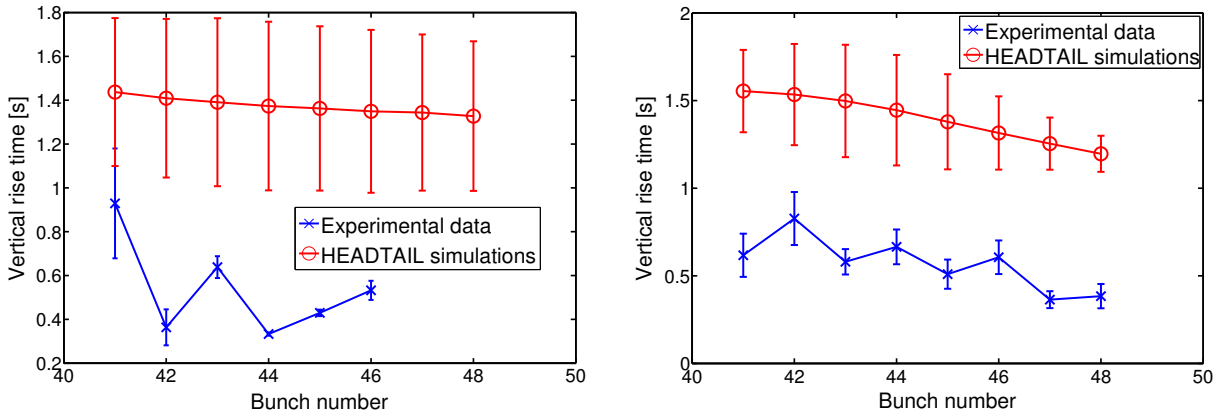

(a) Beam 1 vertical, $I^D_{oct} = I^F_{oct} = 0$ A.

(b) Beam 2 vertical, $I^D_{oct} = I^F_{oct} = 0$ A.

Figure 4.16: Rise times of the last 8 bunches of the train when octupoles are off at 3.5 TeV/c, and comparison with HEADTAIL simulations.

4.4 Several predictions at 7 TeV/c

For the future operation of the LHC at a higher energy (which will take place after the long shutdown in 2013 and 2014), it is useful to make predictions concerning the beam stability under foreseen conditions. We study here particularly the case of 1404 bunches with a 50 ns spacing, which is an important challenger of the initially foreseen 2808 bunches scheme with 25 ns spacing, because the 50 ns spacing allow much lower normalized RMS emittances than the nominal ones (2 mm.mrad instead of 3.75 mm.mrad)

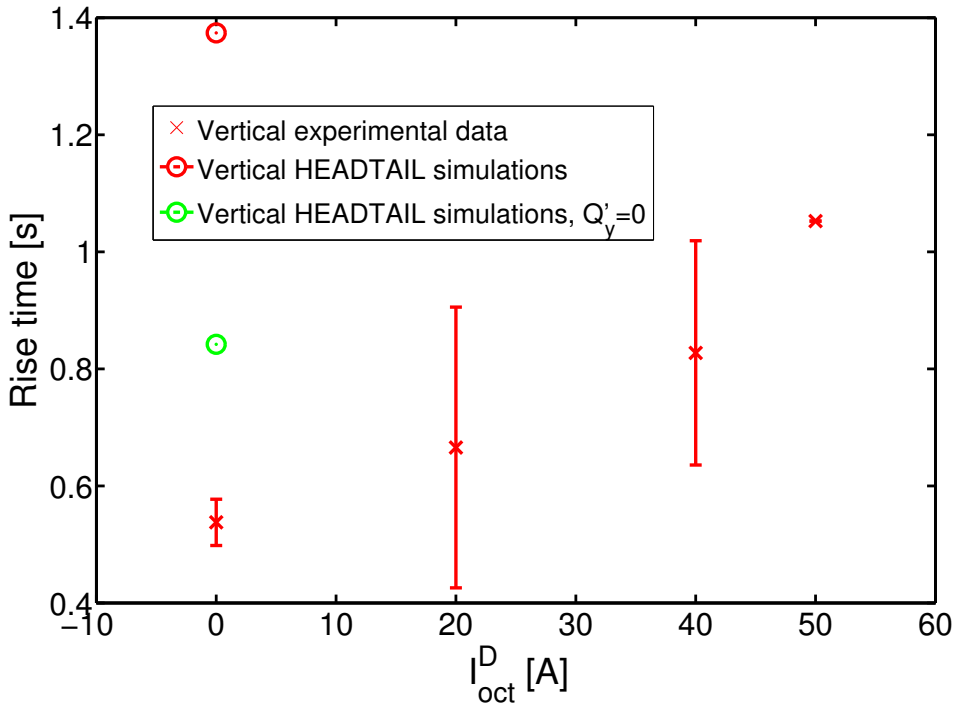

Figure 4.17: Measured vertical rise times vs. octupole current for beam 1 at 3.5 TeV/c, compared to HEADTAIL simulations at zero octupole currents. Results of the simulation with $Q'_y = 0$ are also shown.

and higher bunch intensities than $1.15 \cdot 10^{11}$ protons per bunch. Then, smaller emittances means less Landau damping, which is not necessarily a problem in the case of coupled-bunch rigid modes as those observed in the previous section, because they should be damped by the transverse feedback system. On the other hand this could become a problem for higher order modes, i.e. coupled-bunch modes with intrabunch motion as seen in Section 4.2, because those cannot be damped by the current transverse feedback system.

Another potential limitation comes with higher bunch intensities, as the transverse mode coupling instability [106, 118] (TMCI), also called "strong headtail" instability, appears above a certain intensity threshold when different headtail modes couple to each other. This kind of instability, involving intrabunch motion, cannot be damped by the current transverse feedback system of the LHC, and can already be a limitation with one single bunch in the accelerator. It becomes even more critical when many bunches are in the machine. The intensity threshold of such a coupled-bunch transverse mode coupling instability has been seen to be as low as half the single-bunch one in the case of the PEP-II ring [122].

Here we study the beam stability at 7 TeV/c using the parameters of Table 4.5 (extracted from [84] except for the transverse emittances and the bunch spacing) and the bunch scheme of Eq. (4.1) with the batches of 72 bunches replaced by batches of 36 bunches. The impedance model was computed with the parameters of the 3.5 TeV/c one (see Chapter 2 and Appendix F) except for the relativistic mass factor γ (taken as in Table 4.5), the resistivity of copper in the beam screens (see Table F.7) and the half gaps of the collimators which were all divided by $\sqrt{2}$ with respect to those of beam 1 at 3.5 TeV/c (see Table F.1), to follow the transverse beam size that goes down with energy.

The coupled-bunch transverse mode coupling threshold can be identified as the number of particles

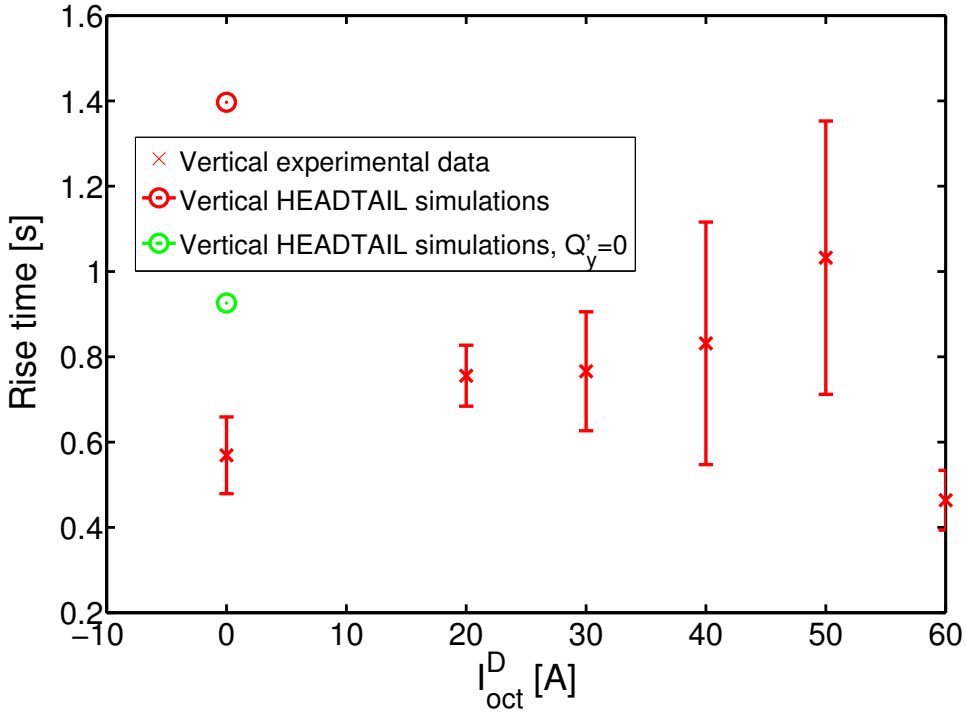

Figure 4.18: Measured vertical rise times vs. octupole current for beam 2 at 3.5 TeV/c, compared to HEADTAIL simulations at zero octupole currents. Results of the simulation with $Q'_y = 0$ are also shown.

per bunch above which the imaginary part of the tune shift (obtained thanks to a fit of the main peak amplitude from SUSSIX) deviates from a linear law with respect to the intensity N_b [107, p. 106]. According to Fig. 4.19, this threshold seems to be around $5 \cdot 10^{11}$ particles per bunch in the horizontal plane, and slightly higher in the vertical plane, at zero chromaticity. Further simulations are required to get a higher precision on this number. This is lower than the single-bunch transverse mode coupling instability threshold, which is at $6.4 \cdot 10^{11}$ particles per bunch with the same parameters, as can be seen in Fig. 4.20. Note that this threshold appears to be much higher than previous predictions [110], because the impedance model (and particularly the graphite resistivity) has been updated. It is here important to note that this threshold depends on the number of slices chosen in the simulation: in the single-bunch case, taking $n_{sl} = 500$ and $n_{MP} = 10^6$ gives a lower threshold, around $5.7 \cdot 10^{11}$. Unfortunately, simulations with 1404 bunches and significantly more slices than 20 take a much longer time and were not yet performed.

With the Gaussian transverse distributions used in the simulations, the beam is stable at nominal intensity ($N_b = 1.15 \cdot 10^{11}$) with $Q' = 2$ in both planes and when the octupole current is set to its maximum and negative in the focusing octupoles, i.e. $I^D_{oct} = -I^F_{oct} = 550$ A. With zero chromaticities at nominal intensity, and either $Q' = 0$ or $Q' = 2$ with ultimate intensity ($N_b = 1.7 \cdot 10^{11}$), the beam is unstable even when $I^D_{oct} = -I^F_{oct} = 550$ A. This can be seen clearly in Fig. 4.21, where the average beam position is plotted vs. turn numbers. This means that under nominal conditions both the rigid-bunch coupled-bunch modes and the coupled-bunch modes with intrabunch activity are harmless in the LHC, provided the transverse distributions are Gaussian, Q' is equal to 2 and the octupoles are set to their maximum currents.

Table 4.5: LHC parameters at 7 TeV/c with 50 ns spacing. Perfect longitudinal matching was assumed.

Number of bunches	1404
Total bunch length= $4\sigma_z$	0.302 m
Longitudinal momentum spread σ_δ	$1.13 \cdot 10^{-4}$
RF voltage V_{rf}	16 MV (non linear bucket)
Harmonic number h	35640
Synchrotron tune Q_s	$2.045 \cdot 10^{-3}$
Bunch spacing	50 ns
Circumference	26658.883 m
Horizontal / vertical tune Q_x / Q_y	64.31 / 59.32
Horizontal / vertical beta function β_x / β_y	65.976 / 71.526 m
Horizontal / vertical normalized RMS emittance ε_x^n / ε_y^n	2 / 2 mm.mrad
Relativistic γ	7460.52
Momentum compaction factor α_p	$3.225 \cdot 10^{-4}$
Number of slices per bunch n_{sl}	20
Number of macroparticles per bunch n_{MP}	100000
Number of turns of memory for the wakes n_{wake}	19

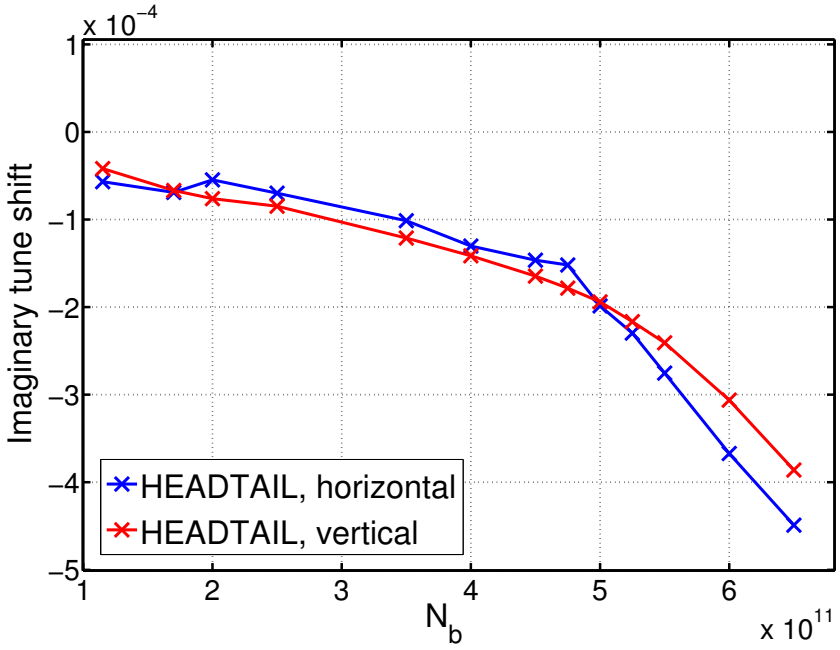

Figure 4.19: Imaginary part of the tune shifts vs. bunch intensity N_b, for 1404 bunches at 7 TeV/c, with zero chromaticites and no octupoles.

4.5 Conclusion

Thanks to the code presented in Chapter 3 and the impedance model of Chapter 2, several aspects of the transverse coupled-bunch instabilities in the LHC were described. In particular, the influence

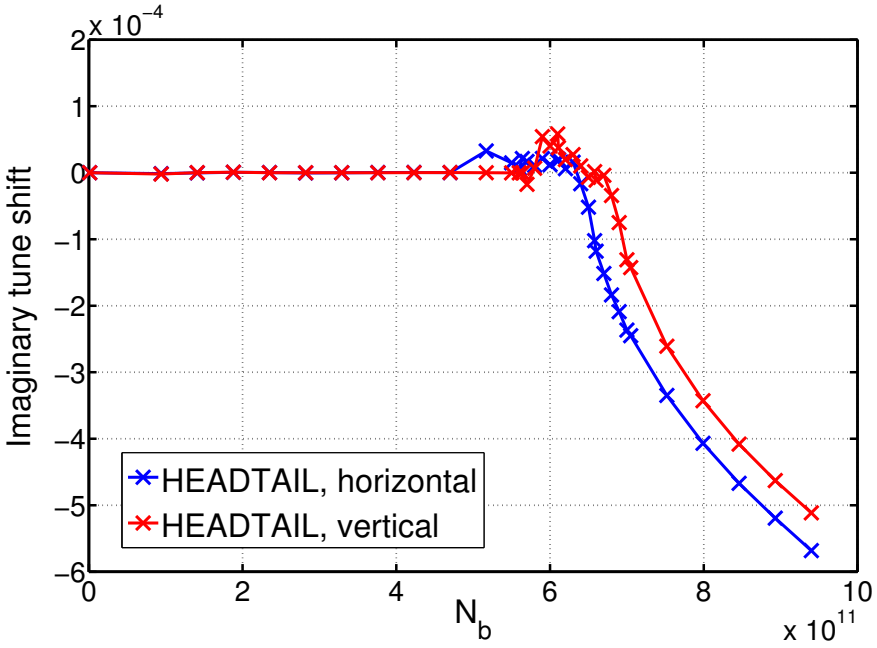

Figure 4.20: Imaginary part of the tune shifts vs. bunch intensity N_b, for a single bunch at 7 TeV/c, with zero chromaticites and no octupoles.

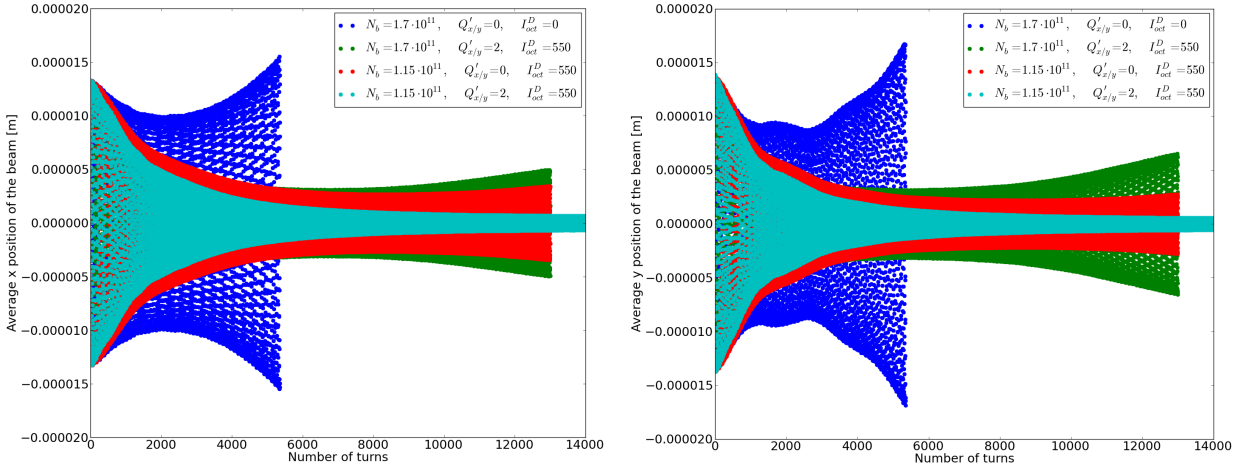

(a) Horizontal plane.

(b) Vertical plane.

Figure 4.21: Average beam transverse position vs. turns, for 1404 bunches at 7 TeV/c.

of the bunch train length with a given spacing has been seen to be rather small on the growth rate of rigid-bunch instabilities. The existence of coupled-bunch instabilities with intrabunch motion has been demonstrated thanks to simulations, and the impact of the number of bunches seems indeed not negligible on the complex tune shift of headtail modes of order higher than zero.

The accuracy of the full approach (impedance model and multibunch simulation code) was checked thanks to beam-based measurements in the LHC, revealing a remarkable agreement at injection energy, while at flat top some significant discrepancies of factor 2-3 were observed. In Appendix G, other comparisons between measurements and simulations using the LHC impedance model are presented, in the single-bunch regime, and also show a discrepancy of factor 2-3.
Finally some predictions concerning the future operation of the LHC at a momentum of 7 TeV/c were obtained, showing in particular that with 1404 bunches (50 n spacing) the coupled-bunch transverse mode coupling instability threshold is around $5 \cdot 10^{11}$ protons per bunch, about 20% lower than the single-bunch TMCI obtained with the same parameters. Also, with Gaussian distributions, the bunches are stable at nominal intensity and when $Q' = 2$ in both planes, with 550 A in the defocusing octupoles (and the opposite current in the focusing ones). At ultimate intensity with $Q' = 0$ or $Q' = 2$, and at nominal intensity with $Q' = 0$, such a current in the octupoles is not enough to stabilize the beam. Note that the transverse feedback system has not been included in the simulations.

5 Conclusion

This thesis aimed at studying several aspects of the LHC transverse coupled-bunch instabilities. To do so, new theories and algorithms were developped, that can be used in many other cases.
The first new results concern the theories of the beam-coupling impedance developped in Chapter 1. For an axisymmetric two-dimensional structure, we generalized Zotter's theories in the sense that all the azimuthal mode numbers (instead of only $m = 0$ and $m = 1$) have been considered, therefore giving the full nonlinear expression of the electromagnetic fields and forces even far from the beam orbit. For an infinite flat two-dimensional structure, we derived a completely new theory, generalizing what has been done by many other authors, and also giving the full nonlinear expression of the electromagnetic fields and forces.
Then, a new approach has been found to compute the wake functions from such analytically obtained beam-coupling impedances, overcoming limitations that could be met with a standard discrete Fourier transform procedure.
The theories and algorithms of the first chapter were extensively used in Chapter 2 to obtain an impedance and wake function model of the LHC, based on the (resistive-)wall impedances of various contributors (collimators, beam screens and vacuum pipe) and additional estimations of the geometrical impedance contributions. This model, giving longitudinal and transverse impedances as well as wake functions, can be used to study other beam dynamics issues than the coupled-bunch instabilities and, obviously, can serve as a basis for an improved model that would be more precise or take into account other impedance contributions.
To obtain results in terms of beam dynamics from any kind of wake function model, the existing code HEADTAIL was improved to allow the simulation of multibunch trains, as shown in Chapter 3. All the features present in the previous version of the code (intrabunch motion, amplitude detuning from the octupoles and chromaticity), at the notable exception of the possibility to simulate the effect of electron cloud, were adapted in this new version, and additional algorithmic improvements including a parallelization over the bunches were included. This code can simulate the beam dynamics of macroparticles under the action of any kind of wake functions, for any bunch filling pattern in any circular machine. To analyse the output given by this code (in particular the bunch average positions), a new technique (based on existing algorithms) was also developped to obtain easily the complex tune shifts of the unstable modes present in the simulations. Both the code and the spectral analysis technique were benchmarked against theory in simplifed cases.
The three first chapters of the thesis just summarized are the independent and necessary stages to obtain results on the specific case of the LHC transverse coupled-bunch instability. Such results are shown in

Chapter 4. They demonstrate the rather small impact on coupled-bunch instabilities of the number of bunches in a train when the bunch spacing is fixed, and the existence of coupled-bunch modes with intrabunch motion which are more critical than their single-bunch counterparts. A full verification of the complete procedure (impedance theories, impedance model and simulation code) was also performed by comparing the simulation results with actual measurements in the LHC, giving a very good agreement at injection energy and a correct order of magnitude at 3.5 TeV/c, where nevertheless the measurement parameters are known more approximately than at injection. Finally, predictions concerning the beam stability at the future 7 TeV/c operation of the machine were performed in the case of 50 ns spacing (1404 bunches), revealing that the coupled-bunch transverse mode coupling instability threshold is around $5 \cdot 10^{11}$ protons per bunch, 20% lower than the single-bunch TMCI. Note that the TMCI threshold has been increased compared to former predictions [110], mainly because the impedance model was updated in the meanwhile (in particular, the resistivity of the graphite collimators was updated and decreased with respect to previous estimations). Stability studies in the transverse plane with Landau octupoles at their maximum currents (but without feedback system) reveal that the beam remains stable at nominal intensity when $Q' = 2$ in both planes, provided the particles transverse distributions are Gaussian. On the other hand the beam is unstable at ultimate intensity either with $Q' = 0$ or $Q' = 2$, or at nominal intensity with $Q' = 0$, even with maximum currents in the octupoles.

Concerning the beam-coupling impedances theories, future possible studies include the same kind of theories for elliptical geometries, or more generally, for any two-dimensional geometry. The LHC impedance model could be improved by adding other impedance contributions, or better models (typically, including the details of the complete 3D geometry) for the machine elements already taken into account. The HEADTAIL beam dynamics simulation code could be also improved by adding other sources of nonlinearities such as space-charge or the beam-beam force at the collision point. Simulation of the transverse feedback system would be also a very useful improvement. Finally, the LHC transverse coupled-bunch instability can be studied in further details, for example the impact of the second derivative of the tune could be evaluated, and many other comparisons between measurements and simulations performed.

A Macroscopic Maxwell equations in frequency domain for a linear medium

In a medium, time domain macroscopic Maxwell equations are derived from the exact microscopic ones that hold for the electromagnetic fields $\vec{e}$ and $\vec{b}$ in vacuum, given the **total** microscopic charge density ρ and current density $\vec{j}$ [11, p. 248], [55, p. 1-2], [55, p. 105]

$$\begin{aligned} \mathrm{div}\vec{e} &= \frac{\rho}{\varepsilon_0}, \\ \vec{\mathrm{curl}}\vec{b} - \frac{\partial \vec{e}}{c^2 \partial t} &= \mu_0 \vec{j}, \\ \vec{\mathrm{curl}}\vec{e} + \frac{\partial \vec{b}}{\partial t} &= 0, \\ \mathrm{div}\vec{b} &= 0, \end{aligned}$$

where c is the speed of light in vacuum, ε_0 the permittivity of vacuum and μ_0 its permeability. When averaging these equations over elements of volume "physically infinitesimal", we get similar equations for the macroscopic averaged quantites $\vec{E} = \overline{\vec{e}}$, $\vec{B} = \overline{\vec{b}}$, $\overline{\rho}$ and $\vec{J} = \overline{\vec{j}}$ [11, p. 250-251]

$$\mathrm{div}\vec{E} = \frac{\overline{\rho}}{\varepsilon_0}, \tag{A.1}$$

$$\vec{\mathrm{curl}}\vec{B} - \frac{\partial \vec{E}}{c^2 \partial t} = \mu_0 \vec{J}, \tag{A.2}$$

$$\vec{\mathrm{curl}}\vec{E} + \frac{\partial \vec{B}}{\partial t} = 0, \tag{A.3}$$

$$\mathrm{div}\vec{B} = 0. \tag{A.4}$$

The total mean charge $\overline{\rho}$ and current $\vec{J}$ are the sum of several terms:

- "External" charges and currents, i.e. independent of the electromagnetic fields and imposed by an external source. For instance, in our study the external charge density comes from the travelling source macroparticle and is given in Eq. (1.1), while the external current density is related to it by $\vec{J}_{ext} = \rho_{ext} v \vec{e}_s$,

- "Induced" charges and currents, i.e. that come from the action of the fields themselves on the medium. The induced charges and currents obviously vanish in vacuum (neglecting quantum effects).

We will now express the induced charges and currents, first in the case of a linear medium without dielectric or magnetic losses, and then in a general linear medium that can exhibit such losses.

A.1 Linear medium without dielectric or magnetic losses

In such a medium, which can be either a dielectric or a conductor and has a certain magnetic permeability, we can identify three terms in the induced charges and currents, as we will see below. From the linear superposition principle we can consider separately the induced charges and currents coming from the dielectric aspect of the material to those coming from its conductive aspect[1]:

- For the dielectric aspect of the material we have [11, p. 153-156], [55, p. 34]

  $$\rho_{induced}^{diel} = -\mathrm{div}\vec{P},$$

  $\vec{P}$ being the polarization, that is, in a linear medium without loss:

  $$\vec{P} = \varepsilon_0 \chi_e \vec{E}, \tag{A.5}$$

  with χ_e the electric susceptibility, which is also equal to $\varepsilon_b - 1$ by definition of the dielectric constant ε_b (using the notations of Section 1.2). So we obtain for the dielectric induced charge density

  $$\rho_{induced}^{diel} = -\varepsilon_0 \mathrm{div}\left(\chi_e \vec{E}\right). \tag{A.6}$$

  The current density is then obtained from the continuity equation [11, p. 3][2]

  $$\frac{\partial \rho_{induced}^{diel}}{\partial t} + \mathrm{div}\vec{J}_{induced} = 0, \tag{A.7}$$

[1] At a given frequency only one of these two aspects will be relevant, the material being either a conductor or a dielectric. Putting both aspects (dielectric and conductor) in the same material can be thought of being somehow artificial, but it enables to write a general formalism that will be suited for both cases (see also Ref. [44, p. 777]).

[2] The continuity equation is not an additional equation to the problem but a consequence of Maxwell equations: taking the divergence of Eq. (A.2), and using Eqs. (B.12) and (A.1) we get

$$\mu_0 \mathrm{div}\vec{J} = -\frac{\partial \mathrm{div}\vec{E}}{c^2 \partial t} = -\frac{1}{\varepsilon_0 c^2}\frac{\partial \overline{\rho}}{\partial t},$$

such that

$$\mathrm{div}\vec{J} + \frac{\partial \overline{\rho}}{\partial t} = 0,$$

from $\varepsilon_0 \mu_0 c^2 = 1$. This continuity equation can be applied separately to each part of the induced charges and currents since it should be true for a dielectric that has no conductivity, or a conductor that has no dielectric susceptibility, or more generally assuming that we can always consider seperately the dielectric charges and currents from the conductive ones.

such that

$$\mathrm{div}\vec{J}_{induced} = \mathrm{div}\frac{\partial \vec{P}}{\partial t},$$

which from Eq. (B.12) gives a current density as the sum of two terms

$$\vec{J}_{induced} = \varepsilon_0 \frac{\partial\left(\chi_e \vec{E}\right)}{\partial t} + \vec{\mathrm{curl}}\vec{M}. \tag{A.8}$$

$\vec{M}$ is a vector field called magnetization, which has nothing to do with the dielectric or conductive aspect of the medium but is related to $\vec{B}$ thanks to the magnetic susceptibility $\chi_m = \mu_r - 1$ (using the notations of Section 1.2) [11, p. 192], [55, p. 105]

$$\vec{M} = \frac{\chi_m}{\mu_0(1+\chi_m)}\vec{B}. \tag{A.9}$$

Therefore we have for the dielectric part of the induced current density

$$\vec{J}^{diel}_{induced} = \varepsilon_0 \frac{\partial\left(\chi_e \vec{E}\right)}{\partial t}, \tag{A.10}$$

and for the induced magnetic part

$$\vec{J}^{mag}_{induced} = \vec{\mathrm{curl}}\left(\frac{\chi_m}{\mu_0(1+\chi_m)}\vec{B}\right). \tag{A.11}$$

- For the conductive aspect of the medium, we have from Ohm's law

$$\vec{J}^{cond}_{induced} = \sigma \vec{E}, \tag{A.12}$$

where σ is the conductivity (see Section 1.2) of the material. From the continuity equation we then get

$$\frac{\partial \rho^{cond}_{induced}}{\partial t} = -\mathrm{div}\left(\sigma \vec{E}\right),$$

such that

$$\rho^{cond}_{induced} = -\int^t \mathrm{d}t' \mathrm{div}\left(\sigma \vec{E}\right). \tag{A.13}$$

Finally, substituting the induced charges and currents from Eqs. (A.6), (A.10), (A.11), (A.12) and (A.13) into the right hand side of Maxwell's inhomogeneous equations (A.1) and (A.2) and adding the external charges and currents ρ_{ext} and $\vec{J}_{ext}$, we get

$$\begin{aligned}
\varepsilon_0 \mathrm{div}\vec{E} &= \rho_{ext} - \varepsilon_0 \mathrm{div}\left(\chi_e \vec{E}\right) - \int^t \mathrm{d}t' \mathrm{div}\left(\sigma \vec{E}\right), \\
\frac{1}{\mu_0}\vec{\mathrm{curl}}\vec{B} - \varepsilon_0 \frac{\partial \vec{E}}{\partial t} &= \vec{J}_{ext} + \varepsilon_0 \frac{\partial\left(\chi_e \vec{E}\right)}{\partial t} + \vec{\mathrm{curl}}\left(\frac{\chi_m}{\mu_0(1+\chi_m)}\vec{B}\right) + \sigma \vec{E},
\end{aligned}$$

which leads to

$$\operatorname{div}\left(\varepsilon_0\varepsilon_b\vec{E}+\int^t \mathrm{d}t'\sigma\vec{E}\right) = \rho_{ext}, \tag{A.14}$$

$$\vec{\operatorname{curl}}\left(\frac{1}{\mu_0\mu_r}\vec{B}\right)-\frac{\partial}{\partial t}\left(\varepsilon_0\varepsilon_b\vec{E}+\int^t \mathrm{d}t'\sigma\vec{E}\right) = \vec{J}_{ext}. \tag{A.15}$$

A.2 Linear medium with dielectric and magnetic losses

In a general linear medium, there can be losses (i.e. dissipation of energy) that are due to some delay between the cause (an electromagnetic field) and its effect on the medium (polarization and/or magnetization). We can introduce them by replacing Eqs. (A.5) and (A.9) by the following integrals over all previous instants [55, p. 266]:

$$\vec{P} = \varepsilon_0\int_0^\infty \mathrm{d}\tau f(\tau)\vec{E}(t-\tau), \tag{A.16}$$

$$\vec{M} = \frac{1}{\mu_0}\int_0^\infty \mathrm{d}\tau g(\tau)\vec{B}(t-\tau), \tag{A.17}$$

where f and g are two functions (usually decaying with time). When substituting these equations into the induced charge and current densities (dielectric and magnetic part, as the conductive part remains the same), we get instead of Eqs. (A.14) and (A.15)

$$\operatorname{div}\left(\varepsilon_0\hat{\varepsilon}_b\vec{E}+\int^t \mathrm{d}t'\sigma\vec{E}\right) = \rho_{ext}, \tag{A.18}$$

$$\vec{\operatorname{curl}}\left(\frac{1}{\mu_0}\widehat{\frac{1}{\mu_r}}\vec{B}\right)-\frac{\partial}{\partial t}\left(\varepsilon_0\hat{\varepsilon}_b\vec{E}+\int^t \mathrm{d}t'\sigma\vec{E}\right) = \vec{J}_{ext}, \tag{A.19}$$

where the linear operators $\hat{\varepsilon}_b$ and $\widehat{\frac{1}{\mu_r}}$ are defined by

$$\hat{\varepsilon}_b\vec{E} = \vec{E}(t)+\int_0^\infty \mathrm{d}\tau f(\tau)\vec{E}(t-\tau),$$

$$\widehat{\frac{1}{\mu_r}}\vec{B} = \vec{B}(t)-\int_0^\infty \mathrm{d}\tau g(\tau)\vec{B}(t-\tau).$$

In frequency domain (that is, after applying a Fourier transform as explained in Section 1.1), we can substitute all occurences of $\frac{\partial}{\partial t}$ by the multiplicative factor $j\omega$ and all occurences of $\int^t \mathrm{d}t'$ by $\frac{1}{j\omega}$. Also, we can replace the convolution product in the linear operator $\hat{\varepsilon}_b$ (respectively, $\widehat{\frac{1}{\mu_r}}$) by a multiplication between the Fourier transform $\tilde{f}$ of f (resp. $\tilde{g}$ for g) and that of $\vec{E}$ (resp. $\vec{B}$). Now we can always write $\tilde{f}$

and $\tilde{g}$ in the form

$$1+\tilde{f} = \varepsilon_b(\omega)\left[1 - j\,\mathrm{sign}(\omega)\tan\vartheta_E(\omega)\right],$$
$$1-\tilde{g} = \frac{1}{\mu_r(\omega)\left[1 - j\,\mathrm{sign}(\omega)\tan\vartheta_M(\omega)\right]},$$

where ε_b, ϑ_E, μ_r and ϑ_M (defined in Section 1.2) are real and can depend on frequency. Finally, we get for the two first (inhomogeneous) Maxwell equations in frequency domain[3]

$$\mathrm{div}\left[\left(\varepsilon_0\varepsilon_b(1 - j\,\mathrm{sign}(\omega)\tan\vartheta_E) + \frac{\sigma}{j\omega}\right)\vec{E}\right] = \rho_{ext}, \tag{A.20}$$

$$\vec{\mathrm{curl}}\left[\frac{1}{\mu_0\mu_r(1 - j\,\mathrm{sign}(\omega)\tan\vartheta_M)}\vec{B}\right] - j\omega\left[\left(\varepsilon_0\varepsilon_b(1 - j\,\mathrm{sign}(\omega)\tan\vartheta_E) + \frac{\sigma}{j\omega}\right)\vec{E}\right] = \vec{J}_{ext}. \tag{A.21}$$

Since the two homogeneous Maxwell's equation (A.3) and (A.4) do not depend on induced charges and currents, we get the equations of Section 1.2 by defining the electric displacement $\vec{D}$ and magnetic field $\vec{H}$ (while $\vec{B}$ is called the magnetic induction) in the following way[4]

$$\vec{D} = \left[\varepsilon_0\varepsilon_b(1 - j\,\mathrm{sign}(\omega)\tan\vartheta_E) + \frac{\sigma}{j\omega}\right]\vec{E}, \tag{A.22}$$

$$\vec{H} = \frac{1}{\mu_0\mu_r(1 - j\,\mathrm{sign}(\omega)\tan\vartheta_M)}\vec{B}, \tag{A.23}$$

therefore obtaining the four general frequency domain macroscopic Maxwell equations in a linear medium with losses

$$\mathrm{div}\vec{D} = \rho_{ext}, \tag{A.24}$$

$$\vec{\mathrm{curl}}\vec{H} - j\omega\vec{D} = \vec{J}_{ext}, \tag{A.25}$$

$$\vec{\mathrm{curl}}\vec{E} + j\omega\vec{B} = 0, \tag{A.26}$$

$$\mathrm{div}\vec{B} = 0. \tag{A.27}$$

We should stress again that these equations suppose linearity of the medium. This is in particular not true for ferromagnetic materials (where the relation between the magnetization and the magnetic field is hysteretic and strongly non-linear), except for small fields in an untreated material (that is, not previously magnetized). Also, isotropy, homogeneity and the validity of Ohm's law have been assumed.

[3] Alternatively, we could have introduced the complex permittivity and permeability directly in the frequency domain equations, as in Ref. [11, p. 262], by assuming the lineary between the electric displacement and the electric field, as well as between the magnetic field and the magnetic induction.

[4] Note that the dielectric loss tangent cannot be easily separated from the conductive part, which also generates an imaginary part in the total permittivity $\varepsilon_b(\omega)\left[1 - j\,\mathrm{sign}(\omega)\tan\vartheta_E(\omega)\right] + \frac{\sigma}{j\omega}$. So we must be careful when applying numerical values from tables in these formulas: for instance, the loss tangent could already "contain" the conductivity.

B Vector operations

B.1 Vector operations in cylindrical coordinates

The following formulas can be found in many textbooks of mechanics or electrodynamics, and in particular in Ref. [55, p. 452-453].

B.1.1 Gradient

For any scalar field f, the gradient in cylindrical coordinates (r,θ,s) (the basis unit vector being $\vec{e}_r$, $\vec{e}_\theta$ and $\vec{e}_s$) is given by

$$\vec{\text{grad}} f = \frac{\partial f}{\partial r}\vec{e}_r + \frac{1}{r}\frac{\partial f}{\partial \theta}\vec{e}_\theta + \frac{\partial f}{\partial s}\vec{e}_s. \tag{B.1}$$

B.1.2 Divergence

For any vector field $\vec{A}$, the divergence in cylindrical coordinates (r,θ,s) is given by

$$\begin{aligned} \text{div}\vec{A} &= \frac{\partial A_r}{\partial r} + \frac{A_r}{r} + \frac{1}{r}\frac{\partial A_\theta}{\partial \theta} + \frac{\partial A_s}{\partial s}, \\ &= \frac{1}{r}\frac{\partial (r A_r)}{\partial r} + \frac{1}{r}\frac{\partial A_\theta}{\partial \theta} + \frac{\partial A_s}{\partial s}. \end{aligned} \tag{B.2}$$

B.1.3 Curl

For any vector field $\vec{A}$, the curl in cylindrical coordinates (r,θ,s) is given by

$$\begin{aligned}
\left(\vec{\mathrm{curl}}\vec{A}\right)_r &= \frac{1}{r}\frac{\partial A_s}{\partial\theta} - \frac{\partial A_\theta}{\partial s}, \\
\left(\vec{\mathrm{curl}}\vec{A}\right)_\theta &= \frac{\partial A_r}{\partial s} - \frac{\partial A_s}{\partial r}, \\
\left(\vec{\mathrm{curl}}\vec{A}\right)_s &= \frac{\partial A_\theta}{\partial r} + \frac{A_\theta}{r} - \frac{1}{r}\frac{\partial A_r}{\partial\theta}, \\
&= \frac{1}{r}\left[\frac{\partial(rA_\theta)}{\partial r} - \frac{\partial A_r}{\partial\theta}\right].
\end{aligned} \tag{B.3}$$

B.1.4 Scalar laplacian

For any scalar field f, the laplacian in cylindrical coordinates (r,θ,s) is given by

$$\nabla^2 f = \frac{1}{r}\frac{\partial}{\partial r}\left(r\frac{\partial f}{\partial r}\right) + \frac{1}{r^2}\frac{\partial^2 f}{\partial\theta^2} + \frac{\partial^2 f}{\partial s^2}. \tag{B.4}$$

B.1.5 Vector laplacian

For any vector field $\vec{A}$, the vector laplacian in cylindrical coordinates (r,θ,s) is given by

$$\begin{aligned}
\left(\nabla^2\vec{A}\right)_r &= \nabla^2 A_r - \frac{A_r}{r^2} - \frac{2}{r^2}\frac{\partial A_\theta}{\partial\theta}, \\
\left(\nabla^2\vec{A}\right)_\theta &= \nabla^2 A_\theta - \frac{A_\theta}{r^2} + \frac{2}{r^2}\frac{\partial A_r}{\partial\theta}, \\
\left(\nabla^2\vec{A}\right)_s &= \nabla^2 A_s.
\end{aligned} \tag{B.5}$$

B.2 Vector operations in cartesian coordinates

The following formulas can be found in many textbooks of mechanics or electrodynamics, and in particular in Refs. [11, cover page] and [55, p. 452] as well as in Ref. [123].

B.2.1 Gradient

For any scalar field f, the gradient in cartesian coordinates (x,y,s) (the basis unit vectors being $\vec{e}_x$, $\vec{e}_y$ and $\vec{e}_s$) is given by

$$\vec{\mathrm{grad}}f = \frac{\partial f}{\partial x}\vec{e}_x + \frac{\partial f}{\partial y}\vec{e}_y + \frac{\partial f}{\partial s}\vec{e}_s. \tag{B.6}$$

B.2.2 Divergence

For any vector field $\vec{A}$, the divergence in cartesian coordinates (x, y, s) is given by

$$\mathrm{div}\vec{A} = \frac{\partial A_x}{\partial x} + \frac{\partial A_y}{\partial y} + \frac{\partial A_s}{\partial s}. \tag{B.7}$$

B.2.3 Curl

For any vector field $\vec{A}$, the curl in cartesian coordinates (x, y, s) is given by

$$\begin{aligned}
\left(\vec{\mathrm{curl}}\vec{A}\right)_x &= \frac{\partial A_s}{\partial y} - \frac{\partial A_y}{\partial s}, \\
\left(\vec{\mathrm{curl}}\vec{A}\right)_y &= \frac{\partial A_x}{\partial s} - \frac{\partial A_s}{\partial x}, \\
\left(\vec{\mathrm{curl}}\vec{A}\right)_s &= \frac{\partial A_y}{\partial x} - \frac{\partial A_x}{\partial y}.
\end{aligned} \tag{B.8}$$

B.2.4 Scalar laplacian

For any scalar field f, the laplacian in cartesian coordinates (x, y, s) is given by

$$\nabla^2 f = \frac{\partial^2 f}{\partial x^2} + \frac{\partial^2 f}{\partial y^2} + \frac{\partial^2 f}{\partial s^2}. \tag{B.9}$$

B.2.5 Vector laplacian

For any vector field $\vec{A}$, the vector laplacian in cartesian coordinates (x, y, s) is given by

$$\begin{aligned}
\left(\nabla^2\vec{A}\right)_x &= \nabla^2 A_x, \\
\left(\nabla^2\vec{A}\right)_y &= \nabla^2 A_y, \\
\left(\nabla^2\vec{A}\right)_s &= \nabla^2 A_s.
\end{aligned} \tag{B.10}$$

B.3 Some relations between vector operations

From for instance Ref. [11, cover page], we know that

$$\vec{\mathrm{curl}}\left(\vec{\mathrm{curl}}\right) = \vec{\mathrm{grad}}\,(\mathrm{div}) - \nabla^2, \tag{B.11}$$

$$\mathrm{div}\left(\vec{\mathrm{curl}}\right) = 0. \tag{B.12}$$

C Various properties of Bessel functions

Unless stated otherwise, in all the following ν and z are complex numbers while m is an integer.

C.1 Differential equations

Modified Bessel functions $I_\nu(z)$ (first kind) and $K_\nu(z)$ (second kind) are independent solutions of the differential equation [124, p. 374]

$$z^2\frac{d^2y}{dz^2}+z\frac{dy}{dz}-\left(z^2+\nu^2\right)y=0. \tag{C.1}$$

The Bessel function of the first kind $J_\nu(z)$ is a solution of [124, p. 358]

$$z^2\frac{d^2y}{dz^2}+z\frac{dy}{dz}+\left(z^2-\nu^2\right)y=0. \tag{C.2}$$

C.2 General properties

From Ref. [124, p. 375-376], we have the following relations between the modified Bessel functions (z^* stands for the complex conjugate of z, and f' is the derivative of a function f)

$$I_{-m}(z) = I_m(z), \tag{C.3}$$
$$K_{-m}(z) = K_m(z), \tag{C.4}$$
$$I_\nu\left(ze^{jm\pi}\right) = e^{j\nu m\pi}I_\nu(z), \tag{C.5}$$
$$I'_\nu(z)K_\nu(z)-K'_\nu(z)I_\nu(z) = \frac{1}{z}, \tag{C.6}$$
$$I'_\nu(z) = I_{\nu-1}(z)-\frac{\nu}{z}I_\nu(z), \tag{C.7}$$
$$K'_\nu(z) = -K_{\nu-1}(z)-\frac{\nu}{z}K_\nu(z), \tag{C.8}$$
$$K'_\nu(z) = -K_{\nu+1}(z)+\frac{\nu}{z}K_\nu(z), \tag{C.9}$$

$$I_m(z^*) = I_m(z)^*, \tag{C.10}$$
$$K_m(z^*) = K_m(z)^*, \tag{C.11}$$
$$I_0'(z) = I_1(z), \tag{C.12}$$
$$K_0'(z) = -K_1(z), \tag{C.13}$$
$$J_m(jz) = j^m I_m(z) \text{ for } -\pi < \arg(z) \leq \frac{\pi}{2}. \tag{C.14}$$

From Ref. [124, p. 361] we have the additional relation

$$J_\nu\left(ze^{jm\pi}\right) = e^{j\nu m\pi} J_\nu(z). \tag{C.15}$$

C.3 Expansion for small arguments

Reference [124, p. 375] gives expansions for small arguments. Assuming $m \geq 0$, we have

$$I_m(z) = \left(\frac{z}{2}\right)^m \sum_{k=0}^{\infty} \frac{\left(\frac{z}{2}\right)^{2k}}{k!(m+k)!} \quad \text{(also valid for } m=-1 \text{ with the convention } (-1)! = \infty), \tag{C.16}$$
$$I_m(z) \sim \frac{\left(\frac{1}{2}z\right)^m}{m!} \qquad \text{when } |z| \to 0, \tag{C.17}$$
$$K_0(z) \sim -\ln(z) \qquad \text{when } |z| \to 0, \tag{C.18}$$
$$K_m(z) \sim \frac{1}{2}(m-1)!\left(\frac{1}{2}z\right)^{-m} \qquad \text{when } |z| \to 0 \quad (m \text{ strictly positive integer}), \tag{C.19}$$

where $m!$ is the factorial of the integer m.

C.4 Expansion for large arguments

From Ref. [124, p. 377-378] we have:

$$I_m(z) \sim \frac{e^z}{\sqrt{2\pi z}} \qquad \text{when } |z| \to +\infty, \quad \text{for } |\arg(z)| < \frac{\pi}{2}, \tag{C.20}$$
$$K_m(z) \sim \sqrt{\frac{\pi}{2z}} e^{-z} \qquad \text{when } |z| \to +\infty, \quad \text{for } |\arg(z)| < \frac{3\pi}{2}. \tag{C.21}$$

In the case when $\arg(z) = \frac{\pi}{2}$ i.e. $z = j\rho$ with $\rho > 0$, we have from Eqs. (C.14) and (C.15)

$$I_m(z) = J_m(jz)\, j^{-m} = J_m(-\rho)\, j^{-m} = j^m J_m(\rho) = j^m J_m(-jz),$$

such that, thanks to Ref. [124, p. 364]:

$$I_m(z) \sim j^m \cos\left(-jz - \frac{m\pi}{2} - \frac{\pi}{4}\right)\sqrt{\frac{2}{-j\pi z}} \quad \text{when } |z| \to +\infty, \quad \text{for } \arg(z) = \frac{\pi}{2}. \tag{C.22}$$

C.5 Summation formulae

From Ref. [124, p. 378] we have

$$e^{\frac{z}{2}\left(t+\frac{1}{t}\right)} = \sum_{m=-\infty}^{\infty} t^m I_m(z) \quad \text{with } t \text{ non zero.} \tag{C.23}$$

We can use it to derive two other summation formulae: using Eq. (C.3)

$$e^{z\cosh u} = e^{\frac{z}{2}\left(e^u+\frac{1}{e^u}\right)} = \sum_{m=-\infty}^{\infty} e^{mu} I_m(z) = I_0(z) + 2\sum_{m=1}^{\infty} \cosh(mu) I_m(z), \tag{C.24}$$

and, thanks to (C.5)

$$e^{-z\cosh u} = I_0(z) + 2\sum_{m=1}^{\infty} (-1)^m \cosh(mu) I_m(z). \tag{C.25}$$

Another useful relation is obtained from Ref. [125, p. 102]: for any complex numbers ϕ, ν, z_1 and z_2 such that $|z_1 e^{\pm j\phi}| < |z_2|$ we have

$$\sum_{m=-\infty}^{\infty} I_m(z_1) K_{\nu+m}(z_2) e^{jm\phi} = K_\nu\left(\sqrt{z_1^2+z_2^2-2z_1z_2\cos\phi}\right)\left(\frac{z_2 - z_1 e^{-j\phi}}{\sqrt{z_1^2+z_2^2-2z_1z_2\cos\phi}}\right)^\nu. \tag{C.26}$$

This in particular gives for $\nu = 0$, $0 < z_1 < z_2$ and ϕ real numbers, taking only the real part of the formula, and recalling Eqs. (C.3) and (C.4)

$$\sum_{m=0}^{\infty} \frac{1}{1+\delta_{m0}} I_m(z_1) K_m(z_2) \cos(m\phi) = \frac{1}{2} K_0\left(\sqrt{z_1^2+z_2^2-2z_1z_2\cos\phi}\right), \tag{C.27}$$

where $\delta_{m0} = 1$ if $m = 0$, 0 otherwise. We can also write Eq. (C.26) in the case when $\nu = n$, $|z_1| < z_2$ and $\phi = p\pi$ where n and p are integers, obtaining

$$\sum_{m=-\infty}^{\infty} I_m(z_1) K_{m+n}(z_2)(-1)^{mp} = K_n\left(z_2 + (-1)^{p+1} z_1\right). \tag{C.28}$$

C.6 Integral formulae

The following integral formula can be found in Ref. [126, p. 17]

$$\int_0^\infty \mathrm{d}k_x \cos(k_x x) \frac{e^{-b\sqrt{k_x^2+a^2}}}{\sqrt{k_x^2+a^2}} = K_0\left(a\sqrt{b^2+x^2}\right) \quad \text{with } \Re(a) > 0 \text{ and } \Re(b) > 0. \tag{C.29}$$

Another useful integral representation is [124, p. 376]

$$K_\nu(z) = \int_0^\infty \mathrm{d}t\, e^{-z\cosh t} \cosh(\nu t) \qquad \text{with } \left|\arg(z)\right| < \frac{\pi}{2}. \tag{C.30}$$

C.7 A generalization of Schläfli's integrals

References [125, p. 82] and [70, p. 903] give an analytical expression for the following sum of integrals given for x, y complex numbers and ν real[1]:

$$\int_0^{\pi} e^{y\cos t}\cos\left(x\sin t-\nu t\right)\mathrm{d}t-\sin\nu\pi\int_0^{\infty} e^{-\nu t-y\cosh t-x\sinh t}\mathrm{d}t \qquad \text{with } \Re(x+y)>0. \tag{C.31}$$

The expressions given in both references are different: according to Ref. [125, p. 82] the result should be

$$\pi\left(\frac{x+y}{x-y}\right)^{\frac{\nu}{2}} J_\nu\left[\left(x^2-y^2\right)^{\frac{1}{2}}\right].$$

In Ref. [70, p. 903] we find on the contrary that this sum of integrals should be

$$\pi\left(x+y\right)^{\nu}\frac{J_\nu\left[\left(x^2+y^2\right)^{\frac{1}{2}}\right]}{\left(x^2-y^2\right)^{\frac{\nu}{2}}}.$$

When comparing those formulae with numerical computations of the integrals (where the one on an infinite range converges very fast so is not computationally intensive), it turns out that both the above formulae seem incorrect. In particular, the first analytical expression above is not even continuous with x when going from $x<y$ to $x>y$ for certain values of ν. Therefore we rederive here the formula, following step by step the derivation given in Ref. [127].
The starting point is the following generalization of Bessel's integral due to Schläfli, which can be found in equivalent forms in Refs. [124, p. 360], [70, p. 903], [127] and [128, p. 176]:

$$\text{For } \Re(a)>0\ ,\ J_\nu(a)=\frac{1}{\pi}\int_0^{\pi}\cos\left(\nu t-a\sin t\right)\mathrm{d}t-\frac{\sin\nu\pi}{\pi}\int_0^{\infty} e^{-\nu t-a\sinh t}\mathrm{d}t. \tag{C.32}$$

Then, for any y complex and t real, we have the general formula

$$\sum_{n=0}^{\infty}\frac{y^n}{n!}e^{jnt}=\sum_{n=0}^{\infty}\frac{\left(ye^{jt}\right)^n}{n!}=e^{ye^{jt}}=e^{y\cos t}\left[\cos\left(y\sin t\right)+j\sin\left(y\sin t\right)\right].$$

Using this relation for both t and $-t$ and adding (respectively subtracting) the results, we get

$$\sum_{n=0}^{\infty}\frac{y^n}{n!}\cos(nt)=e^{y\cos t}\cos\left(y\sin t\right),$$
$$\sum_{n=0}^{\infty}\frac{y^n}{n!}\sin(nt)=e^{y\cos t}\sin\left(y\sin t\right).$$

From these and the relation

$$\cos\left[\left(\nu+n\right)t-a\sin t\right]=\cos\left(\nu t-a\sin t\right)\cos\left(nt\right)-\sin\left(\nu t-a\sin t\right)\sin\left(nt\right),$$

[1] In Ref. [70] there is an error in the upper bound of the first integral, which is taken as ∞ instead of π.

we obtain

$$\sum_{n=0}^{\infty}\frac{y^n}{n!}\cos\left[(\nu+n)t-a\sin t\right]=e^{y\cos t}\left[\cos\left(y\sin t\right)\cos\left(\nu t-a\sin t\right)-\sin\left(y\sin t\right)\sin\left(\nu t-a\sin t\right)\right]$$
$$=e^{y\cos t}\cos\left[\nu t-(a-y)\sin t\right]. \tag{C.33}$$

We also have

$$\sum_{n=0}^{\infty}\frac{y^n}{n!}\sin\left[(\nu+n)\pi\right]e^{-nt}=\sum_{n=0}^{\infty}\frac{\left(-ye^{-t}\right)^n}{n!}\sin(\nu\pi)$$
$$=e^{-ye^{-t}}\sin(\nu\pi),$$

such that

$$\sum_{n=0}^{\infty}\frac{y^n}{n!}\sin\left[(\nu+n)\pi\right]e^{-nt-\nu t-a\sinh t}=\sin(\nu\pi)\,e^{-y(\cosh t-\sinh t)-\nu t-a\sinh t}$$
$$=\sin(\nu\pi)\,e^{-\nu t-y\cosh t-(a-y)\sinh t}. \tag{C.34}$$

Thanks to Eqs. (C.32), (C.33) and (C.34) we have upon integration

$$\int_0^{\pi}e^{y\cos t}\cos\left[\nu t-(a-y)\sin t\right]\mathrm{d}t-\sin(\nu\pi)\int_0^{\infty}e^{-\nu t-y\cosh t-(a-y)\sinh t}\mathrm{d}t$$
$$=\sum_{n=0}^{\infty}\frac{y^n}{n!}\int_0^{\pi}\cos\left[(\nu+n)t-a\sin t\right]\mathrm{d}t-\sum_{n=0}^{\infty}\frac{y^n}{n!}\sin\left[(\nu+n)\pi\right]\int_0^{\infty}e^{-nt-\nu t-a\sinh t}\mathrm{d}t$$
$$=\pi\sum_{n=0}^{\infty}\frac{y^n}{n!}J_{\nu+n}(a)\qquad\text{for }\Re(a)>0. \tag{C.35}$$

The latter sum can be computed thanks to Ref. [128, p. 141], giving

$$\sum_{n=0}^{\infty}\frac{y^n}{n!}J_{\nu+n}(a)=\left(1-\frac{2y}{a}\right)^{-\frac{\nu}{2}}J_{\nu}\left(a\sqrt{1-\frac{2y}{a}}\right). \tag{C.36}$$

Note that Eq. (C.36) is not exactly the same as the correspondant formula in Ref. [127]: in the latter the argument of the Bessel function has been replaced by $\sqrt{a^2-2ay}$ which turns out not to be same as $a\sqrt{1-\frac{2y}{a}}$ when $\arg a+\arg\left(1-\frac{2y}{a}\right)>\pi$ or $\arg a+\arg\left(1-\frac{2y}{a}\right)\leq-\pi$ as we know from e.g. Ref. [124, p. 70]. Here only a is restricted to have an argument between $-\frac{\pi}{2}$ and $\frac{\pi}{2}$, but not $1-\frac{2y}{a}$.
Combining Eqs. (C.35) and (C.36) and letting $x=a-y$ we get

$$\int_0^{\pi}e^{y\cos t}\cos(x\sin t-\nu t)\,\mathrm{d}t-\sin\nu\pi\int_0^{\infty}e^{-\nu t-y\cosh t-x\sinh t}\mathrm{d}t=$$
$$\pi\left(\frac{x-y}{x+y}\right)^{-\frac{\nu}{2}}J_{\nu}\left[(x+y)\left(\frac{x-y}{x+y}\right)^{\frac{1}{2}}\right],\qquad\text{valid for }\Re(x+y)>0. \tag{C.37}$$

There are two differences between Eq. (C.37) and the equation given in Ref. [125, p. 82]. The first one concerns the argument of the Bessel function, as we already pointed out. The second one is in the way the factor $\left(\frac{x-y}{x+y}\right)^{-\frac{\nu}{2}}$ is written. It was replaced by $\left(\frac{x+y}{x-y}\right)^{\frac{\nu}{2}}$ which does not give an identical value in some

cases, for the same reason as already mentioned above: from Ref. [124, p. 70] $a^\nu \left(\frac{1}{a}\right)^\nu \neq 1$ if $\arg a = \pi$ (because then $\arg \frac{1}{a} = \pi$ so $\arg a + \arg \frac{1}{a} > \pi$).
One can get a slightly more compact form after some additional algebra. Letting $x - y = ae^{j\theta}$ and $x + y = be^{j\phi}$ with $a > 0$, $b > 0$, $-\pi < \theta \leq \pi$ and $-\pi < \phi \leq \pi$, we write

$$(x+y)\sqrt{\frac{x-y}{x+y}} = (x+y)e^{\frac{1}{2}\ln\left(\frac{x-y}{x+y}\right)} = be^{j\phi}e^{\frac{1}{2}(\ln a - \ln b + j\theta - j\phi + 2jm\pi)} = \sqrt{ab}e^{\frac{j}{2}(\theta+\phi)}e^{jm\pi},$$

with m an integer such that $m = 0$ if $-\pi < \theta - \phi \leq \pi$, $m = 1$ if $\theta - \phi \leq -\pi$ and $m = -1$ if $\theta - \phi > \pi$. Similarly, we have

$$\sqrt{x^2 - y^2} = e^{\frac{1}{2}\ln[(x-y)(x+y)]} = \sqrt{ab}e^{\frac{j}{2}(\theta+\phi)}e^{jn\pi} = (x+y)\sqrt{\frac{x-y}{x+y}}e^{j(n-m)\pi},$$

with n an integer such that $n = 0$ if $-\pi < \theta + \phi \leq \pi$, $n = 1$ if $\theta + \phi \leq -\pi$ and $n = -1$ if $\theta + \phi > \pi$. Therefore, using Eq. (C.15) we can write

$$J_\nu\left(\sqrt{x^2 - y^2}\right) = J_\nu\left[(x+y)\left(\frac{x-y}{x+y}\right)^{\frac{1}{2}}\right]e^{j\nu(n-m)\pi}.$$

Now, we also have, with the same m and n defined above:

$$\left(\frac{x-y}{x+y}\right)^{-\frac{\nu}{2}} = e^{-\frac{\nu}{2}\ln\left(\frac{x-y}{x+y}\right)} = \left(\frac{b}{a}\right)^{\frac{\nu}{2}}e^{j\frac{\nu}{2}(\phi-\theta)}e^{-j\nu m\pi},$$

and

$$\frac{(x+y)^\nu}{\left(x^2-y^2\right)^{\frac{\nu}{2}}} = \frac{b^\nu e^{j\nu\phi}}{(ab)^{\frac{\nu}{2}}e^{j\frac{\nu}{2}(\theta+\phi)}e^{j\nu n\pi}} = \left(\frac{b}{a}\right)^{\frac{\nu}{2}}e^{j\frac{\nu}{2}(\phi-\theta)}e^{-j\nu n\pi} = \left(\frac{x-y}{x+y}\right)^{-\frac{\nu}{2}}e^{j\nu(m-n)\pi}.$$

We finally obtain:

$$J_\nu\left[(x+y)\left(\frac{x-y}{x+y}\right)^{\frac{1}{2}}\right]\left(\frac{x-y}{x+y}\right)^{-\frac{\nu}{2}} = J_\nu\left(\sqrt{x^2-y^2}\right)\frac{(x+y)^\nu}{\left(x^2-y^2\right)^{\frac{\nu}{2}}},$$

such that we can write an equivalent form of Eq. (C.37)

$$\int_0^\pi e^{y\cos t}\cos(x\sin t - \nu t)\,\mathrm{d}t - \sin\nu\pi\int_0^\infty e^{-\nu t - y\cosh t - x\sinh t}\mathrm{d}t = \pi J_\nu\left(\sqrt{x^2-y^2}\right)\frac{(x+y)^\nu}{\left(x^2-y^2\right)^{\frac{\nu}{2}}}, \qquad \text{valid for } \Re(x+y) > 0. \quad \text{(C.38)}$$

This relation, which is a generalization of Schläfli's integrals, is quite similar to Eq. 8.413 in Ref. [70, p. 903] that we have quoted above, but according to our derivation there seems to be a sign error in the argument of the Bessel function, in addition to the already mentioned incorrect upper limit of the first integral.

From this equation we would like to compute the following integral, used in Sections 1.5.5 and E.2.3:

$$\int_0^\pi \mathrm{d}\phi \cos\left(n\phi\right)\cos\left(k_x r\sin\phi\right) e^{r\cos\phi\sqrt{k_x^2+\frac{k^2}{\gamma^2}}}.$$

To do so we first write

$$\cos\left(n\phi\right)\cos\left(k_x r\sin\phi\right) = \frac{1}{2}\left[\cos\left(k_x r\sin\phi + n\phi\right) + \cos\left(k_x r\sin\phi - n\phi\right)\right].$$

For the first term we can apply Eq. (C.38) with $x = k_x r$, $y = r\sqrt{k_x^2+\frac{k^2}{\gamma^2}}$ and $\nu = -n$, giving (since $\sin\nu\pi = 0$ here):

$$\begin{aligned}
\frac{1}{2}\int_0^\pi \mathrm{d}\phi \cos\left(k_x r\sin\phi + n\phi\right) e^{r\cos\phi\sqrt{k_x^2+\frac{k^2}{\gamma^2}}} &= \frac{\pi}{2}\frac{r^{-n}\left(k_x+\sqrt{k_x^2+\frac{k^2}{\gamma^2}}\right)^{-n}}{\left(-\frac{k^2r^2}{\gamma^2}\right)^{-\frac{n}{2}}} J_{-n}\left(j\frac{kr}{\gamma}\right) \\
&= \frac{\pi}{2} j^n \left(k_x+\sqrt{k_x^2+\frac{k^2}{\gamma^2}}\right)^{-n} \frac{k^n}{\gamma^n} j^{-n} I_n\left(\frac{kr}{\gamma}\right) \\
&\qquad \text{using Eqs. (C.3) and (C.14)} \\
&= \frac{\pi}{2}\left(k_x+\sqrt{k_x^2+\frac{k^2}{\gamma^2}}\right)^{-n} \frac{k^n}{\gamma^n} I_n\left(\frac{kr}{\gamma}\right).
\end{aligned}$$

Similarly we get for the other term, this time with $\nu = n$ in Eq. (C.38)

$$\begin{aligned}
\frac{1}{2}\int_0^\pi \mathrm{d}\phi \cos\left(k_x r\sin\phi - n\phi\right) e^{r\cos\phi\sqrt{k_x^2+\frac{k^2}{\gamma^2}}} &= \frac{\pi}{2}\frac{r^{n}\left(k_x+\sqrt{k_x^2+\frac{k^2}{\gamma^2}}\right)^{n}}{\left(-\frac{k^2r^2}{\gamma^2}\right)^{\frac{n}{2}}} J_{n}\left(j\frac{kr}{\gamma}\right) \\
&= \frac{\pi}{2} j^{-n} \left(k_x+\sqrt{k_x^2+\frac{k^2}{\gamma^2}}\right)^{n} \frac{\gamma^n}{k^n} j^{n} I_n\left(\frac{kr}{\gamma}\right) \\
&= \frac{\pi}{2}\left(k_x+\sqrt{k_x^2+\frac{k^2}{\gamma^2}}\right)^{n} \frac{\gamma^n}{k^n} I_n\left(\frac{kr}{\gamma}\right).
\end{aligned}$$

Adding the two we finally get

$$\begin{aligned}
&\int_0^\pi \mathrm{d}\phi \cos\left(n\phi\right)\cos\left(k_x r\sin\phi\right) e^{r\cos\phi\sqrt{k_x^2+\frac{k^2}{\gamma^2}}} = \\
&\qquad \frac{\pi}{2} I_n\left(\frac{kr}{\gamma}\right)\left[\left(k_x+\sqrt{k_x^2+\frac{k^2}{\gamma^2}}\right)^{-n}\frac{k^n}{\gamma^n} + \left(k_x+\sqrt{k_x^2+\frac{k^2}{\gamma^2}}\right)^{n}\frac{\gamma^n}{k^n}\right]. \qquad \text{(C.39)}
\end{aligned}$$

D Various mathematical relations

D.1 Inversion of a two-by-two matrix

Given a 2×2 matrix of the form

$$M = \begin{bmatrix} a & b \\ c & d \end{bmatrix}, \tag{D.1}$$

whose determinant $ad - bc$ is non zero, its inverse is given by

$$M^{-1} = \frac{1}{ad-bc} \begin{bmatrix} d & -b \\ -c & a \end{bmatrix}. \tag{D.2}$$

This can be checked simply by multiplying the two matrices.

D.2 Some integrals involving exponentials

The following well-known integral can be readily computed

$$\int_0^\infty \mathrm{d}\omega e^{j\omega t} = \frac{j}{t} \qquad \text{if } \Im(t) > 0, \tag{D.3}$$

j being the imaginary constant. From this result we can also get, for any positive integer n

$$\int_0^\infty \mathrm{d}\omega e^{j\omega t}\omega^n = \frac{1}{j^n}\frac{d^n}{dt^n}\left(\int_0^\infty \mathrm{d}\omega e^{j\omega t}\right) = \frac{(-1)^n n!}{j^{(n-1)}t^{n+1}} = n!\left(\frac{j}{t}\right)^{n+1} \qquad \text{if } \Im(t) > 0. \tag{D.4}$$

Similar integrals with different bounds can be computed in the same way: for any complex number x we have

$$\int_0^1 \mathrm{d}h e^{jhx} = \frac{e^{jx}-1}{jx}, \tag{D.5}$$

$$\int_0^1 \mathrm{d}h e^{jhx} h = \frac{1}{j}\frac{d}{dx}\left(\frac{e^{jx}-1}{jx}\right) = -\frac{jxe^{jx}+1-e^{jx}}{x^2} = -\frac{je^{jx}}{x} + \frac{e^{jx}-1}{x^2}, \tag{D.6}$$

$$\int_0^1 \mathrm{d}h e^{jhx} h^2 = \frac{1}{j}\frac{d}{dx}\left(\int_0^1 \mathrm{d}h e^{jhx} h\right) = \frac{1}{j}\frac{d}{dx}\left(-\frac{je^{jx}}{x} + \frac{e^{jx}-1}{x^2}\right) = -\frac{je^{jx}}{x} + \frac{2e^{jx}}{x^2} + \frac{2j\left(e^{jx}-1\right)}{x^3}, \tag{D.7}$$

$$\begin{aligned}\int_0^1 \mathrm{d}h e^{jhx} h^3 = \frac{1}{j}\frac{d}{dx}\left(\int_0^1 \mathrm{d}h e^{jhx} h^2\right) &= \frac{1}{j}\frac{d}{dx}\left(-\frac{je^{jx}}{x} + \frac{2e^{jx}}{x^2} + \frac{2j\left(e^{jx}-1\right)}{x^3}\right) \\ &= -\frac{je^{jx}}{x} + \frac{3e^{jx}}{x^2} + \frac{6je^{jx}}{x^3} - \frac{6\left(e^{jx}-1\right)}{x^4}.\end{aligned} \tag{D.8}$$

E Derivations used for the impedance and wake function calculations

E.1 Axisymmetric multilayer chamber

E.1.1 Transverse components of the electromagnetic fields

From the transverse components of Maxwell equations (1.9) and (1.10) written in cylindrical coordinates thanks to Eqs. (B.3), assuming $y \neq a_1$ and omitting the superscript (p), we have the relations

$$\frac{1}{r}\frac{\partial H_s}{\partial \theta} - \frac{\partial H_\theta}{\partial s} = j\omega\varepsilon_c E_r, \tag{E.1}$$

$$\frac{\partial H_r}{\partial s} - \frac{\partial H_s}{\partial r} = j\omega\varepsilon_c E_\theta, \tag{E.2}$$

$$\frac{1}{r}\frac{\partial E_s}{\partial \theta} - \frac{\partial E_\theta}{\partial s} = -j\omega\mu H_r, \tag{E.3}$$

$$\frac{\partial E_r}{\partial s} - \frac{\partial E_s}{\partial r} = -j\omega\mu H_\theta. \tag{E.4}$$

Differentiating with respect to s Eq. (E.4) and combining it to Eq. (E.1), we get, knowing that E_s is proportional to e^{-jks} from Eqs. (1.42) and (1.43)

$$\frac{\partial^2 E_r}{\partial s^2} + \omega^2\varepsilon_c\mu E_r = -jk\frac{\partial E_s}{\partial r} - j\omega\mu\frac{1}{r}\frac{\partial H_s}{\partial \theta}. \tag{E.5}$$

In the same way, we can differentiate with respect to s Eqs. (E.3), (E.2) and (E.1), then combine them respectively to Eqs. (E.2), (E.3) and (E.4), obtaining

$$\frac{\partial^2 E_\theta}{\partial s^2} + \omega^2\varepsilon_c\mu E_\theta = -jk\frac{1}{r}\frac{\partial E_s}{\partial \theta} + j\omega\mu\frac{\partial H_s}{\partial r}, \tag{E.6}$$

$$\frac{\partial^2 H_r}{\partial s^2} + \omega^2\varepsilon_c\mu H_r = j\omega\varepsilon_c\frac{1}{r}\frac{\partial E_s}{\partial \theta} - jk\frac{\partial H_s}{\partial r}, \tag{E.7}$$

$$\frac{\partial^2 H_\theta}{\partial s^2} + \omega^2\varepsilon_c\mu H_\theta = -j\omega\varepsilon_c\frac{\partial E_s}{\partial r} - jk\frac{1}{r}\frac{\partial H_s}{\partial \theta}. \tag{E.8}$$

If we now introduce the decompositions from Eqs. (1.20) and (1.21) and identify the integrand and each terms in the Fourier series (since the equations are valid for any s and any θ), we get

$$\left(-k'^2+\omega^2\varepsilon_c\mu\right)\hat{E}_r^{m,c} = -jk\frac{d\hat{E}_s^{m,c}}{dr} - j\omega\mu\frac{m}{r}\hat{H}_s^{m,s}, \tag{E.9}$$

$$\left(-k'^2+\omega^2\varepsilon_c\mu\right)\hat{E}_r^{m,s} = -jk\frac{d\hat{E}_s^{m,s}}{dr} + j\omega\mu\frac{m}{r}\hat{H}_s^{m,c}, \tag{E.10}$$

$$\left(-k'^2+\omega^2\varepsilon_c\mu\right)\hat{E}_\theta^{m,c} = -jk\frac{m}{r}\hat{E}_s^{m,s} + j\omega\mu\frac{d\hat{H}_s^{m,c}}{dr}, \tag{E.11}$$

$$\left(-k'^2+\omega^2\varepsilon_c\mu\right)\hat{E}_\theta^{m,s} = jk\frac{m}{r}\hat{E}_s^{m,c} + j\omega\mu\frac{d\hat{H}_s^{m,s}}{dr}, \tag{E.12}$$

$$\left(-k'^2+\omega^2\varepsilon_c\mu\right)\hat{H}_r^{m,c} = j\omega\varepsilon_c\frac{m}{r}\hat{E}_s^{m,s} - jk\frac{d\hat{H}_s^{m,c}}{dr}, \tag{E.13}$$

$$\left(-k'^2+\omega^2\varepsilon_c\mu\right)\hat{H}_r^{m,s} = -j\omega\varepsilon_c\frac{m}{r}\hat{E}_s^{m,c} - jk\frac{d\hat{H}_s^{m,s}}{dr}, \tag{E.14}$$

$$\left(-k'^2+\omega^2\varepsilon_c\mu\right)\hat{H}_\theta^{m,c} = -j\omega\varepsilon_c\frac{d\hat{E}_s^{m,c}}{dr} - jk\frac{m}{r}\hat{H}_s^{m,s}, \tag{E.15}$$

$$\left(-k'^2+\omega^2\varepsilon_c\mu\right)\hat{H}_\theta^{m,s} = -j\omega\varepsilon_c\frac{d\hat{E}_s^{m,s}}{dr} + jk\frac{m}{r}\hat{H}_s^{m,c}. \tag{E.16}$$

From the right hand side of the above equations, and knowing that the field matching conditions between different cylindrical layers will relate together only the same component of the fields $\vec{E}$ and $\vec{H}$ (i.e. it will relate radial components between them, azimuthal ones between them and longitudinal ones between them, but for instance not E_r to E_s – see Section E.1.2), we can notice that $\hat{E}_s^{m,c}$ and $\hat{H}_s^{m,s}$ are coupled together, as well as $\hat{E}_s^{m,s}$ and $\hat{H}_s^{m,c}$, and that $\hat{E}_s^{m,c}$ is never coupled to $\hat{E}_s^{m,s}$ or $\hat{H}_s^{m,c}$. This means, since no external excitation appears in Eqs. (1.32) and (1.33), and using the same argument as in Section 1.4.1, that

$$\hat{E}_s^{m,s} = \hat{H}_s^{m,c} = 0. \tag{E.17}$$

Using then Eqs. (E.10), (E.11), (E.13) and (E.16), we have

$$\hat{E}_r^{m,s} = \hat{E}_\theta^{m,c} = \hat{H}_r^{m,c} = \hat{H}_\theta^{m,s} = 0. \tag{E.18}$$

The non zero transverse components are, from Eqs. (E.9) to (E.15), all proportional to $\delta(k'-k)$ as $\hat{E}_s^{m,c}$ and $\hat{H}_s^{m,s}$, and multiplying by $e^{-jk's}$, integrating over k' and applying the definitions from Eqs. (1.24) and (1.25) we finally get (assuming $\nu \neq 0$, see Section 1.4.1)

$$E_r^{m,c} = \frac{jk}{\nu^2}\left(\frac{dE_s^{m,c}}{dr} + \frac{m\upsilon\mu}{r}H_s^{m,s}\right), \tag{E.19}$$

$$E_\theta^{m,s} = \frac{jk}{\nu^2}\left(-\frac{m}{r}E_s^{m,c} - \upsilon\mu\frac{dH_s^{m,s}}{dr}\right), \tag{E.20}$$

$$H_r^{m,s} = \frac{jk}{\nu^2}\left(\frac{m\upsilon\varepsilon_c}{r}E_s^{m,c} + \frac{dH_s^{m,s}}{dr}\right), \tag{E.21}$$

$$H_\theta^{m,c} = \frac{jk}{\nu^2}\left(\upsilon\varepsilon_c\frac{dE_s^{m,c}}{dr} + \frac{m}{r}H_s^{m,s}\right). \tag{E.22}$$

Those formulae were also obtained in Refs. [1, 14].

E.1.2 Field matching between the layers

We derive here the recurrent relation existing between adjacent layers for the integration constants of Eqs. (1.56) and (1.57). To do so we consider the boundary condition at $r = b^{(p)}$ for $1 \leq p \leq N-1$ (see Fig. 1.1). Since there are no externally imposed surface charges or currents between the cylindrical layers, from Ref. [11, p. 18] and Eqs. (1.12) and (1.13) the following relations hold across the boundary (for any θ, s and ω)

$$\begin{aligned}
\varepsilon_c^{(p)} E_r^{(p)}\left(b^{(p)},\theta,s;\omega\right) &= \varepsilon_c^{(p+1)} E_r^{(p+1)}\left(b^{(p)},\theta,s;\omega\right),\\
E_\theta^{(p)}\left(b^{(p)},\theta,s;\omega\right) &= E_\theta^{(p+1)}\left(b^{(p)},\theta,s;\omega\right),\\
E_s^{(p)}\left(b^{(p)},\theta,s;\omega\right) &= E_s^{(p+1)}\left(b^{(p)},\theta,s;\omega\right),\\
\mu^{(p)} H_r^{(p)}\left(b^{(p)},\theta,s;\omega\right) &= \mu^{(p+1)} H_r^{(p+1)}\left(b^{(p)},\theta,s;\omega\right),\\
H_\theta^{(p)}\left(b^{(p)},\theta,s;\omega\right) &= H_\theta^{(p+1)}\left(b^{(p)},\theta,s;\omega\right),\\
H_s^{(p)}\left(b^{(p)},\theta,s;\omega\right) &= H_s^{(p+1)}\left(b^{(p)},\theta,s;\omega\right).
\end{aligned}$$

When decomposing these according to Eqs. (1.22) and (1.23) (ignoring the zero terms from Eqs. (E.17) and (E.18)), term by term identification gives for any m, s and ω

$$\varepsilon_c^{(p)} E_r^{m,c(p)}\left(b^{(p)},s;\omega\right) = \varepsilon_c^{(p+1)} E_r^{m,c(p+1)}\left(b^{(p)},s;\omega\right), \tag{E.23}$$

$$E_\theta^{m,s(p)}\left(b^{(p)},s;\omega\right) = E_\theta^{m,s(p+1)}\left(b^{(p)},s;\omega\right), \tag{E.24}$$

$$E_s^{m,c(p)}\left(b^{(p)},s;\omega\right) = E_s^{m,c(p+1)}\left(b^{(p)},s;\omega\right), \tag{E.25}$$

$$\mu^{(p)} H_r^{m,s(p)}\left(b^{(p)},s;\omega\right) = \mu^{(p+1)} H_r^{m,s(p+1)}\left(b^{(p)},s;\omega\right), \tag{E.26}$$

$$H_\theta^{m,c(p)}\left(b^{(p)},s;\omega\right) = H_\theta^{m,c(p+1)}\left(b^{(p)},s;\omega\right), \tag{E.27}$$

$$H_s^{m,s(p)}\left(b^{(p)},s;\omega\right) = H_s^{m,s(p+1)}\left(b^{(p)},s;\omega\right). \tag{E.28}$$

When plugging them in Eqs. (1.56) and (1.57), Eqs. (E.25) and (E.28) read respectively, in terms of the integration constants

$$C_{Ie}^{m\,(p)} I_m\left(\nu^{(p)} b^{(p)}\right) + C_{Ke}^{m\ (p)} K_m\left(\nu^{(p)} b^{(p)}\right) = C_{Ie}^{m\,(p+1)} I_m\left(\nu^{(p+1)} b^{(p)}\right) + C_{Ke}^{m\ (p+1)} K_m\left(\nu^{(p+1)} b^{(p)}\right), \tag{E.29}$$

$$C_{Ih}^{m\,(p)} I_m\left(\nu^{(p)} b^{(p)}\right) + C_{Kh}^{m\ (p)} K_m\left(\nu^{(p)} b^{(p)}\right) = C_{Ih}^{m\,(p+1)} I_m\left(\nu^{(p+1)} b^{(p)}\right) + C_{Kh}^{m\ (p+1)} K_m\left(\nu^{(p+1)} b^{(p)}\right), \tag{E.30}$$

while Eqs. (E.27) and (E.24), using Eqs. (E.22) and (E.20), can be written

$$\frac{1}{\left(\nu^{(p)}\right)^2}\left[\upsilon\varepsilon_c^{(p)}\left.\frac{dE_s^{m,c(p)}}{dr}\right|_{b^{(p)}}+\frac{m}{b^{(p)}}H_s^{m,s(p)}\left(b^{(p)}\right)\right]$$
$$=\frac{1}{\left(\nu^{(p+1)}\right)^2}\left[\upsilon\varepsilon_c^{(p+1)}\left.\frac{dE_s^{m,c(p+1)}}{dr}\right|_{b^{(p)}}+\frac{m}{b^{(p)}}H_s^{m,s(p+1)}\left(b^{(p)}\right)\right],$$
$$\frac{1}{\left(\nu^{(p)}\right)^2}\left[-\frac{m}{b^{(p)}}E_s^{m,c(p)}\left(b^{(p)}\right)-\upsilon\mu^{(p)}\left.\frac{dH_s^{m,s(p)}}{dr}\right|_{b^{(p)}}\right]$$
$$=\frac{1}{\left(\nu^{(p+1)}\right)^2}\left[-\frac{m}{b^{(p)}}E_s^{m,c(p+1)}\left(b^{(p)}\right)-\upsilon\mu^{(p+1)}\left.\frac{dH_s^{m,s(p+1)}}{dr}\right|_{b^{(p)}}\right],$$

which, using Eqs. (1.56) and (1.57), become

$$\frac{1}{\left(\nu^{(p)}\right)^2}\left[\upsilon\varepsilon_c^{(p)}\nu^{(p)}\left\{C_{Ie}^{m\,(p)}I_m'\left(\nu^{(p)}b^{(p)}\right)+C_{Ke}^{m\,(p)}K_m'\left(\nu^{(p)}b^{(p)}\right)\right\}\right.$$
$$\left.+\frac{m}{b^{(p)}}\left\{C_{Ih}^{m\,(p)}I_m\left(\nu^{(p)}b^{(p)}\right)+C_{Kh}^{m\,(p)}K_m\left(\nu^{(p)}b^{(p)}\right)\right\}\right]$$

$$=\frac{1}{\left(\nu^{(p+1)}\right)^2}\left[\upsilon\varepsilon_c^{(p+1)}\nu^{(p+1)}\left\{C_{Ie}^{m\,(p+1)}I_m'\left(\nu^{(p+1)}b^{(p)}\right)+C_{Ke}^{m\,(p+1)}K_m'\left(\nu^{(p+1)}b^{(p)}\right)\right\}\right.$$
$$\left.+\frac{m}{b^{(p)}}\left\{C_{Ih}^{m\,(p+1)}I_m\left(\nu^{(p+1)}b^{(p)}\right)+C_{Kh}^{m\,(p+1)}K_m\left(\nu^{(p+1)}b^{(p)}\right)\right\}\right], \quad \text{(E.31)}$$

and

$$\frac{1}{\left(\nu^{(p)}\right)^2}\left[-\frac{m}{b^{(p)}}\left\{C_{Ie}^{m\,(p)}I_m\left(\nu^{(p)}b^{(p)}\right)+C_{Ke}^{m\,(p)}K_m\left(\nu^{(p)}b^{(p)}\right)\right\}\right.$$
$$\left.-\upsilon\mu^{(p)}\nu^{(p)}\left\{C_{Ih}^{m\,(p)}I_m'\left(\nu^{(p)}b^{(p)}\right)+C_{Kh}^{m\,(p)}K_m'\left(\nu^{(p)}b^{(p)}\right)\right\}\right]$$

$$=\frac{1}{\left(\nu^{(p+1)}\right)^2}\left[-\frac{m}{b^{(p)}}\left\{C_{Ie}^{m\,(p+1)}I_m\left(\nu^{(p+1)}b^{(p)}\right)+C_{Ke}^{m\,(p+1)}K_m\left(\nu^{(p+1)}b^{(p)}\right)\right\}\right.$$
$$\left.-\upsilon\mu^{(p+1)}\nu^{(p+1)}\left\{C_{Ih}^{m\,(p+1)}I_m'\left(\nu^{(p+1)}b^{(p)}\right)+C_{Kh}^{m\,(p+1)}K_m'\left(\nu^{(p+1)}b^{(p)}\right)\right\}\right]. \quad \text{(E.32)}$$

We can express Eq. (E.31) using Eq. (E.30), leading to

$$\frac{1}{\nu^{(p)}}\upsilon\varepsilon_c^{(p)}\left[C_{Ie}^{m\,(p)}I_m'\left(\nu^{(p)}b^{(p)}\right)+C_{Ke}^{m\,(p)}K_m'\left(\nu^{(p)}b^{(p)}\right)\right]$$
$$+\left(\frac{1}{\left(\nu^{(p)}\right)^2}-\frac{1}{\left(\nu^{(p+1)}\right)^2}\right)\frac{m}{b^{(p)}}\left[C_{Ih}^{m\,(p)}I_m\left(\nu^{(p)}b^{(p)}\right)+C_{Kh}^{m\,(p)}K_m\left(\nu^{(p)}b^{(p)}\right)\right]$$

$$=\frac{1}{\nu^{(p+1)}}\upsilon\varepsilon_c^{(p+1)}\left[C_{Ie}^{m\,(p+1)}I_m'\left(\nu^{(p+1)}b^{(p)}\right)+C_{Ke}^{m\,(p+1)}K_m'\left(\nu^{(p+1)}b^{(p)}\right)\right]. \quad \text{(E.33)}$$

Similarly we rewrite Eq. (E.32) using Eq. (E.29), to get

$$\left(\frac{1}{\left(\nu^{(p+1)}\right)^2}-\frac{1}{\left(\nu^{(p)}\right)^2}\right)\frac{m}{b^{(p)}}\left[C_{Ie}^{m\,(p)}I_m\left(\nu^{(p)}b^{(p)}\right)+C_{Ke}^{m\ (p)}K_m\left(\nu^{(p)}b^{(p)}\right)\right]=$$

$$\upsilon\left[\frac{\mu^{(p)}}{\nu^{(p)}}\left\{C_{Ih}^{m\,(p)}I'_m\left(\nu^{(p)}b^{(p)}\right)+C_{Kh}^{m\ (p)}K'_m\left(\nu^{(p)}b^{(p)}\right)\right\}\right.$$
$$\left.-\frac{\mu^{(p+1)}}{\nu^{(p+1)}}\left\{C_{Ih}^{m\,(p+1)}I'_m\left(\nu^{(p+1)}b^{(p)}\right)+C_{Kh}^{m\ (p+1)}K'_m\left(\nu^{(p+1)}b^{(p)}\right)\right\}\right]. \quad \text{(E.34)}$$

To determine the constants in front of the modified Bessel functions in the expression of E_s and H_s of Eqs. (1.56) and (1.57) (four integration constants per layer), we will use the continuity at the boundaries between the different materials of $E_\theta^{(p)}$, $E_s^{(p)}$, $H_\theta^{(p)}$ and $H_s^{(p)}$ as expressed in Eqs. (E.29), (E.30), (E.33) and (E.34). Continuity of $\varepsilon_c^{(p)}E_r^{(p)}$ and $\mu^{(p)}H_r^{(p)}$ give redundant equations, which can be readily seen from Eqs. (E.1) and (E.3)[1].
With the definitions

$$\begin{aligned}
Z_0 &= \frac{1}{\varepsilon_0 c}=\mu_0 c=\sqrt{\frac{\mu_0}{\varepsilon_0}}, && \text{(E.35)}\\
\vec{G} &= Z_0\vec{H},\\
C_{Ig}^{m\,(p)} &= Z_0 C_{Ih}^{m\,(p)},\\
C_{Kg}^{m\ (p)} &= Z_0 C_{Kh}^{m\ (p)},\\
x^{p+1,p} &= \nu^{(p+1)}b^{(p)},\\
x^{p,p} &= \nu^{(p)}b^{(p)}, && \text{(E.36)}
\end{aligned}$$

the continuity of E_s and H_s is given by Eqs. (E.29) and (E.30) which we can rewrite, using the above notations:

$$C_{Ie}^{m\,(p)}I_m(x^{p,p})+C_{Ke}^{m\ (p)}K_m(x^{p,p}) = C_{Ie}^{m\,(p+1)}I_m(x^{p+1,p})+C_{Ke}^{m\ (p+1)}K_m(x^{p+1,p}), \quad \text{(E.37)}$$
$$C_{Ig}^{m\,(p)}I_m(x^{p,p})+C_{Kg}^{m\ (p)}K_m(x^{p,p}) = C_{Ig}^{m\,(p+1)}I_m(x^{p+1,p})+C_{Kg}^{m\ (p+1)}K_m(x^{p+1,p}). \quad \text{(E.38)}$$

[1] Note that the redundancy of D_r continuity would not have occurred if (as done in Refs. [1, 14]) we had used $\vec{D}=\varepsilon_0\varepsilon_b\vec{E}$ instead of Eq. (1.12) for the definition of the electric displacement field used in Eq. (1.8), while Eqs. (1.9) and (E.1) remain the same. In the absence of surface charges at the boundaries, this would lead to the following boundary condition in replacement of Eq. (E.23)

$$\varepsilon_b^{(p)}E_r^{(p)}\left(b^{(p)},\theta,s;\omega\right)=\varepsilon_b^{(p+1)}E_r^{(p+1)}\left(b^{(p)},\theta,s;\omega\right),$$

and consequently to one additional equation per boundary and necessarily to an inconsistency. Still, it had no impact on the final results of Refs. [1, 14] because the continuity of the radial components was never used. Also, consistency is recovered simply by saying that in such a formalism there exists a surface charge density at the layers boundary (physically, those charges are actually induced charges, created by the discontinuity of the complex permittivity – particularly its conductive part – which results in a discontinuity in the current density at that boundary – see also Appendix A).

The continuity of H_θ and E_θ can be written, from Eqs. (E.33) and (E.34), by virtue of the above definitions

$$\frac{\beta\varepsilon_1^{(p)}}{\nu^{(p)}}\left[C_{Ie}^{m\,(p)}I'_m(x^{p,p})+C_{Ke}^{m\ (p)}K'_m(x^{p,p})\right]$$
$$+\left(\frac{1}{\left(\nu^{(p)}\right)^2}-\frac{1}{\left(\nu^{(p+1)}\right)^2}\right)\frac{m}{b^{(p)}}\left[C_{Ig}^{m\,(p)}I_m(x^{p,p})+C_{Kg}^{m\ (p)}K_m(x^{p,p})\right]$$
$$=\frac{\beta\varepsilon_1^{(p+1)}}{\nu^{(p+1)}}\left[C_{Ie}^{m\,(p+1)}I'_m(x^{p+1,p})+C_{Ke}^{m\ (p+1)}K'_m(x^{p+1,p})\right], \quad \text{(E.39)}$$

and

$$\frac{\beta\mu_1^{(p)}}{\nu^{(p)}}\left[C_{Ig}^{m\,(p)}I'_m(x^{p,p})+C_{Kg}^{m\ (p)}K'_m(x^{p,p})\right]$$
$$+\left(\frac{1}{\left(\nu^{(p)}\right)^2}-\frac{1}{\left(\nu^{(p+1)}\right)^2}\right)\frac{m}{b^{(p)}}\left[C_{Ie}^{m\,(p)}I_m(x^{p,p})+C_{Ke}^{m\ (p)}K_m(x^{p,p})\right]$$
$$=\frac{\beta\mu_1^{(p+1)}}{\nu^{(p+1)}}\left[C_{Ig}^{m\,(p+1)}I'_m(x^{p+1,p})+C_{Kg}^{m\ (p+1)}K'_m(x^{p+1,p})\right]. \quad \text{(E.40)}$$

We can write Eqs. (E.37) and (E.39) in matrix form:

$$\begin{bmatrix} I_m(x^{p+1,p}) & K_m(x^{p+1,p}) \\ \frac{\beta\varepsilon_1^{(p+1)}}{\nu^{(p+1)}}I'_m(x^{p+1,p}) & \frac{\beta\varepsilon_1^{(p+1)}}{\nu^{(p+1)}}K'_m(x^{p+1,p}) \end{bmatrix}\cdot\begin{bmatrix} C_{Ie}^{m\,(p+1)} \\ C_{Ke}^{m\ (p+1)} \end{bmatrix}=$$

$$\begin{bmatrix} C_{Ie}^{m\,(p)}I_m(x^{p,p})+C_{Ke}^{m\ (p)}K_m(x^{p,p}) \\ \frac{\beta\varepsilon_1^{(p)}}{\nu^{(p)}}\left\{C_{Ie}^{m\,(p)}I'_m(x^{p,p})+C_{Ke}^{m\ (p)}K'_m(x^{p,p})\right\}+ \\ \left(\frac{1}{(\nu^{(p)})^2}-\frac{1}{(\nu^{(p+1)})^2}\right)\frac{m}{b^{(p)}}\left\{C_{Ig}^{m\,(p)}I_m(x^{p,p})+C_{Kg}^{m\ (p)}K_m(x^{p,p})\right\} \end{bmatrix}.$$

This can be readily solved for $\begin{bmatrix} C_{Ie}^{m\,(p+1)} \\ C_{Ke}^{m\ (p+1)} \end{bmatrix}$, knowing that the determinant of the first matrix is proportional to the wronskian of the modified Bessel functions, more precisely equal to (see Eq. (C.6)) $-\frac{\beta\varepsilon_1^{(p+1)}}{\left(\nu^{(p+1)}\right)^2 b^{(p)}}$. We get, using the inversion formula of a 2×2 matrix (see Appendix D.1)

$$\begin{bmatrix} C_{Ie}^{m\,(p+1)} \\ \\ C_{Ke}^{m\ (p+1)} \end{bmatrix} = -\frac{\left(\nu^{(p+1)}\right)^2 b^{(p)}}{\beta\varepsilon_1^{(p+1)}} \begin{bmatrix} \frac{\beta\varepsilon_1^{(p+1)}}{\nu^{(p+1)}} K'_m(x^{p+1,p}) & -K_m(x^{p+1,p}) \\ \\ -\frac{\beta\varepsilon_1^{(p+1)}}{\nu^{(p+1)}} I'_m(x^{p+1,p}) & I_m(x^{p+1,p}) \end{bmatrix} \cdot$$

$$\left(\begin{bmatrix} I_m(x^{p,p}) & K_m(x^{p,p}) \\ \\ \frac{\beta\varepsilon_1^{(p)}}{\nu^{(p)}} I'_m(x^{p,p}) & \frac{\beta\varepsilon_1^{(p)}}{\nu^{(p)}} K'_m(x^{p,p}) \end{bmatrix} \cdot \begin{bmatrix} C_{Ie}^{m\,(p)} \\ \\ C_{Ke}^{m\ (p)} \end{bmatrix} + \right.$$

$$\left. \left\{ \frac{1}{\left(\nu^{(p)}\right)^2} - \frac{1}{\left(\nu^{(p+1)}\right)^2} \right\} \frac{m}{b^{(p)}} \begin{bmatrix} 0 & 0 \\ \\ I_m(x^{p,p}) & K_m(x^{p,p}) \end{bmatrix} \cdot \begin{bmatrix} C_{Ig}^{m\,(p)} \\ \\ C_{Kg}^{m\ (p)} \end{bmatrix} \right). \quad \text{(E.41)}$$

Very similarly we can write for $\begin{bmatrix} C_{Ig}^{m\,(p+1)} \\ C_{Kg}^{m\ (p+1)} \end{bmatrix}$, from Eqs. (E.38) and (E.40) (we only need to substitute ε_1 with μ_1 in the above 2×2 matrices):

$$\begin{bmatrix} C_{Ig}^{m\,(p+1)} \\ \\ C_{Kg}^{m\ (p+1)} \end{bmatrix} = -\frac{\left(\nu^{(p+1)}\right)^2 b^{(p)}}{\beta\mu_1^{(p+1)}} \begin{bmatrix} \frac{\beta\mu_1^{(p+1)}}{\nu^{(p+1)}} K'_m(x^{p+1,p}) & -K_m(x^{p+1,p}) \\ \\ -\frac{\beta\mu_1^{(p+1)}}{\nu^{(p+1)}} I'_m(x^{p+1,p}) & I_m(x^{p+1,p}) \end{bmatrix} \cdot$$

$$\left(\begin{bmatrix} I_m(x^{p,p}) & K_m(x^{p,p}) \\ \\ \frac{\beta\mu_1^{(p)}}{\nu^{(p)}} I'_m(x^{p,p}) & \frac{\beta\mu_1^{(p)}}{\nu^{(p)}} K'_m(x^{p,p}) \end{bmatrix} \cdot \begin{bmatrix} C_{Ig}^{m\,(p)} \\ \\ C_{Kg}^{m\ (p)} \end{bmatrix} + \right.$$

$$\left. \left\{ \frac{1}{\left(\nu^{(p)}\right)^2} - \frac{1}{\left(\nu^{(p+1)}\right)^2} \right\} \frac{m}{b^{(p)}} \begin{bmatrix} 0 & 0 \\ \\ I_m(x^{p,p}) & K_m(x^{p,p}) \end{bmatrix} \cdot \begin{bmatrix} C_{Ie}^{m(p)} \\ \\ C_{Ke}^{m\ (p)} \end{bmatrix} \right). \quad \text{(E.42)}$$

Let us now define the four following 2×2 matrices, enabling the computation of the values of the constants for the $p+1$ region knowing those of the p region:

$$P^{p+1,p} = -\frac{\left(\nu^{(p+1)}\right)^2 b^{(p)}}{\beta\varepsilon_1^{(p+1)}} \begin{bmatrix} \frac{\beta\varepsilon_1^{(p+1)}}{\nu^{(p+1)}} K'_m(x^{p+1,p}) & -K_m(x^{p+1,p}) \\ -\frac{\beta\varepsilon_1^{(p+1)}}{\nu^{(p+1)}} I'_m(x^{p+1,p}) & I_m(x^{p+1,p}) \end{bmatrix} \cdot \begin{bmatrix} I_m(x^{p,p}) & K_m(x^{p,p}) \\ \frac{\beta\varepsilon_1^{(p)}}{\nu^{(p)}} I'_m(x^{p,p}) & \frac{\beta\varepsilon_1^{(p)}}{\nu^{(p)}} K'_m(x^{p,p}) \end{bmatrix},$$

$$Q^{p+1,p} = -\left(\frac{\left(\nu^{(p+1)}\right)^2}{\left(\nu^{(p)}\right)^2} - 1\right) \frac{m}{\beta\varepsilon_1^{(p+1)}} \begin{bmatrix} \frac{\beta\varepsilon_1^{(p+1)}}{\nu^{(p+1)}} K'_m(x^{p+1,p}) & -K_m(x^{p+1,p}) \\ -\frac{\beta\varepsilon_1^{(p+1)}}{\nu^{(p+1)}} I'_m(x^{p+1,p}) & I_m(x^{p+1,p}) \end{bmatrix} \cdot \begin{bmatrix} 0 & 0 \\ I_m(x^{p,p}) & K_m(x^{p,p}) \end{bmatrix},$$

$$R^{p+1,p} = -\frac{\left(\nu^{(p+1)}\right)^2 b^{(p)}}{\beta\mu_1^{(p+1)}} \begin{bmatrix} \frac{\beta\mu_1^{(p+1)}}{\nu^{(p+1)}} K'_m(x^{p+1,p}) & -K_m(x^{p+1,p}) \\ -\frac{\beta\mu_1^{(p+1)}}{\nu^{(p+1)}} I'_m(x^{p+1,p}) & I_m(x^{p+1,p}) \end{bmatrix} \cdot \begin{bmatrix} I_m(x^{p,p}) & K_m(x^{p,p}) \\ \frac{\beta\mu_1^{(p)}}{\nu^{(p)}} I'_m(x^{p,p}) & \frac{\beta\mu_1^{(p)}}{\nu^{(p)}} K'_m(x^{p,p}) \end{bmatrix},$$

$$S^{p+1,p} = -\left(\frac{\left(\nu^{(p+1)}\right)^2}{\left(\nu^{(p)}\right)^2} - 1\right) \frac{m}{\beta\mu_1^{(p+1)}} \begin{bmatrix} \frac{\beta\mu_1^{(p+1)}}{\nu^{(p+1)}} K'_m(x^{p+1,p}) & -K_m(x^{p+1,p}) \\ -\frac{\beta\mu_1^{(p+1)}}{\nu^{(p+1)}} I'_m(x^{p+1,p}) & I_m(x^{p+1,p}) \end{bmatrix} \cdot \begin{bmatrix} 0 & 0 \\ I_m(x^{p,p}) & K_m(x^{p,p}) \end{bmatrix},$$

such that Eqs. (E.41) and (E.42) become

$$\begin{bmatrix} C_{Ie}^{m\,(p+1)} \\ C_{Ke}^{m\,(p+1)} \end{bmatrix} = P^{p+1,p} \cdot \begin{bmatrix} C_{Ie}^{m\,(p)} \\ C_{Ke}^{m\,(p)} \end{bmatrix} + Q^{p+1,p} \cdot \begin{bmatrix} C_{Ig}^{m\,(p)} \\ C_{Kg}^{m\,(p)} \end{bmatrix}, \tag{E.43}$$

$$\begin{bmatrix} C_{Ig}^{m\,(p+1)} \\ C_{Kg}^{m\,(p+1)} \end{bmatrix} = R^{p+1,p} \cdot \begin{bmatrix} C_{Ig}^{m\,(p)} \\ C_{Kg}^{m\,(p)} \end{bmatrix} + S^{p+1,p} \cdot \begin{bmatrix} C_{Ie}^{m\,(p)} \\ C_{Ke}^{m\,(p)} \end{bmatrix}. \tag{E.44}$$

It is crucial to be able to compute accurately these four matrices, which is not straightforward since components can be equal to a difference between very large numbers, especially when $\nu^{(p)} b^{(p)}$ or $\nu^{(p+1)} b^{(p)}$ becomes large: for large arguments I_m and I'_m are exponentially growing while K_m and K'_m are exponentially decaying (see Eqs. (C.20) and (C.21), as well as formulas 9.7.1 to 9.7.4 in Ref. [56]). It is therefore better to write them in the following way

$$
\begin{aligned}
P^{p+1,p} &= -\frac{\left(\nu^{(p+1)}\right)^2 b^{(p)}}{\varepsilon_1^{(p+1)}} \left[\begin{array}{l}
I_m(x^{p,p}) K_m(x^{p+1,p}) \left\{ \frac{\varepsilon_1^{(p+1)}}{\nu^{(p+1)}} \frac{K_m'(x^{p+1,p})}{K_m(x^{p+1,p})} - \frac{\varepsilon_1^{(p)}}{\nu^{(p)}} \frac{I_m'(x^{p,p})}{I_m(x^{p,p})} \right\} \\
I_m(x^{p,p}) I_m(x^{p+1,p}) \left\{ -\frac{\varepsilon_1^{(p+1)}}{\nu^{(p+1)}} \frac{I_m'(x^{p+1,p})}{I_m(x^{p+1,p})} + \frac{\varepsilon_1^{(p)}}{\nu^{(p)}} \frac{I_m'(x^{p,p})}{I_m(x^{p,p})} \right\} \\
K_m(x^{p,p}) K_m(x^{p+1,p}) \left\{ \frac{\varepsilon_1^{(p+1)}}{\nu^{(p+1)}} \frac{K_m'(x^{p+1,p})}{K_m(x^{p+1,p})} - \frac{\varepsilon_1^{(p)}}{\nu^{(p)}} \frac{K_m'(x^{p,p})}{K_m(x^{p,p})} \right\} \\
K_m(x^{p,p}) I_m(x^{p+1,p}) \left\{ -\frac{\varepsilon_1^{(p+1)}}{\nu^{(p+1)}} \frac{I_m'(x^{p+1,p})}{I_m(x^{p+1,p})} + \frac{\varepsilon_1^{(p)}}{\nu^{(p)}} \frac{K_m'(x^{p,p})}{K_m(x^{p,p})} \right\}
\end{array} \right], \qquad \text{(E.45)} \\
Q^{p+1,p} &= -\left(\frac{\left(\nu^{(p+1)}\right)^2}{\left(\nu^{(p)}\right)^2} - 1 \right) \frac{m}{\beta \varepsilon_1^{(p+1)}} \left[\begin{array}{ll}
-I_m(x^{p,p}) K_m(x^{p+1,p}) & -K_m(x^{p,p}) K_m(x^{p+1,p}) \\
I_m(x^{p,p}) I_m(x^{p+1,p}) & K_m(x^{p,p}) I_m(x^{p+1,p})
\end{array} \right], \qquad \text{(E.46)} \\
R^{p+1,p} &= -\frac{\left(\nu^{(p+1)}\right)^2 b^{(p)}}{\mu_1^{(p+1)}} \left[\begin{array}{l}
I_m(x^{p,p}) K_m(x^{p+1,p}) \left\{ \frac{\mu_1^{(p+1)}}{\nu^{(p+1)}} \frac{K_m'(x^{p+1,p})}{K_m(x^{p+1,p})} - \frac{\mu_1^{(p)}}{\nu^{(p)}} \frac{I_m'(x^{p,p})}{I_m(x^{p,p})} \right\} \\
I_m(x^{p,p}) I_m(x^{p+1,p}) \left\{ -\frac{\mu_1^{(p+1)}}{\nu^{(p+1)}} \frac{I_m'(x^{p+1,p})}{I_m(x^{p+1,p})} + \frac{\mu_1^{(p)}}{\nu^{(p)}} \frac{I_m'(x^{p,p})}{I_m(x^{p,p})} \right\} \\
K_m(x^{p,p}) K_m(x^{p+1,p}) \left\{ \frac{\mu_1^{(p+1)}}{\nu^{(p+1)}} \frac{K_m'(x^{p+1,p})}{K_m(x^{p+1,p})} - \frac{\mu_1^{(p)}}{\nu^{(p)}} \frac{K_m'(x^{p,p})}{K_m(x^{p,p})} \right\} \\
K_m(x^{p,p}) I_m(x^{p+1,p}) \left\{ -\frac{\mu_1^{(p+1)}}{\nu^{(p+1)}} \frac{I_m'(x^{p+1,p})}{I_m(x^{p+1,p})} + \frac{\mu_1^{(p)}}{\nu^{(p)}} \frac{K_m'(x^{p,p})}{K_m(x^{p,p})} \right\}
\end{array} \right], \qquad \text{(E.47)} \\
S^{p+1,p} &= \frac{\varepsilon_1^{(p+1)}}{\mu_1^{(p+1)}} Q^{p+1,p}, \qquad \text{(E.48)}
\end{aligned}
$$

in which the quotients involving modified Bessel functions and their derivatives can be computed accurately using Eqs. (C.7) and (C.8)

$$
\begin{aligned}
\frac{I_m'(z)}{I_m(z)} &= \frac{I_{m-1}(z)}{I_m(z)} - \frac{m}{z}, \\
\frac{K_m'(z)}{K_m(z)} &= -\frac{K_{m-1}(z)}{K_m(z)} - \frac{m}{z}, \qquad \text{(E.49)}
\end{aligned}
$$

and we can normalize the Bessel functions in the first quotient of these expressions with e^z for I_m and e^{-z} for K_m, which does not change the quotient value.
We can then define the 4×4 matrix $M^{p+1,p}$ by

$$
M^{p+1,p} = \begin{bmatrix} P^{p+1,p} & Q^{p+1,p} \\ S^{p+1,p} & R^{p+1,p} \end{bmatrix}, \qquad \text{(E.50)}
$$

such that

$$\begin{bmatrix} C_{Ie}^{m\,(p+1)} \\ C_{Ke}^{m\,(p+1)} \\ C_{Ig}^{m\,(p+1)} \\ C_{Kg}^{m\,(p+1)} \end{bmatrix} = M^{p+1,p} \cdot \begin{bmatrix} C_{Ie}^{m\,(p)} \\ C_{Ke}^{m\,(p)} \\ C_{Ig}^{m\,(p)} \\ C_{Kg}^{m\,(p)} \end{bmatrix}, \tag{E.51}$$

which is the relation looked for.

E.1.3 Direct space-charge impedances

When injecting in Eq. (1.97) the longitudinal electric field due to the direct space charge from Eq. (1.90) together with the definition of $\mathscr{C}$ in Eq. (1.62), one gets the following longitudinal space-charge impedance:

$$Z_{\parallel}^{SC,direct} = -\frac{j\omega\mu_0 L}{2\pi\beta^2\gamma^2} K_0\left(\frac{k\sqrt{a_1^2+a_2^2-2a_1a_2\cos(\theta_2-\theta_1)}}{\gamma}\right). \tag{E.52}$$

Using Eqs. (1.98) and (1.99) with Eqs. (1.90), (C.13) and (1.62), we find for the transverse space-charge impedances:

$$\begin{aligned} Z_x^{SC,direct} &= -\frac{\mathscr{C}L}{Q\gamma} K_1\left(\frac{k}{\gamma}\sqrt{a_1^2+a_2^2-2a_1a_2\cos(\theta_2-\theta_1)}\right)\left[-\cos\theta_2\frac{a_2-a_1\cos(\theta_2-\theta_1)}{\sqrt{a_1^2+a_2^2-2a_1a_2(\theta_2-\theta_1)}}\right. \\ &\qquad \left. +\frac{\sin\theta_2}{a_2}\frac{a_1a_2\sin(\theta_2-\theta_1)}{\sqrt{a_1^2+a_2^2-2a_1a_2\cos(\theta_2-\theta_1)}}\right] \\ &= \frac{j\omega\mu_0 L}{2\pi\beta^2\gamma^3} K_1\left(\frac{k\sqrt{a_1^2+a_2^2-2a_1a_2\cos(\theta_2-\theta_1)}}{\gamma}\right)\frac{a_2\cos\theta_2-a_1\cos\theta_1}{\sqrt{a_1^2+a_2^2-2a_1a_2\cos(\theta_2-\theta_1)}}, \end{aligned} \tag{E.53}$$

$$\begin{aligned} Z_y^{SC,direct} &= -\frac{\mathscr{C}L}{Q\gamma} K_1\left(\frac{k}{\gamma}\sqrt{a_1^2+a_2^2-2a_1a_2\cos(\theta_2-\theta_1)}\right)\left[-\sin\theta_2\frac{a_2-a_1\cos(\theta_2-\theta_1)}{\sqrt{a_1^2+a_2^2-2a_1a_2\cos(\theta_2-\theta_1)}}\right. \\ &\qquad \left. -\frac{\cos\theta_2}{a_2}\frac{a_1a_2\sin(\theta_2-\theta_1)}{\sqrt{a_1^2+a_2^2-2a_1a_2\cos(\theta_2-\theta_1)}}\right] \\ &= \frac{j\omega\mu_0 L}{2\pi\beta^2\gamma^3} K_1\left(\frac{k\sqrt{a_1^2+a_2^2-2a_1a_2\cos(\theta_2-\theta_1)}}{\gamma}\right)\frac{a_2\sin\theta_2-a_1\sin\theta_1}{\sqrt{a_1^2+a_2^2-2a_1a_2\cos(\theta_2-\theta_1)}}. \end{aligned} \tag{E.54}$$

E.1.4 Wall impedances

The total longitudinal wall impedance is obtained when plugging the wall part of the longitudinal electric field from Eq. (1.92) into the definition (1.97):

$$Z_{\parallel}^{Wall} = 2\frac{\mathscr{C}L}{Q}\sum_{m=0}^{\infty}\frac{\alpha_{\mathrm{TM}}^{m}\cos\left(m\left(\theta_2-\theta_1\right)\right)}{1+\delta_{m0}}I_m\left(\frac{ka_1}{\gamma}\right)I_m\left(\frac{ka_2}{\gamma}\right). \tag{E.55}$$

This expression gives the general nonlinear longitudinal wall impedance. To get the first order terms in the source and test positions (for small $\frac{ka_1}{\gamma}$ and $\frac{ka_2}{\gamma}$), we inject the development in Taylor series of I_m from Eq. (C.16). We see that to go up to the second order in both the source and test positions, we need to go up to $m=1$ in the above sum. Approximating then up to second order the modified Bessel functions thanks to Eq. (C.16) and using

$$\cos\left(\theta_2-\theta_1\right)=\cos\theta_2\cos\theta_1+\sin\theta_2\sin\theta_1=\frac{x_1x_2+y_1y_2}{a_1a_2},$$

we get

$$\begin{aligned}Z_{\parallel}^{Wall} &\approx 2\frac{\mathscr{C}L}{Q}\left[\frac{\alpha_{\mathrm{TM}}^{0}}{2}\left\{1+\left(\frac{ka_1}{2\gamma}\right)^2+\left(\frac{ka_2}{2\gamma}\right)^2\right\}+\alpha_{\mathrm{TM}}^{1}\frac{x_1x_2+y_1y_2}{a_1a_2}\frac{ka_1}{2\gamma}\frac{ka_2}{2\gamma}\right]\\ &\approx \frac{\mathscr{C}L}{Q}\left[\alpha_{\mathrm{TM}}^{0}+\frac{k^2\alpha_{\mathrm{TM}}^{0}}{4\gamma^2}x_1^2+\frac{k^2\alpha_{\mathrm{TM}}^{0}}{4\gamma^2}y_1^2+\frac{k^2\alpha_{\mathrm{TM}}^{0}}{4\gamma^2}x_2^2+\frac{k^2\alpha_{\mathrm{TM}}^{0}}{4\gamma^2}y_2^2+\frac{k^2\alpha_{\mathrm{TM}}^{1}}{2\gamma^2}x_1x_2+\frac{k^2\alpha_{\mathrm{TM}}^{1}}{2\gamma^2}y_1y_2\right].\end{aligned} \tag{E.56}$$

In a similar way, the total horizontal wall impedance is obtained when plugging Eq. (1.92) into the definition (1.98):

$$\begin{aligned}Z_x^{Wall} = 2\frac{\mathscr{C}L}{kQ}\sum_{m=0}^{\infty}\frac{\alpha_{\mathrm{TM}}^{m}}{1+\delta_{m0}}I_m\left(\frac{ka_1}{\gamma}\right)\Bigg[&\frac{k\cos\theta_2\cos\left(m\left(\theta_2-\theta_1\right)\right)}{\gamma}I_m'\left(\frac{ka_2}{\gamma}\right)\\ &+\frac{m\sin\theta_2\sin\left(m\left(\theta_2-\theta_1\right)\right)}{a_2}I_m\left(\frac{ka_2}{\gamma}\right)\Bigg],\end{aligned} \tag{E.57}$$

such that, with Eq. (C.7):

$$\begin{aligned}Z_x^{Wall} = 2\frac{\mathscr{C}L}{kQ}\sum_{m=0}^{\infty}\frac{\alpha_{\mathrm{TM}}^{m}}{1+\delta_{m0}}I_m\left(\frac{ka_1}{\gamma}\right)\Bigg[&\frac{k\cos\theta_2\cos\left(m\left(\theta_2-\theta_1\right)\right)}{\gamma}I_{m-1}\left(\frac{ka_2}{\gamma}\right)\\ &-\frac{m\cos\left(\theta_2+m\left(\theta_2-\theta_1\right)\right)}{a_2}I_m\left(\frac{ka_2}{\gamma}\right)\Bigg].\end{aligned} \tag{E.58}$$

From this and Eq. (C.16) we see that we need to go up to $m=1$ to obtain Z_x^{Wall} up to the second order in the source and test coordinates. Approximating the Bessel functions up to that order we obtain

$$\begin{aligned}Z_x^{Wall} &\approx 2\frac{\mathscr{C}L}{kQ}\left[\frac{\alpha_{\mathrm{TM}}^{0}}{2}\left(1+\left(\frac{ka_1}{2\gamma}\right)^2\right)\frac{k^2x_2}{2\gamma^2}+\alpha_{\mathrm{TM}}^{1}\frac{ka_1}{2\gamma}\left(\frac{k\cos\theta_2\cos\left(\theta_2-\theta_1\right)}{\gamma}-\frac{k\cos\left(2\theta_2-\theta_1\right)}{2\gamma}\right)\right]\\ &\approx 2\frac{\mathscr{C}L}{kQ}\left[\frac{\alpha_{\mathrm{TM}}^{0}}{2}\frac{k^2x_2}{2\gamma^2}+\alpha_{\mathrm{TM}}^{1}\frac{k^2a_1}{4\gamma^2}\cos\theta_1\right],\end{aligned}$$

where we have used various trigonometric identities. The total horizontal impedance up to second order can be rewritten

$$Z_x^{Wall} \approx \frac{\mathscr{C}Lk}{2\gamma^2 Q}\left(\alpha_{\mathrm{TM}}^1 x_1 + \alpha_{\mathrm{TM}}^0 x_2\right). \tag{E.59}$$

The next non-zero terms are of third order.
Similarly, the total vertical wall impedance is obtained when plugging Eq. (1.92) into the definition (1.99), using also Eq. (C.7):

$$\begin{aligned} Z_y^{Wall} &= 2\frac{\mathscr{C}L}{kQ}\sum_{m=0}^{\infty}\frac{\alpha_{\mathrm{TM}}^m}{1+\delta_{m0}} I_m\left(\frac{ka_1}{\gamma}\right)\left[\frac{k\sin\theta_2\cos\left(m\left(\theta_2-\theta_1\right)\right)}{\gamma} I_m'\left(\frac{ka_2}{\gamma}\right)\right. \\ &\qquad \left. -\frac{m\cos\theta_2\sin\left(m\left(\theta_2-\theta_1\right)\right)}{a_2} I_m\left(\frac{ka_2}{\gamma}\right)\right], \qquad \text{(E.60)} \\ &= 2\frac{\mathscr{C}L}{kQ}\sum_{m=0}^{\infty}\frac{\alpha_{\mathrm{TM}}^m}{1+\delta_{m0}} I_m\left(\frac{ka_1}{\gamma}\right)\left[\frac{k\sin\theta_2\cos\left(m\left(\theta_2-\theta_1\right)\right)}{\gamma} I_{m-1}\left(\frac{ka_2}{\gamma}\right)\right. \\ &\qquad \left. -\frac{m\sin\left(\theta_2+m\left(\theta_2-\theta_1\right)\right)}{a_2} I_m\left(\frac{ka_2}{\gamma}\right)\right]. \qquad \text{(E.61)} \end{aligned}$$

Again, as above we approximate Z_y^{Wall} up to the second order in the source and test coordinates thanks to Eq. (C.16) and going up to $m=1$:

$$\begin{aligned} Z_y^{Wall} &\approx 2\frac{\mathscr{C}L}{kQ}\left[\frac{\alpha_{\mathrm{TM}}^0}{2}\left(1+\left(\frac{ka_1}{2\gamma}\right)^2\right)\frac{k^2y_2}{2\gamma^2}+\alpha_{\mathrm{TM}}^1\frac{ka_1}{2\gamma}\left(\frac{k\sin\theta_2\cos\left(\theta_2-\theta_1\right)}{\gamma}-\frac{k\sin\left(2\theta_2-\theta_1\right)}{2\gamma}\right)\right] \\ &\approx 2\frac{\mathscr{C}L}{kQ}\left[\frac{\alpha_{\mathrm{TM}}^0}{2}\frac{k^2y_2}{2\gamma^2}+\alpha_{\mathrm{TM}}^1\frac{k^2a_1}{4\gamma^2}\sin\theta_1\right] \\ &\approx \frac{\mathscr{C}Lk}{2\gamma^2Q}\left(\alpha_{\mathrm{TM}}^1 y_1+\alpha_{\mathrm{TM}}^0 y_2\right). \end{aligned} \tag{E.62}$$

Again, the next non-zero terms are of third order.

E.1.5 Panofsky-Wenzel theorem

We check here that the beam-coupling impedances derived in Section 1.4.6 comply with the Panofsky-Wenzel theorem. First, for the space-charge impedances in Eqs. (1.100), (1.101) and (1.102), we have, thanks to Eq. (C.13)

$$\begin{aligned} \frac{\partial}{\partial x_2}Z_{\parallel}^{SC,direct} &= -\frac{j\omega\mu_0 L}{2\pi\beta^2\gamma^2}\frac{k}{\gamma}K_0'\left(\frac{k\sqrt{(x_2-x_1)^2+(y_2-y_1)^2}}{\gamma}\right)\frac{x_2-x_1}{\sqrt{(x_2-x_1)^2+(y_2-y_1)^2}} \\ &= kZ_x^{SC,direct}, \qquad \text{(E.63)} \\ \frac{\partial}{\partial y_2}Z_{\parallel}^{SC,direct} &= -\frac{j\omega\mu_0 L}{2\pi\beta^2\gamma^2}\frac{k}{\gamma}K_0'\left(\frac{k\sqrt{(x_2-x_1)^2+(y_2-y_1)^2}}{\gamma}\right)\frac{y_2-y_1}{\sqrt{(x_2-x_1)^2+(y_2-y_1)^2}} \\ &= kZ_y^{SC,direct}. \qquad \text{(E.64)} \end{aligned}$$

For the wall impedances, we begin by stating that

$$a_2 = \sqrt{x_2^2 + y_2^2}, \qquad \text{and} \quad \left(\frac{a_2}{a_1}\right)^m \left[\cos\left(m(\theta_2-\theta_1)\right) + j\sin\left(m(\theta_2-\theta_1)\right)\right] = \frac{a_2^m e^{jm\theta_2}}{a_1^m e^{jm\theta_1}} = \frac{(x_2+jy_2)^m}{(x_1+jy_1)^m},$$

such that

$$\cos\left(m(\theta_2-\theta_1)\right) = \frac{1}{2}\left(\frac{a_1}{a_2}\right)^m \left[\left(\frac{x_2+jy_2}{x_1+jy_1}\right)^m + \left(\frac{x_2-jy_2}{x_1-jy_1}\right)^m\right],$$
$$j\sin\left(m(\theta_2-\theta_1)\right) = \frac{1}{2}\left(\frac{a_1}{a_2}\right)^m \left[\left(\frac{x_2+jy_2}{x_1+jy_1}\right)^m - \left(\frac{x_2-jy_2}{x_1-jy_1}\right)^m\right].$$

From these we obtain the following derivatives:

$$\frac{\partial a_2}{\partial x_2} = \frac{x_2}{\sqrt{x_2^2+y_2^2}} = \cos\theta_2, \qquad \frac{\partial a_2}{\partial y_2} = \frac{y_2}{\sqrt{x_2^2+y_2^2}} = \sin\theta_2,$$

$$\begin{aligned}
\frac{\partial \cos\left(m(\theta_2-\theta_1)\right)}{\partial x_2} &= \frac{a_1^m}{2}\left\{-\frac{m\cos\theta_2}{a_2^{m+1}}\left[\left(\frac{x_2+jy_2}{x_1+jy_1}\right)^m + \left(\frac{x_2-jy_2}{x_1-jy_1}\right)^m\right] + a_2^{-m}\left[\frac{m}{x_2+jy_2}\left(\frac{x_2+jy_2}{x_1+jy_1}\right)^m \right.\right. \\
&\qquad \left.\left. + \frac{m}{x_2-jy_2}\left(\frac{x_2-jy_2}{x_1-jy_1}\right)^m\right]\right\} \\
&= -\frac{m\cos\theta_2}{a_2}\cos\left(m(\theta_2-\theta_1)\right) + \frac{m}{2a_2^2}\left(\frac{a_1}{a_2}\right)^m \left[\left(x_2-jy_2\right)\left(\frac{x_2+jy_2}{x_1+jy_1}\right)^m \right. \\
&\qquad \left. + \left(x_2+jy_2\right)\left(\frac{x_2-jy_2}{x_1-jy_1}\right)^m\right] \\
&= -\frac{m\cos\theta_2}{a_2}\cos\left(m(\theta_2-\theta_1)\right) + \frac{m}{a_2^2}\left[x_2\cos\left(m(\theta_2-\theta_1)\right) + y_2\sin\left(m(\theta_2-\theta_1)\right)\right] \\
&= \frac{m\sin\theta_2}{a_2}\sin\left(m(\theta_2-\theta_1)\right),
\end{aligned}$$

$$\begin{aligned}
\frac{\partial \cos\left(m(\theta_2-\theta_1)\right)}{\partial y_2} &= \frac{a_1^m}{2}\left\{-\frac{m\sin\theta_2}{a_2^{m+1}}\left[\left(\frac{x_2+jy_2}{x_1+jy_1}\right)^m + \left(\frac{x_2-jy_2}{x_1-jy_1}\right)^m\right] + a_2^{-m}\left[\frac{jm}{x_2+jy_2}\left(\frac{x_2+jy_2}{x_1+jy_1}\right)^m \right.\right. \\
&\qquad \left.\left. - \frac{jm}{x_2-jy_2}\left(\frac{x_2-jy_2}{x_1-jy_1}\right)^m\right]\right\} \\
&= -\frac{m\sin\theta_2}{a_2}\cos\left(m(\theta_2-\theta_1)\right) + \frac{jm}{2a_2^2}\left(\frac{a_1}{a_2}\right)^m \left[\left(x_2-jy_2\right)\left(\frac{x_2+jy_2}{x_1+jy_1}\right)^m \right. \\
&\qquad \left. - \left(x_2+jy_2\right)\left(\frac{x_2-jy_2}{x_1-jy_1}\right)^m\right] \\
&= -\frac{m\sin\theta_2}{a_2}\cos\left(m(\theta_2-\theta_1)\right) + \frac{m}{a_2^2}\left[-x_2\sin\left(m(\theta_2-\theta_1)\right) + y_2\cos\left(m(\theta_2-\theta_1)\right)\right] \\
&= -\frac{m\cos\theta_2}{a_2}\sin\left(m(\theta_2-\theta_1)\right).
\end{aligned}$$

Using the above and Eq. (1.103) we obtain

$$\frac{\partial}{\partial x_2} Z_{\parallel}^{Wall} = 2\frac{\mathscr{C}L}{Q}\sum_{m=0}^{\infty}\frac{\alpha_{\mathrm{TM}}^{m}}{1+\delta_{m0}} I_m\left(\frac{ka_1}{\gamma}\right)\left[\cos\left(m\left(\theta_2-\theta_1\right)\right)\frac{k\cos\theta_2}{\gamma} I'_m\left(\frac{ka_2}{\gamma}\right)\right.$$
$$\left. + \frac{m\sin\theta_2}{a_2}\sin\left(m(\theta_2-\theta_1)\right) I_m\left(\frac{ka_2}{\gamma}\right)\right]$$
$$= kZ_x^{Wall} \qquad \text{from Eq. (E.57)}, \tag{E.65}$$

$$\frac{\partial}{\partial y_2} Z_{\parallel}^{Wall} = 2\frac{\mathscr{C}L}{Q}\sum_{m=0}^{\infty}\frac{\alpha_{\mathrm{TM}}^{m}}{1+\delta_{m0}} I_m\left(\frac{ka_1}{\gamma}\right)\left[\cos\left(m\left(\theta_2-\theta_1\right)\right)\frac{k\sin\theta_2}{\gamma} I'_m\left(\frac{ka_2}{\gamma}\right)\right.$$
$$\left. - \frac{m\cos\theta_2}{a_2}\sin\left(m(\theta_2-\theta_1)\right) I_m\left(\frac{ka_2}{\gamma}\right)\right]$$
$$= kZ_y^{Wall} \qquad \text{from Eq. (E.60)}, \tag{E.66}$$

which are in agreement with the Panofsky-Wenzel theorem as stated in Ref. [7, p. 90].

E.2 Flat multilayer chamber

E.2.1 Transverse components of the electromagnetic fields

From the transverse components of Maxwell equations (1.9) and (1.10) written in cartesian coordinates (see Appendix B.2), assuming $y \neq y_1$ and omitting the superscript (p), we have the relations

$$\frac{\partial H_s}{\partial y} - \frac{\partial H_y}{\partial s} = j\omega\varepsilon_c E_x, \tag{E.67}$$
$$\frac{\partial H_x}{\partial s} - \frac{\partial H_s}{\partial x} = j\omega\varepsilon_c E_y, \tag{E.68}$$
$$\frac{\partial E_s}{\partial y} - \frac{\partial E_y}{\partial s} = -j\omega\mu H_x, \tag{E.69}$$
$$\frac{\partial E_x}{\partial s} - \frac{\partial E_s}{\partial x} = -j\omega\mu H_y. \tag{E.70}$$

Differentiating with respect to s Eq. (E.70) and combining it to Eq. (E.67), we get, knowing the longitudinal dependence of E_s

$$\frac{\partial^2 E_x}{\partial s^2} + \omega^2\varepsilon_c\mu E_x = -jk\frac{\partial E_s}{\partial x} - j\omega\mu\frac{\partial H_s}{\partial y}. \tag{E.71}$$

In the same way, we can differentiate with respect to s Eqs. (E.69), (E.68) and (E.67), then combine them respectively to Eqs. (E.68), (E.69) and (E.70), to get

$$\frac{\partial^2 E_y}{\partial s^2} + \omega^2 \varepsilon_c \mu E_y = -jk\frac{\partial E_s}{\partial y} + j\omega\mu\frac{\partial H_s}{\partial x}, \tag{E.72}$$

$$\frac{\partial^2 H_x}{\partial s^2} + \omega^2 \varepsilon_c \mu H_x = j\omega\varepsilon_c\frac{\partial E_s}{\partial y} - jk\frac{\partial H_s}{\partial x}, \tag{E.73}$$

$$\frac{\partial^2 H_y}{\partial s^2} + \omega^2 \varepsilon_c \mu H_y = -j\omega\varepsilon_c\frac{\partial E_s}{\partial x} - jk\frac{\partial H_s}{\partial y}. \tag{E.74}$$

If we now introduce the decompositions from Eqs. (1.113) and (1.114) and identify the integrands and each cosine and sine term (since those equations are valid for any s and x), we get

$$\left(-k'^2 + \omega^2\varepsilon_c\mu\right)\tilde{E}_x^c = -jkk_x\tilde{E}_s^s - j\omega\mu\frac{d\tilde{H}_s^c}{dy}, \tag{E.75}$$

$$\left(-k'^2 + \omega^2\varepsilon_c\mu\right)\tilde{E}_x^s = jkk_x\tilde{E}_s^c - j\omega\mu\frac{d\tilde{H}_s^s}{dy}, \tag{E.76}$$

$$\left(-k'^2 + \omega^2\varepsilon_c\mu\right)\tilde{E}_y^c = -jk\frac{d\tilde{E}_s^c}{dy} + j\omega\mu k_x\tilde{H}_s^s, \tag{E.77}$$

$$\left(-k'^2 + \omega^2\varepsilon_c\mu\right)\tilde{E}_y^s = -jk\frac{d\tilde{E}_s^s}{dy} - j\omega\mu k_x\tilde{H}_s^c, \tag{E.78}$$

$$\left(-k'^2 + \omega^2\varepsilon_c\mu\right)\tilde{H}_x^c = j\omega\varepsilon_c\frac{d\tilde{E}_s^c}{dy} - jkk_x\tilde{H}_s^s, \tag{E.79}$$

$$\left(-k'^2 + \omega^2\varepsilon_c\mu\right)\tilde{H}_x^s = j\omega\varepsilon_c\frac{d\tilde{E}_s^s}{dy} + jkk_x\tilde{H}_s^c, \tag{E.80}$$

$$\left(-k'^2 + \omega^2\varepsilon_c\mu\right)\tilde{H}_y^c = -j\omega\varepsilon_c k_x\tilde{E}_s^s - jk\frac{d\tilde{H}_s^c}{dy}, \tag{E.81}$$

$$\left(-k'^2 + \omega^2\varepsilon_c\mu\right)\tilde{H}_y^s = j\omega\varepsilon_c k_x\tilde{E}_s^c - jk\frac{d\tilde{H}_s^s}{dy}. \tag{E.82}$$

From the right hand side of the above equations, and knowing that the field matching conditions between different layers will relate together only the same component of the fields $\vec{E}$ and $\vec{H}$ (i.e. it will relate horizontal components between them, vertical ones between them and longitudinal ones between them, but for instance not E_x to E_s – see Section E.2.2), we can notice that $\tilde{E}_s^c$ and $\tilde{H}_s^s$ are coupled together, as well as $\tilde{E}_s^s$ and $\tilde{H}_s^c$, and that $\tilde{E}_s^c$ is never coupled to $\tilde{E}_s^s$ or $\tilde{H}_s^c$. This means, since no external excitation appears in Eqs. (1.125) and (1.126), and using the same argument as in Section 1.5.1, that

$$\tilde{E}_s^s = \tilde{H}_s^c = 0. \tag{E.83}$$

Using then Eqs. (E.75), (E.78), (E.80) and (E.81), we have

$$\tilde{E}_x^c = \tilde{E}_y^s = \tilde{H}_x^s = \tilde{H}_y^c = 0. \tag{E.84}$$

The non zero transverse components are, from Eqs. (E.76) to (E.82), all proportional to $\delta(k'-k)$ as $\tilde{E}_s^c$ and $\tilde{H}_s^s$, and upon multiplication by $e^{-jk's}$ and integration over k', we finally obtain, assuming that $\nu \neq 0$ and using the definitions from Eqs. (1.117), (1.118) and (1.39):

$$E_x^s = \frac{jk}{\nu^2}\left(-k_x E_s^c + \upsilon\mu\frac{dH_s^s}{dy}\right), \tag{E.85}$$

$$E_y^c = \frac{jk}{\nu^2}\left(\frac{dE_s^c}{dy} - k_x \upsilon\mu H_s^s\right), \tag{E.86}$$

$$H_x^c = \frac{jk}{\nu^2}\left(-\upsilon\varepsilon_c\frac{dE_s^c}{dy} + k_x H_s^s\right), \tag{E.87}$$

$$H_y^s = \frac{jk}{\nu^2}\left(-k_x \upsilon\varepsilon_c E_s^c + \frac{dH_s^s}{dy}\right). \tag{E.88}$$

E.2.2 Field matching between the layers

We derive here the recurrent relation existing between adjacent layers for the integration constants of Eqs. (1.147) and (1.148). To do so we consider the boundary condition at $y = b^{(p)}$ for $1 \leq p \leq N-1$ or $-M+1 \leq p \leq -1$ (see Fig. 1.3). There are no externally imposed surface charges or currents between the layers and the boundary is perpendicular to $\vec{e}_y$, so according to Ref. [11, p. 18] and Eqs. (1.12) and (1.13) the following relations hold across the boundary (for any x, s and ω)

$$\begin{aligned}
E_x^{(p)}\left(x, b^{(p)}, s; \omega\right) &= E_x^{(p\pm1)}\left(x, b^{(p)}, s; \omega\right), \\
\varepsilon_c^{(p)} E_y^{(p)}\left(x, b^{(p)}, s; \omega\right) &= \varepsilon_c^{(p\pm1)} E_y^{(p\pm1)}\left(x, b^{(p)}, s; \omega\right), \\
E_s^{(p)}\left(x, b^{(p)}, s; \omega\right) &= E_s^{(p\pm1)}\left(x, b^{(p)}, s; \omega\right), \\
H_x^{(p)}\left(x, b^{(p)}, s; \omega\right) &= H_x^{(p\pm1)}\left(x, b^{(p)}, s; \omega\right), \\
\mu^{(p)} H_y^{(p)}\left(x, b^{(p)}, s; \omega\right) &= \mu^{(p\pm1)} H_y^{(p\pm1)}\left(x, b^{(p)}, s; \omega\right), \\
H_s^{(p)}\left(x, b^{(p)}, s; \omega\right) &= H_s^{(p\pm1)}\left(x, b^{(p)}, s; \omega\right),
\end{aligned}$$

where in the superscripts the plus sign is selected for the layers in the upper part ($y > 0$), and the minus sign for the layers in the lower part ($y < 0$).
When decomposing the above equations according to Eqs. (1.115) and (1.116) (ignoring the zero terms from Eqs. (E.83) and (E.84)), integrand identification gives, for any k_x, s and ω

$$E_x^{s\,(p)}\left(b^{(p)}, s; k_x, \omega\right) = E_x^{s\,(p\pm1)}\left(b^{(p)}, s; k_x, \omega\right), \tag{E.89}$$

$$\varepsilon_c^{(p)} E_y^{c\,(p)}\left(b^{(p)}, s; k_x, \omega\right) = \varepsilon_c^{(p\pm1)} E_y^{c\,(p\pm1)}\left(b^{(p)}, s; k_x, \omega\right), \tag{E.90}$$

$$E_s^{c\,(p)}\left(b^{(p)}, s; k_x, \omega\right) = E_s^{c\,(p\pm1)}\left(b^{(p)}, s; k_x, \omega\right), \tag{E.91}$$

$$H_x^{c\,(p)}\left(b^{(p)}, s; k_x, \omega\right) = H_x^{c\,(p\pm1)}\left(b^{(p)}, s; k_x, \omega\right), \tag{E.92}$$

$$\mu^{(p)} H_y^{s\,(p)}\left(b^{(p)}, s; k_x, \omega\right) = \mu^{(p\pm1)} H_y^{s\,(p\pm1)}\left(b^{(p)}, s; k_x, \omega\right), \tag{E.93}$$

$$H_s^{s\,(p)}\left(b^{(p)}, s; k_x, \omega\right) = H_s^{s\,(p\pm1)}\left(b^{(p)}, s; k_x, \omega\right). \tag{E.94}$$

We focus first on the upper layers and assume therefore $1 \le p \le N-1$. In terms of the integration constants, Eqs. (E.91) and (E.94) read respectively, when plugging in Eqs. (1.147) and (1.148)

$$C_{e+}^{(p)} e^{k_y^{(p)} b^{(p)}} + C_{e-}^{(p)} e^{-k_y^{(p)} b^{(p)}} = C_{e+}^{(p+1)} e^{k_y^{(p+1)} b^{(p)}} + C_{e-}^{(p+1)} e^{-k_y^{(p+1)} b^{(p)}}, \tag{E.95}$$

$$C_{h+}^{(p)} e^{k_y^{(p)} b^{(p)}} + C_{h-}^{(p)} e^{-k_y^{(p)} b^{(p)}} = C_{h+}^{(p+1)} e^{k_y^{(p+1)} b^{(p)}} + C_{h-}^{(p+1)} e^{-k_y^{(p+1)} b^{(p)}}, \tag{E.96}$$

while Eqs. (E.89) and (E.92), using Eqs. (E.85) and (E.87), can be written

$$\begin{aligned}
\frac{1}{\left(\nu^{(p)}\right)^2}\left(-k_x E_s^{c(p)}\left(b^{(p)}\right) + v\mu^{(p)} \left.\frac{dH_s^{s(p)}}{dy}\right|_{b^{(p)}}\right) &= \frac{1}{\left(\nu^{(p+1)}\right)^2}\left(-k_x E_s^{c(p+1)}\left(b^{(p)}\right) + v\mu^{(p+1)} \left.\frac{dH_s^{s(p+1)}}{dy}\right|_{b^{(p)}}\right), \\
\frac{1}{\left(\nu^{(p)}\right)^2}\left(-v\varepsilon_c^{(p)} \left.\frac{dE_s^{c(p)}}{dy}\right|_{b^{(p)}} + k_x H_s^{s(p)}\left(b^{(p)}\right)\right) &= \frac{1}{\left(\nu^{(p+1)}\right)^2}\left(-v\varepsilon_c^{(p+1)} \left.\frac{dE_s^{c(p+1)}}{dy}\right|_{b^{(p)}} + k_x H_s^{s(p+1)}\left(b^{(p)}\right)\right),
\end{aligned}$$

which, using again Eqs. (1.147) and (1.148), become

$$\begin{aligned}
&\frac{1}{\left(\nu^{(p)}\right)^2}\left[-k_x\left\{C_{e+}^{(p)} e^{k_y^{(p)} b^{(p)}} + C_{e-}^{(p)} e^{-k_y^{(p)} b^{(p)}}\right\} + v\mu^{(p)} k_y^{(p)}\left\{C_{h+}^{(p)} e^{k_y^{(p)} b^{(p)}} - C_{h-}^{(p)} e^{-k_y^{(p)} b^{(p)}}\right\}\right] \\
&= \frac{1}{\left(\nu^{(p+1)}\right)^2}\left[-k_x\left\{C_{e+}^{(p+1)} e^{k_y^{(p+1)} b^{(p)}} + C_{e-}^{(p+1)} e^{-k_y^{(p+1)} b^{(p)}}\right\}\right. \\
&\qquad \left. + v\mu^{(p+1)} k_y^{(p+1)}\left\{C_{h+}^{(p+1)} e^{k_y^{(p+1)} b^{(p)}} - C_{h-}^{(p+1)} e^{-k_y^{(p+1)} b^{(p)}}\right\}\right],
\end{aligned} \tag{E.97}$$

and

$$\begin{aligned}
&\frac{1}{\left(\nu^{(p)}\right)^2}\left[-v\varepsilon_c^{(p)} k_y^{(p)}\left\{C_{e+}^{(p)} e^{k_y^{(p)} b^{(p)}} - C_{e-}^{(p)} e^{-k_y^{(p)} b^{(p)}}\right\} + k_x\left\{C_{h+}^{(p)} e^{k_y^{(p)} b^{(p)}} + C_{h-}^{(p)} e^{-k_y^{(p)} b^{(p)}}\right\}\right] \\
&= \frac{1}{\left(\nu^{(p+1)}\right)^2}\left[-v\varepsilon_c^{(p+1)} k_y^{(p+1)}\left\{C_{e+}^{(p+1)} e^{k_y^{(p+1)} b^{(p)}} - C_{e-}^{(p+1)} e^{-k_y^{(p+1)} b^{(p)}}\right\}\right. \\
&\qquad \left. + k_x\left\{C_{h+}^{(p+1)} e^{k_y^{(p+1)} b^{(p)}} + C_{h-}^{(p+1)} e^{-k_y^{(p+1)} b^{(p)}}\right\}\right].
\end{aligned} \tag{E.98}$$

To determine the integration constants in the expression of E_s^c and H_s^s (four such constants per layer, so $4(N+M)$ of them in total), we will use the continuity at the boundaries between the different layers, of $E_x^{(p)}$, $E_s^{(p)}$, $H_x^{(p)}$ and $H_s^{(p)}$ as expressed in Eqs. (E.95) to (E.98). Continuity of $\varepsilon_c^{(p)} E_y^{(p)}$ and $\mu^{(p)} H_y^{(p)}$ give redundant equations, which can be readily seen from Eqs. (E.68) and (E.70) (see also the discussion in Section E.1.2, in particular footnote 1).

First we introduce as in the cylindrical case the free space impedance Z_0 and the field $\vec{G}$ which has the same dimension as the electric field $\vec{E}$

$$Z_0 = \frac{1}{\varepsilon_0 c} = \mu_0 c = \sqrt{\frac{\mu_0}{\varepsilon_0}} \qquad \text{and} \qquad \vec{G} = Z_0 \vec{H},$$

and the corresponding constant coefficients for $\vec{G}$

$$C_{g+}^{(p)} = Z_0 C_{h+}^{(p)} \qquad \text{and} \qquad C_{g-}^{(p)} = Z_0 C_{h-}^{(p)}.$$

We can rewrite the continuity of E_s and H_s given by Eqs. (E.95) and (E.96) thanks to the above definitions

$$C_{e+}^{(p)} e^{k_y^{(p)} b^{(p)}} + C_{e-}^{(p)} e^{-k_y^{(p)} b^{(p)}} = C_{e+}^{(p+1)} e^{k_y^{(p+1)} b^{(p)}} + C_{e-}^{(p+1)} e^{-k_y^{(p+1)} b^{(p)}}, \tag{E.99}$$

$$C_{g+}^{(p)} e^{k_y^{(p)} b^{(p)}} + C_{g-}^{(p)} e^{-k_y^{(p)} b^{(p)}} = C_{g+}^{(p+1)} e^{k_y^{(p+1)} b^{(p)}} + C_{g-}^{(p+1)} e^{-k_y^{(p+1)} b^{(p)}}. \tag{E.100}$$

Then, the continuity of E_x and H_x can be written, from Eqs. (E.97) and (E.98), with the use of the above equations and the definitions in Eqs. (1.12) and (1.13)

$$\left(\frac{1}{\left(\nu^{(p+1)}\right)^2} - \frac{1}{\left(\nu^{(p)}\right)^2} \right) k_x \left[C_{e+}^{(p)} e^{k_y^{(p)} b^{(p)}} + C_{e-}^{(p)} e^{-k_y^{(p)} b^{(p)}} \right] = \beta \left[\frac{k_y^{(p+1)} \mu_1^{(p+1)}}{\left(\nu^{(p+1)}\right)^2} \left\{ C_{g+}^{(p+1)} e^{k_y^{(p+1)} b^{(p)}} - C_{g-}^{(p+1)} e^{-k_y^{(p+1)} b^{(p)}} \right\} - \frac{k_y^{(p)} \mu_1^{(p)}}{\left(\nu^{(p)}\right)^2} \left\{ C_{g+}^{(p)} e^{k_y^{(p)} b^{(p)}} - C_{g-}^{(p)} e^{-k_y^{(p)} b^{(p)}} \right\} \right], \tag{E.101}$$

and

$$\left(\frac{1}{\left(\nu^{(p+1)}\right)^2} - \frac{1}{\left(\nu^{(p)}\right)^2} \right) k_x \left[C_{g+}^{(p)} e^{k_y^{(p)} b^{(p)}} + C_{g-}^{(p)} e^{-k_y^{(p)} b^{(p)}} \right] = \beta \left[\frac{k_y^{(p+1)} \varepsilon_1^{(p+1)}}{\left(\nu^{(p+1)}\right)^2} \left\{ C_{e+}^{(p+1)} e^{k_y^{(p+1)} b^{(p)}} - C_{e-}^{(p+1)} e^{-k_y^{(p+1)} b^{(p)}} \right\} - \frac{k_y^{(p)} \varepsilon_1^{(p)}}{\left(\nu^{(p)}\right)^2} \left\{ C_{e+}^{(p)} e^{k_y^{(p)} b^{(p)}} - C_{e-}^{(p)} e^{-k_y^{(p)} b^{(p)}} \right\} \right]. \tag{E.102}$$

We can write Eqs. (E.99) and (E.102) in matrix form:

$$\begin{bmatrix} e^{k_y^{(p+1)} b^{(p)}} & e^{-k_y^{(p+1)} b^{(p)}} \\ \frac{\beta k_y^{(p+1)} \varepsilon_1^{(p+1)}}{\left(\nu^{(p+1)}\right)^2} e^{k_y^{(p+1)} b^{(p)}} & \frac{-\beta k_y^{(p+1)} \varepsilon_1^{(p+1)}}{\left(\nu^{(p+1)}\right)^2} e^{-k_y^{(p+1)} b^{(p)}} \end{bmatrix} \cdot \begin{bmatrix} C_{e+}^{(p+1)} \\ C_{e-}^{(p+1)} \end{bmatrix} = \begin{bmatrix} C_{e+}^{(p)} e^{k_y^{(p)} b^{(p)}} + C_{e-}^{(p)} e^{-k_y^{(p)} b^{(p)}} \\ \frac{\beta k_y^{(p)} \varepsilon_1^{(p)}}{\left(\nu^{(p)}\right)^2} \left\{ C_{e+}^{(p)} e^{k_y^{(p)} b^{(p)}} - C_{e-}^{(p)} e^{-k_y^{(p)} b^{(p)}} \right\} + \\ \left(\frac{1}{\left(\nu^{(p+1)}\right)^2} - \frac{1}{\left(\nu^{(p)}\right)^2} \right) k_x \left\{ C_{g+}^{(p)} e^{k_y^{(p)} b^{(p)}} + C_{g-}^{(p)} e^{-k_y^{(p)} b^{(p)}} \right\} \end{bmatrix}.$$

This can be readily solved for $\begin{bmatrix} C_{e+}^{(p+1)} \\ C_{e-}^{(p+1)} \end{bmatrix}$, knowing that the determinant of the left hand side matrix is equal to $-\frac{2\beta k_y^{(p+1)} \varepsilon_1^{(p+1)}}{\left(\nu^{(p+1)}\right)^2}$. We get, assuming that[2] $k_y^{(p+1)} \neq 0$ and using the inversion formula of a 2×2 matrix

[2] $k_y^{(p+1)} = 0$ can happen if $\nu^{(p+1)}$ is purely imaginary (Cherenkov radiation in the layer considered, see e.g. Refs. [11, p. 637], [14, p. 11] or [55, p. 406]) and if $k_x^2 = -\left(\nu^{(p+1)}\right)^2$ from Eq. (1.149). This can be the case for only a finite number of k_x values (one for each layer where $\nu^{(p+1)}$ is purely imaginary), so is not a concern since we will in the end perform a continuous integration over k_x. Moreover even a small imaginary part in ε_c (thanks to a non-zero conductivity for instance) will be enough to suppress

(see Appendix D.1)

$$\begin{bmatrix} C_{e+}^{(p+1)} \\ C_{e-}^{(p+1)} \end{bmatrix} = -\frac{\left(\nu^{(p+1)}\right)^2}{2\beta k_y^{(p+1)} \varepsilon_1^{(p+1)}} \begin{bmatrix} \frac{-\beta k_y^{(p+1)} \varepsilon_1^{(p+1)}}{\left(\nu^{(p+1)}\right)^2} e^{-k_y^{(p+1)} b^{(p)}} & -e^{-k_y^{(p+1)} b^{(p)}} \\ \frac{-\beta k_y^{(p+1)} \varepsilon_1^{(p+1)}}{\left(\nu^{(p+1)}\right)^2} e^{k_y^{(p+1)} b^{(p)}} & e^{k_y^{(p+1)} b^{(p)}} \end{bmatrix} \cdot$$

$$\left(\begin{bmatrix} e^{k_y^{(p)} b^{(p)}} & e^{-k_y^{(p)} b^{(p)}} \\ \frac{\beta k_y^{(p)} \varepsilon_1^{(p)}}{\left(\nu^{(p)}\right)^2} e^{k_y^{(p)} b^{(p)}} & \frac{-\beta k_y^{(p)} \varepsilon_1^{(p)}}{\left(\nu^{(p)}\right)^2} e^{-k_y^{(p)} b^{(p)}} \end{bmatrix} \cdot \begin{bmatrix} C_{e+}^{(p)} \\ C_{e-}^{(p)} \end{bmatrix} + \right.$$

$$\left. \left\{ \frac{1}{\left(\nu^{(p+1)}\right)^2} - \frac{1}{\left(\nu^{(p)}\right)^2} \right\} k_x \begin{bmatrix} 0 & 0 \\ e^{k_y^{(p)} b^{(p)}} & e^{-k_y^{(p)} b^{(p)}} \end{bmatrix} \cdot \begin{bmatrix} C_{g+}^{(p)} \\ C_{g-}^{(p)} \end{bmatrix} \right). \quad \text{(E.103)}$$

Very similarly we can write for $\begin{bmatrix} C_{g+}^{(p+1)} \\ C_{g-}^{(p+1)} \end{bmatrix}$, from Eqs. (E.100) and (E.101) (we simply need to replace ε_1 by μ_1 in the above matrices)

$$\begin{bmatrix} C_{g+}^{(p+1)} \\ C_{g-}^{(p+1)} \end{bmatrix} = -\frac{\left(\nu^{(p+1)}\right)^2}{2\beta k_y^{(p+1)} \mu_1^{(p+1)}} \begin{bmatrix} \frac{-\beta k_y^{(p+1)} \mu_1^{(p+1)}}{\left(\nu^{(p+1)}\right)^2} e^{-k_y^{(p+1)} b^{(p)}} & -e^{-k_y^{(p+1)} b^{(p)}} \\ \frac{-\beta k_y^{(p+1)} \mu_1^{(p+1)}}{\left(\nu^{(p+1)}\right)^2} e^{k_y^{(p+1)} b^{(p)}} & e^{k_y^{(p+1)} b^{(p)}} \end{bmatrix} \cdot$$

$$\left(\begin{bmatrix} e^{k_y^{(p)} b^{(p)}} & e^{-k_y^{(p)} b^{(p)}} \\ \frac{\beta k_y^{(p)} \mu_1^{(p)}}{\left(\nu^{(p)}\right)^2} e^{k_y^{(p)} b^{(p)}} & \frac{-\beta k_y^{(p)} \mu_1^{(p)}}{\left(\nu^{(p)}\right)^2} e^{-k_y^{(p)} b^{(p)}} \end{bmatrix} \cdot \begin{bmatrix} C_{g+}^{(p)} \\ C_{g-}^{(p)} \end{bmatrix} + \right.$$

$$\left. \left\{ \frac{1}{\left(\nu^{(p+1)}\right)^2} - \frac{1}{\left(\nu^{(p)}\right)^2} \right\} k_x \begin{bmatrix} 0 & 0 \\ e^{k_y^{(p)} b^{(p)}} & e^{-k_y^{(p)} b^{(p)}} \end{bmatrix} \cdot \begin{bmatrix} C_{e+}^{(p)} \\ C_{e-}^{(p)} \end{bmatrix} \right). \quad \text{(E.104)}$$

such singularities.

Let us now define the four following 2×2 matrices, enabling the computation of the values of the constants for the $p+1$ region knowing those of the p region:

$$P^{p+1,p} = \frac{-\left(\nu^{(p+1)}\right)^2}{2\beta k_y^{(p+1)} \varepsilon_1^{(p+1)}} \begin{bmatrix} \frac{-\beta k_y^{(p+1)} \varepsilon_1^{(p+1)}}{\left(\nu^{(p+1)}\right)^2} e^{-k_y^{(p+1)} b^{(p)}} & -e^{-k_y^{(p+1)} b^{(p)}} \\ \frac{-\beta k_y^{(p+1)} \varepsilon_1^{(p+1)}}{\left(\nu^{(p+1)}\right)^2} e^{k_y^{(p+1)} b^{(p)}} & e^{k_y^{(p+1)} b^{(p)}} \end{bmatrix} \cdot \begin{bmatrix} e^{k_y^{(p)} b^{(p)}} & e^{-k_y^{(p)} b^{(p)}} \\ \frac{\beta k_y^{(p)} \varepsilon_1^{(p)}}{\left(\nu^{(p)}\right)^2} e^{k_y^{(p)} b^{(p)}} & \frac{-\beta k_y^{(p)} \varepsilon_1^{(p)}}{\left(\nu^{(p)}\right)^2} e^{-k_y^{(p)} b^{(p)}} \end{bmatrix},$$

$$Q^{p+1,p} = \frac{k_x \left(\frac{\left(\nu^{(p+1)}\right)^2}{\left(\nu^{(p)}\right)^2} - 1 \right)}{2\beta k_y^{(p+1)} \varepsilon_1^{(p+1)}} \begin{bmatrix} \frac{-\beta k_y^{(p+1)} \varepsilon_1^{(p+1)}}{\left(\nu^{(p+1)}\right)^2} e^{-k_y^{(p+1)} b^{(p)}} & -e^{-k_y^{(p+1)} b^{(p)}} \\ \frac{-\beta k_y^{(p+1)} \varepsilon_1^{(p+1)}}{\left(\nu^{(p+1)}\right)^2} e^{k_y^{(p+1)} b^{(p)}} & e^{k_y^{(p+1)} b^{(p)}} \end{bmatrix} \cdot \begin{bmatrix} 0 & 0 \\ e^{k_y^{(p)} b^{(p)}} & e^{-k_y^{(p)} b^{(p)}} \end{bmatrix},$$

$$R^{p+1,p} = \frac{-\left(\nu^{(p+1)}\right)^2}{2\beta k_y^{(p+1)} \mu_1^{(p+1)}} \begin{bmatrix} \frac{-\beta k_y^{(p+1)} \mu_1^{(p+1)}}{\left(\nu^{(p+1)}\right)^2} e^{-k_y^{(p+1)} b^{(p)}} & -e^{-k_y^{(p+1)} b^{(p)}} \\ \frac{-\beta k_y^{(p+1)} \mu_1^{(p+1)}}{\left(\nu^{(p+1)}\right)^2} e^{k_y^{(p+1)} b^{(p)}} & e^{k_y^{(p+1)} b^{(p)}} \end{bmatrix} \cdot \begin{bmatrix} e^{k_y^{(p)} b^{(p)}} & e^{-k_y^{(p)} b^{(p)}} \\ \frac{\beta k_y^{(p)} \mu_1^{(p)}}{\left(\nu^{(p)}\right)^2} e^{k_y^{(p)} b^{(p)}} & \frac{-\beta k_y^{(p)} \mu_1^{(p)}}{\left(\nu^{(p)}\right)^2} e^{-k_y^{(p)} b^{(p)}} \end{bmatrix},$$

$$S^{p+1,p} = \frac{k_x \left(\frac{\left(\nu^{(p+1)}\right)^2}{\left(\nu^{(p)}\right)^2} - 1 \right)}{2\beta k_y^{(p+1)} \mu_1^{(p+1)}} \begin{bmatrix} \frac{-\beta k_y^{(p+1)} \mu_1^{(p+1)}}{\left(\nu^{(p+1)}\right)^2} e^{-k_y^{(p+1)} b^{(p)}} & -e^{-k_y^{(p+1)} b^{(p)}} \\ \frac{-\beta k_y^{(p+1)} \mu_1^{(p+1)}}{\left(\nu^{(p+1)}\right)^2} e^{k_y^{(p+1)} b^{(p)}} & e^{k_y^{(p+1)} b^{(p)}} \end{bmatrix} \cdot \begin{bmatrix} 0 & 0 \\ e^{k_y^{(p)} b^{(p)}} & e^{-k_y^{(p)} b^{(p)}} \end{bmatrix},$$

such that Eqs. (E.103) and (E.104) become

$$\begin{bmatrix} C_{e+}^{(p+1)} \\ C_{e-}^{(p+1)} \end{bmatrix} = P^{p+1,p} \cdot \begin{bmatrix} C_{e+}^{(p)} \\ C_{e-}^{(p)} \end{bmatrix} + Q^{p+1,p} \cdot \begin{bmatrix} C_{g+}^{(p)} \\ C_{g-}^{(p)} \end{bmatrix}, \tag{E.105}$$

$$\begin{bmatrix} C_{g+}^{(p+1)} \\ C_{g-}^{(p+1)} \end{bmatrix} = R^{p+1,p} \cdot \begin{bmatrix} C_{g+}^{(p)} \\ C_{g-}^{(p)} \end{bmatrix} + S^{p+1,p} \cdot \begin{bmatrix} C_{e+}^{(p)} \\ C_{e-}^{(p)} \end{bmatrix}. \tag{E.106}$$

We can rewrite these four matrices in the following way

$$P^{p+1,p} = \frac{1}{2}\begin{bmatrix} \left(1+\frac{(\nu^{(p+1)})^2}{(\nu^{(p)})^2}\frac{k_y^{(p)}}{k_y^{(p+1)}}\frac{\varepsilon_1^{(p)}}{\varepsilon_1^{(p+1)}}\right)e^{\left(k_y^{(p)}-k_y^{(p+1)}\right)b^{(p)}} & \left(1-\frac{(\nu^{(p+1)})^2}{(\nu^{(p)})^2}\frac{k_y^{(p)}}{k_y^{(p+1)}}\frac{\varepsilon_1^{(p)}}{\varepsilon_1^{(p+1)}}\right)e^{\left(-k_y^{(p)}-k_y^{(p+1)}\right)b^{(p)}} \\ \left(1-\frac{(\nu^{(p+1)})^2}{(\nu^{(p)})^2}\frac{k_y^{(p)}}{k_y^{(p+1)}}\frac{\varepsilon_1^{(p)}}{\varepsilon_1^{(p+1)}}\right)e^{\left(k_y^{(p)}+k_y^{(p+1)}\right)b^{(p)}} & \left(1+\frac{(\nu^{(p+1)})^2}{(\nu^{(p)})^2}\frac{k_y^{(p)}}{k_y^{(p+1)}}\frac{\varepsilon_1^{(p)}}{\varepsilon_1^{(p+1)}}\right)e^{\left(k_y^{(p+1)}-k_y^{(p)}\right)b^{(p)}} \end{bmatrix}, \tag{E.107}$$

$$Q^{p+1,p} = \frac{k_x\left(\frac{(\nu^{(p+1)})^2}{(\nu^{(p)})^2}-1\right)}{2\beta k_y^{(p+1)}\varepsilon_1^{(p+1)}}\begin{bmatrix} -e^{\left(k_y^{(p)}-k_y^{(p+1)}\right)b^{(p)}} & -e^{\left(-k_y^{(p)}-k_y^{(p+1)}\right)b^{(p)}} \\ e^{\left(k_y^{(p)}+k_y^{(p+1)}\right)b^{(p)}} & e^{\left(k_y^{(p+1)}-k_y^{(p)}\right)b^{(p)}} \end{bmatrix}, \tag{E.108}$$

$$R^{p+1,p} = \frac{1}{2}\begin{bmatrix} \left(1+\frac{(\nu^{(p+1)})^2}{(\nu^{(p)})^2}\frac{k_y^{(p)}}{k_y^{(p+1)}}\frac{\mu_1^{(p)}}{\mu_1^{(p+1)}}\right)e^{\left(k_y^{(p)}-k_y^{(p+1)}\right)b^{(p)}} & \left(1-\frac{(\nu^{(p+1)})^2}{(\nu^{(p)})^2}\frac{k_y^{(p)}}{k_y^{(p+1)}}\frac{\mu_1^{(p)}}{\mu_1^{(p+1)}}\right)e^{\left(-k_y^{(p)}-k_y^{(p+1)}\right)b^{(p)}} \\ \left(1-\frac{(\nu^{(p+1)})^2}{(\nu^{(p)})^2}\frac{k_y^{(p)}}{k_y^{(p+1)}}\frac{\mu_1^{(p)}}{\mu_1^{(p+1)}}\right)e^{\left(k_y^{(p)}+k_y^{(p+1)}\right)b^{(p)}} & \left(1+\frac{(\nu^{(p+1)})^2}{(\nu^{(p)})^2}\frac{k_y^{(p)}}{k_y^{(p+1)}}\frac{\mu_1^{(p)}}{\mu_1^{(p+1)}}\right)e^{\left(k_y^{(p+1)}-k_y^{(p)}\right)b^{(p)}} \end{bmatrix}, \tag{E.109}$$

$$S^{p+1,p} = \frac{\varepsilon_1^{(p+1)}}{\mu_1^{(p+1)}}Q^{p+1,p}. \tag{E.110}$$

Then we define the 4×4 matrix $M^{p+1,p}$ by

$$M^{p+1,p} = \begin{bmatrix} P^{p+1,p} & Q^{p+1,p} \\ S^{p+1,p} & R^{p+1,p} \end{bmatrix}, \tag{E.111}$$

such that

$$\begin{bmatrix} C_{e+}^{(p+1)} \\ C_{e-}^{(p+1)} \\ C_{g+}^{(p+1)} \\ C_{g-}^{(p+1)} \end{bmatrix} = M^{p+1,p}\cdot\begin{bmatrix} C_{e+}^{(p)} \\ C_{e-}^{(p)} \\ C_{g+}^{(p)} \\ C_{g-}^{(p)} \end{bmatrix}. \tag{E.112}$$

All the above was performed for the upper part of the chamber, i.e. the layers 1 to N. For the lower part of the chamber we can essentially obtain the same results: for this we simply need to consider p between

$-M$ and -1 and replace the $(p+1)$ superscript by $(p-1)$. This gives the following definitions:

$$P^{p-1,p} = \frac{1}{2}\begin{bmatrix} \left(1+\frac{\left(\nu^{(p-1)}\right)^2}{\left(\nu^{(p)}\right)^2}\frac{k_y^{(p)}}{k_y^{(p-1)}}\frac{\varepsilon_1^{(p)}}{\varepsilon_1^{(p-1)}}\right)e^{\left(k_y^{(p)}-k_y^{(p-1)}\right)b^{(p)}} & \left(1-\frac{\left(\nu^{(p-1)}\right)^2}{\left(\nu^{(p)}\right)^2}\frac{k_y^{(p)}}{k_y^{(p-1)}}\frac{\varepsilon_1^{(p)}}{\varepsilon_1^{(p-1)}}\right)e^{\left(-k_y^{(p)}-k_y^{(p-1)}\right)b^{(p)}} \\ \left(1-\frac{\left(\nu^{(p-1)}\right)^2}{\left(\nu^{(p)}\right)^2}\frac{k_y^{(p)}}{k_y^{(p-1)}}\frac{\varepsilon_1^{(p)}}{\varepsilon_1^{(p-1)}}\right)e^{\left(k_y^{(p)}+k_y^{(p-1)}\right)b^{(p)}} & \left(1+\frac{\left(\nu^{(p-1)}\right)^2}{\left(\nu^{(p)}\right)^2}\frac{k_y^{(p)}}{k_y^{(p-1)}}\frac{\varepsilon_1^{(p)}}{\varepsilon_1^{(p-1)}}\right)e^{\left(k_y^{(p-1)}-k_y^{(p)}\right)b^{(p)}} \end{bmatrix}, \tag{E.113}$$

$$Q^{p-1,p} = \frac{k_x\left(\frac{\left(\nu^{(p-1)}\right)^2}{\left(\nu^{(p)}\right)^2}-1\right)}{2\beta k_y^{(p-1)}\varepsilon_1^{(p-1)}}\begin{bmatrix} -e^{\left(k_y^{(p)}-k_y^{(p-1)}\right)b^{(p)}} & -e^{\left(-k_y^{(p)}-k_y^{(p-1)}\right)b^{(p)}} \\ e^{\left(k_y^{(p)}+k_y^{(p-1)}\right)b^{(p)}} & e^{\left(k_y^{(p-1)}-k_y^{(p)}\right)b^{(p)}} \end{bmatrix}, \tag{E.114}$$

$$R^{p-1,p} = \frac{1}{2}\begin{bmatrix} \left(1+\frac{\left(\nu^{(p-1)}\right)^2}{\left(\nu^{(p)}\right)^2}\frac{k_y^{(p)}}{k_y^{(p-1)}}\frac{\mu_1^{(p)}}{\mu_1^{(p-1)}}\right)e^{\left(k_y^{(p)}-k_y^{(p-1)}\right)b^{(p)}} & \left(1-\frac{\left(\nu^{(p-1)}\right)^2}{\left(\nu^{(p)}\right)^2}\frac{k_y^{(p)}}{k_y^{(p-1)}}\frac{\mu_1^{(p)}}{\mu_1^{(p-1)}}\right)e^{\left(-k_y^{(p)}-k_y^{(p-1)}\right)b^{(p)}} \\ \left(1-\frac{\left(\nu^{(p-1)}\right)^2}{\left(\nu^{(p)}\right)^2}\frac{k_y^{(p)}}{k_y^{(p-1)}}\frac{\mu_1^{(p)}}{\mu_1^{(p-1)}}\right)e^{\left(k_y^{(p)}+k_y^{(p-1)}\right)b^{(p)}} & \left(1+\frac{\left(\nu^{(p-1)}\right)^2}{\left(\nu^{(p)}\right)^2}\frac{k_y^{(p)}}{k_y^{(p-1)}}\frac{\mu_1^{(p)}}{\mu_1^{(p-1)}}\right)e^{\left(k_y^{(p-1)}-k_y^{(p)}\right)b^{(p)}} \end{bmatrix}, \tag{E.115}$$

$$S^{p-1,p} = \frac{\varepsilon_1^{(p-1)}}{\mu_1^{(p-1)}}Q^{p-1,p}. \tag{E.116}$$

We can then define the 4×4 matrix $M^{p-1,p}$ by

$$M^{p-1,p} = \begin{bmatrix} P^{p-1,p} & Q^{p-1,p} \\ S^{p-1,p} & R^{p-1,p} \end{bmatrix}, \tag{E.117}$$

and the relations between the integration constants for $-M+1 \le p \le -1$ become

$$\begin{bmatrix} C_{e+}^{(p-1)} \\ C_{e-}^{(p-1)} \\ C_{g+}^{(p-1)} \\ C_{g-}^{(p-1)} \end{bmatrix} = M^{p-1,p}\cdot\begin{bmatrix} C_{e+}^{(p)} \\ C_{e-}^{(p)} \\ C_{g+}^{(p)} \\ C_{g-}^{(p)} \end{bmatrix}. \tag{E.118}$$

E.2.3 Wall term of the longitudinal electric field

In the vacuum region of a flat chamber, the wall term of the electric field is written as (see Section 1.5.5)

$$E_s^{vac,W} = e^{-jks}\int_0^\infty \mathrm{d}k_x \cos(k_x x)\left[C_{e+}^{(1)}e^{k_y^{(1)}y} + C_{e-}^{(-1)}e^{-k_y^{(1)}y}\right]. \tag{E.119}$$

To identify the dependencies in the test particle coordinates as well as in the source particle offset y_1, the idea is to try to get back to a formula in the form of a series involving modified Bessel functions of the first kind I_m of argument proportional to the coordinates of the source and test particles, in a similar way to what was found in the case of an axisymmetric geometry.
We begin by introducing the cylindrical coordinates (r,θ,s) associated to the cartesian ones we have

considered up to now, i.e. $x = r\cos\theta$ and $y = r\sin\theta$. For convenience we make an additional change of angle, defining ϕ as

$$\phi = \theta - \frac{\pi}{2},$$

such that

$$x = -r\sin\phi \quad \text{and} \quad y = r\cos\phi.$$

Then from the invariance of $E_s^{vac,W}$ with the sign of x we have the symmetry relation

$$\begin{aligned} E_s^{vac,W}(r,-\phi,s) &= E_s^{vac,W}(x = r\sin\phi, y = r\cos\phi, s) \\ &= E_s^{vac,W}(x = -r\sin\phi, y = r\cos\phi, s) \\ &= E_s^{vac,W}(r,\phi,s). \end{aligned}$$

The main idea is then to decompose $E_s^{vac,W}$ into a Fourier series with respect to the angle ϕ. Since this function is even, there is no sine term in the series and the coefficients are given by [129]:

$$a_n = \frac{1}{\pi}\int_{-\pi}^{\pi} \mathrm{d}\phi \cos(n\phi)\, E_s^{vac,W},$$

such that

$$E_s^{vac,W} = \sum_{n=0}^{\infty} \frac{a_n}{1+\delta_{n0}} \cos\left(n\phi\right), \tag{E.120}$$

where $\delta_{n0} = 1$ if $n = 0$, 0 otherwise. Using first the parity of $E_s^{vac,W}$ with ϕ, recalling that $k_y^{(1)} = \sqrt{k_x^2 + \frac{k^2}{\gamma^2}}$ and inverting then the order in the integrals in k_x and ϕ, we can obtain for a_n:

$$\begin{aligned} a_n &= \frac{2}{\pi} e^{-jks} \int_0^{\pi} \mathrm{d}\phi \cos(n\phi) \int_0^{\infty} \mathrm{d}k_x \cos\left(k_x r\sin\phi\right) \left[C_{e+}^{(1)} e^{\sqrt{k_x^2+\frac{k^2}{\gamma^2}}\, r\cos\phi} + C_{e-}^{(-1)} e^{-\sqrt{k_x^2+\frac{k^2}{\gamma^2}}\, r\cos\phi} \right] \\ &= \frac{2}{\pi} e^{-jks} \int_0^{\infty} \mathrm{d}k_x \left[C_{e+}^{(1)} \int_0^{\pi} \mathrm{d}\phi \cos(n\phi) \cos\left(k_x r\sin\phi\right) e^{r\cos\phi\sqrt{k_x^2+\frac{k^2}{\gamma^2}}} \right. \\ &\qquad \left. + C_{e-}^{(-1)} \int_0^{\pi} \mathrm{d}\phi \cos(n\phi) \cos\left(k_x r\sin\phi\right) e^{-r\cos\phi\sqrt{k_x^2+\frac{k^2}{\gamma^2}}} \right] \\ &= \frac{2}{\pi} e^{-jks} \int_0^{\infty} \mathrm{d}k_x \left[C_{e+}^{(1)} + (-1)^n C_{e-}^{(-1)} \right] \int_0^{\pi} \mathrm{d}\phi \cos(n\phi) \cos\left(k_x r\sin\phi\right) e^{r\cos\phi\sqrt{k_x^2+\frac{k^2}{\gamma^2}}}, \end{aligned}$$

thanks to the change of variable $\phi \to \pi - \phi$ for the second integral in ϕ. It turns out that the final integral in ϕ can be computed analytically as shown in Appendix C.7. By virtue of Eq. (C.39) we get

$$\begin{aligned} a_n &= e^{-jks} I_n\left(\frac{kr}{\gamma}\right) \int_0^\infty \mathrm{d}k_x \left[C_{e+}^{(1)} + (-1)^n C_{e-}^{(-1)}\right] \left[\left(k_x + \sqrt{k_x^2 + \frac{k^2}{\gamma^2}}\right)^{-n} \frac{k^n}{\gamma^n} + \left(k_x + \sqrt{k_x^2 + \frac{k^2}{\gamma^2}}\right)^{n} \frac{\gamma^n}{k^n}\right] \\ &= e^{-jks} \frac{k}{\gamma} I_n\left(\frac{kr}{\gamma}\right) \int_0^\infty \mathrm{d}u \left[C_{e+}^{(1)} + (-1)^n C_{e-}^{(-1)}\right] \cosh u \left[(\cosh u + \sinh u)^{-n} + (\cosh u + \sinh u)^{n}\right] \\ &\qquad \text{with the change of variable } \; k_x = \frac{k}{\gamma} \sinh u \\ &= e^{-jks} \frac{2k}{\gamma} I_n\left(\frac{kr}{\gamma}\right) \int_0^\infty \mathrm{d}u \left[C_{e+}^{(1)} + (-1)^n C_{e-}^{(-1)}\right] \cosh u \cosh(nu). \end{aligned} \tag{E.121}$$

This, when combined with (E.120), gives the dependence of E_s in the test particle transverse position (r,ϕ). To get the dependence in the source particle position we need some additional steps. First, in a_n we replace $C_{e+}^{(1)}$ and $C_{e-}^{(-1)}$ by their expressions from Eqs. (1.176), using the fact that $k_x = \frac{k}{\gamma}\sinh u$ and $k_y^{(1)} = \frac{k}{\gamma}\cosh u$ in our change of variable:

$$\begin{aligned} a_n = -2\mathscr{C} e^{-jks} I_n\left(\frac{kr}{\gamma}\right) \int_0^\infty \mathrm{d}u \Bigg[&\left\{\chi_1\left(\frac{k}{\gamma}\sinh u\right) e^{\frac{ky_1}{\gamma}\cosh u} + \eta_1\left(\frac{k}{\gamma}\sinh u\right) e^{-\frac{ky_1}{\gamma}\cosh u}\right\} \\ &+ (-1)^n \left\{\chi_2\left(\frac{k}{\gamma}\sinh u\right) e^{\frac{ky_1}{\gamma}\cosh u} + \eta_2\left(\frac{k}{\gamma}\sinh u\right) e^{-\frac{ky_1}{\gamma}\cosh u}\right\}\Bigg] \cosh(nu). \end{aligned}$$

From Eqs. (C.24) and (C.25) applied with $z = \frac{ky_1}{\gamma}$, this can be decomposed into

$$\begin{aligned} a_n = -4\mathscr{C} e^{-jks} I_n\left(\frac{kr}{\gamma}\right) \int_0^\infty \mathrm{d}u \cosh(nu) \sum_{m=0}^{\infty} \frac{\cosh(mu)}{1+\delta_{m0}} I_m\left(\frac{ky_1}{\gamma}\right) \Bigg[&\chi_1\left(\frac{k}{\gamma}\sinh u\right) \\ &+ (-1)^m \eta_1\left(\frac{k}{\gamma}\sinh u\right) + (-1)^n \chi_2\left(\frac{k}{\gamma}\sinh u\right) + (-1)^{m+n} \eta_2\left(\frac{k}{\gamma}\sinh u\right)\Bigg]. \end{aligned}$$

Now we can invert the order of the integral and the sum, before plugging the result into Eq. (E.120), to obtain finally (using also $\phi = \theta - \frac{\pi}{2}$):

$$E_s^{vac,W} = -4\mathscr{C} e^{-jks} \sum_{m,n=0}^{\infty} \frac{\alpha_{mn} \cos\left[n\left(\theta - \frac{\pi}{2}\right)\right]}{(1+\delta_{m0})(1+\delta_{n0})} I_m\left(\frac{ky_1}{\gamma}\right) I_n\left(\frac{kr}{\gamma}\right), \tag{E.122}$$

with α_{mn} defined by the integral

$$\begin{aligned} \alpha_{mn} = \int_0^\infty \mathrm{d}u \cosh(mu)\cosh(nu) \Bigg[&\chi_1\left(\frac{k}{\gamma}\sinh u\right) + (-1)^m \eta_1\left(\frac{k}{\gamma}\sinh u\right) \\ &+ (-1)^n \chi_2\left(\frac{k}{\gamma}\sinh u\right) + (-1)^{m+n} \eta_2\left(\frac{k}{\gamma}\sinh u\right)\Bigg]. \end{aligned} \tag{E.123}$$

We can also write $E_s^{vac,W}$ in cartesian coordinates: using $r = \sqrt{x^2+y^2}$ and

$$\cos\left[n\left(\theta-\frac{\pi}{2}\right)\right] = \cos\left(n\phi\right) = \Re\left(e^{jn\phi}\right) = \Re\left[\left(\cos\phi + j\sin\phi\right)^n\right]$$
$$= \frac{1}{r^n}\Re\left[\left(y-jx\right)^n\right] = \frac{1}{2r^n}\left[\left(y-jx\right)^n + \left(y+jx\right)^n\right], \quad \text{(E.124)}$$

where $\Re$ is the real part of a complex number, we obtain

$$E_s^{vac,W} = -2\mathscr{C}e^{-jks}\sum_{m,n=0}^{\infty}\frac{\alpha_{mn}\left[\left(y-jx\right)^n+\left(y+jx\right)^n\right]}{\left(x^2+y^2\right)^{\frac{n}{2}}\left(1+\delta_{m0}\right)\left(1+\delta_{n0}\right)}I_m\left(\frac{ky_1}{\gamma}\right)I_n\left(\frac{k\sqrt{x^2+y^2}}{\gamma}\right). \quad \text{(E.125)}$$

E.2.4 Wall impedances

In the case when $x_1 = 0$, the total longitudinal wall impedance of a flat chamber is obtained when plugging Eq. (1.187) into the definition (1.192):

$$Z_{\parallel}^{Wall} = 4\frac{\mathscr{C}L}{Q}\sum_{m,n=0}^{\infty}\frac{\alpha_{mn}\cos\left(n\phi_2\right)}{\left(1+\delta_{m0}\right)\left(1+\delta_{n0}\right)}I_m\left(\frac{ky_1}{\gamma}\right)I_n\left(\frac{kr_2}{\gamma}\right), \quad \text{(E.126)}$$

where $r_2 = \sqrt{x_2^2+y_2^2}$ and ϕ_2 is such that $x_2 = -r_2\sin\phi_2$ and $y_2 = r_2\cos\phi_2$ (see Appendix E.2.3). This expression gives the general nonlinear longitudinal wall impedance. We can identify the first order terms in the source and test positions, so for small $\frac{ky_1}{\gamma}$ and $\frac{kr_2}{\gamma}$. From the development in Taylor series of I_m and I_n in Eq. (C.16) we see that to go up to the second order in both the source and test positions, we need to go up to $m = 2$ and $n = 2$ in the above summation. Approximating then up to second order the Bessel functions thanks to Eq. (C.16) and using $\cos\phi_2 = \frac{y_2}{r_2}$ and $\cos 2\phi_2 = 2\cos^2\phi_2 - 1 = \frac{2y_2^2}{r_2^2} - 1$ we get

$$\begin{aligned}
Z_{\parallel}^{Wall} &\approx 4\frac{\mathscr{C}L}{Q}\left[\frac{\alpha_{00}}{4}\left\{1+\left(\frac{ky_1}{2\gamma}\right)^2+\left(\frac{kr_2}{2\gamma}\right)^2\right\}+\frac{\alpha_{01}}{2}\frac{y_2}{r_2}\frac{kr_2}{2\gamma}+\frac{\alpha_{02}}{2}\left(\frac{2y_2^2}{r_2^2}-1\right)\frac{1}{2}\left(\frac{kr_2}{2\gamma}\right)^2\right.\\
&\qquad\left.+\frac{\alpha_{10}}{2}\frac{ky_1}{2\gamma}+\alpha_{11}\frac{y_2}{r_2}\frac{ky_1}{2\gamma}\frac{kr_2}{2\gamma}+\frac{\alpha_{20}}{2}\frac{1}{2}\left(\frac{ky_1}{2\gamma}\right)^2\right]\\
&\approx \frac{\mathscr{C}L}{Q}\left[\alpha_{00}+\frac{k\alpha_{10}}{\gamma}y_1+\frac{k\alpha_{01}}{\gamma}y_2+k^2\left(\frac{\alpha_{00}+\alpha_{20}}{4\gamma^2}\right)y_1^2+k^2\left(\frac{\alpha_{00}-\alpha_{02}}{4\gamma^2}\right)x_2^2\right.\\
&\qquad\left.+k^2\left(\frac{\alpha_{00}+\alpha_{02}}{4\gamma^2}\right)y_2^2+\frac{k^2\alpha_{11}}{\gamma^2}y_1y_2\right].
\end{aligned}$$

In a similar way, the total horizontal wall impedance for $x_1 = 0$ is obtained when plugging Eq. (1.187) into the definition (1.193):

$$Z_x^{Wall} = 4\frac{\mathscr{C}L}{kQ}\sum_{m,n=0}^{\infty}\frac{\alpha_{mn}}{\left(1+\delta_{m0}\right)\left(1+\delta_{n0}\right)}I_m\left(\frac{ky_1}{\gamma}\right)\left[I_n\left(\frac{kr_2}{\gamma}\right)\left.\frac{\partial\cos\left(n\phi\right)}{\partial x}\right|_{x_2,y_2}\right.$$
$$\left.+\frac{k\cos\left(n\phi_2\right)}{\gamma}I_n'\left(\frac{kr_2}{\gamma}\right)\left.\frac{\partial r}{\partial x}\right|_{x_2,y_2}\right].$$

Now we have, using in particular Eq. (E.124)

$$\begin{aligned}
\left.\frac{\partial r}{\partial x}\right|_{x_2,y_2} &= \frac{x_2}{r_2},\\
\left.\frac{\partial \cos\left(n\phi\right)}{\partial x}\right|_{x_2,y_2} &= \frac{nj}{2r_2^n}\left[-\left(y_2-jx_2\right)^{n-1}+\left(y_2+jx_2\right)^{n-1}\right]-\frac{nx_2}{2r_2^{n+2}}\left[\left(y_2-jx_2\right)^{n}+\left(y_2+jx_2\right)^{n}\right]\\
&= \frac{nj}{2r_2}\left[-\left(\cos\phi_2+j\sin\phi_2\right)^{n-1}+\left(\cos\phi_2-j\sin\phi_2\right)^{n-1}\right]+\frac{n\sin\phi_2}{r_2}\cos\left(n\phi_2\right)\\
&= \frac{n}{r_2}\left[\sin\left\{(n-1)\phi_2\right\}+\sin\phi_2\cos\left(n\phi_2\right)\right]\\
&= \frac{ny_2}{r_2^2}\sin\left(n\phi_2\right).
\end{aligned}$$

We then obtain

$$Z_x^{Wall} = 4\frac{\mathscr{C}L}{kQ}\sum_{m,n=0}^{\infty}\frac{\alpha_{mn}}{\left(1+\delta_{m0}\right)\left(1+\delta_{n0}\right)}I_m\left(\frac{ky_1}{\gamma}\right)\frac{1}{r_2}\left[\frac{ny_2\sin\left(n\phi_2\right)}{r_2}I_n\left(\frac{kr_2}{\gamma}\right)+\frac{kx_2\cos\left(n\phi_2\right)}{\gamma}I_n'\left(\frac{kr_2}{\gamma}\right)\right]. \tag{E.127}$$

Upon differentiation of Eq. (C.16) we have for small z

$$I_n'(z)\approx\frac{1}{2(n-1)!}\left(\frac{z}{2}\right)^{n-1}+\frac{n+2}{2(n+1)!}\left(\frac{z}{2}\right)^{n+1},$$

where $l!$ is the factorial of the integer l, with the convention $(-1)!=\infty$. From this and Eq. (C.16) we see that we need to go up to $m=2$ and $n=3$ to obtain Z_x^{Wall} up to the second order in the source and test coordinates. Approximating the Bessel functions up to second order we obtain

$$\begin{aligned}
Z_x^{Wall} \approx\ & 4\frac{\mathscr{C}L}{kQ}\left[\frac{\alpha_{00}}{4}\frac{k^2x_2}{2\gamma^2}+\frac{\alpha_{01}}{2}\left\{1+\frac{k^2y_1^2}{4\gamma^2}\right\}\left\{\frac{k\sin\left(\phi_2\right)y_2}{2\gamma r_2}+\frac{k^3\sin\left(\phi_2\right)y_2r_2}{16\gamma^3}\right.\right.\\
&\left.+\frac{kx_2\cos\phi_2}{2\gamma r_2}+\frac{3k^3x_2\cos\phi_2 r_2}{16\gamma^3}\right\}+\frac{\alpha_{02}}{2}\left\{\frac{2y_2\sin(2\phi_2)k^2}{8\gamma^2}+\frac{k^2x_2\cos\left(2\phi_2\right)}{4\gamma^2}\right\}\\
&+\frac{\alpha_{03}}{2}\left\{\frac{3y_2\sin\left(3\phi_2\right)k^3r_2}{48\gamma^3}+\frac{k^3x_2\cos\left(3\phi_2\right)r_2}{16\gamma^3}\right\}+\frac{\alpha_{10}}{2}\frac{ky_1}{2\gamma}\frac{k^2x_2}{2\gamma^2}\\
&+\alpha_{11}\frac{ky_1}{2\gamma}\left\{\frac{y_2\sin\left(\phi_2\right)k}{2\gamma r_2}+\frac{kx_2\cos\left(\phi_2\right)}{2\gamma r_2}\right\}+\alpha_{12}\frac{ky_1}{2\gamma}\left\{\frac{y_2\sin\left(2\phi_2\right)k^2}{4\gamma^2}+\frac{k^2x_2\cos\left(2\phi_2\right)}{4\gamma^2}\right\}\\
&\left.+\alpha_{21}\frac{k^2y_1^2}{8\gamma^2}\left\{\frac{y_2\sin\left(\phi_2\right)k}{2\gamma r_2}+\frac{kx_2\cos\left(\phi_2\right)}{2\gamma r_2}\right\}\right],\\
\approx\ & 4\frac{\mathscr{C}L}{kQ}\left[\frac{\alpha_{00}k^2}{8\gamma^2}x_2+\frac{\alpha_{01}k^3}{16\gamma^3}x_2y_2-\frac{\alpha_{02}k^2}{8\gamma^2}x_2-\frac{\alpha_{03}k^3}{16\gamma^3}x_2y_2+\frac{\alpha_{10}k^3}{8\gamma^3}y_1x_2-\frac{\alpha_{12}k^3}{8\gamma^3}y_1x_2\right],
\end{aligned}$$

where we have used various trigonometric identities and

$$\cos\phi_2=\frac{y_2}{r_2},\quad \sin\phi_2=-\frac{x_2}{r_2},\quad \sin(2\phi_2)=-2\frac{x_2y_2}{r_2^2}.$$

The horizontal impedance for $x_1 = 0$ up to second order can be rewritten

$$Z_x^{Wall} \approx \frac{\mathscr{C}Lk}{2\gamma^2 Q}\left[(\alpha_{00}-\alpha_{02})\,x_2 + k\frac{\alpha_{10}-\alpha_{12}}{\gamma}y_1 x_2 + k\frac{\alpha_{01}-\alpha_{03}}{2\gamma}x_2 y_2\right].$$

Finally, the total vertical wall impedance for $x_1 = 0$ is obtained when plugging Eq. (1.187) into the definition (1.194):

$$Z_y^{Wall} = 4\frac{\mathscr{C}L}{kQ}\sum_{m,n=0}^{\infty}\frac{\alpha_{mn}}{(1+\delta_{m0})(1+\delta_{n0})}I_m\left(\frac{ky_1}{\gamma}\right)\left[I_n\left(\frac{kr_2}{\gamma}\right)\left.\frac{\partial\cos(n\phi)}{\partial y}\right|_{x_2,y_2} + \frac{k\cos(n\phi_2)}{\gamma}I_n'\left(\frac{kr_2}{\gamma}\right)\left.\frac{\partial r}{\partial y}\right|_{x_2,y_2}\right].$$

As above we can write

$$\left.\frac{\partial r}{\partial y}\right|_{x_2,y_2} = \frac{y_2}{r_2},$$

$$\begin{aligned}\left.\frac{\partial\cos(n\phi)}{\partial y}\right|_{x_2,y_2} &= \frac{n}{2r_2^n}\left[(y_2-jx_2)^{n-1}+(y_2+jx_2)^{n-1}\right] - \frac{ny_2}{2r_2^{n+2}}\left[(y_2-jx_2)^n+(y_2+jx_2)^n\right]\\ &= \frac{n}{r_2}\left[\cos\{(n-1)\phi_2\}-\cos\phi_2\cos(n\phi_2)\right]\\ &= -\frac{nx_2}{r_2^2}\sin(n\phi_2).\end{aligned}$$

We then get

$$Z_y^{Wall} = 4\frac{\mathscr{C}L}{kQ}\sum_{m,n=0}^{\infty}\frac{\alpha_{mn}}{(1+\delta_{m0})(1+\delta_{n0})}I_m\left(\frac{ky_1}{\gamma}\right)\frac{1}{r_2}\left[-\frac{nx_2\sin(n\phi_2)}{r_2}I_n\left(\frac{kr_2}{\gamma}\right) + \frac{ky_2\cos(n\phi_2)}{\gamma}I_n'\left(\frac{kr_2}{\gamma}\right)\right]. \quad \text{(E.128)}$$

With the same approximation as above for I_m, I_n and I'_n, and going up to second order we can approximate the vertical impedance for $x_1 = 0$ by

$$\begin{aligned}
Z_y^{Wall} \approx 4\frac{\mathscr{C}L}{kQ}\Bigg[& \frac{\alpha_{00}}{4}\frac{k^2 y_2}{2\gamma^2} + \frac{\alpha_{01}}{2}\left\{1+\frac{k^2 y_1^2}{4\gamma^2}\right\}\left\{-\frac{x_2\sin\phi_2 k}{2\gamma r_2} - \frac{x_2\sin\phi_2 k^3 r_2}{16\gamma^3} + \frac{k y_2\cos\phi_2}{2\gamma r_2}\right. \\
& \left. + \frac{3k^3 y_2\cos\phi_2 r_2}{16\gamma^3}\right\} + \frac{\alpha_{02}}{2}\left\{-\frac{2x_2\sin\left(2\phi_2\right)k^2}{8\gamma^2} + \frac{k^2 y_2\cos\left(2\phi_2\right)}{4\gamma^2}\right\} \\
& + \frac{\alpha_{03}}{2}\left\{-\frac{3x_2\sin\left(3\phi_2\right)k^3 r_2}{48\gamma^3} + \frac{k^3 y_2\cos\left(3\phi_2\right)r_2}{16\gamma^3}\right\} + \frac{\alpha_{10}}{2}\frac{k y_1}{2\gamma}\frac{k^2 y_2}{2\gamma^2} \\
& + \alpha_{11}\frac{k y_1}{2\gamma}\left\{-\frac{x_2\sin\phi_2 k}{2\gamma r_2} + \frac{k y_2\cos\phi_2}{2\gamma r_2}\right\} + \alpha_{12}\frac{k y_1}{2\gamma}\left\{-\frac{2x_2\sin\left(2\phi_2\right)k^2}{8\gamma^2}\right. \\
& \left. + \frac{k^2 y_2\cos\left(2\phi_2\right)}{4\gamma^2}\right\} + \alpha_{21}\frac{k^2 y_1^2}{8\gamma^2}\left\{-\frac{x_2\sin\phi_2 k}{2\gamma r_2} + \frac{k y_2\cos\phi_2}{2\gamma r_2}\right\}\Bigg] \\
\approx 4\frac{\mathscr{C}L}{kQ}\Bigg[& \frac{\alpha_{00}k^2}{8\gamma^2}y_2 + \frac{\alpha_{01}k}{4\gamma} + \frac{\alpha_{01}k^3}{16\gamma^3}y_1^2 + \frac{\alpha_{01}k^3}{32\gamma^3}x_2^2 + \frac{3\alpha_{01}k^3}{32\gamma^3}y_2^2 + \frac{\alpha_{02}k^2}{8\gamma^2}y_2 + \frac{\alpha_{03}k^3}{32\gamma^3}y_2^2 \\
& - \frac{\alpha_{03}k^3}{32\gamma^3}x_2^2 + \frac{\alpha_{10}k^3}{8\gamma^3}y_1 y_2 + \frac{\alpha_{11}k^2}{4\gamma^2}y_1 + \frac{\alpha_{12}k^3}{8\gamma^3}y_1 y_2 + \frac{\alpha_{21}k^3}{16\gamma^3}y_1^2\Bigg],
\end{aligned}$$

using again some trigonometric identities and

$$\cos\phi_2 = \frac{y_2}{r_2}, \quad \sin\phi_2 = -\frac{x_2}{r_2}, \quad \cos(2\phi_2) = 2\frac{y_2^2}{r_2^2} - 1 = \frac{y_2^2 - x_2^2}{r_2^2}.$$

Our approximation of the total vertical impedance up to second order can be rewritten

$$\begin{aligned}
Z_y^{Wall} \approx \frac{\mathscr{C}L}{\gamma Q}\Bigg[& \alpha_{01} + \frac{\alpha_{11}k}{\gamma}y_1 + k\frac{\alpha_{00}+\alpha_{02}}{2\gamma}y_2 + k^2\frac{\alpha_{01}+\alpha_{21}}{4\gamma^2}y_1^2 + k^2\frac{\alpha_{01}-\alpha_{03}}{8\gamma^2}x_2^2 \\
& + k^2\frac{3\alpha_{01}+\alpha_{03}}{8\gamma^2}y_2^2 + k^2\frac{\alpha_{10}+\alpha_{12}}{2\gamma^2}y_1 y_2\Bigg].
\end{aligned}$$

E.2.5 The case of two perfectly conducting plates

Here we compare the longitudinal electric field obtained from the theory of Section 1.5 to the one we would get with the method of images [64, chap. 4], in the case of a flat chamber made of two perfectly conducting plates. The method of images consists in placing several sources (i.e. point-like charge and current density as in Eqs. (1.4) and (1.7)) such as to enforce automatically the boundary condition $E_s = 0$ on the plates at $y = \pm b$, which is the only condition needed to get the longitudinal component of the electric field. The basic idea is then that if one such source is at $x = 0$ and $y = y_1$ and another one with an opposite charge $-Q$ is at $x = 0$ and $y = 2b - y_1$ (i.e. symmetrically placed with respect to the plate at $y = b$), all of this being in vacuum, then we get automatically $E_s = 0$ on the plate at $y = b$. This can be seen using Eq. (1.184) which represents E_s created by the first of those source in vacuum: from the superposition principle the longitudinal component of the electric field created by those two sources

would be

$$E_s = \mathscr{C} e^{-jks} \left[K_0\left(\frac{k}{\gamma}\sqrt{x^2+(y-y_1)^2}\right) - K_0\left(\frac{k}{\gamma}\sqrt{x^2+(y+y_1-2b)^2}\right)\right],$$

which is obviously zero[3] for $y = b$. Then, to get $E_s = 0$ at $y = -b$ one needs as well to symmetrize in the same way the two sources previously mentioned, with respect to the plane $y = -b$, obtaining two new sources, one of charge $-Q$ at $y = -2b - y_1$ and one of charge Q at $y = -4b + y_1$. These again should have their symmetric counterparts with respect to the first plate, thus we need two more images on the upper part, and we repeat the process to get an infinite number of sources farther and farther away from the plates, such that in the end the overall sum converges to the solution with the desired boundary condition $E_s = 0$ for $y = \pm b$. The images arrangement is illustrated in Fig. E.1: we get in the end sources of charge Q at positions $4lb + y_1$ and sources of charge $-Q$ at positions $2(2l+1)b - y_1$ (l being a positive or negative integer).
Finally the total longitudinal component of the electric field will be given by the sum of E_s from all the sources, each being obtained thanks to Eq. (1.184):

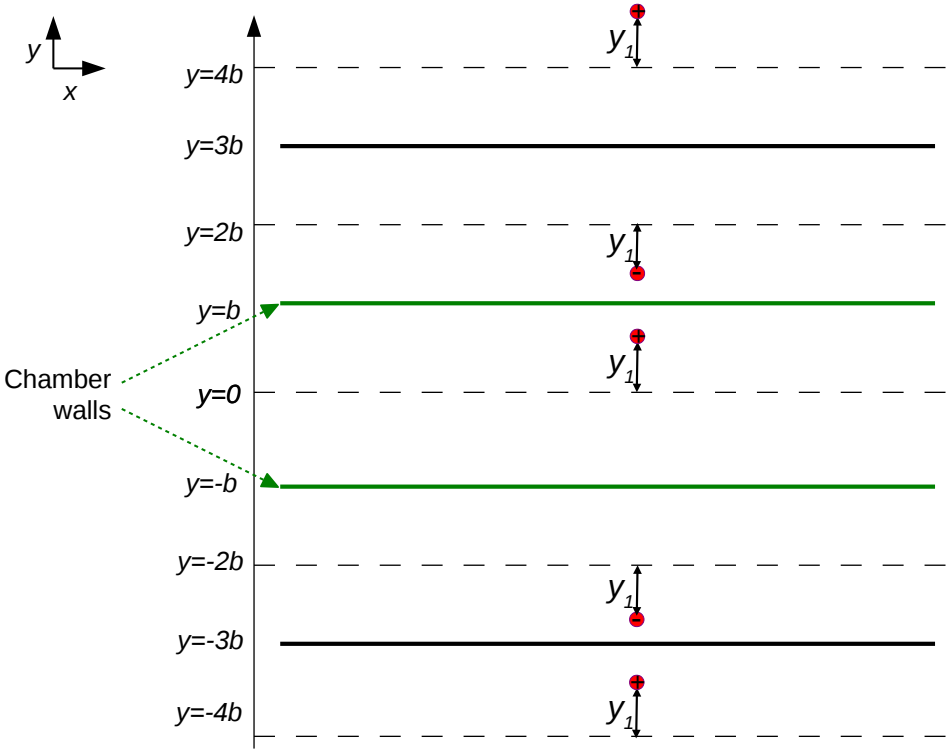

Figure E.1: Several of the electric images used to impose the boundary condition $E_s = 0$ on the plates at $y = \pm b$. Images with a plus sign denotes a charge of Q while those with a minus sign have a charge of $-Q$.

[3] More general arguments exist [64, chap. 4] to prove that E_s (and even the tangential component) is zero at the plane equidistant to two such sources. For instance it can be seen in time domain (and therefore in frequency domain from the linearity of the Fourier transform) by changing the reference frame to the rest frame of the two point-like sources (which go at the same velocity v). Upon application of Coulomb's law in the rest frame for each source, one can clearly see that the tangential component on the plate is zero after summation of the two Coulomb's fields. Then, using the Lorentz transform of the fields one would directly obtain the result.

$$
\begin{aligned}
E_s^{PC,images} &= \mathscr{C} e^{-jks}\left[\sum_{l=-\infty}^{\infty} K_0\left(\frac{k}{\gamma}\sqrt{x^2+\left(y-4lb-y_1\right)^2}\right) - \sum_{l=-\infty}^{\infty} K_0\left(\frac{k}{\gamma}\sqrt{x^2+\left(y-2b(2l+1)+y_1\right)^2}\right)\right] \\
&= \mathscr{C} e^{-jks}\left[\sum_{l=-\infty}^{\infty} (-1)^{2l} K_0\left(\frac{k}{\gamma}\sqrt{x^2+\left(y-2b(2l)-(-1)^{2l}y_1\right)^2}\right)\right. \\
&\qquad \left. + \sum_{l=-\infty}^{\infty} (-1)^{2l+1} K_0\left(\frac{k}{\gamma}\sqrt{x^2+\left(y-2b(2l+1)-(-1)^{2l+1}y_1\right)^2}\right)\right] \\
&= \mathscr{C} e^{-jks} \sum_{l=-\infty}^{\infty} (-1)^{l} K_0\left(\frac{k}{\gamma}\sqrt{x^2+\left(y-2lb-(-1)^{l}y_1\right)^2}\right). \qquad \text{(E.129)}
\end{aligned}
$$

Now, we would like to compare this expression with the one obtained from the approach developped in Chapter 1. To do so we first rewrite the α_{mn} constants from Eq. (1.214) as

$$
\begin{aligned}
\alpha_{mn}^{PC} &= \left[(-1)^{m+n}+1\right]\int_0^{\infty} \mathrm{d}u \frac{\cosh(mu)\cosh(nu)}{e^{2\frac{kb}{\gamma}\cosh u}\left(1-e^{-4\frac{kb}{\gamma}\cosh u}\right)}\left[1-(-1)^m e^{-2\frac{kb}{\gamma}\cosh u}\right] \\
&= \frac{(-1)^{m+n}+1}{2}\int_0^{\infty} \mathrm{d}u \left\{\left[\cosh\{(m+n)u\}+\cosh\{(m-n)u\}\right] e^{-2\frac{kb}{\gamma}\cosh u}\sum_{l=0}^{\infty} e^{-4l\frac{kb}{\gamma}\cosh u}\right. \\
&\qquad \left.\left[1-(-1)^m e^{-2\frac{kb}{\gamma}\cosh u}\right]\right\} \quad \text{using a geometric series decomposition of } \frac{1}{1-e^{-4\frac{kb}{\gamma}\cosh u}} \\
&= \frac{(-1)^{m+n}+1}{2}\int_0^{\infty} \mathrm{d}u \left\{\left[\cosh\{(m+n)u\}+\cosh\{(m-n)u\}\right]\left[\sum_{l=0}^{\infty}(-1)^{(m+1)(2l+2)} e^{-2(2l+1)\frac{kb}{\gamma}\cosh u}\right.\right. \\
&\qquad \left.\left. + \sum_{l=0}^{\infty}(-1)^{(m+1)(2l+3)} e^{-2(2l+2)\frac{kb}{\gamma}\cosh u}\right]\right\} \\
&= \frac{(-1)^{m+n}+1}{2}\int_0^{\infty} \mathrm{d}u \left[\cosh\{(m+n)u\}+\cosh\{(m-n)u\}\right]\left[\sum_{l=1}^{\infty}(-1)^{(m+1)(l+1)} e^{-2l\frac{kb}{\gamma}\cosh u}\right] \\
&= \frac{(-1)^{m+n}+1}{2}\sum_{l=1}^{\infty}(-1)^{(m+1)(l+1)}\int_0^{\infty} \mathrm{d}u \left[\cosh\{(m+n)u\}+\cosh\{(m-n)u\}\right] e^{-2l\frac{kb}{\gamma}\cosh u} \\
&= \frac{(-1)^{m+n}+1}{2}\sum_{l=1}^{\infty}(-1)^{(m+1)(l+1)}\left[K_{m+n}\left(2l\frac{kb}{\gamma}\right)+K_{m-n}\left(2l\frac{kb}{\gamma}\right)\right],
\end{aligned}
$$

where we used Eq. (C.30) for the last step. Reinserting this into Eq. (1.187), adding also the direct space-charge part from Eq. (1.184), we get, with $\phi = \theta - \frac{\pi}{2}$:

$$
\begin{aligned}
E_s^{PC} &= \mathscr{C} e^{-jks} \left\{ K_0\left(\frac{k}{\gamma}\sqrt{x^2+\left(y-y_1\right)^2}\right) - 2\sum_{l=1}^{\infty}\sum_{m,n=0}^{\infty}(-1)^{l+1}\frac{\left((-1)^{m(l+1)}+(-1)^{ml+n}\right)\cos\left(n\phi\right)}{\left(1+\delta_{m0}\right)\left(1+\delta_{n0}\right)} \right. \\
&\qquad \left. I_m\left(\frac{ky_1}{\gamma}\right) I_n\left(\frac{kr}{\gamma}\right)\left[K_{m+n}\left(2l\frac{kb}{\gamma}\right)+K_{m-n}\left(2l\frac{kb}{\gamma}\right)\right]\right\} \\
&= \mathscr{C} e^{-jks} \left\{ K_0\left(\frac{k}{\gamma}\sqrt{x^2+\left(y-y_1\right)^2}\right) + 2\sum_{l=1}^{\infty}(-1)^{l}\sum_{n=0}^{\infty}\frac{\cos\left(n\phi\right)}{\left(1+\delta_{n0}\right)} I_n\left(\frac{kr}{\gamma}\right) \right. \\
&\qquad \left. \sum_{m=0}^{\infty}\frac{(-1)^{m(l+1)}+(-1)^{ml+n}}{1+\delta_{m0}} I_m\left(\frac{ky_1}{\gamma}\right)\left[K_{m+n}\left(2l\frac{kb}{\gamma}\right)+K_{-m+n}\left(2l\frac{kb}{\gamma}\right)\right]\right\} \quad \text{using Eq. (C.4)} \\
&= \mathscr{C} e^{-jks} \left\{ K_0\left(\frac{k}{\gamma}\sqrt{x^2+\left(y-y_1\right)^2}\right) + 2\sum_{l=1}^{\infty}(-1)^{l}\sum_{n=0}^{\infty}\frac{\cos\left(n\phi\right)}{\left(1+\delta_{n0}\right)} I_n\left(\frac{kr}{\gamma}\right) \right. \\
&\qquad \left. \sum_{m=-\infty}^{\infty}\left[(-1)^{m(l+1)}+(-1)^{ml+n}\right] I_m\left(\frac{ky_1}{\gamma}\right) K_{m+n}\left(2l\frac{kb}{\gamma}\right)\right\} \qquad \text{using Eq. (C.3)} \\
&= \mathscr{C} e^{-jks} \left\{ K_0\left(\frac{k}{\gamma}\sqrt{x^2+\left(y-y_1\right)^2}\right) + 2\sum_{l=1}^{\infty}(-1)^{l}\sum_{n=0}^{\infty}\frac{\cos\left(n\phi\right)}{\left(1+\delta_{n0}\right)} I_n\left(\frac{kr}{\gamma}\right)\left[K_n\left(\frac{k}{\gamma}\left(2lb+(-1)^l y_1\right)\right)\right. \right. \\
&\qquad \left. \left. +(-1)^n K_n\left(\frac{k}{\gamma}\left(2lb+(-1)^{l+1} y_1\right)\right)\right]\right\},
\end{aligned}
$$

where we used Eq. (C.28) in the last step, knowing that $\left|y_1\right| < 2lb$ for $l \geq 1$. Then, since $0 < r < b < 2lb \pm y_1$ we can obtain from Eq. (C.27):

$$
\begin{aligned}
E_s^{PC} &= \mathscr{C} e^{-jks} \left\{ K_0\left(\frac{k}{\gamma}\sqrt{x^2+\left(y-y_1\right)^2}\right) \right. \\
&\qquad + \sum_{l=1}^{\infty}(-1)^{l}\left[K_0\left(\frac{k}{\gamma}\sqrt{r^2+\left(2lb+(-1)^l y_1\right)^2-2r\left(2lb+(-1)^l y_1\right)\cos\phi}\right)\right. \\
&\qquad\qquad \left. \left. +K_0\left(\frac{k}{\gamma}\sqrt{r^2+\left(2lb+(-1)^{l+1} y_1\right)^2+2r\left(2lb+(-1)^{l+1} y_1\right)\cos\phi}\right)\right]\right\} \\
&= \mathscr{C} e^{-jks} \left\{ K_0\left(\frac{k}{\gamma}\sqrt{x^2+\left(y-y_1\right)^2}\right) + \sum_{l=1}^{\infty}(-1)^{l}\left[K_0\left(\frac{k}{\gamma}\sqrt{x^2+\left(y-2lb-(-1)^l y_1\right)^2}\right)\right. \right. \\
&\qquad \left. \left. +K_0\left(\frac{k}{\gamma}\sqrt{x^2+\left(y+2lb-(-1)^l y_1\right)^2}\right)\right]\right\} \qquad \text{from } y = r\cos\phi \text{ and } r^2 = x^2+y^2 \\
&= \mathscr{C} e^{-jks} \sum_{l=-\infty}^{\infty}(-1)^{l} K_0\left(\frac{k}{\gamma}\sqrt{x^2+\left(y-2lb-(-1)^l y_1\right)^2}\right). \qquad \text{(E.130)}
\end{aligned}
$$

This is exactly the result in Eq. (E.129) obtained with the method of images.

E.3 Fourier integrals computation

E.3.1 Asymptotic approximation of a Fourier integral

We treat here the second and semi-infinite part of the integral in Eq. (1.231) thanks to an asymptotic approximation. First, we perform a Taylor's expansion of the function f around ω_{max} [124, p. XII]:

$$f(\omega) = \sum_{n=0}^{\infty} \frac{(\omega-\omega_{max})^n}{n!} f^{(n)}(\omega_{max}),$$

where $f^{(n)}$ is the n^{th} derivative of f. If we insert this expansion into the second term in the right hand side of Eq. (1.231), we get

$$I_{\omega_{max}}(t) \equiv \int_{\omega_{max}}^{\infty} \mathrm{d}\omega e^{j\omega t} f(\omega) = \int_{\omega_{max}}^{\infty} \mathrm{d}\omega \sum_{n=0}^{\infty} e^{j\omega t} \frac{(\omega-\omega_{max})^n}{n!} f^{(n)}(\omega_{max}). \tag{E.131}$$

Since f is integrable, the definition of $I_{\omega_{max}}(t)$ is actually valid for any complex number t with $\Im(t) \geq 0$. As a consequence we can also write the above relation for $t + j\varepsilon$ where t is real and $\varepsilon > 0$ (with the change of variable $\omega \to \omega + \omega_{max}$):

$$I_{\omega_{max}}(t+j\varepsilon) = e^{j\omega_{max}(t+j\varepsilon)} \sum_{n=0}^{\infty} \frac{f^{(n)}(\omega_{max})}{n!} \int_0^{\infty} \mathrm{d}\omega \omega^n e^{j\omega(t+j\varepsilon)} = e^{j\omega_{max}(t+j\varepsilon)} \sum_{n=0}^{\infty} \frac{j^{n+1} f^{(n)}(\omega_{max})}{(t+j\varepsilon)^{n+1}},$$

thanks to Eq. (D.4) in Appendix D.2. Since both the right hand side and the left hand side admit a well-defined limit when $\varepsilon \to 0$, we can take the limit of both expressions and obtain, for any real t:

$$I_{\omega_{max}}(t) = e^{j\omega_{max}t} \sum_{n=0}^{\infty} \frac{j^{n+1} f^{(n)}(\omega_{max})}{t^{n+1}}. \tag{E.132}$$

The above equation was obtained in Refs. [69, p. 590] and [73]. We can approximate $I_{\omega_{max}}(t)$ by taking only the first term of the expansion:

$$I_{\omega_{max}}(t) \approx e^{j\omega_{max}t} \frac{j f(\omega_{max})}{t}. \tag{E.133}$$

E.3.2 Fourier integral on a finite interval of a linear function

Given a linear function $p_i(\omega)$ defined as the linear interpolation of a function f on the interval $[\omega_i, \omega_{i+1}]$, i.e. such that

$$p_i(\omega) = f_i + \left(f_{i+1} - f_i\right) \frac{\omega-\omega_i}{\Delta_i} = f_i \frac{\omega_{i+1}-\omega}{\Delta_i} + f_{i+1} \frac{\omega-\omega_i}{\Delta_i}, \tag{E.134}$$

with $f_i = f(\omega_i)$ and $\Delta_i = \omega_{i+1} - \omega_i$, we can compute its finite Fourier integral on $[\omega_i, \omega_{i+1}]$:

$$\begin{aligned} I_i(t) \equiv \int_{\omega_i}^{\omega_{i+1}} \mathrm{d}\omega e^{j\omega t} p_i(\omega) &= f_i \int_{\omega_i}^{\omega_{i+1}} \mathrm{d}\omega e^{j\omega t} \frac{\omega_{i+1} - \omega}{\Delta_i} + f_{i+1} \int_{\omega_i}^{\omega_{i+1}} \mathrm{d}\omega e^{j\omega t} \frac{\omega - \omega_i}{\Delta_i} \\ &= \Delta_i \left[f_i e^{j\omega_{i+1} t} \int_0^1 \mathrm{d}h e^{-j\Delta_i h t} h + f_{i+1} e^{j\omega_i t} \int_0^1 \mathrm{d}h e^{j\Delta_i h t} h \right] \\ &= \Delta_i \left[f_i e^{j\omega_{i+1} t} \Lambda(-\Delta_i t) + f_{i+1} e^{j\omega_i t} \Lambda(\Delta_i t) \right], \end{aligned} \tag{E.135}$$

with Λ a function defined, and calculated by virtue of Eq. (D.6), as

$$\Lambda(x) \equiv \int_0^1 \mathrm{d}h e^{jhx} h = -\frac{j e^{jx}}{x} + \frac{e^{jx} - 1}{x^2}. \tag{E.136}$$

When the argument of Λ is very small compared to unity, the analytical formula in the above equation is subject to high numerical errors, because one tries to compute a difference between almost equal and very large numbers. One way around this problem is to write this function in terms of its Taylor's expansion, knowing the one of the exponential function:

$$\begin{aligned} \Lambda(x) &= -\frac{j}{x} \sum_{n=0}^{\infty} \frac{(jx)^n}{n!} + \frac{1}{x^2} \sum_{n=0}^{\infty} \frac{(jx)^n}{n!} - \frac{1}{x^2} \\ &= -\frac{j}{x} + \sum_{n=0}^{\infty} \frac{(jx)^n}{(n+1)!} + \frac{1}{x^2} + \frac{j}{x} - \sum_{n=0}^{\infty} \frac{(jx)^n}{(n+2)!} - \frac{1}{x^2} \\ &= \sum_{n=0}^{\infty} \frac{1}{n+2} \frac{(jx)^n}{n!}. \end{aligned} \tag{E.137}$$

To allow numerical computation, the infinite sum has to be truncated. To do so accurately, one has to be sure the remainder of the sum is small enough, which can be controlled thanks to the following inequality:

$$\left| \sum_{n=p+1}^{\infty} \frac{1}{n+2} \frac{(jx)^n}{n!} \right| \leq \sum_{n=p+1}^{\infty} \frac{1}{n+2} \frac{|x|^n}{n!} \leq \frac{1}{p+3} \sum_{n=0}^{\infty} \frac{|x|^{n+p+1}}{(n+p+1)!} \leq \frac{|x|^{p+1}}{(p+3)(p+1)!} e^{|x|}, \tag{E.138}$$

which can be made smaller than any given number when $|x| \leq 1$, such that Λ can be computed within any required accuracy.

E.3.3 Fourier integral on a finite interval of a cubic polynomial

Given a cubic polynomial $p_i(\omega)$ defined as the cubic Hermite interpolation of a function f on the interval $[\omega_i, \omega_{i+1}]$, i.e. such that

$$p_i(\omega) = f_i \phi\left(\frac{\omega_{i+1} - \omega}{\Delta_i}\right) + f_{i+1} \phi\left(\frac{\omega - \omega_i}{\Delta_i}\right) - d_i \Delta_i \psi\left(\frac{\omega_{i+1} - \omega}{\Delta_i}\right) + d_{i+1} \Delta_i \psi\left(\frac{\omega - \omega_i}{\Delta_i}\right), \tag{E.139}$$

with

$$d_i = p_i'(\omega_i), \quad \phi(h) = 3h^2 - 2h^3 \quad \text{and} \quad \psi(h) = h^3 - h^2, \tag{E.140}$$

one obtains for its Fourier integral on the interval $[\omega_i, \omega_{i+1}]$

$$\begin{aligned}
I_i(t) &= \int_{\omega_i}^{\omega_{i+1}} \mathrm{d}\omega e^{j\omega t} p_i(\omega) \\
&= f_i \int_{\omega_i}^{\omega_{i+1}} \mathrm{d}\omega e^{j\omega t} \phi\left(\frac{\omega_{i+1}-\omega}{\Delta_i}\right) + f_{i+1} \int_{\omega_i}^{\omega_{i+1}} \mathrm{d}\omega e^{j\omega t} \phi\left(\frac{\omega-\omega_i}{\Delta_i}\right) \\
&\qquad - d_i\Delta_i \int_{\omega_i}^{\omega_{i+1}} \mathrm{d}\omega e^{j\omega t} \psi\left(\frac{\omega_{i+1}-\omega}{\Delta_i}\right) + d_{i+1}\Delta_i \int_{\omega_i}^{\omega_{i+1}} \mathrm{d}\omega e^{j\omega t} \psi\left(\frac{\omega-\omega_i}{\Delta_i}\right) \\
&= \Delta_i \left[f_i e^{j\omega_{i+1}t} \int_0^1 \mathrm{d}h e^{-j\Delta_i h t} \phi(h) + f_{i+1} e^{j\omega_i t} \int_0^1 \mathrm{d}h e^{j\Delta_i h t} \phi(h) \right. \\
&\qquad \left. - d_i\Delta_i e^{j\omega_{i+1}t} \int_0^1 \mathrm{d}h e^{-j\Delta_i h t} \psi(h) + d_{i+1}\Delta_i e^{j\omega_i t} \int_0^1 \mathrm{d}h e^{j\Delta_i h t} \psi(h) \right] \\
&= \Delta_i \left[f_i e^{j\omega_{i+1}t} \Phi(-\Delta_i t) + f_{i+1} e^{j\omega_i t} \Phi(\Delta_i t) - d_i\Delta_i e^{j\omega_{i+1}t} \Psi(-\Delta_i t) + d_{i+1}\Delta_i e^{j\omega_i t} \Psi(\Delta_i t) \right],
\end{aligned} \tag{E.141}$$

where the functions Φ and Ψ are defined, and calculated thanks to Eqs. (D.7) and (D.8), as

$$\Phi(x) \equiv \int_0^1 \mathrm{d}h e^{jhx} \phi(h) = -\frac{j e^{jx}}{x} - \frac{6j\left(e^{jx}+1\right)}{x^3} + \frac{12\left(e^{jx}-1\right)}{x^4}, \tag{E.142}$$

$$\Psi(x) \equiv \int_0^1 \mathrm{d}h e^{jhx} \psi(h) = \frac{e^{jx}}{x^2} + \frac{2j\left(2e^{jx}+1\right)}{x^3} - \frac{6\left(e^{jx}-1\right)}{x^4}. \tag{E.143}$$

As for the case of the linear interpolation, the analytical formulae in Eqs. (E.142) and (E.143) are subject to high numerical errors when $|x| \ll 1$, because differences between very large numbers that are almost equal appear. Again, a way around this problem is to write those functions in terms of their Taylor's expansions:

$$\begin{aligned}
\Phi(x) &= -\frac{j}{x} \sum_{n=0}^{\infty} \frac{(jx)^n}{n!} - \frac{6j}{x^3} - \frac{6j}{x^3} \sum_{n=0}^{\infty} \frac{(jx)^n}{n!} - \frac{12}{x^4} + \frac{12}{x^4} \sum_{n=0}^{\infty} \frac{(jx)^n}{n!} \\
&= -\frac{j}{x} + \sum_{n=0}^{\infty} \frac{(jx)^n}{(n+1)!} - \frac{12j}{x^3} + \frac{6}{x^2} + \frac{3j}{x} - \sum_{n=0}^{\infty} \frac{6}{(n+2)(n+3)} \frac{(jx)^n}{(n+1)!} \\
&\qquad + \frac{12j}{x^3} - \frac{6}{x^2} - \frac{2j}{x} + \sum_{n=0}^{\infty} \frac{12}{(n+2)(n+3)(n+4)} \frac{(jx)^n}{(n+1)!} \\
&= \sum_{n=0}^{\infty} \frac{n+6}{(n+3)(n+4)} \frac{(jx)^n}{n!},
\end{aligned} \tag{E.144}$$

and

$$\begin{aligned}\Psi(x) &= \frac{1}{x^2}\sum_{n=0}^{\infty}\frac{(jx)^n}{n!} + \frac{2j}{x^3} + \frac{4j}{x^3}\sum_{n=0}^{\infty}\frac{(jx)^n}{n!} + \frac{6}{x^4} - \frac{6}{x^4}\sum_{n=0}^{\infty}\frac{(jx)^n}{n!}\\ &= \frac{1}{x^2} + \frac{j}{x} - \sum_{n=0}^{\infty}\frac{(jx)^n}{(n+2)!} + \frac{6j}{x^3} - \frac{4}{x^2} - \frac{2j}{x} + \sum_{n=0}^{\infty}\frac{4}{n+3}\frac{(jx)^n}{(n+2)!}\\ &\qquad - \frac{6j}{x^3} + \frac{3}{x^2} + \frac{j}{x} - \sum_{n=0}^{\infty}\frac{6}{(n+3)(n+4)}\frac{(jx)^n}{(n+2)!}\\ &= -\sum_{n=0}^{\infty}\frac{1}{(n+3)(n+4)}\frac{(jx)^n}{n!}.\end{aligned} \tag{E.145}$$

When truncating those infinite sums in order to evaluate them numerically, the remainders can be controlled thanks to the inequalities

$$\left|\sum_{n=p+1}^{\infty}\frac{n+6}{(n+3)(n+4)}\frac{(jx)^n}{n!}\right| \leq \sum_{n=p+1}^{\infty}\frac{2n+6}{(n+3)(n+4)}\frac{|x|^n}{n!} \leq \frac{2}{p+5}\sum_{n=0}^{\infty}\frac{|x|^{n+p+1}}{(n+p+1)!} \leq \frac{2|x|^{p+1}e^{|x|}}{(p+5)(p+1)!}, \tag{E.146}$$

and

$$\left|\sum_{n=p+1}^{\infty}\frac{1}{(n+3)(n+4)}\frac{(jx)^n}{n!}\right| \leq \frac{1}{(p+4)(p+5)}\sum_{n=0}^{\infty}\frac{|x|^{n+p+1}}{(n+p+1)!} \leq \frac{|x|^{p+1}e^{|x|}}{(p+5)(p+4)(p+1)!}. \tag{E.147}$$

When $|x| \leq 1$, Φ and Ψ can therefore be computed within any required accuracy.

E.4 Impedances of a rotated flat chamber

We consider a flat chamber whose walls are parallel to the $(Ox's)$ plane, where the transverse coordinates (x', y') are obtained by a rotation of angle $\frac{\pi}{2} - \alpha$ of the (x, y) ones, as in Fig. 2.2. Knowing the impedances $Z_{x'}$ and $Z_{y'}$ from Eqs. (1.199) and (1.200) as

$$\begin{aligned}Z_{x'}^{Wall} &\approx Z_{x'}^{Wall,dip}x'_1 + Z_{x'}^{Wall,quad}x'_2,\\ Z_{y'}^{Wall} &\approx Z_{y'}^{Wall,0} + Z_{y'}^{Wall,dip}y'_1 + Z_{y'}^{Wall,quad}y'_2.\end{aligned} \tag{E.148}$$

we can compute Z_x and Z_y in the initial coordinate system (x, y) thanks to

$$\begin{bmatrix}x'\\ y'\end{bmatrix} = \begin{bmatrix}\sin\alpha & \cos\alpha\\ -\cos\alpha & \sin\alpha\end{bmatrix}\cdot\begin{bmatrix}x\\ y\end{bmatrix} \qquad \text{and} \qquad \begin{bmatrix}Z_x\\ Z_y\end{bmatrix} = \begin{bmatrix}\sin\alpha & -\cos\alpha\\ \cos\alpha & \sin\alpha\end{bmatrix}\cdot\begin{bmatrix}Z_{x'}\\ Z_{y'}\end{bmatrix}, \tag{E.149}$$

since Z_x and Z_y behave in a change of coordinates as the components of the electromagnetic force vector (see the impedances definitions in Eqs. (1.95) and (1.96)). By virtue of Eqs. (E.148) and (E.149) we

get

$$\begin{aligned}
Z_x^{Wall} &\approx \sin\alpha \left[Z_{x'}^{Wall,dip} \left(x_1 \sin\alpha + y_1 \cos\alpha \right) + Z_{x'}^{Wall,quad} \left(x_2 \sin\alpha + y_2 \cos\alpha \right) \right] \\
&\quad - \cos\alpha \left[Z_{y'}^{Wall,0} + Z_{y'}^{Wall,dip} \left(-x_1 \cos\alpha + y_1 \sin\alpha \right) + Z_{y'}^{Wall,quad} \left(-x_2 \cos\alpha + y_2 \sin\alpha \right) \right], \\
&\approx -\cos\alpha Z_{y'}^{Wall,0} + \left(Z_{x'}^{Wall,dip} \sin^2\alpha + Z_{y'}^{Wall,dip} \cos^2\alpha \right) x_1 \\
&\quad + \cos\alpha \sin\alpha \left(Z_{x'}^{Wall,dip} - Z_{y'}^{Wall,dip} \right) y_1 + \left(Z_{x'}^{Wall,quad} \sin^2\alpha + Z_{y'}^{Wall,quad} \cos^2\alpha \right) x_2 \\
&\quad + \cos\alpha \sin\alpha \left(Z_{x'}^{Wall,quad} - Z_{y'}^{Wall,quad} \right) y_2,
\end{aligned}$$

and

$$\begin{aligned}
Z_y^{Wall} &\approx \cos\alpha \left[Z_{x'}^{Wall,dip} \left(x_1 \sin\alpha + y_1 \cos\alpha \right) + Z_{x'}^{Wall,quad} \left(x_2 \sin\alpha + y_2 \cos\alpha \right) \right] \\
&\quad + \sin\alpha \left[Z_{y'}^{Wall,0} + Z_{y'}^{Wall,dip} \left(-x_1 \cos\alpha + y_1 \sin\alpha \right) + Z_{y'}^{Wall,quad} \left(-x_2 \cos\alpha + y_2 \sin\alpha \right) \right], \\
&\approx \sin\alpha Z_{y'}^{Wall,0} + \cos\alpha \sin\alpha \left(Z_{x'}^{Wall,dip} - Z_{y'}^{Wall,dip} \right) x_1 \\
&\quad + \left(Z_{x'}^{Wall,dip} \cos^2\alpha + Z_{y'}^{Wall,dip} \sin^2\alpha \right) y_1 + \cos\alpha \sin\alpha \left(Z_{x'}^{Wall,quad} - Z_{y'}^{Wall,quad} \right) x_2 \\
&\quad + \left(Z_{x'}^{Wall,quad} \cos^2\alpha + Z_{y'}^{Wall,quad} \sin^2\alpha \right) y_2.
\end{aligned}$$

F LHC machine elements parameters

F.1 Obtaining the beta functions from MAD-X twiss files

The impedances of the various elements of the machine need to be weighted by the mean beta function at their location over the beta function at the point of observation (see Section 2.3.2). To find the beta functions, we used the code MAD-X [90, 130] with the LHC optics. To obtain the "twiss" files giving all required beta functions (if necessary interpolated on a finer mesh before computing an average), the following parameters have been used [131]:

- LHC optics version [132]: V6.503.
- Sequence used: latest version of the thick optics (as of September 2011), from the file /afs/cern.ch/eng/lhc/optics/V6.503/V6.5.as-built.seq. This sequence is slightly different from the design sequence (V6.5.seq) in the sense that it should be more realistic with respect to the actual LHC machine (phase 1). We have checked that choosing one or the other of these two sequences has anyway a very little impact (maximum relative differences on the beta function is $1.2 \cdot 10^{-5}$, both at injection and collision and for both beams).
- Magnet strengths used: from the file */afs/cern.ch/eng/lhc/optics/V6.503/V6.5.inj.str* for injection settings, and from */afs/cern.ch/eng/lhc/optics/V6.503/V6.5.coll_special.3.5TeV_1.5m10m1.5m3m.str* for collision settings (squeeze of 1.5 m in IP1 and IP5, 3 m in IP8 and 10 m in IP2). Thick optics are used because they are more realistic than the thin ones.
- All the parameters concerning the IPs (crossing angles, beam separations, optimization flags, strength of the magnets from the experiments) have basically no impact on the beta functions and can be set to any value.
- Flag for the direction of rotation *bv*: *bv*= 1 for beam 1, *bv*= −1 for beam 2.

With these settings, interpolating the beta functions on a fine mesh (points every 10 cm) and integrating using the trapezoidal rule, we get the average beta functions at injection (for beam 1 and beam 2)

$$\begin{aligned} &< \beta_x^{inj}(b1) > \approx 96.8\text{m} \quad \text{and} \quad < \beta_y^{inj}(b1) > \approx 100.9\text{m}, \\ &< \beta_x^{inj}(b2) > \approx 96.6\text{m} \quad \text{and} \quad < \beta_y^{inj}(b2) > \approx 102.4\text{m}, \end{aligned} \tag{F.1}$$

and at collision with the 1.5 m squeeze in IP1 and IP5:

$$\begin{aligned} &< \beta_x^{coll}(b1) > \approx 138\text{m} \qquad \text{and} \qquad < \beta_y^{coll}(b1) > \approx 142.2\text{m}, \\ &< \beta_x^{coll}(b2) > \approx 137.5\text{m} \qquad \text{and} \qquad < \beta_y^{coll}(b2) > \approx 143.8\text{m}. \end{aligned} \tag{F.2}$$

Note that this is quite different from the usual smooth approximation [133] which in the case of the LHC would give at injection (for both beams)

$$< \beta_x^{smooth,inj} > = \frac{C}{2\pi Q_x^{inj}} \approx 66.01\text{m} \qquad \text{and} \qquad < \beta_y^{smooth,inj} > = \frac{C}{2\pi Q_y^{inj}} \approx 71.54\text{m}, \tag{F.3}$$

and at collision (for both beams)

$$< \beta_x^{smooth,coll} > = \frac{C}{2\pi Q_x^{coll}} \approx 65.98\text{m} \qquad \text{and} \qquad < \beta_y^{smooth,coll} > = \frac{C}{2\pi Q_y^{coll}} \approx 71.53\text{m}. \tag{F.4}$$

where $C = 26658.883$ m [84, chap. 2, p. 6] is the LHC total length while the tunes are given by [84, chap. 2, p. 6]

$$\begin{aligned} &Q_x^{inj} = 64.28 \qquad \text{and} \qquad Q_y^{inj} = 59.31, \\ &Q_x^{coll} = 64.31 \qquad \text{and} \qquad Q_y^{coll} = 59.32. \end{aligned} \tag{F.5}$$

F.2 Obtaining the relaxation time

In Tables F.4 and F.7, the relaxation time for the AC conductivity τ_{AC} (see Eq. (1.14)) is either taken directly from the indicated reference, or calculated using the formulae [44]

$$\tau_{AC} = \frac{m_e \sigma_{DC}}{n e^2}, \tag{F.6}$$

$$n = 6.022 \cdot 10^{23} \frac{Z \rho_m}{A} \tag{F.7}$$

with m_e the electron mass, n the number of charge carriers for the conduction per m^3, e the elementary charge, ρ_m the mass density in g/m^3 (given by the reference indicated in the column giving τ_{AC}), A the atomic mass in g/mol and Z the number of charge carriers provided by each atom. Z is actually chosen almost arbitrarily; for metals it is taken as the number of electrons in the outermost electron shell ($Z = 1$ for copper, $Z = 2$ for tungsten and for titanium). For CFC and graphite, $Z = 2 \cdot 10^{-5}$ is given by Ref. [134, p. 273], which is confirmed by Ref. [135]. For titanium the relaxation time obtained in this way is very small (less than 10^{-15} s) so of no significance, and we rather set it to zero.

F.3 Collimators data

Tables F.1, F.2, F.3 and F.4 summarize all the parameters used in the LHC impedance model for the collimators (see Section 2.1.1).

Table F.1: Parameters of the beam 1 collimators [88, 92, 136–139]. Half gaps and beta functions are given at injection and collision (3.5 TeV/c, squeeze of 1.5 m in IP1 and IP5, 3 m in IP8 and 10 m in IP2). The half gaps were measured on May 8th, 2011 (see Chapter 4.3), and the beta functions are from MAD-X (see Section F.1). All the jaws have a thickness of 25 mm except for the TDI (see Table F.3) and the TCLIA (33 mm).

Collimator name	Jaw mat.	Half gap b (injection) [mm]	Half gap b (collision) [mm]	Angle α [rad]	Length L [m]	β_x (inj.) [m]	β_y (inj.) [m]	β_x (coll.) [m]	β_y (coll.) [m]
TCL.5R1.B1	Cu	25	25	0	1	146	133	72.1	355
TCTH.4L2.B1	W	9.18	5.46	0	1	47.3	47.8	47.3	47.8
TDI.4L2		4.94	20	$\pi/2$	4.1	114	46.5	114	46.5
TCTVB.4L2	W	8.30	5.78	$\pi/2$	1	128	52.3	128	52.3
TCLIA.4R2	C	6.71	25	$\pi/2$	1	48.9	121	48.9	121
TCLIB.6R2.B1	CFC	3.55	25	$\pi/2$	1	261	37.9	261	37.9
TCP.6L3.B1	CFC	7.83	4.2	0	0.6	131	145	132	145
TCSG.5L3.B1	CFC	5.87	3.54	0	1	54.3	299	54.3	299
TCSG.4R3.B1	CFC	4.08	2.47	0	1	26.4	394	26.4	394
TCSG.A5R3.B1	CFC	5.25	3.16	2.98	1	36.6	341	36.6	341
TCSG.B5R3.B1	CFC	5.94	3.57	0.199	1	46.5	310	46.5	310
TCLA.A5R3.B1	W	11.3	7.14	$\pi/2$	1	145	174	145	174
TCLA.B5R3.B1	W	10.5	6.62	0	1	154	167	154	167
TCLA.6R3.B1	W	9.71	6.12	0	1	127	171	127	171
TCLA.7R3.B1	W	6.97	4.41	0	1	65.9	88.2	68.3	88.2
TCTH.4L5.B1	W	14.6	10.1	0	1	159	79.5	582	229
TCTVA.4L5.B1	W	10	7.12	$\pi/2$	1	158	79.6	584	237
TCL.5R5.B1	Cu	25	25	0	1	145	133	72.2	356
TCDQA.A4R6.B1	C	16.9	6.47	0	3	495	165	495	165
TCDQA.B4R6.B1	C	16.9	6.47	0	3	506	170	506	170
TCSG.4R6.B1	CFC	15	6.51	0	1	520	175	520	175
TCP.D6L7.B1	CFC	4.32	1.56	$\pi/2$	0.6	159	78.3	159	78.3
TCP.C6L7.B1	CFC	5.96	2.12	0	0.6	151	82.8	151	82.8
TCP.B6L7.B1	CFC	5.04	1.80	2.22	0.6	142	87.5	142	87.5
TCSG.A6L7.B1	CFC	6.29	2.77	2.46	1	39.3	229	39.3	229
TCSG.B5L7.B1	CFC	7.1	3.30	2.5	1	163	164	163	164
TCSG.A5L7.B1	CFC	7.48	3.37	0.71	1	189	143	189	143
TCSG.D4L7.B1	CFC	5.44	2.16	$\pi/2$	1	335	68	334	68
TCSG.B4L7.B1	CFC	7.24	3.09	0	1	138	132	138	132
TCSG.A4L7.B1	CFC	6.56	3.01	2.35	1	127	143	127	143
TCSG.A4R7.B1	CFC	6.48	3.02	0.808	1	117	154	117	154
TCSG.B5R7.B1	CFC	8.30	3.51	2.47	1	124	264	124	264
TCSG.D5R7.B1	CFC	7.64	3.5	0.897	1	217	156	217	156
TCSG.E5R7.B1	CFC	7.64	3.51	2.28	1	245	133	245	133
TCSG.6R7.B1	CFC	10.9	4.76	0.00873	1	333	47.3	333	47.3
TCLA.A6R7.B1	W	5.77	3.74	$\pi/2$	1	294	48.3	294	48.3
TCLA.B6R7.B1	W	11.4	6.83	0	1	158	77.2	158	77.2
TCLA.C6R7.B1	W	11.4	6.67	$\pi/2$	1	67.7	153	67.7	153
TCLA.D6R7.B1	W	7.08	4.38	0	1	64.2	159	64.2	159
TCLA.A7R7.B1	W	7.07	4.3	0	1	65.4	144	65.4	144
TCTH.4L8.B1	W	7.82	5.45	0	1	47.3	47.8	244	302
TCTVB.4L8	W	7.92	5.75	$\pi/2$	1	128	52.3	537	335
TCTH.4L1.B1	W	13.8	10.1	0	1	159	79.5	582	229
TCTVA.4L1.B1	W	10.1	7.1	$\pi/2$	1	158	79.6	584	237

Table F.2: Parameters of the beam 2 collimators [88, 92, 137–139]. Half gaps and beta functions are given at injection and collision (3.5 TeV/c, squeeze of 1.5 m in IP1 and IP5, 3 m in IP8 and 10 m in IP2). The half gaps were measured on May 8th, 2011 (see Section 4.3), and the beta functions are from MAD-X (see Section F.1). All the jaws have a thickness of 25 mm except for the TDI (see Table F.3) and the TCLIA (33 mm).

Collimator name	Jaw mat.	Half gap b (injection) [mm]	Half gap b (collision) [mm]	Angle α [rad]	Length L [m]	β_x (inj.) [m]	β_y (inj.) [m]	β_x (coll.) [m]	β_y (coll.) [m]
TCTVA.4R1.B2	W	10.8	7.1	$\pi/2$	1	158	79.6	584	237
TCTH.4R1.B2	W	14.2	10.1	0	1	161	79.4	581	222
TCTVB.4R2	W	6.76	5.78	$\pi/2$	1	128	52.3	128	52.3
TCTH.4R2.B2	W	7.75	5.45	0	1	46.6	48.9	46.6	48.9
TCLA.7L3.B2	W	6.94	4.37	0	1	65.9	94.4	65.9	94.4
TCLA.6L3.B2	W	9.71	6.11	0	1	132	167	132	167
TCLA.B5L3.B2	W	10.5	6.62	0	1	149	171	149	171
TCLA.A5L3.B2	W	11.3	7.15	$\pi/2$	1	140	178	140	178
TCSG.B5L3.B2	CFC	5.9	3.56	0.189	1	44.6	315	44.6	315
TCSG.A5L3.B2	CFC	5.24	3.16	2.98	1	35.2	347	35.2	347
TCSG.4L3.B2	CFC	4.09	2.46	0	1	26.1	397	26.1	397
TCSG.5R3.B2	CFC	5.87	3.53	0	1	54.9	298	54.9	298
TCP.6R3.B2	CFC	7.85	4.22	0	0.6	132	145	132	145
TCL.5L5.B2	Cu	25	25	0	1	141	137	74.6	361
TCTVA.4R5.B2	W	9.4	7.12	$\pi/2$	1	158	79.6	584	237
TCTH.4R5.B2	W	13.9	10.1	0	1	161	79.4	581	222
TCSG.4L6.B2	CFC	14.8	6.54	0	1	521	173	522	173
TCDQA.B4L6.B2	C	17.9	7.32	0	3	511	169	511	169
TCDQA.A4L6.B2	C	17.9	7.32	0	3	500	165	500	165
TCLA.A7L7.B2	W	6.29	4.5	0	1	65.1	145	65.1	145
TCLA.D6L7.B2	W	7.47	4.35	0	1	65.9	156	65.9	156
TCLA.C6L7.B2	W	11	6.66	$\pi/2$	1	69.5	150	69.5	150
TCLA.B6L7.B2	W	11.3	6.81	0	1	161	75.6	161	75.6
TCLA.A6L7.B2	W	6.3	3.76	$\pi/2$	1	300	48	300	48
TCSG.6L7.B2	CFC	10.4	4.78	0.00873	1	339	47.4	339	47.4
TCSG.E5L7.B2	CFC	7.74	3.48	2.28	1	238	139	238	139
TCSG.D5L7.B2	CFC	7.79	3.48	0.897	1	211	161	211	161
TCSG.B5L7.B2	CFC	7.96	3.46	2.47	1	119	271	119	271
TCSG.A4L7.B2	CFC	6.94	3	0.735	1	101	174	101	174
TCSG.A4R7.B2	CFC	6.43	3.08	2.31	1	141	130	141	130
TCSG.B4R7.B2	CFC	7.33	3.2	0	1	153	120	153	120
TCSG.D4R7.B2	CFC	5.07	2.14	$\pi/2$	1	331	69.8	331	69.8
TCSG.A5R7.B2	CFC	7.15	3.37	0.71	1	183	148	183	148
TCSG.B5R7.B2	CFC	7.67	3.29	2.51	1	157	169	157	169
TCSG.A6R7.B2	CFC	7.16	2.79	2.47	1	40.5	225	40.5	225
TCP.B6R7.B2	CFC	5.04	1.79	2.23	0.6	142	87.5	142	87.5
TCP.C6R7.B2	CFC	5.95	2.13	0	0.6	151	82.8	151	82.8
TCP.D6R7.B2	CFC	4.3	1.54	$\pi/2$	0.6	159	78.3	159	78.3
TCLIB.6L8.B2	CFC	2.41	25	$\pi/2$	1	229	21.3	263	12
TCLIA.4L8	C	6.73	25	$\pi/2$	1	50.1	123	334	522
TCTVB.4R8	W	8.48	5.75	$\pi/2$	1	128	52.3	537	335
TDI.4R8		4.56	20	$\pi/2$	4.1	104	42.7	465	327
TCTH.4R8.B2	W	7.90	5.47	0	1	46.6	48.9	239	301
TCL.5L1.B2	Cu	25	25	0	1	140	137	74.7	362

Table F.3: Parameters of each longitudinal block of material in the TDI collimator [136, 140, 141].

Collimator name	Block material	Coating material	Jaw thickness [mm]	Coating thickness [μm]	Block length L [m]
TDI.4L2 or TDI.4R8	Cu	-	54	-	0.7
	Al	-	54	-	0.6
	hBN	Ti	54	3[a]	2.8

[a] It was found recently [142] that the titanium coating on the hBN block of the TDI is actually thicker than what was expected (5 μm instead of 3 μm) [143]. This has not yet been taken into account in the LHC impedance model.

Table F.4: Collimator material electromagnetic properties at 300 K (see parameters definition in Eqs. (1.14) and (1.15), and Section F.2 for the way to obtain relaxation times). Magnetic properties have been neglected for those materials, as well as the dielectric constants of metals. When available we indicate in the first column the provider and commercial name of the material, between parentheses.

Material full name	Symbol	ε_b	ρ_{DC} [Ω.m]	τ_{AC} [ps]	μ_r	$\tan\vartheta_E$	$\tan\vartheta_M$
Copper	Cu	1	$1.7\cdot10^{-8}$ [144]	0.027 [44]	1	0	0
Carbon-carbon[b] (Tatsuno AC150)	CFC	1	$5\cdot10^{-6}$ [145, 146]	4.2 [145, 146]	1	0	0
Graphite (SGL R4550)	C	1	$1.5\cdot10^{-5}$ [145, 147]	1.3 [145]	1	0	0
Tungsten	W	1	$5.4\cdot10^{-8}$ [144]	0.005 [144]	1	0	0
Titanium	Ti	1	$4.3\cdot10^{-7}$ [144][c]	0	1	0	0
Aluminum	Al	1	$2.7\cdot10^{-8}$ [144]	0.008 [44]	1	0	0
Hexagonal boron nitride[d] (Syntec BN5000)	hBN	4 [148][e]	$4\cdot10^{12}$ [149]	0	1	0	0
Stainless steel (304L)	ss304L	1	$7.2\cdot10^{-7}$ [144]	0	1	0	0

[b] This CFC is actually an anisotropic material (more precisely, orthotropic with a transverse isotropy): it has different properties in the plane parallel to the jaw (the plane that "sees" the beam) and in the direction perpendicular to that plane [137]. In particular, the resistivity is 5 times higher in the direction perpendicular to the jaw than in the plane parallel to the jaw [146]. We quote here only the latter resistivity (in-plane), as the image currents flow in a direction parallel to the beam orbit. The effect of the anisotropy has been therefore totally neglected, which is justified by the agreement between theory and measurements of the impedance of CFC collimator jaws in Ref. [9]. Note finally that previous versions of the LHC impedance model used the value of $10^{-5}\Omega$.m for ρ_{DC}, which was actually a design value rather than the real resistivity measured in the CFC jaws [150].

[c] It was found recently [142] that the titanium coating on the hBN block of the TDI got contaminated by the hBN ceramic, possibly increasing its resistivity to $\rho \approx 2.5\cdot10^{-6}\,\Omega$.m [143]. This has not yet been taken into account in the LHC impedance model.

[d] hBN is actually anisotropic (during manufacturing it is pressed along the longitudinal direction, parallel to the beam orbit [151]), but this has very little impact on its electric properties, and we will neglect it here.

[e] The dielectric constant is not known on this specific type of hBN, we use the value given by another provider on a similar material. Still, when hBN is coated by a 3 μm layer of titanium, it was checked that the beam coupling impedances and wake functions do not depend on ε_b between 2 and 5, on the frequency range (or time range) useful for the LHC.

F.4 Beam screens data

Tables F.5, F.6 and F.7 summarize all the parameters useful to compute the beam-coupling impedances and wake functions of the beam screens (see Section 2.1.2).

Table F.5: Beam screens parameters [96]. The Yokoya factors [23] are those obtained for an elliptic geometry of semi-axes b and w (b being in the direction indicated in the column "Orientation"), with respect to a round geometry of radius b.

Type of beam screen	Orientation	b [mm]	w [mm]	Length L [m]	Yokoya factors			
					x dip.	y dip.	x quad.	y quad.
50A	V	18.375	23.175	21992.03	0.651	0.898	-0.238	0.241
50L	V	18.775	23.575	167.23	0.655	0.899	-0.234	0.238
53V	V	20.175	24.975	31.59	0.667	0.901	-0.223	0.229
53H	H	20.175	24.975	31.59	0.901	0.667	0.229	-0.223
63V	V	25.225	30.025	284.22	0.715	0.913	-0.193	0.199
63H	H	25.225	30.025	94.98	0.913	0.715	0.199	-0.193
69	V	28.075	32.875	130.64	0.738	0.918	-0.180	0.185
74	V	30.475	35.325	64.61	0.751	0.921	-0.171	0.175

Table F.6: Beam screens average beta functions from MAD-X (see Section F.1), for each beam, at injection and collision with a squeeze of 1.5 m in IP1 and IP5, 3 m in IP8 and 10 m in IP2.

Type of beam screen	β_x (B1, inj.)	β_y (B1, inj.)	β_x (B1, coll.)	β_y (B1, coll.)	β_x (B2, inj.)	β_y (B2, inj.)	β_x (B2, coll.)	β_y (B2, coll.)
50A	86.3	91.1	86.4	91.2	86.4	91.2	86.4	91.5
50L	146	148	149	145	149	145	146	168
53V	77.1	77.1	350	350	77.1	77.1	350	350
53H	77.1	77.1	273	273	77.1	77.1	273	273
63V	160	160	396	398	157	164	397	399
63H	149	149	574	574	149	149	574	574
69	152	132	262	242	140	165	250	275
74	124	124	429	429	124	124	429	429

F.5 Warm vacuum pipe data

Tables F.8 and F.9 summarize all the parameters useful to compute the beam-coupling impedances and wake functions of the warm vacuum pipe (see Section 2.1.3). Electromagnetic properties of copper can be found in Table F.4.

Table F.7: Beam screens materials properties at 20 K (see Section F.2 for the way to obtain relaxation times). For copper, to take into account its magnetoresistance, resistivity is given for several magnetic induction amplitudes B (expressed in terms of proton momentum in the bending radius of the LHC dipoles, i.e. $R = 2803.9$ m). Magnetic properties and dielectric constants have been neglected. The copper coating thickness taken in the model is $50\,\mu$m.

Material name	Proton momentum [GeV/c]	ε_b	ρ_{DC} [Ω.m]	τ_{AC} [ps]	μ_r	$\tan\vartheta_E$	$\tan\vartheta_M$
Copper[f]	450	1	$2.8\cdot10^{-10}$ [99, 101]	1.5 [144]	1	0	0
Copper[f]	3500	1	$5.1\cdot10^{-10}$ [99, 101]	0.8 [144]	1	0	0
Copper[f]	7000	1	$7.7\cdot10^{-10}$ [99, 101]	0.5 [144]	1	0	0
Stainless steel (grade P506)	any	1	$6{\cdot}10^{-7}$ [95, 96]	0	1	0	0

[f] Magnetoresistance has been taken into account thanks to the empirical law [101]

$$\rho(B,\, T = 20\,\mathrm{K}) = \rho(B = 0,\, T = 20\,\mathrm{K})\,[1.0048 + 0.0038 \times B \times \mathrm{RRR}]\,,$$

where, according to Ref. [99], RRR= $\frac{\rho(B=0,\,T=300\,\mathrm{K})}{\rho(B=0,\,T=20\,\mathrm{K})} = 70$ ("residual resistivity ratio") and $\rho(B = 0,\, T = 20\,\mathrm{K}) = 2.4\cdot10^{-10}\,\Omega$.m.

Table F.8: Warm vacuum pipe parameters [84, chap. 5, p. 98]. For the MQWs, Yokoya factors [23] are those obtained for an elliptic geometry of semi-axes b and w (b being in the direction indicated in the column "Orientation"), with respect to a round geometry of radius b. MBW and the rest of the vacuum pipe have circular cross-sections. The chamber is assumed to be made of 2 mm-thick copper (see properties in Table F.4) surrounded by infinite vacuum.

Type of vacuum pipe	Orientation	b [mm]	w [mm]	Length L [m]	Yokoya factors			
					x dip.	y dip.	x quad.	y quad.
MBW	-	22	22	70.6	-	-	-	-
MQW_V	V	14.5	25.5	74.59	0.484	0.848	-0.364	0.364
MQW_H	H	14.5	25.5	74.59	0.848	0.484	0.364	-0.364
Rest of the circumference	-	40	40	3592.71	-	-	-	-

Table F.9: Warm vacuum pipe average beta functions from MAD-X (see Section F.1), for each beam, at injection and collision with a squeeze of 1.5 m in IP1 and IP5, 3 m in IP8 and 10 m in IP2.

Type of vacuum pipe	β_x (B1, inj.)	β_y (B1, inj.)	β_x (B1, coll.)	β_y (B1, coll.)	β_x (B2, inj.)	β_y (B2, inj.)	β_x (B2, coll.)	β_y (B2, coll.)
MBW	139	135	139	135	138	136	138	136
MQW_V	192	210	192	210	192	210	192	210
MQW_H	192	210	192	210	192	210	192	210
Rest of the circumference	145	146	215	216	143	155	213	227

F.6 Skin depth

According to Ref. [11, p. 354], the skin depth in a conductor is written

$$\delta_s = \sqrt{\frac{2\rho_{DC}}{\mu_0 \mu_r \omega}}. \tag{F.8}$$

We show in Fig. F.1 the skin depth versus frequency for the conductors mentioned in the previous sections, computed thanks to the resistivites of Tables F.4 and F.7.

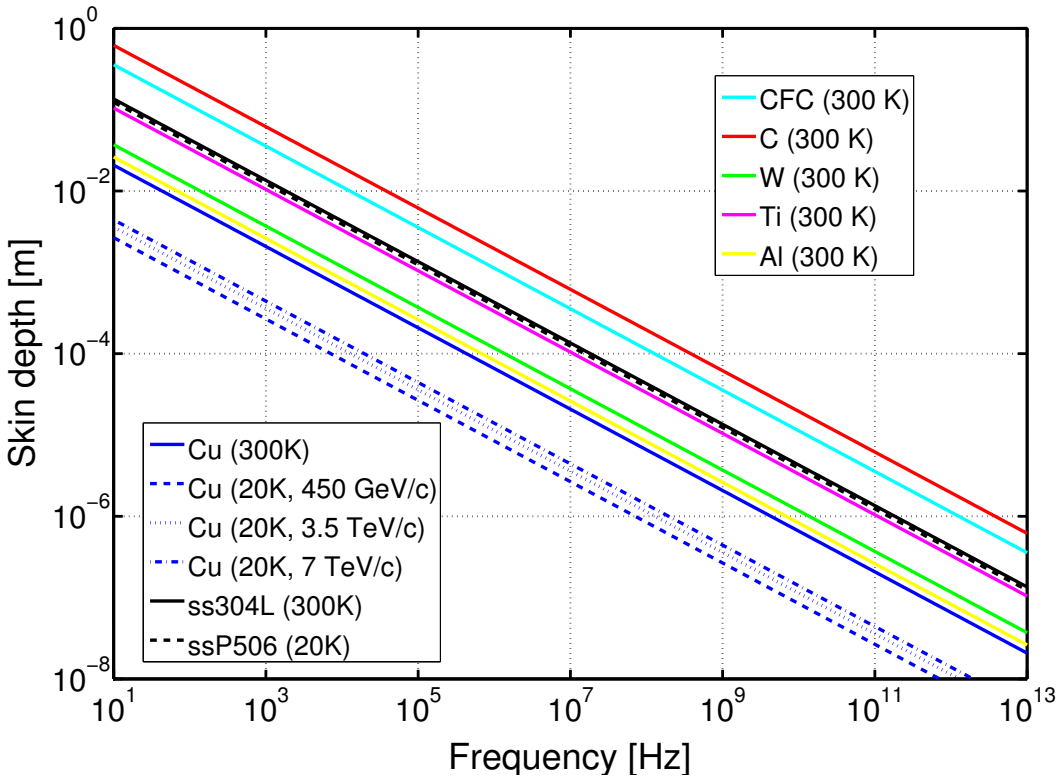

Figure F.1: Skin depth as a function of frequency for the conductors present in the various machine elements. The resistivities of Tables F.4 and F.7 were used.

G Comparisons between single-bunch measurements and the LHC impedance model

We compare here the results from the simulation code HEADTAIL using the wake functions from the LHC impedance model described in Chapter 2, with beam-based measurements of tune shifts and instability rise times performed in 2010 and 2011, in single-bunch regime. The plots and conclusions shown below are the result of a collaborative work that was presented during the LHC beam operation workshop in Evian, in December 2011 [152].

At 450 GeV/c, tune shifts measurements were performed on May 28$^{\text{th}}$, 2010 [153]. The total tune shift due to the impedance of the machine was measured using either an overinjection of a high-intensity bunch on a previously injected low-intensity one or an intensity scraping done thanks to one collimator. The specific contributions given to the tune shift by certain collimators were separately quantified, by moving groups of collimators together, in particular the injection protection collimators – TDI, TCLIA and TCLIB – and the collimators in the IR7 insertion region. On November 1$^{\text{st}}$, 2011 [154] additional measurements were done on the TDI alone, by moving this collimator and measuring the corresponding tune shift. At 3.5 TeV/c some measurements of the tune shift due to a subset of collimators (in particular those of IR7) were performed on May 7$^{\text{th}}$, 2011 [155]. An instability rise time measurement took place on May 17$^{\text{th}}$, 2010 [110, 156].

Results of all these experiments, compared to HEADTAIL simulations using the LHC impedance model, are shown in Figs. G.1 and G.2 in respectively horizontal and vertical. The tune shifts normalized by the bunch intensity are then shown in Figs. G.3 and G.4. Note that the other beam or machine parameters (e.g. bunch length and chromaticity) can differ slightly between the various measurements, and this was taken into account in the simulations. Finally, the discrepancy factors between the measurements and the simulations are exhibited in Figs. G.5 and G.6. In most cases, we find a disagreement between the model and the measurements by a factor 2-3. At 3.5 TeV/c, simulations tend to be closer to the measurements than at 450 GeV/c, especially when taking into account the experimental error bars which are visible in Figs. G.1 and G.2. One can also note the systematic and yet unexplained discrepancy between the overinjection measurements and the scraping ones, the former giving a higher discrepancy factor with respect to the model than the latter. Finally, the tune shift due to the injection protection collimators, which is expected to be dominated by the TDI contribution (in particular its ceramic block) has changed drastically between 2010 and 2011. This could be explained either by a rather bad quality of the measurement in 2010 with respect to that of 2011, or by some damage done to the titanium coating on the ceramic part of the TDI jaw, resulting in a reduction of its thickness [154]. Visual inspection of the TDI jaws did not reveal any absence of coating, but its thickness has not been measured. On the other hand, the beam screens around the jaws were observed to be deformed.

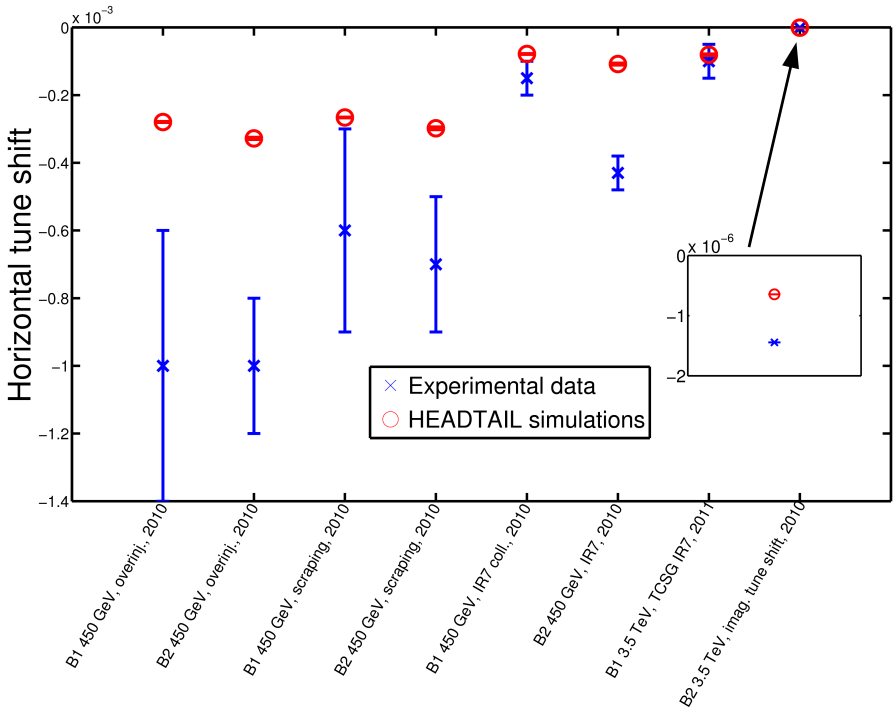

Figure G.1: Horizontal single-bunch tune shifts measured and simulated, in various cases.

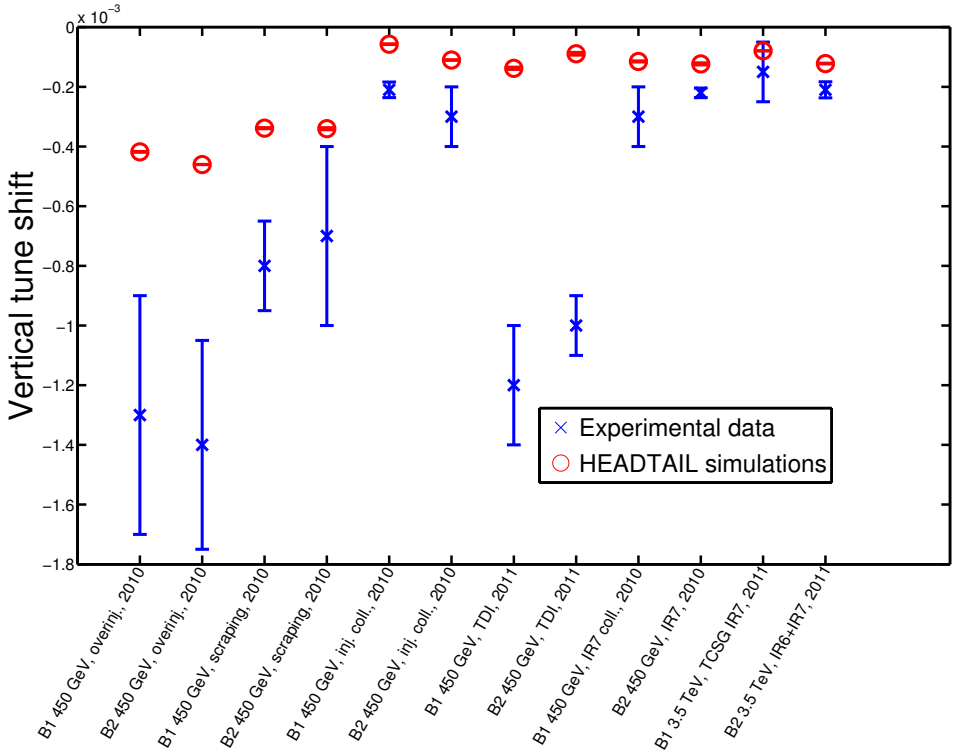

Figure G.2: Vertical single-bunch tune shifts measured and simulated, in various cases.

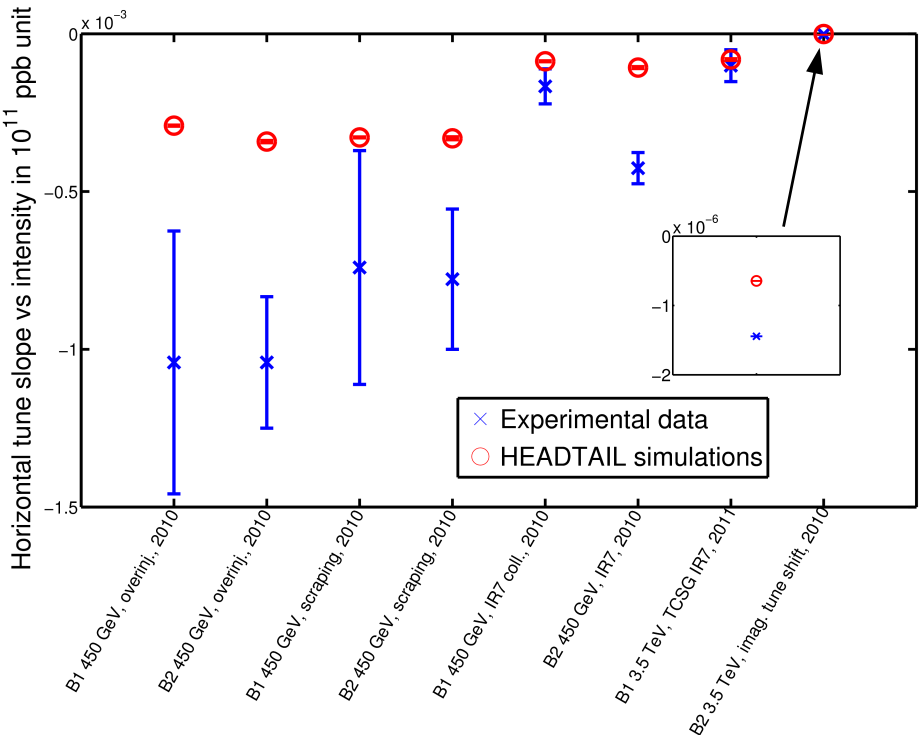

Figure G.3: Horizontal single-bunch tune shifts measured and simulated in various cases, normalized with the bunch intensity in units of 10^{11} particles per bunch.

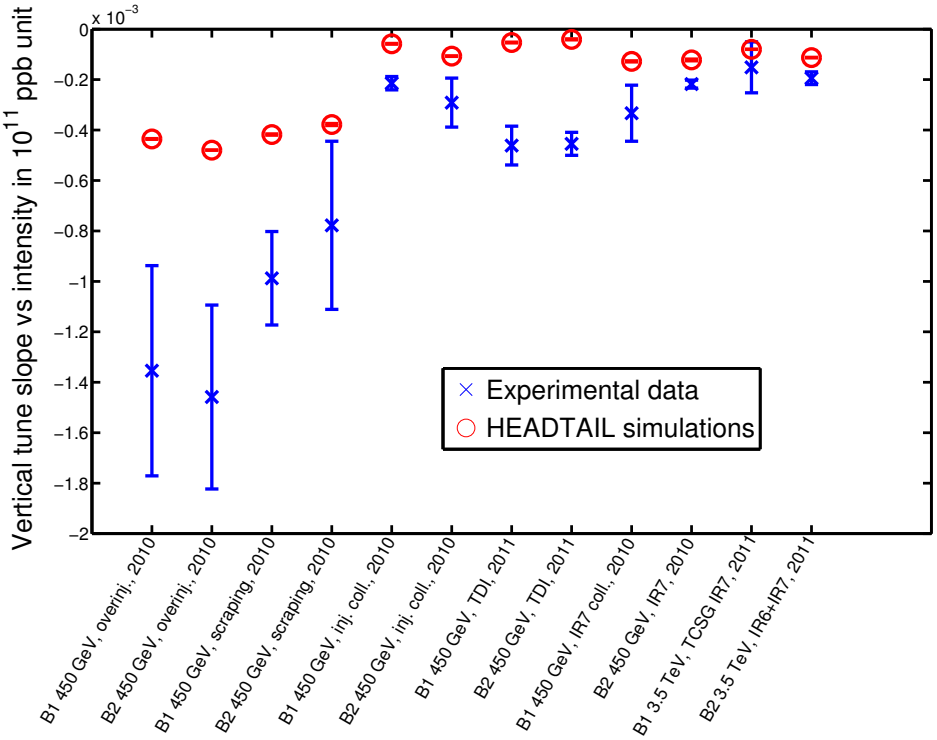

Figure G.4: Vertical single-bunch tune shifts measured and simulated in various cases, normalized with the bunch intensity in units of 10^{11} particles per bunch.

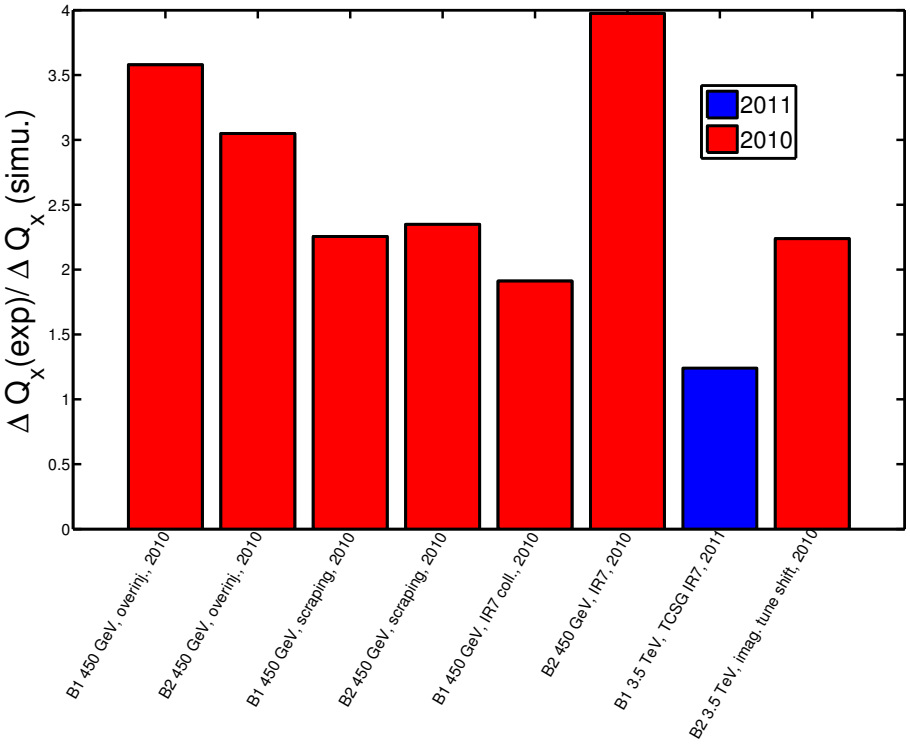

Figure G.5: Discrepancy factor between the horizontal single-bunch tune shifts measured and simulated, in various cases.

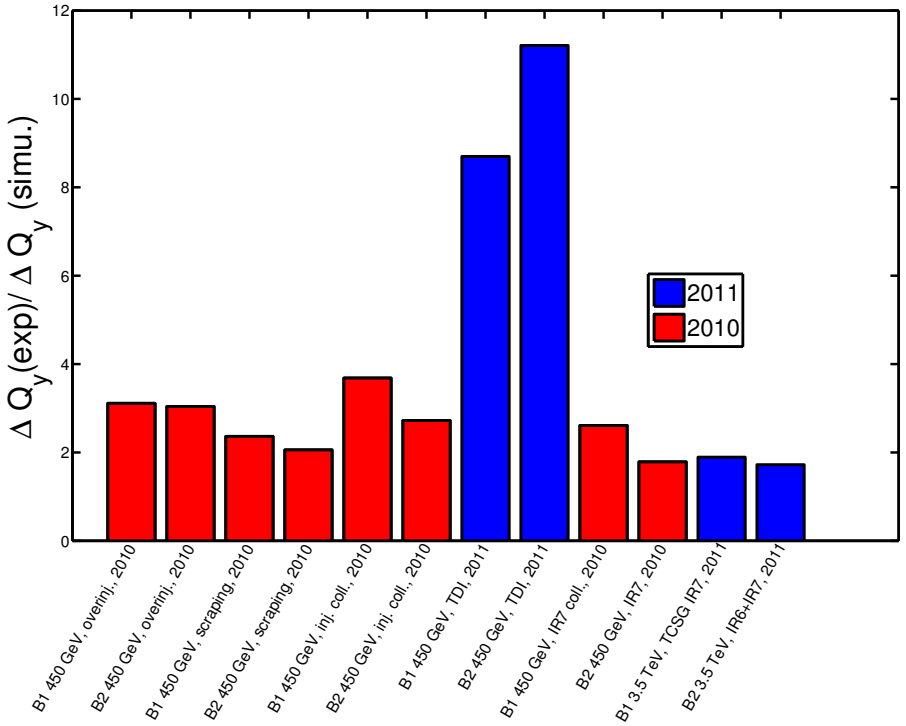

Figure G.6: Discrepancy factor between the vertical single-bunch tune shifts measured and simulated, in various cases.

Bibliography

[1] E. Métral, B. Zotter, and B. Salvant. Resistive-wall impedance of an infinitely long multi-layer cylindrical beam pipe. In *22nd Particle Accelerator Conference, Albuquerque, USA*, pages 4216–4218, 2007.

[2] D. Angal-Kalinin. Review of coupled bunch instabilities in the LHC, 2002. CERN LHC Project Report 595.

[3] G. Rumolo and F. Zimmermann. Electron cloud simulations: beam instabilities and wakefields. *Phys. Rev. ST Accel. Beams*, 5(121002), 2002.

[4] G. Rumolo and E. Métral. Simulations of single bunch collective effects using HEADTAIL. In *Proceedings of ICAP 2006, Chamonix, France*, pages 59–64, 2006.

[5] B. Zotter and F. J. Sacherer. Transverse instabilities of relativistic particle beams in accelerators and storage rings. In M. H. Blewett, editor, *1st International School of Particle Accelerators "Ettore Majorana"*, pages 175–218. CERN, Nov. 1976. Report No. CERN-77-13.

[6] J. L. Laclare. Bunched beam coherent instabilities. In S. Turner, editor, *CAS - CERN Accelerator School : Accelerator Physics, Oxford, UK, 16 - 27 Sep 1985*, pages 264–326. CERN, 1987. Report No. CERN-87-03-V-1, http://cdsweb.cern.ch/record/611596/files/p264.pdf.

[7] B. Zotter and S. Kheifeits. *Impedances and Wakes in High-Energy Particle Accelerators*. World Scientific, 1998.

[8] L. J. Laslett, V. K. Neil, and A. M. Sessler. Transverse resistive instabilities of intense coasting beams in particle accelerators. *Rev. Sci. Instrum.*, 36:436–448, 1965.

[9] F. Roncarolo, F. Caspers, T. Kroyer, E. Métral, N. Mounet, B. Salvant, and B. Zotter. Comparison between laboratory measurements, simulations and analytical predictions of the transverse wall impedance at low frequencies. *Phys. Rev. ST Accel. Beams*, 12(084401), 2009.

[10] A. W. Chao. *Physics of Collective Beams Instabilities in High Energy Accelerators*. John Wiley and Sons, 1993.

[11] J. D. Jackson. *Classical Electrodynamics*. John Wiley and Sons, 3rd edition, 1998.

[12] B. Zotter. Transverse oscillations of a relativistic particle beam in a laminated vacuum chamber, 1969. Report No. CERN-69-15.

[13] B. Zotter. Longitudinal instabilities of charged particle beams inside cylindrical walls of finite thickness. *Part. Accel.*, 1:311–326, 1970.

[14] B. Zotter. New results on the impedance of resistive metal walls of finite thickness, 2005. Report No. CERN-AB-2005-043.

[15] E. Keil and B. Zotter. The impedance of layered vacuum chambers. In *6th European Particle Accelerator Conference, Stockholm, Sweden*, pages 963–965, 1998.

[16] N. Mounet and E. Métral. Electromagnetic fields created by a macroparticle in an infinitely long and axisymmetric multilayer beam pipe, 2009. Report No. CERN-BE-2009-039.

[17] A. Burov and V. Lebedev. Tranverse resistive wall impedance for multi-layer round chambers. In *8th European Particle Accelerator Conference, Paris, France*, pages 1452–1454, 2002.

[18] N. Wang and Q. Qin. Resistive-wall impedance of two-layer tube. *Phys. Rev. ST Accel. Beams*, 10 (111003), 2007.

[19] H. Hahn. Matrix solution of coupling impedance in multi-layer circular cylindrical structures. In *23rd Particle Accelerator Conference, Vancouver, Canada*, 2009.

[20] M. Ivanyan, E. Laziev, V. Tsakanov, A. Vardanyan, S. Heifets, and A. Tsakanian. Multilayer tube impedance and external radiation. *Phys. Rev. ST Accel. Beams*, 11(084001), 2008.

[21] H. Hahn. Matrix solution to longitudinal impedance of multi-layer circular structures, 2008. Report No. BNL-81867-2008-IR.

[22] R. L. Gluckstern, J. van Zeijts, and B. Zotter. Coupling impedance of beam pipes of general cross section. *Phys. Rev. E*, 47:656–663, 1993.

[23] K. Yokoya. Resistive wall impedance of beam pipes of general cross section. *Part. Acc.*, 41:221, 1993. Also published as KEK Preprint 92-196.

[24] L. J. Laslett. On intensity limitations imposed by transverse space-charge effects in circular particle accelerators. In J. W. Bittner, editor, *Brookhaven Summer Study on Storage Rings, Accelerators and Experimentation at Super-High Energies, BNL, Upton, NY*, pages 324–367, 1963. Brookhaven National Laboratory Report BNL-7534.

[25] B. Salvant, N. Mounet, C. Zannini, E. Métral, and G. Rumolo. Quadrupolar transverse impedance of simple models of kickers. In *1st International Particle Accelerator Conference, Kyoto, Japan*, pages 2054–2056, 2010.

[26] A. Piwinski. Wake fields and ohmic losses in flat vacuum chambers, 1992. Report No. DESY-HERA 92-04.

[27] K. Bane, Y. Cai, A. Drozhdin, R. Helm, L. Keller, J. Irwin, R. Messner, R. Nelson, T. Raubenheimer, G. Stupakov, F. Tian, D. Walz, M. Woodley, Y. Yan, and F. Zimmermann. Chap. 9: Collimation systems. In *Zeroth-Order design report for the Next Linear Collider*, page 571. SLAC, 1996. Report No. LBNL-5424, SLAC-R-474, UC-414, UCRL-ID-124161; http://www.slac.stanford.edu/accel/nlc/zdr/Snowmass96/ZDRCH09.PDF.

[28] F. Zimmermann. Coherent and incoherent tune shift induced by the nonlinear flat-chamber resistive-wall wake field with an application to the LHC collimator experiment in the SPS, 2006. CERN-AB-Note-2006-007 ABP.

[29] H. Henke and O. Napoly. Wake fields between two parallel resistive plates. In *2nd European Particle Accelerator Conference, Nice, France*, pages 1046–1048, 1990.

[30] A. Piwinski. Longitudinal and transverse wake fields in flat vacuum chambers, 1984. Report No. DESY 84-097.

[31] A. Burov and V. Lebedev. Tranverse resistive wall impedance for multi-layer flat chambers. In *8th European Particle Accelerator Conference, Paris, France*, pages 1455–1457, 2002.

[32] K. L. F. Bane. The short range resistive wall wakefields, 1991. SLAC/AP-87.

[33] O. Henry and O. Napoly. The resistive-pipe wake potentials for short bunches, 1991. CLIC Note 142.

[34] A. Faltens and L. J. Laslett. Longitudinal coupling impedance of a stationary electron ring in a cylindrical geometry. *Part. Accel.*, 4:151–157, 1973.

[35] R. L. Warnock and P. Morton. Fields excited by a beam in a smooth toroidal chamber. Part 1: Longitudinal coupling impedance, 1988. SLAC - PUB - 4562 - also published in Part. Accel., vol. 25 (1990), p. 113.

[36] K. Y. Ng, 1990. In Part. Accel.(1990), vol. 25, p. 153.

[37] B. Zotter. Potential and wave equations in toroidal coordinates, 1977. Report No. CERN ISR-TH/77-56.

[38] H. Hahn. Longitudinal coupling impedance of toroidal beam tube, 1988. Report No. BNL-41654 DE88 016762.

[39] H. Hahn and S. Tepikian. On the longitudinal coupling impedance of a toroidal beam tube. In *2nd European Particle Accelerator Conference, Nice, France*, 1990.

[40] A. Burov. Transverse impedance of ferrite elements, 2004. CERN LHC Project Note 353 (revised).

[41] E. W. Weisstein. Delta function. MathWorld - A Wolfram Web Resource, 2011. http://mathworld.wolfram.com/DeltaFunction.html.

[42] R. L. Gluckstern. Analytic methods for calculating coupling impedances, 2000. Report No. CERN-2000-011.

[43] T. Suzuki. Fundamentals of the theory of collective beam instabilities, 1998. KEK Preprint 98-127.

[44] N. W. Ashcroft and N. D. Mermin. *Solid State Physics*. Saunders College Holt, Rinehart and Winston, international edition, 1976.

[45] J. T. Rogers, S. De Panfilis, A. C. Melissinos, B. E. Moskowitz, Y. K. Semertzidis, W. U. Wuensch, H. J. Halama, A. G. Prodell, W. B. Fowler, and F. A. Nezrick. Anomalous RF magnetoresistance in copper at 4 K. *Appl. Phys. Lett.*, 52:2266–2268, 1988.

[46] G. E. H. Reuter and E. H. Sondheimer. The theory of the anomalous skin effect in metals. *Proc. R. Soc. London, Ser. A*, 195:336–364, 1948.

[47] H. London. The high-frequency resistance of superconducting tin. *Proc. R. Soc. London, Ser. A*, 176:522–533, 1940.

[48] A. B. Pippard. The surface impedance of superconductors and normal metals at high frequencies. II. The anomalous skin effect in normal metals. *Proc. R. Soc. London, Ser. A*, 191:385–399, 1947.

[49] R. G. Chambers. The anomalous skin effect. *Proc. R. Soc. London, Ser. A*, 215:481–497, 1952.

[50] D. C. Mattis and J. Bardeen. Theory of the anomalous skin effect in normal and superconducting metals. *Phys. Rev.*, 111:412–417, 1958.

[51] J. P. Turneaure, J. Halbritter, and H. A. Schwettman. The surface impedance of superconductors and normal conductors: The Mattis-Bardeen theory. *J. Superconductivity*, 4:341–355, 1991.

[52] W. Chou and F. Ruggiero. Anomalous skin effect and resistive wall heating, 1995. CERN LHC Project Note No. 2 (SL/AP).

[53] F. Zimmermann and K. Oide. Resistive-wall wake and impedance for nonultrarelativistic beams. *Phys. Rev. ST Accel. Beams*, 7(044201), 2004.

[54] A. R. von Hippel. *Dielectrics and Waves*, pages 4–5. Artech House, Boston, 2nd edition, 1995.

[55] L. D. Landau, E. M. Lifshitz, and L. P. Pitaevskii. *Electrodynamics of Continuous Media*. Elsevier Butterworth-Heinemann, 2nd edition, 1993.

[56] M. Abramowitz and I. A. Stegun, editors. *Pocketbook of Mathematical Functions*, pages 118–122. Verlag Harri Deutsch, 1984. Abridged edition of Handbook of Mathematical Functions, selected by M. Danos and J. Rafelski.

[57] H. Hahn and D. Davino. Resistive coatings on layered accelerator structures with rectangular cross section, 2002. BNL/SNS Technical note 103.

[58] Mathematica®, 2012. ©Wolfram Research, Inc., Champaign, Illinois , USA.

[59] F. J. Sacherer. Transverse bunched beam instabilitites - theory. In *9th International Conference on High Energy Accelerators, Stanford, California, USA*, pages 347–351, 1974.

[60] H. Tsutsui. On single wire technique for transverse coupling impedance measurement, 2002. CERN-SL-Note-2002-034 AP.

[61] F. Ruggiero. Single-beam collective effects in the LHC, 1995. CERN LHC Project Note No. 313 (SL/AP).

[62] A. Burov and V. Danilov. Suppression of transverse bunch instabilities by asymmetries in the chamber geometry. *Phys. Rev. Lett.*, 82:2286–2289, 1999.

[63] N. Mounet and E. Métral. Electromagnetic fields and beam coupling impedances in a multilayer flat chamber, 2010. CERN-ATS-Note-2010-056 TECH.

[64] K. Y. Ng. *Physics of Intensity Dependent Instabilities*. Asian Scientific, 2006. Also in USPAS Lecture Notes by K. Y. Ng, Los Angeles, Jan. 2002, http://www-ap.fnal.gov/ng/uspas02/.

[65] L. N. G. Filon. On a quadrature formula for trigonometric integrals. *Proc. Roy. Soc. Edinburgh*, 49: 38–47, 1928.

[66] Matlab® R2008b, 1994-2012. The Mathworks™, Natick, Massachusetts, USA.

[67] G. C. Danielson and C. Lanczos. Some improvements in practical Fourier analysis and their application to X-ray scattering from liquids. *J. Franklin Inst.*, 233(4-5):365–380 & 435–452, 1942.

[68] J. W. Cooley and J. W. Tukey. An algorithm for the machine calculation of complex Fourier series. *Math. Comput.*, 19(2):297–301, 1965. Reprinted in Digital Signal Processing, ed. L. R. Rabiner & C. M. Rader, pp. 223-227, New York, IEEE Press, 1972.

[69] W. H. Press, S. A. Teukolsky, W. T. Vetterling, and B. P. Flannery. *Numerical recipes in C*. Cambridge University Press, 2nd edition, 1999. http://apps.nrbook.com/c/index.html.

[70] I. S. Gradshteyn and I. M. Ryzhik. *Table of Integrals, Series, and Products*. Academic Press, 6th edition, 2000. Editors A. Jeffrey and D. Zwillinger.

[71] E. O. Tuck. A simple "Filon-trapezoidal" rule. *Math. Comp.*, 21:239–241, 1967.

[72] G. Pantis. The evaluation of integrals with oscillatory integrands. *J. Comp. Phys.*, 17:229–233, 1975.

[73] A. Iserles and S. Norsett. Efficient quadrature of highly oscillatory integrals using derivatives. *Proc. Roy. Soc. A*, 461:1383–1399, 2005.

[74] D. Huybrechs and S. Vandewalle. On the evaluation of highly oscillatory integrals by analytic continuation, 2005. Report No. TW431, Dep. Comp. Science, K.U.Leuven.

[75] F. N. Fritsch and R. E. Carlson. Monotone piecewise cubic interpolation. *SIAM J. Numerical Analysis*, 17(2):238–246, 1980.

[76] B. Salvant. *Impedance model of the CERN SPS and aspects of LHC single-bunch stability*. PhD thesis, EPFL, 2010. 4585.

[77] N. Mounet, 2011. ImpedanceWake2D, https://impedance.web.cern.ch/impedance/Codes/ImpedanceWake2D/ImpedanceWake2D_todate.tar.gz.

[78] N. Mounet and E. Métral. Generalized form factors for the beam coupling impedances in a flat chamber. In *1st International Particle Accelerator Conference, Kyoto, Japan*, pages 2042–2044, 2010.

[79] N. Mounet and E. Métral. Impedances of two dimensional multilayer cylindrical and flat chambers in the non-ultrarelativistic case. In *HB2010, 46th ICFA Advanced Beam Dynamics Workshop on High-Intensity and High-Brightness Hadron Beams, Morschach, Switzerland*, pages 353–357, 2010.

[80] N. Biancacci, N. Wang, Q. Qin, E. Métral, N. Mounet, B. Salvant, C. Zannini, M. Migliorati, A. Mostacci, and L. Palumbo. Impedance calculations for simple models of kickers in the non-ultrarelativistic regime. In *2nd International Particle Accelerator Conference, San Sebastian, Spain*, 2011.

[81] A. Koschik. *Simulation of Transverse Multi-Bunch Instabilities of Proton Beams in LHC*. PhD thesis, Tech. Univ. Graz, 2004.

[82] N. Mounet and E. Métral. The six electromagnetic field components at low frequency in an axisymmetric infinitely thick single-layer resistive beam pipe. In *1st International Particle Accelerator Conference, Kyoto, Japan*, pages 2048–2050, 2010.

[83] J.-B. Jeanneret, D Leroy, L. R. Oberli, and T. Trenkler. Quench levels and transient beam losses in LHC magnets, 1996. CERN LHC Project Report 44.

[84] O. S. Brüning, P. Collier, P. Lebrun, S. Myers, R. Ostojic, J. Poole, and P. Proudlock, editors. *LHC Design Report. Volume 1: the LHC Main Ring*, 2004. CERN. Report No. CERN-2004-003-V-1.

[85] R. W. Assmann et al. The final collimation system for the LHC. In *10th European Particle Accelerator Conference, Edinburgh, Scotland*, pages 986–988, 2006.

[86] D. Wollmann et al. First cleaning with LHC collimators. In *1st International Particle Accelerator Conference, Kyoto, Japan*, pages 1237–1239, 2010.

[87] R. W. Assmann et al, 2004. http://lhc-collimation-project.web.cern.ch/lhc-collimation-project/pictures.htm.

[88] R. W. Assmann et al, 2007. http://lhc-collimation-project.web.cern.ch/lhc-collimation-project/collimator_list.htm.

[89] C. Bracco. *Commissioning Scenarios and Tests for the LHC Collimation System*. PhD thesis, EPFL, 2009. 4271, http://cdsweb.cern.ch/record/1174254/files/EuCARD-DIS-2009-004.pdf.

[90] 2010. MAD-X, http://madx.web.cern.ch/madx/.

[91] R. W. Assmann et al, 2004. http://lhc-collimation-project.web.cern.ch/lhc-collimation-project/new%20ir7%20july.htm#Collimator%20data.

[92] R. Bruce, 2011. Private communication.

[93] E. Métral. Wake fields and impedances, 2009. USPAS Course on Collective Effects in Beam Dynamics for Particle Accelerators, Albuquerque, New Mexico, USA, http://impedance.web.cern.ch/impedance/USPAS/WakeFieldsAndImpedances.pdf.

[94] V. Baglin et al. Conceptual design of the LHC interaction region upgrade – phase-I, 2008. CERN LHC Project Report 1163.

[95] E. Métral and F. Caspers. Answers to Nicolaas Kos for his paper "Cold beam vacuum system for the LHC IR upgrade phase-1", 2010. http://impedance.web.cern.ch/impedance/LHC/PumpingSlots_AnswersToNicolaasKos_Final.pdf.

[96] N. Kos, 2010. Private communication.

[97] A. Mostacci. *Beam-Wall Interaction in the LHC Liner*. PhD thesis, Università degli Studi di Roma La Sapienza, 2001. http://cdsweb.cern.ch/record/516355/files/thesis-2001-014.pdf.

[98] C. Zannini, E. Métral, G. Rumolo, and B. Salvant. Impedance simulations of the LHC beam screen including the weld, 2010. http://impedance.web.cern.ch/impedance/documents/CzanniniBeemscreen_weld_impedance.pptx.

[99] F. Caspers, M. Morvillo, F. Ruggiero, J. Tan, and H. Tsutsui. Surface resistance measurements of LHC dipole beam screen samples. In *7th European Particle Accelerator Conference, Vienna, Austria*, pages 376–378, 2000.

[100] V. Baglin and N. Kos. Beam screens for the LHC long straight sections, 2007. Functional Specification, LHC Project, LHC-VSS-ES-0002 rev 1.3, EDMS Document No. 334961, CERN.

[101] C. Rathjen. Electrical measurements of beam screen wall samples in magnetic fields, 2007. Investigation report, LHC, EDMS Document No. 329882, CERN.

[102] M. Martini. An introduction to transverse beam dynamics in accelerators. In *Joint Universities Accelerator School - JUAS: Accelerator Physics and Associated Technologies, Archamps, France, 1996*. CERN, Jan.-Mar. 1996. Report No. CERN-PS-96-011-PA, http://cdsweb.cern.ch/record/311384/files/ps-96-011.pdf.

[103] L. Rivkin. Introduction to particle accelerators, lecture on imperfections, . Course at EPFL, Fall 2010, http://lpap.web.psi.ch/Fall10/pdfs/Imperfections.pdf.

[104] A. Burov and V. Lebedev. Coherent motion with linear coupling. *Phys. Rev. ST Accel. Beams*, 10 (044402), 2007.

[105] P. B. Wilson and L. Rivkin. Threshold current for the transverse instability in PEP, 1982. SLAC, PEP-NOTE-374, Stanford, CA.

[106] K. Satoh and Y. Chin. Transverse mode coupling in a bunched beam. *Nucl. Instr. Meth.*, 207, 1983.

[107] J. Scott Berg. *Coherent Modes for Multiple Non-rigid Bunches in a Storage Ring*. PhD thesis, Stanford Univ., 1996. SLAC-R-478.

[108] G. Rumolo and E. Métral. Multi-bunch simulations with HEADTAIL. In *23rd Particle Accelerator Conference, Vancouver, Canada*, pages 4661–4663, 2009.

[109] J. Gareyte, J. P. Koutchouk, and F. Ruggiero. Landau damping, dynamic aperture and octupoles in LHC, 1997. CERN LHC Project Report 91 (revised).

[110] E. Métral, N. Mounet, and B. Salvant. Single-bunch instability studies in the LHC at 3.5 TeV/c, 2010. Presentation, CERN/BE/ABP/LCU meeting, http://impedance.web.cern.ch/impedance/documents/SBInstabilityStudiesInTheLHCAt3500GeV_LCU.pdf.

[111] S. Fartoukh and O. Brüning. Field quality specification for the LHC main dipole magnets, 2001. CERN LHC Project Report 501.

[112] R. Bartolini and F. Schmidt. SUSSIX: A computer code for frequency analysis of non–linear betatron motion, 1998. Report No. CERN-SL-Note-98-017.

[113] M. J. Corinthios. Laplace spectrum for exponential decomposition and pole-zero estimation. *IEE Proc.-Vis. Image Signal Process.*, 148:305–314, 2001.

[114] G. Arduini, T. Bohl, K. Cornelis, W. Höfle, E. Métral, and F. Zimmermann. Beam observations with electron cloud in the CERN PS & SPS complex. In *Ecloud'04: 31st Advanced ICFA Beam Dynamics Workshop on Electron-Cloud Effects*, pages 31–47, 2004. CERN–2005–001, CARE-Conf-05-001-HHH, LBNL-56372, SNS-104000000-TR0024-R00.

[115] Y. Ohnishi, H. Fukuma, E. Kikutani, K. Oide, and M. Tobiyama. Study of fast ion instability at KEKB electron ring. In *7th European Particle Accelerator Conference, Vienna, Austria*, pages 1167–1169, 2000.

[116] E. Métral. Bunched-beam transverse coherent instabilities, 2009. USPAS Course on Collective Effects in Beam Dynamics for Particle Accelerators, Albuquerque, New Mexico, USA, http://impedance.web.cern.ch/impedance/USPAS/BunchedBeamTransverseCoherentInstabilities.pdf.

[117] E. Métral. Transverse instabilities, 2009. CERN Accelerator School (CAS), Intermediate Accelerator Physics Course, Darmstadt, Germany, http://emetral.web.cern.ch/emetral/CAS09course/TransverseInstabilities.pdf.

[118] A. W. Chao. Transverse instability excited by R.F. deflecting modes for PEP, 1979. SLAC/PEP-Note-321.

[119] G. Arduini, W. Herr, E. Métral, and T. Pieloni. Alternative bunch filling schemes for the LHC, 2007. CERN LHC Project Note 401.

[120] J. Scott Berg and F. Ruggiero. Landau damping with two-dimensional betatron tune spread, 1996. CERN SL-AP-96-71 (AP).

[121] G. Rumolo et al. Electron cloud observation in LHC. In *2nd International Particle Accelerator Conference, San Sebastian, Spain*, 2011.

[122] J. J. Scott Berg and R. D. Ruth. Transverse instabilities for multiple nonrigid bunches in a storage ring, 1995. SLAC-PUB-95-6829.

[123] E. W. Weisstein. Cartesian coordinates. MathWorld - A Wolfram Web Resource, 2011. http://mathworld.wolfram.com/CartesianCoordinates.html.

[124] M. Abramowitz and I. A. Stegun, editors. *Handbook of Mathematical Functions With Formulas, Graphs, and Mathematical Tables*. US Dep. of Commerce, National Bureau of Standards, 1972. Tenth Printing, with corrections, http://www.iopb.res.in/~somen/abramowitz_and_stegun/toc.htm.

[125] A. Erdélyi, W. Magnus, F. Oberhettinger, and F. G. Tricomi. *Higher Transcendental Functions*, volume 2. McGraw-Hill, 1953.

[126] A. Erdélyi, W. Magnus, F. Oberhettinger, and F. G. Tricomi. *Tables of Integral Transforms*, volume 1. McGraw-Hill, 1954.

[127] C. G. Lambe. A generalization of Bessel's integrals. *J. London Math. Soc.*, 6:257–259, 1931.

[128] G. N. Watson. *A Treatise on the Theory of Bessel Functions*. Cambridge University Press, 2nd edition, 1966.

[129] E. W. Weisstein. Fourier series. MathWorld - A Wolfram Web Resource, 2011. http://mathworld.wolfram.com/FourierSeries.html.

[130] W. Herr and F. Schmidt. A MAD-X primer, 2004. Report No. CERN-AB-2004-027-ABP, http://frs.web.cern.ch/frs/report/mad_x_primer.pdf.

[131] E. Laface, 2010. Private communication.

[132] 2011. LHC optics web page, http://proj-lhc-optics-web.web.cern.ch/proj-lhc-optics-web/.

[133] L. Rivkin. Introduction to particle accelerators, lecture on linear optics, . Course at EPFL, Fall 2009, http://lpap.web.psi.ch/Fall09/pdfs/LinearOptics09.pdf.

[134] B. T. Kelly. *Physics of Graphite*. Applied Science, 1981.

[135] J.-C. Charlier, X. Gonze, and J.-P. Michenaud. First-principles study of the electronic properties of graphite. *Phys. Rev. B*, 43(6), 1991.

[136] A. Rossi, 2010. Private communication.

[137] A. Bertarelli, 2011. Private communication.

[138] O. Aberle, 2011. Private communication.

[139] W. Weterings, 2011. Private communication.

[140] E. Métral. Resistive heat load for the TDI, 2004. Presentation, LCE meeting, https://impedance.web.cern.ch/impedance/LHC/TDI/ResistiveHeatLoad_TDI%_11-06-2004.ppt.

[141] F. Loprete, 2010. Private communication.

[142] S. Calatroni, 2012. Private communication.

[143] W. Vollenberg. Resistive titanium coating on BN absorber blocs for TDU. Technical report, 2010. EDMS Document No. 1085514, CERN.

[144] D. R. Lide, editor. *CRC Handbook of Chemistry and Physics*. CRC Press, 89th edition, 2009.

[145] O. Aberle, A. Bertarelli, S. Calatroni, B. Riffaud, W. Vollenberg, and W. Weterings, 2005. Electrical resistivity measurements on graphite and CFC materials, and datasheets from the providers (unpublished).

[146] A. I. Ryazanov et al. Effect of high-energy proton beam irradiation on the behaviour of graphite collimator materials for LHC, 2010. CERN-ATS-Note-2010-042 MD.

[147] O. Aberle and F. Caspers. Surface resistance on collimator jaw material, 2004. Presentation, CERN LHC collimation working group, http://lhc-collimation.web.cern.ch/lhc-collimation/files/OAberle_19Mar04.pdf.

[148] Boron nitride grade CA datasheet, 2002. http://accuratus.com/boron.html, AccuratusCeramicCorp.

[149] BN 5000 datasheet, Syntec Keramik Ltd.

[150] R. W. Assmann, 2011. Private communication.

[151] L. Bruno, 2011. Private communication.

[152] N. Mounet, X. Buffat, R. Bruce, W. Herr, E. Métral, G. Rumolo, and B. Salvant. Impedance effects on beam stability. In *LHC Beam Operation Workshop, Evian, France*, 2011.

[153] B. Salvant, R. W. Assmann, R. Bruce, A. Rossi, G. H. Hemelsoet, W. Venturini, V. Kain, G. Crockford, H. Burkhardt, W. Höfle, E. Métral, and N. Mounet. Status from the collimator impedance MD in the LHC, 2010. Presentation, CERN/BE/ABP/LCU meeting, https://impedance.web.cern.ch/impedance/documents/LCU-10June2010.ppt.

[154] B. Salvant, V. Baglin, H. Bartosik, C. Bracco, J. Esteban Muller, E. Métral, N. Mounet, G. Papotti, S. Redaelli, and J. Uythoven. TDI impedance MD, 2011. Presentation at the 13$^{\text{th}}$ LHC Studies Working Group, https://indico.cern.ch/getFile.py/access?contribId=4&resId=1&materialId=slides&confId=161034.

[155] R. W. Assmann, R. Bruce, F. Burkart, M. Cauchi, D. Deboy, L. Lari, E. Métral, N. Mounet, S. Redaelli, A. Rossi, B. Salvant, G. Valentino, and D. Wollmann. Summary of MD on nominal collimator settings, 2011. CERN-ATS-Note-2011-036 MD.

[156] E. Métral, B. Salvant, and N. Mounet. Stabilization of the LHC single-bunch transverse instability at high-energy by Landau octupoles. In *2nd International Particle Accelerator Conference, San Sebastian, Spain*, pages 775–777, 2011.

Nicolas Mounet

French citizen, born on December 2nd, 1980

Mobile phone : (33).6.71.61.16.21
Email : nicolas.mounet@m4x.org

EDUCATIONAL BACKGROUND

From Feb. 2009 **Ecole Polytechnique Fédérale de Lausanne** (Lausanne, Switzerland), doctoral program in physics. Specialization in accelerator and beam physics, with emphasis on collective effects, in particular beam-coupling impedances and related instabilities. Teaching assistant for the Master's level course « Introduction to Particle Accelerators ».

PhD thesis supervised by Prof. Leonid Rivkin and Dr. Elias Métral, entitled « The LHC transverse coupled-bunch instability »; defense on January 26th, 2012.

Sept. 2003 – June 2005 **Massachusetts Institute of Technology** (Cambridge, USA), department of materials science and engineering. Broad and in-depth materials science studies.

Master's thesis entitled: « Structural, vibrational and thermodynamic properties of carbon allotropes from first-principles: diamond, graphite, and nanotubes ».

Sept.2000 – July 2003 **Ecole Polytechnique** (Palaiseau, France) – General scientific education including physics, mechanics and applied mathematics. Majoring in physics during third year, especially solid state physics and quantum optics.

Sept. 1998 – June 2000 Lycée du Parc (Lyon, France) – Training classes, preparing entrance examination for the « Grandes écoles d'ingénieur ». First place award in physics in a written contest in Lyon in October 1998.

June 1998 « Baccalauréat » in Sciences after high school, passed with distinction.

WORK EXPERIENCE

From Feb. 2009 **PhD Student with Dr. Elias Métral, beam physics department, European Organization for Nuclear Research (Geneva, Switzerland)**

Study of the LHC coupled-bunch transverse instabilities, from the theoretical computation of the self-generated fields responsible for it, until the simulations of their effects for various configurations of the machine, comparing the final results to beam-based measurements in the LHC. In particular, derivation of new impedances theories, and extension and parallelization of a wake fields simulation code.

Publications:

- F. Roncarolo, F. Caspers, T. Kroyer, E. Métral, N. Mounet, B. Salvant and B. Zotter, « *Comparison between laboratory measurements, simulations, and analytical predictions of the transverse wall impedance at low frequencies* », Phys. Rev. ST Accel. Beams 12, 084401 (2009),
- N. Mounet and E. Métral, « *Electromagnetic fields created by a macroparticle in an infinitely long and axisymmetric multilayer beam pipe* », CERN-BE-2009-039 (2009),
- N. Mounet and E. Métral, « *Electromagnetic fields and beam coupling impedances in a multilayer flat chamber* », CERN-ATS-Note-2010-056 TECH (2010),
- N. Mounet and E. Métral, *« Impedances of an infinitely long and axisymmetric multilayer beam pipe: matrix formalism and multimode analysis »*, Proceedings of IPAC'10, Kyoto, Japan, p. 2039-2041 (2010),
- N. Mounet and E. Métral, *« Generalized form factors for the beam coupling impedances in a flat chamber »*, Proceedings of IPAC'10, Kyoto, Japan, p. 2042-2044 (2010),
- N. Mounet and E. Métral, *« The six electromagnetic field components at low frequency in an axisymmetric infinitely thick single-layer resistive beam pipe »*, Proceedings of IPAC'10, Kyoto, Japan, p. 2048-2050 (2010),
- R. Mutzner, N. Mounet, T. Pieloni, G. Rumolo and R. Tomás, *« Multi-bunch effect of resistive wall in the CLIC BDS »*, Proceedings of IPAC'10, Kyoto, Japan, p. 2051-2053 (2010),
- N. Mounet and E. Métral, *« Impedances of two dimensional multilayer cylindrical and flat chambers in the non-ultrarelativistic case »*, Proceedings of HB2010, Morschach, Switzerland, p. 353-357 (2010),

– N. Mounet, E. Metral, W. Höfle, R. Alemany Fernandez, D. Jacquet, V. Kain, L. Ponce, S. Redaelli, R. Suykerbuyk, D. Valuch « *Transverse coupled-bunch instability rise times in the LHC at injection and top energy* », CERN-ATS-Note-2011-035 MD (2011),

– N. Mounet, E. Métral and G. Rumolo, *« Simulation of multibunch motion with the HEADTAIL code and application to the CERN SPS and LHC »*, Proceedings of IPAC'11, San Sebastian, Spain, p. 778-780 (2011),

– N. Biancacci, N. Mounet, E. Métral, B. Salvant, C. Zannini, N. Biancacci, M. Migliorati, A. Mostacci, L. Palumbo, Q. Qin and N. Wang, *« Impedance calculation for simple models of kickers in the non-ultrarelativistic regime »*, Proceedings of IPAC'11, San Sebastian, Spain, p. 772-774 (2011),

– E. Métral, B. Salvant and N. Mounet, *« Stabilization of the LHC single-bunch transverse instability at high-energy by Landau octupoles »*, Proceedings of IPAC'11, San Sebastian, Spain, p. 775-777 (2011),

– E. Koukovini, K.S.B. Li, N. Mounet, G. Rumolo and B. Salvant, *« Impedance effects in the CLIC damping rings »*, Proceedings of IPAC'11, San Sebastian, Spain, p. 1111-1113 (2011),

– N. Mounet, X. Buffat, R. Bruce, W. Herr, E. Métral, G. Rumolo and B. Salvant, *« Impedance effects on beam stability »*, LHC Beam Operation Workshop, Evian, France (2011).

Sept. 2005 – Jan. 2009

Researcher at the Michelin technology center (Clermont-Ferrand, France)

Experimental study and computational modeling of the mechanical behavior of rubber compounds under various loading conditions. Responsible for the scientific and technical side of the project « Constitutive laws for rubbers ». Supervision of trainees.

Jan. 2004 – June 2005

Research assistant in Prof. Nicola Marzari's group, department of materials science and engineering, MIT (Cambridge, USA)

Study of the structural, vibrational and thermodynamical properties of carbon materials such as diamond, graphite, graphene and nanotubes, using atomistic computational calculations based on density-functional theory, density-functional perturbation theory and the quasi-harmonic approximation. In particular, thermal contraction of nanotubes and graphene exhibited.

Publications:

– N. Mounet & N. Marzari, « *First-principles determination of the structural, vibrational and thermodynamic properties of diamond, graphite, and derivatives* », Phys. Rev. B 71, 205214 (2005),

– N. Mounet and N. Marzari, *« Phonon dispersions of a single-wall (8,0) carbon nanotube: effects of the rotational acoustic sum rule and of surface attachment »*, Materials Research Society Symposium Proceedings, Fall meeting (2004),

– N. Mounet, Master's thesis, http://hdl.handle.net/1721.1/33400 (2005).

April 2003 – July. 2003

Research internship at the Institute of semiconductor physics (Novosibirsk, Russia)

Experimental study of the growth process of compound thin-films semiconductors such as GaAsP and InAsP, using molecular beam epitaxy.

Sept. 2000 – May 2001

Leadership training (France)

Two months at the Ecole Supérieure Militaire de St-Cyr de Coëtquidan, then junior officer, part of a team supervising the training of young soldiers, at the 511ème Régiment du Train.

LANGUAGES AND OTHER SKILLS

French	Native language.
English	Fluent: two years studying in the USA.
Russian	Good skills: a total of six months spent in Russia, including a one month linguistic training course and three months in a research laboratory.
Computer science	Good command of C, C++, Matlab, Python and Fortran 90 programming; skills in Mathematica; good command of Unix-like operating systems.